Hot Deformation and Corrosion Behaviour of Mg-Ce alloy

Thesis submitted to University of Hyderabad for the award of

Doctor of Philosophy

Degree in Materials Engineering

by

Bhomik Ketari Deogade

Under the supervision of

Dr. Swati Ghosh Acharyya
Professor
SEST, UoH

School of Engineering Sciences and Technology
University of Hyderabad
Hyderabad - 500046
India

December 2023

DECLARATION

I, **Bhomik Ketari Deogade** hereby declare that this thesis work entitled ***"Hot Deformation and Corrosion Behaviour of Mg-Ce alloy"*** submitted in partial fulfilment of the requirements for the award of **Doctor of Philosophy** (in **Materials Engineering**) in the School of Engineering Sciences and Technology (SEST), University of Hyderabad is a bonafide record of the work which was carried out by me under the supervision of **Dr. Swati Ghosh Acharyya.** I also declare that this thesis has not been submitted earlier, as a whole or in part, to this University or any other University/ Institution for the award of any degree or equivalent.

14/12/2023

(Bhomik Ketari Deogade)
Registration Number: 12ETPM02
School of Engineering Sciences and Technology
University of Hyderabad

CERTIFICATE

This is to certify that the thesis work entitled ***"Hot Deformation and Corrosion Behaviour of Mg-Ce alloy"***, submitted by **Bhomik Ketari Deogade** bearing Reg. No. **12ETPM02** in partial fulfilment of the requirements for the award of the degree of **Doctor of Philosophy** in **Materials Engineering** is a bonafide record of research work that has been carried out by him under our guidance and supervision. The content of this thesis has not been submitted earlier, as a whole or in part, to this or any other University/Institution for the award of any degree or equivalent.

14/12/23

Thesis Supervisor

Prof. Swati Ghosh Acharyya
Professor
Materials Engineering
School of Engineering Sciences
and Technology
University of Hyderabad
Hyderabad

Approved by

14/12/2023

Prof. Jai Prakash Gautam
Dean
School of Engineering Sciences and Technology
University of Hyderabad

CERTIFICATE

This is to certify that the thesis entitled "**Hot Deformation and Corrosion Behaviour of Mg-Ce alloy**" submitted by **Bhomik Ketari Deogade** bearing registration number **12ETPM02** in partial fulfillment of the requirements for award of **Doctor of Philosophy** (in **Materials Engineering**) in the School of Engineering Sciences and Technology (SEST) is a bonafide work carried out by him under my supervision and guidance.

This thesis is free from plagiarism and has not been submitted previously in part or in full to this or any other University or Institution for award of any degree or diploma.

Parts of this thesis have been published in

1. **Bhomik Ketari Deogade** ***et. al.*** Transaction of Indian Institute of Metals. (doi.org/10.1007/s12666-023-03022-z). Chapter 4, Section 4.1
2. **Bhomik Ketari Deogade** has made the presentation in the following conferences
    1. NMD-ATM 2015, Chapter 4, Section 4.1
    2. iMagCon 2016, Chapter 4, Section 4.2

Further, the student has passed the following courses towards fulfillment of course work requirement for Ph.D.

Course code	Course Title	Credits	Pass/Fail
MT801	Thermodynamics and Phase Equilibria	4	Pass
MT802	Characterization of Materials	4	Pass
MT803	Advanced Engineering Mathematics	4	Pass
MT804	Seminar	2	Pass
MT805	Mechanical behaviour of Materials/Selection of Materials	4	Pass
MT806	Concepts of Materials Science	4	Pass
MT807	Materials Processing and Characterization Laboratory	4	Pass
MT808	Dislocation and Plasticity	2	Pass
MT601	Research Methodology	4	Pass

14/12/23

Supervisor

14/12/2023

Dean SEST

Dr. Jai Prakash Gautam
Professor, SEST
University of Hyderabad
Hyderabad-500 046.

ACKNOWLEDGEMENTS

Even though only my name appears on the cover of this dissertation, a great many people have contributed to its production. I owe my gratitude to all those people who have made this dissertation possible.

First and foremost, I would like to extend my deepest gratitude to my doctoral supervisor Dr. Swati Ghosh Acharyya, Associate Professor, School of Engineering Sciences and Technologies, University of Hyderabad for her commendable and unique guidance, constant encouragement, precious suggestions and enthusiasm during my PhD. I am indebted for her expertise, keen interest and also freedom to execute my doctoral work.

Secondly, I would like to express my honor to my co-supervisor Dr. K S Suresh, Assistant Professor, Metallurgical and Materials Engineering Department, Indian Institute of Technology, Roorkee for his support. The ecstasy and fervour he has for research were contagious and motivational for me. Needless to say that none of this would have been possible without his dedicated mentorship and drive.

I would be eternally grateful to my project advisor Prof. Satyam Suwas, Chairman, Department of Materials Engineering, Indian Institute of Science, Bangalore, for initiating this research work under National Resource Centre – Materials, Department of Materials Engineering, Indian Institute of Science, Bangalore and SEST, University of Hyderabad, Hyderabad. His tremendous patience, guidance and generosity during the tenure of this research that helped me mature from faculty to a visiting researcher. Without his constant support and encouragement this research would have been impossible. In particular, I cherish our discussions not only on matters of science but as well as several mundane topics that will always enliven my spirits in the future.

I am grateful to Prof. Jai Prakash Gautam, Dean, School of Engineering Sciences and Technology, for always pushing me a wee bit further. My deepest respect to former Deans Prof. K Bhanu Sankara Rao, Prof. M. Sundararaman, Prof. Rajendar Singh, Prof. M. Ghanashyam Krishna and Prof. Dibakar Das for providing me an opportunity to pursue my doctoral studies and providing all the facilities in the school. It was an extremely gratifying and cherishing experience to explore the materials world from structure – properties co-relationship during my research tenure at SEST, University of Hyderabad, Hyderabad.

My esteem regards to Prof. K. Bhanu Sankara Rao, paving a road map for budding faculties to develop themselves in the materials research by introducing part-time Ph.D. Program at SEST, University of Hyderabad, Hyderabad.

I thank my doctoral committee members (Prof. Jai Prakash Gautam, Prof. R Koteswara Rao and Prof. Swati Ghosh Acharyya) for their critical comments and valuable suggestions timely.

My sincere thanks to my Texture Lab-mates, Department of Materials Engineering, Indian Institute of Science, Bangalore

Dr. Rama Krushna Sabat for initiating the very first stage of my doctoral work. Ms. Nikki Kamble for helping me to develop processing maps.

Dr. Rajib Kalsar, helping in EBSD and XRD Texture characterization as well as fixing slots for materials testing and also for being a cherished friend, and guide throughout my stay at IISc, Bangalore.

Dr. Abhishek More supported me in executing much aspects research from sample cutting to demarcation of the research plan.

Dr. Nitish Bhibhanshu helps me initially getting Fractograph and later in TEM imaging and also surfacing analytical approach on deformation kinetics and on processing maps. He also helped me in correcting the contour line in processing maps.

Dr. Atanu Chaudhari advise me correct way to draw compression stress-strain curves and also gave useful tips on sample preparation for EBSD.

Dr. Anuj Bisht helped me getting Fractograph of tensile samples.

Dr. Devender Yadav educated me how to use Orientation Imaging Microscopy Software.

Dr. Sumit Mishra and Mr. Y N Aditya who gave me unhindered scientific help regarding texture plotting.

Mr. Awadh Kishore Gupta for his practical assistance in micro-hardness measurement.

My heartfelt thanks to my other Texture Labmates, Dr. Amit Sharma, Dr. Sumit Bahl, Dr. Srijan Acharya, Dr. Chandrashekar Perugu, Dr. Gyan Shankar, Dr. Yazar, Dr. RJ Vikram, Dr. Deepak Pandey, Soumita Mondal and Tejnath. I would always treasure our tea-break discussions, late-night and weekend conversations, we had at IISc, on topics ranging from all spectrums. Many thanks for being like an extended family member to me.

My deepest respect to Dr. Indumathi Vijey, Incharge, Surface Engineering Department, DRDL, Hyderabad for extending her laboratory facilities for pursing electrochemical test. Special thanks to Ms Gayatri, SRF, and Mr. Kali Sampath and Mr. Dauv Srinivas Patel, Surface Engineering Department, DRDL, Hyderabad in completing the electrochemical test.

My sincere thanks to Dr. Ashutosh Jangde from Department of Materials Engineering, IISc, Bangalore for his technical support in analysis the result of electrochemical test.

My sincere thanks to Ms. Adapala Priyanka from Fontana Lab for extending her help in the analysis of electrochemical test results.

I am incredibly thankful to Mr. V Srikant, Scientist D, Materials Structural Development and Testing, DRDL, Hyderabad for his unhindered scientific help in microstructure characterization. Special thanks to Mr. Chammi Naidu and Mr. Vishal Kulkarni for getting microstructure at MSDT, DRDL, Hyderabad.

My sincere thanks to my students Mr. Anil Chikkam, USA and Dr. Phani Shashanka Karamched, Support Scientist, Department of Materials Engineering, Oxford University, for his help and suggestions in sample preparation for EBSD.

My sincere thanks to Dr Koundinya, IIT Madras and Mr. Sai Ram Goud, IIT Hyderabad for their help during EBSD scanning and using OIM software.

My sincere thanks to Prof. GVS Nageswara Rao, NIT Warangal, for his permission and technical support in using their Non-Destructive Testing Facility – Impluse Excitation Techniques Resonance Frequency Damping Analysis (RFDA) system for estimating the physical properties. Special thanks to Dr. P Prakash in performing Impulse Excitation Techniques

My sincere gratitude to my Corrosion Lab-mates at SEST, UoH.

First and foremost Dr. P Sunil Kumar for his comprehensive support from consumables to procedural requisites for my work.

Dr. Kamal Mankari for taking SEM microstructures.

I would like to acknowledge to Dr. Ravi Kiran for scientifically enriching with their stimulating discussions and ideas.

Amit Kumar for his invaluable contribution in EBSD imaging and many futile attempts in specimen preparation.

Dr. K V Srinivasulu for his help in merging two different plots and building confidence in me at every instant.

Dr. Santhosh for scientifically enriching with the knowledge of Electrochemical Impedance.

Dr. Y Pardhu for his encouragement and practical advice in the analysis of XRD pattern.

Moshin Hassan for his unhindered scientific help in taking microstructure and TEM sample preparation. Dr. Johnny Verghese supported me during specimen preparation.

Mr. Parthidan for helping me in imaging the surface roughness in the samples.

I thank Mr. Mallesh, Dinakar Sir and Mr. Balakishen for their assistance in the lab. The help and cooperation of the nonteaching staff Mr. Venu, of the School of Engineering Sciences and Technology is highly acknowledged.

I thank my doctoral committee members for their critical comments and valuable suggestions timely.

My deepest respect to all the Faculty members of SEST, UoH.

I want to record my sincere thanks to Mr. Dhiraj Ramesh Dhote for his expertise in system administration, making my life comfortable both personally and professionally.

My heartfelt thanks to my colleagues at Mahatma Gandhi Institute of Technology, Hyderabad Dr. S P Singh from ECE Department for his generous guidance on fundamentals of Bode and Nyquist plots.

Dr. PVSL Narayana's support in all aspects being at MGIT and also reviewing by a portion of my thesis. Dr. S Santhi and Dr. J Jhansi motivated me to complete my thesis time to time.

Dr. RVSM Ramakrishna, Dr. M Vijayalakshmi, and Paul M Souza from MME Department for their professional and practical assistance during my research.

My deepest gratitude towards men of golden era at MGIT, Dr. J Viplava Kumar, my torchbearer, and Mr. P K Subramanian, my HoD.

Let me take this opportunity in thanking my school buddies Dr. Vinod Nair, Mr. Rajesh Vaidya and Mr. Vijay Kawade.

Everlasting friendship of my Undergraduates friends at NIT, Jamshedpur: Dr. Subbarao Mekala, Mr. Samir Patra, Chandan Jyoti Das, Mr. Pradeep Bansod, Mr. Pravin Jangle, and Dr. Devendra Wasnik who gave me first job break before MGIT.

Small but cherishful association with Postgraduate pals at IIT Roorkee: Mr. Puneet Bandari, Mr. Vidhu Shekar Pandey, Mr. Kailash Dahiya, Mr. Vilas Dabrase, Mr. Nishant Bhalerao, Mr. Pravin Motghare and Mr. Bhupesh Patil.

Mere thanking will be very small, in fact words are insufficient for giving me second life for an Unknown Railway protection force person, who saved me getting under the wheel while lighting the train at Kalyan Junction Railway Station.

Loving regards to my sibling Mr. Manish Ketari Deogade and Ms. Karuna for putting on toe.

I wish to express my most profound gratitude and reverence to my parents, Late Ketari Dewaji Deogade and Mrs. Nilima Ketari Deogade, for their endless perseverance, for their epitome of patience and strong support that helped me go through every hardship in my life. Their love and belief in my abilities always picked me whenever I have felt down, and words cannot suffice my gratitude for their presence in my life.

My Special thanks to my better half Mrs. Smita for her unconditional love and support provided me a deep sense of fulfilment and security. Without her constant encouragement and understanding I would not have finished my Ph.D. work and subsequently the Thesis.

Above all, I owe my thanks to my idols for inspiring and giving strength and the required patience to wade through the ebbs and tides of my research.

Contents

List of Figures ……... i
List of Tables ……. ii
List of Abbreviations ……. iii
Abstract ……. iv

Chapter 1: INTRODUCTION ……..... 1
1.1 Introduction……...……..... 1
1.2 Motivation and Objective of the Work ……..... 5
1.3 Organization of Thesis ……..……... 7

Chapter 2: LITERATURE REVIEW……. 9
2.1 Deformation Behaviour of Mg and its alloys …….. 9
2.1.1 Slip Modes of Deformation in Mg and its alloys……..... 11
2.1.2 Deformation Twinning …….…… 17
2.1.3 Detwinning …….…….. 21
2.1.4 Shear Band Formation …….……. 23
2.1.5 Effect of Grain Size …….……. 27
2.1.6 Evolution of Texture…….……. 28
2.2 Restoration Mechanisms …….……. 29
2.2.1 Recovery in Mg alloys…….…….. 30
2.2.2 Recrystallization in Mg alloys…….…….. 31
2.2.2.1 Recrystallisation Mechanisms of Nucleation……. 33
2.2.2.1.1 Grain Boundary Nucleation …….……... 34
2.2.2.1.2 Sub-Grain Boundary Migration …….. 35
2.2.2.1.3 Shear Band Nucleation (SBN) …… 36
2.2.2.1.4 Deformation Twinning Nucleation (DTN) ……. 36
2.2.2.1.5 Particle Stimulated Nucleation (PSN) ……. 38
2.2.2.2 Microstructure Evolution during Recrystallization in Mg alloys …….. 38
2.2.2.3 Progression of Textures of Recrystallization ……. 43
2.2.2.4 Grain Rotation during Recrystallization …… 45
2.3 Magnesium Rare Earth (RE) alloys ……. 46

2.3.1 Phase Transformations in Mg-REs alloys ……. 46
2.3.2 Mg-Ce Phase Diagram …….. 46
2.3.3 Texture Alteration in Mg alloys: Effect of RE Element addition……..... 47
2.3.4 Recovery in Mg-RE alloys…… 51
2.4 Processing Maps……... 52
2.5 Numerical Methods for Constitute Analysis……. 54
2.5.1 Hyperbolic Sine Arrhenius Model……. 55
2.5.1.1 Temperature-Strain rate compensation to calculate predicted flow stress……... 56
2.5.1.2 Strain-compensation to calculate predicted flow stress…….. 56
2.5.1.3 Strain rate-compensation to calculate predicted flow stress…… 57
2.5.2 Verification of the Constitutive Equation Accuracy…….. 57
2.6 Rolling…….. 58
2.6.1 Anisotropy Calculation…….. 59
2.7 Corrosion Behaviour of Hot Rolled Mg alloy…….. 60
2.7.1 Fundamentals of Metallic Corrosion…….. 61
2.7.1.1 Electrochemical characteristics of Corrosion……..… 61
2.7.1.2 Thermodynamics of Corrosion……... 63
2.7.1.3 Kinetics of Corrosion …… 65
2.7.1.4 Passivation Behaviour of Metals……..… 66
2.7.2 Electrochemistry of Mg and Mg Alloys……. 67
2.7.2.1 Corrosion behaviour of Pure Magnesium……..... 68
2.7.3 Electrochemical Techniques…….. 70
2.7.3.1 Potentiodynamic Polarization Test……. 70
2.7.3.2 Open Circuit Potential ……..…… 71
2.7.3.3 Potentiodynamic Polarization (PDP) measurement of Mg alloys ……... 71
2.7.3.2 Electrochemical Impedance Spectroscopy……. 72
2.6.3.3 Electrochemical Impedance Spectroscopy of Mg and its alloy……... 78

Chapter 3: EXPERIMENTAL DETAILS ……..……..... 80
3.1 Materials Used ……. 80
3.2 Material Processing and Testing Methods ……..... 80
3.2.1 Hot Compression Test ……..... 80
3.2.2 Hot Rolling ……..... 81

3.2.3 Room Temperature Uniaxial Tensile Test …… 82
3.2.4 Room Temperature Vickers Hardness …….. 83
3.3 Electrochemical Testing and Characterization ……. 84
3.3.1 Potentiodynamic Polarization (PDP) Test …… 84
3.3.2 Electrochemical Impedance Spectroscopy (EIS) ……. 85
3.4 Metallography Practices …….. 86
3.4.1 Optical Microscopy (OM): Metallurgical Microscope …….. 86
3.4.2 Scanning Electron Microscopy (SEM) ……. 88
3.4.3 Electron Backscattered Diffraction (EBSD) ……. 89
3.4.4 Surface Profilometer ……. 90
3.4.5 X-Ray Diffraction (XRD) ……. 90

Chapter 4: RESULTS AND DISCUSSIONS ……..……..... 92
4.1 Hot Deformation Behaviour ……. 92
4.1.1 Starting Material ……... 92
4.1.2 Hot Compression Test ……... 93
4.1.2.1 Stress - Strain Curves ……. 94
4.1.2.2 Processing Maps ……..... 98
4.1.2.2.1 Stability Domain ……. 100
4.1.2.2.2 Instability Domain ……..... 100
4.1.3.3 Microstructure Evolution ……... 101
4.1.3.5 Constitutive Equation Analysis: Hyperbolic Sine Arrhenius Model …….. 108
4.1.3.5.1 Temperature-Strain rate compensation to calculate predicted flow stress ……. 111
4.1.3.5.2 Strain-compensation to calculate predicted flow stress ……. 113
4.1.3.5.3 Strain rate-compensation to calculate predicted flow stress …….. 115
4.1.3.6 Verification of the Constitutive Equations' Accuracy ……. 116
4.2 Effect of Strain Path on Anisotropic Behaviour of Hot Rolled Mg-0.5wt% Ce alloy. 118
4.2.1 X-Ray Diffraction (XRD) …… 118
4.2.2 Microstructural Analysis …….. 119
4.2.2.1 SEM and SEM-EDS analysis …… 119
4.2.2.2 EBSD Analysis …….. 123
4.2.3 Texture Evolution: Local Texture ……. 128
4.2.2 Hardness Test of As-Extruded, UDR and MSCR ……. 131

4.2.3 Tensile Test ……... 132
4.2.3.1 True Stress-Strain Curve ……... 132
4.2.3.2 Anisotropy Calculations ……. 134
4.2.3.3 Fractography …….. 137
4.3 Effect of Deformation Modes on Corrosion Behaviour of Mg-0.5wt%Ce alloy ……... 139
4.3.1 Surface Roughness Measurement Before Corrosion Test …… 139
4.3.2 Corrosion/Electrochemical Testing ……... 140
4.3.2.1 Potentiodynamic Polarization (PDP) Measurements …… 141
4.3.2.2 Electrochemical Impedance Spectroscopy (EIS) Measurement ……... 147
4.3.2.3 Corrosion Product Film …….. 154
4.3.2.4 Corrosion Morphology …….. 156

Chapter 5: CONCLUSIONS ……... 158

SCOPE OF FUTURE WORK …… 161

REFERENCES …… 162

List of Figures

Chapter 1

Fig. 1.1 Variation of specific strength with elongation-to-failure for Mg alloys vis-à-vis some other materials

Fig. 1.2 Materials property (a) Quasi-static strength vs density and (b) Specific stiffness vs Specific strength

Fig. 1.3 (a) Comparative weight analysis of a Volkswagen Passat boot lid across various materials and (b) Assessment of variation of mass savings potential in automobile sectors for high performance materials with mild steel in body frame panels, considering the corresponding flexural stiffness and flexural strength.

Chapter 2

Fig. 2.1 Stacking sequence in *hcp* structure

Fig. 2.2 Hexagonal prism (a) Unit cell with a_1, a_2 and c axis, (b) atomic position in special distribution and (c) in basal plane

Fig. 2.3 Slip planes in *hcp* structures

Fig. 2.4: Mechanisms of basal dislocations cross-slipping onto planes of prismatic.
(a) Occurrence of cross slip at a restriction of a stacking fault on basal plane known as Friedel mechanism and (b) the double jog mechanism occurs by the prismatic dislocations as the jogs between basal planes

Fig. 2.5 Progression of the nucleation of <c+a> dislocation in pyramidal slip system

Fig. 2.6 Twinning of the host crystal (a) Atomic reorientation in twinned and host crystal and (b) Part of twinned and host crystal arranged on same twinned plane called habit plane.

Fig. 2.7: Planes and directions within a twin. K_1 represents the twinning plane or habit plane, and K_2 is the reciprocal twinning plane, P is the shear plane. η_1 and η_2 are the twinning and reciprocal twinning directions.

Fig. 2.8 Representation of $\{10\bar{1}1\}$ - $\{10\bar{1}2\}$double twin along the $<11\bar{2}0>$ axis in the basal planes

Fig. 2.9 Microstructures acquired during *in-situ* tensile test in various loading states with direction as shown by arrows.

Fig. 2.10 Variation of twin volume fraction and microstructural progression of Mg-Al-Mn alloy during plastic deformation

Fig. 2.11 Shear band formation from the clusters of recrystallized grains

Fig. 2.12 Shear band structure and $\{10\bar{1}2\}-$ twins in 30% reduction during cold rolling of pure Mg shown in EBSD Kikuchi band contrast map.
Fig. 2.13 Shear band observed in deformed Mg 3wt-%Y taken from TEM-BF images along with corresponding pole figures.
Fig. 2.14 Shear band formation model in pure Mg and alloys of Mg-Y
Fig. 2.15 **G**rowth potential of a recrystallization nucleus in a deformed structure
Fig. 2.16 DRX at grain boundaries after deformation
Fig. 2.17 (a) DRX process shows serration at grain boundaries resulting in (b) smaller stress free grains.
Fig. 2.18 Meyers model of rotational DRX (RDRX) mechanism
Fig. 2.19 Nucleation of recrystallized small grains inside shear bands in the TEM micrograph
Fig. 2.20 DRX inside twins in AZ31 alloy in (a) SE mode of SEM and (b) Optical images
Fig. 2.21 (a) Zone of Deformation around the particle [120]; (b) finely recrystallized grains forming next to the particles.
Fig. 2.22 (a) Together with IPF scatter data, green recrystallized grains predominate over blue deformed grains with a misorientation of 30^ <0001> in magnesium. The distribution map of grain boundary misorientation (b) displays the maximum misorientation at 30˚.
Fig. 2.23 Twinning behaviour in Mg single crystals at 200 °C
Fig. 2.24 At 370°C, single crystals of magnesium exhibit distorted and double DRX textures.
Fig. 2.25 Representation of instantaneous slip instigated lattice rotation and break up while DRX in compression twins and double twins.
Fig. 2.26 Pinning and variant inhibition
Fig. 2.27 Mg-Ce phase diagram
Fig. 2.28 The $<11\bar{2}1>$ directions of shear band orientations parallel to ED in Mg-Res
Fig. 2.29 Recrystallization by shear band in hot rolled ZE10 alloy.
Fig. 2.30 Schematic of a three-electrode electrochemical cell setup
Fig. 2.31 Pourbaix diagram of pure metals (aluminium).
Fig. 2.32 Theoretical current – potential diagram for a metallic electrode
Fig. 2.33 Polarization diagram exhibiting transitions from active corrosion to passive behaviour and to the transpassive state.
Fig. 2.34 Pourbaix Diagram of pure Mg
Fig. 2.35 Potentiodynamic polarization curve of pure Mg in 3.5wt.% NaCl solution
Fig. 2.36 Schematic illustration of (a) the Nyquist plot and (b) the Bode plot for a resistor.

Fig. 2.37 Schematic illustration of (a) the Nyquist plot and (b) the Bode plot for a capacitor.
Fig. 2.38 Nyquist and Bode plots for a R (RC) circuit.
Fig. 2.39 Nyquist plot with and without depression
Fig. 2.40 Electrochemical Impedance Spectroscopy – Nyquist plot for (a) pure Mg and Alumina coated Mg metal in 3.5wt.% NaCl and (b) for pure Mg, AZ31 and AZ91 alloys in 3.5wt.% NaCl after 1 ½ h of exposure.

Chapter 3

Fig. 3.1 Compression test material (a) sample with dimension and (b) test samples extracted from extruded rod.
Fig. 3.2 Simple representation of the strain paths in rolling routes: (a) UDR and (b) MSCR
Fig. 3.3 Tensile test samples: (a) Tensile test sample dimension, (b) UDR and MSCR rolled sheets cut along final RD at 0^{o}, 45^{o}, 90^{o}, and (c) UDR and MSCR rolled sheets cut along marked directions.
Fig. 3.4. Vickers hardness measurement on the sample using diamond indenter having squared-shaped pyramidal.
Fig. 3.5: Specimens of extruded rod, UDR and MSCR sheet prepared for corrosion test
Fig. 3.6. Optical arrangement of (a) Polarized Light microscopy and (b) DIC microscopy in reflected light illumination.

Chapter 4

Fig. 4.1 Inverse Pole Figure (IPF) (a) and Pole Figure Map of As-extruded samples from EBSD image
Fig. 4.2 True stress–true strain curves obtained for Mg-0.5% (wt.) Ce alloy in hot compression at 5 different temperatures and 5 different strain rates as indicated in each curve.
Fig. 4.3 Variation of flow stress with temperature from 0.1 and 0.5 strains
Fig. 4.4 True stress–true strain curves obtained for Mg-0.5% (wt.) Ce alloy in hot compression at 5 different temperatures and 5 different strain rates as indicated in each curve.
Fig. 4.5 Processing maps for Mg-0.5% (wt.) Ce alloy at 0.1 to 0.5 strain
Fig. 4.6 Optical microstructures of As-extruded specimen at 100X and 500X of compression tested specimen of Mg-0.5% (wt.) Ce alloy.
Fig. 4.7 EBSD Inverse Pole Figure (IPF) of (a) As-extruded specimen and (b-e) Compression tested specimen of Mg-0.5wt% Ce alloy.

Fig. 4.8 EBSD Grain orientation spread (GOS) microstructures of (a) As-extruded specimen and (b-g) Compression tested specimens of Mg-0.5% (wt.) Ce alloy.

Fig. 4.9 Quantification of EBSD data with (a) Grain orientation spread (GOS), (b) Grain Size distribution and (c) Grain Mis-orientation Angle of as-extruded specimen and compression tested specimens of Mg-0.5% (wt.) Ce alloy.

Fig. 4.10: Estimation of materials constants, (flow stress) vs Ln (strain rate) at (a) 0.2 strain and (b) 0.4 strain and Ln (flow stress) vs Ln (strain rate) at (c) 0.2 strain and (d) 0.4 strain

Fig. 4.11: Determination of apparent activation energy, Q estimated by material constant from Ln (sinh ($\alpha\sigma$)) Vs 1000/T at (a) 0.2 strain and 0.4 strain and Ln (strain rate) Vs Ln (sinh ($\alpha\sigma$)) at (c) 0.2 strain and 0.4 strain.

Fig. 4.12: Estimation of materials constants ln(A) using ln(Z) vs ln (sinh ($\alpha\sigma$)) at (a) 0.2 strain and (b) 0.4 strain.

Fig. 4.13: Comparison of true stress - strain (a) Experimental flow stress and Predicted flow stress modified constitutive equation by Temperature-Strain rate compensated and (b) Consolidated comparison.

Fig. 4.14: Variation of materials constant (a), (b), (c), (d), and (e) with strain fitted by 4^{th} degree of polynomial.

Fig. 4.15: Comparison of true stress-strain curves (a) Experimental flow stress and Predicted flow stress modified constitutive equation by strain-compensated and (b) consolidated comparison.

Fig. 4.16: Comparison of true stress - strain curves (a) – Experimental flow stress and Predicted flow stress using modified Zener-Holloman parameter, Z by 0.85 strain rate compensated and (b) Consolidated comparison.

Fig. 4.17: XRD of As-Extruded rod, UDR and MSCR sheet specimens

Fig. 4.18: FESEM images at 1000X and 5000X of (a) As-Extruded rod, (b) UDR and (c) MSCR sheet specimens after 20^{th} pass.

Fig. 4.19: SEM-EDS elemental mapping of (a) extruded rod, (b) UDR and (c) MSCR sheet specimens.

Fig. 4.20 EBSD – Inverse Pole Figure maps for (a) As Extruded, (b) UDR at 15^{th} pass and (c) UDR at 20^{th} pass

Fig. 4.21 EBSD – Inverse Pole Figure maps for (a) As Extruded, (b) MSCR at 15^{th} pass and (c) MSCR at 20^{th} pass.

Fig. 4.22 EBSD – Grain orientation spread maps for (a) As Extruded, (b) UDR at 15^{th} pass and (c) UDR at 20^{th} pass

Fig. 4.23 EBSD – Grain orientation spread maps for (a) As Extruded, (b) MSCR at 15th pass and (c) MSCR at 20th pass.
Fig. 4.24 EBSD microstructures statistics as Grain Size Distribution of As-Extruded compared with (a) UDR 15 and UDR 20 and (b) MSCR 15 and MSCR 20
Fig. 4.25 EBSD microstructures statistics on Misorientation Angle of As-Extruded compared with (a) UDR 15 and UDR 20 and (b) MSCR 15 and MSCR 20
Fig. 4.26 EBSD microstructures statistics on Grain Orientation Spread of As-Extruded compared with (a) UDR 15 and UDR 20 and (b) MSCR 15 and MSCR 20
Fig. 4.27 Comparison of EBSD - Pole figures at different planes for As-Extruded with hot rolled sheet specimens of UDR at 15th pass and UDR at 20th pass.
Fig. 4.28 Comparison of EBSD - Pole figures at different planes for As-Extruded with hot rolled sheet specimens of MSCR at 15th pass and MSCR at 20th pass.
Fig. 4.29: Variation of Vickers Hardness values with As-Extruded rod, and (a) based on change in strain path of UDR and MSCR sheet specimens and (b) based on angle of orientation along RD of UDR and MSCR sheet specimens.
Fig. 4.30 True Stress-True Strain curves of Tension test of (a) UDR and (b) MSCR rolled sheets cut along final RD at 0º, 45º, 90º.
Fig. 4.31 Rolled Sheet along RD at 0º, 45º, 90º Vs (a) Yield Stress, (b) Ultimate Tensile Stress, (c) % Elongation (d) Fracture Strain
Fig. 4.32 Anisotropy calculation give (a) Variation of Lankford parameter (R-value) for hot rolled UDR and MSCR sheet specimens with the angle of specimen orientation along RD and (b) Variation of Normal and Planar anisotropy parameters with modes of hot rolling (i.e., UDR and MSCR)
Fig. 4.33 Fractography of tensile tested UDR sheets cut along final RD at 0º, 45º, 90º.
Fig. 4.34 Fractography of Tensile Tested MSCR sheets cut along final RD at 0º, 45º, 90º.
Fig. 4.35: Surface roughness images of extruded rod, UDR and MSCR sheet specimens
Fig. 4.36 PDP curves of extruded, UDR and MSCR specimens after 1½ h immersed in a Test Electrolyte.
Fig. 4.37 (a) Corrosion rates and (b) Polarization resistance (Rp) of extruded, UDR and MSCR specimens after 1½ h immersion in the test electrolyte during Potentiodynamic Polarization test.
Fig. 4.38 (a) Corrosion current and (b) Corrosion potential of As-Extruded, UDR and MSCR specimens after 1½ h submersion in the test electrolyte during Potentiodynamic Polarization (PDP) test.

Fig. 4.39 Bode Plot - Variation of Frequency with Impedance (a) and Phase Angle (b) from Electrochemical Impedance Spectroscopy Test of As-Extruded, UDR and MSCR specimens after 1½ h immersion in the test electrolyte.
Fig. 4.40 Nyquist Plot – Variation between Real and Imaginary parts of Impedance from Electrochemical Impedance Spectroscopy Test of As-Extruded, UDR and MSCR specimens after 1½ h immersion in the test electrolyte.
Fig. 4.41 Equivalent Circuit Model for fitting Electrochemical Impedance Spectroscopy Test data of (a) UDR, (b) Extruded, and MSCR specimens after 1½ h immersion in the test electrolyte.
Fig. 4.42 Equivalent Circuit Model values fitted with Electrochemical Impedance Spectroscopy Test data of (a) UDR, (b) Extruded, and MSCR specimens after 1½ h immersion in the test electrolyte.
Fig. 4.43 SEM microstructure at 500X and 1000X of (a) extruded rod, (b) UDR and (c) MSCR sheets specimens after 1½ h immersion in the test electrolyte.

List of Tables

Chapter 2

Table 2.1 Slip systems in *hcp*

Table 2.2 Different modes of twinning in Mg, in terms of misorientation about <11$\bar{2}$0> axis rotation between the twin and un-twinned crystal.

Chapter 3

Table 3.1 Details of operating parameters followed in XRD.

Chapter 4

Table 4.1: 4^{th} order polynomials coefficients for the fitted materials constants and strain curves

Table 4.2 Mechanical properties from tensile test on hot rolled UDR and MSCR samples

Table 4.3 Plastic anisotropy values of hot rolled sheet in UDR and MSCR modes of rolling.

Table 4.4: Surface roughness data of extruded rod, UDR and MSCR sheet specimens

Table 4.5: Electrochemical data observed during Polarization test

Table 4.6: Electrochemical data of Polarization test after Tafel Fitting

Table 4.7. Electrochemical Impedance Spectroscopy Test results

Table 4.8: Equivalent Circuit Parameter values of Fitted Nyquist Plots

NOMENCLATURE

S.No	SYMBOL	ABBREVIATION
1	ε_u	*Uniform elongation*
2	ε_f	*Elongation to failure*
3	σ	*Stress* [MPa]
4	1-D/3-D	*One-/Three-dimensional*
5	CD	*Compression direction*
6	CRSS	*Critical resolved shear stress* [MPa]
7	DRX	*Dynamic recrystallization*
8	DTN	*Deformation twin nucleation*
9	EBSD	*Electron back scattered diffraction*
10	*fcc*	*Face-cantered cubic*
11	GOS	*Grain orientation spread* [°]
12	HSFE	*High stacking fault energy* [mJ/m2]
13	LSFE	*Low stacking fault energy* [mJ/m2]
14	HAGB	*High-angle grain boundary*
15	*hcp*	*Hexagonal close-packed*
16	IPF	*Inverse pole figure*
17	IQ	*Image quality*
18	LAB	*Low angle boundaries*
19	LD	*Longitudinal direction*
20	MRD	*Multiples of random distribution*
21	$Pdrag$	*Solute drag pressure* [J/m2]
22	PGG	*Curvature driven grain growth pressure* [J/m2]
23	PSC	*Plane strain compression*
24	PSN	*Particle stimulated nucleation.*
25	RD	*Rolling direction.*
26	REE/RE	*Rare-earth element/ Rare earth*
27	SBN	*Shear band nucleation*
28	SEM	*Scanning electron microscopy.*
29	SF	*Schmid factor*
30	TD	*Transverse direction*
31	TYS/YTS	*Tensile yield strength* [MPa]
32	UTS	*Ultimate tensile strength* [MPa]
33	XRD	*X-Ray diffraction*
34	*Z*	*Zener – Holloman Parameter*
35	*Zreal*	*Real part of Impedance*
36	*Zimag*	*Imaginary part of Impedance*
37	$\|Z\|$	*Absolute Impedance*

Abstract

Magnesium has lowest density 1.638 g/cm^3 among the structural materials, but also known for limited ductility at room temperature bearing c/a ratio of 1.624 just lower than ideal value for any *hcp* lattice. Addition of Ce in Mg improves the restricted ductility owing to limited number of deformation components and also being *hcp* lattice as in pure Mg. Improvement in ductility is attributed to the weak basal texture as in the starting material in the extruded rod. Enhancement in the ductility can be understood in term of flow behaviour of Mg-0.5 (wt%) Ce alloy to justify the deformation mechanisms. In this study, hot compression test of extruded Mg-0.5wt% Ce alloy was conducted using UTM to locate the deformation regime in the processing maps requisite for further manufacturing operations. The processing maps were generated using experimental data of flow stress spread over five temperatures from 523 K, 573 K, 623 K, 673 K to 723 K and five strain rates 0.001 s^{-1}, 0.01 s^{-1}, 0.1 s^{-1}, 1 s^{-1} and 10 s^{-1}. The deformation behaviour exhibited by the true stress-strain curves depicts flow stress increases with increase in strain rates but decreases with increase in the temperature and significantly depended on the strain. The flow stress behaviour of plastic deformation during hot compression of Mg-Ce alloy is governed by constitutive equations desired for the designing appropriate manufacturing operation for defect-free component and its service performance. A new physical model for hot deformation characteristics of Mg-Ce alloy considering constitutive equations, based on the hyperbolic-sinusoidal Arrhenius-type have been established as a function of strain rate and deformation temperature and later characterized by a temperature compensated strain rate parameter known as Zener-Holloman parameter. The authority of various material constants on true strain ranging from 0.1 to 0.5 was established using a mathematical correlation. These material constants were found to be suitable to fit the true strain dependency with 4th order polynomial relations. The average apparent activation energy for hot deformation is calculated to be 332 kJ/mol. The average absolute relative error (AARE) and correlation coefficient (R) was used to access the accuracy of the developed constitutive equations based on the obtained values of AARE was 10.59 % and R was 0.95, resulting sensible predictions of the modified flow stress. The outcome of predicted flow stress behaviour of the Mg-0.5wt%Ce alloy shows a substantial approximation over a wide range of temperature and strain rate and for larger strain using developed constitutive equations. The processing maps for the Mg-0.5wt%Ce alloy are constructed at strains of 0.1 to 0.5, based on the dynamic material model and the Prasad's instability criterion. The processing maps exhibit a domain of dynamic recovery (DRV) occurring at the temperature of 673-723 K and strain

rate of 0.001–0.1s^{-1}, corresponding to the optimum hot working regime. The instability zones of flow behaviour are also recognized from the maps possibly due to strain localization in form of shear bands. Optical microstructures and EBSD images (IPF, IQ and GOS) from FESEM explains the microstructures evolution during this deformation. The XRD-texture pole figures explain the bulk texture evolution with respect to six important planes i.e., (0002), $(10\bar{1}0)$, $(10\bar{1}1)$, $(10\bar{1}2)$, $(10\bar{1}3)$, $(11\bar{2}0)$.

Changes in strain path have been known to weaken the basal texture during deformation in of hot rolling. The effect of change in strain path on the anisotropy of hot rolled sheets made by two different modes of Uni-Directional Rolling (UDR) and Multi-Step Cross Rolling (MSCR) were employed on cuboidal samples of as-extruded Mg-0.5wt% Ce alloys. Hot rolling was induced a true strain of 2.0 at 723 K and at strain of 0.1 per pass. Tensile tests specimens were sectioned from the rolled sheet samples of UDR and MSCR modes at three (at 0°, at 45°, at 90°) different orientation angles with respect to the final rolling direction. Tensile test was executed at room temperature and at 10^{-3} s^{-1} strain rate. Dynamic recovery is found to be the dominant restoration mechanism operating during hot rolling. Both the yield strength and ultimate tensile strength values of the UDR samples obtained at different angles with respect to the rolling directions, are higher than the MSCR samples. The yield strength measured along the transverse direction of the UDR sample is much lower compared to rolling direction. The anisotropy from tensile strength is less in the MSCR samples than UDR. Ductility was found to be more for the MSCR samples compared to UDR samples. EBSD images (IPF, IQ and GOS) and the pole figure from FESEM explain the microstructures and local texture evolution during this deformation. The XRD-texture pole figures explain the bulk texture evolution with respect to six important planes (0002), $(10\bar{1}0)$, $(10\bar{1}1)$, $(10\bar{1}2)$, $(10\bar{1}3)$, $(11\bar{2}0)$.

Magnesium is most active structural metal in electromotive series can descend with minor addition of rare-earth metal (e.g., Ce,). The wrought processing route diminishes intrinsic defects of cast Mg alloy to enhance significant industrial applications. In this study, Mg-0.5 (wt%) Ce alloy hot rolled sheet with two variants i.e. unidirectional (UDR) and multi-step cross rolling (MSCR) were subjected to corrosion test using electrochemical techniques investigated in the 3.5 wt. % NaCl solution saturated with Mg $(OH)_2$ solution. Corrosion behaviour was evaluated with Tafel's polarization curve using Potentiodynamic polarization method, while Bode and Nyquist plots through electrochemical impedance spectroscopy measurements. Corrosion behaviour was characterized before with FESEM, Vickers Hardness, XRD and after the test with FESEM. Severity of electrolytes in corrosion test favoured anodic oxidation but

gets passivated in this alloy due to formation of protective film of corrosion products on the alloy surface clearly impeding the corrosion attributed to Ce addition distinct in extruded and unidirectional rolled samples. Kinetics of corrosion reaction is predominantly fast in MSCR than that of extruded and UDR samples.

Chapter 1: INTRODUCTION

1.1 Introduction

Magnesium (Mg) is the 8th most plentiful element, accounts for 2wt% of the complete weight of the Earth's crust. Mg is the lowest density structural metal having density of 1.738 g/cm^3. Mg has *hcp* structure with lattice constant at 20ºC as a= 0.32 nm, c = 0.52 nm [1]. Mg is regarded as the best green material of 21 century [2]. Mg and its alloys additionally exhibit host of numerous favourable properties like high specific strength and stiffness, excellent damping capabilities with superior machining abilities, excellent bio-compatibility, substantial hydrogen storage capacity, high theoretical specific capacity for batteries, impressive castability, low melting temperature, minimal melting energy, and promising recycling potential [3]. The Mg alloys are appropriate for many potential uses in the areas of aerospace, automobile and laptops, mobile and electronic device), bio-medical and batteries energy [4]. Some of these beneficial properties played a pivotal role in the dawn of World War II for Mg alloys especially in the aviation in the form of edge flaps in front and rear, regulated surfaces, actuators, door borders, wheels, housings for engine gear etc. [5]. However, poor corrosion resistance of Mg alloy has cessed the prospective growth possible in its application [6]. Post WW II, limited applications were seen in aerospace such as Convair B-36 Peacemaker and Convair XC-99 and also in the spacecraft for example Vanguard, Jupiter, Titan I etc. [7]. Applications in the automobile manufacturing in the chassis of the freight truck towards the end of 1950s.

Off lately in past three decades, the need for Mg market surfaced again because environmental apprehensions and surplus carbon emissions that changed global outlook. The major reason for this environmental calamity lies on vehicular and thermal power plant emissions from the exhaust. Consequently, the reason for vehicular exhaust emissions identified as heavier weighing vehicles. Subsequently, the lightweighting vehicles became the point of focus. An exceptional rush is perceived in the quest toward attainting lightweight materials in aerospace, automotive and other industries. In order develop the lightweighting vehicles, usage of Mg alloy components becomes the most appropriate answer [8].

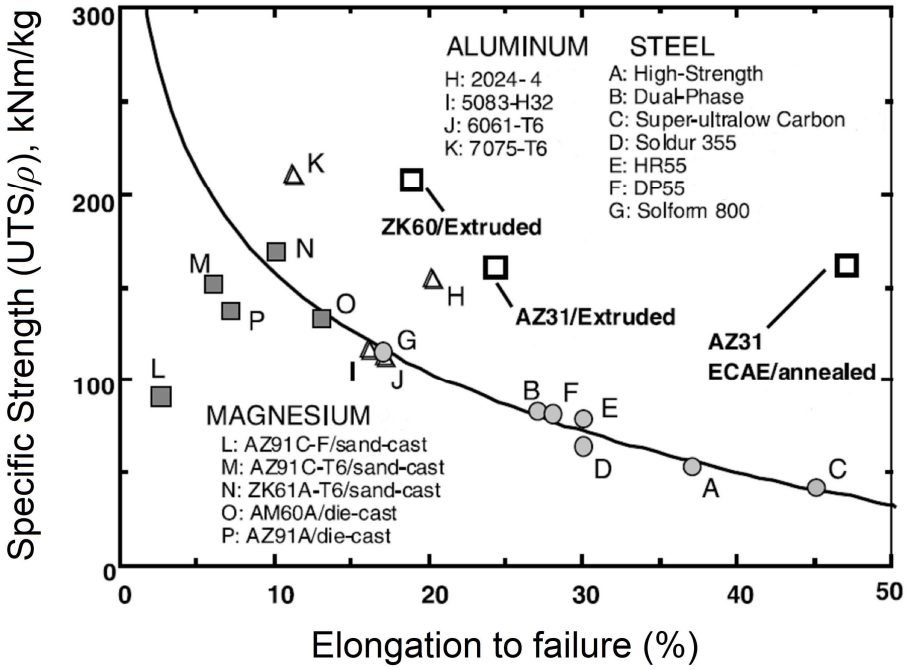

Fig. 1.1 Variation of specific strength with elongation-to-failure for Mg alloys vis-à-vis some other materials [9].

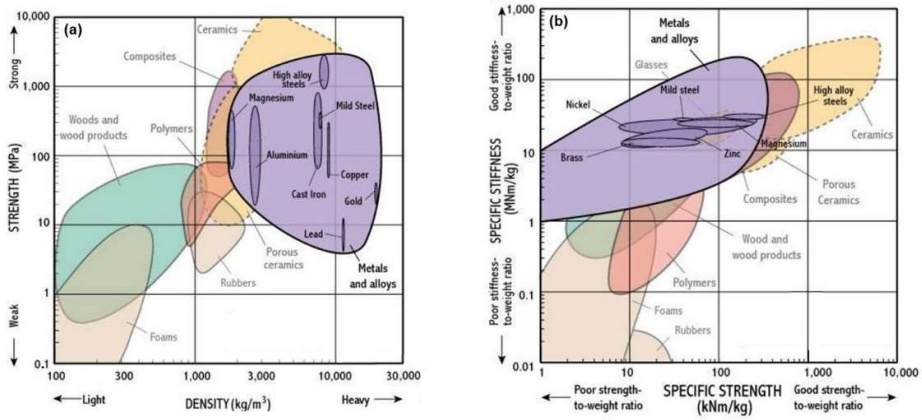

Fig. 1.2 Materials property (a) Quasi-static strength vs density and (b) Specific stiffness vs Specific strength [10].

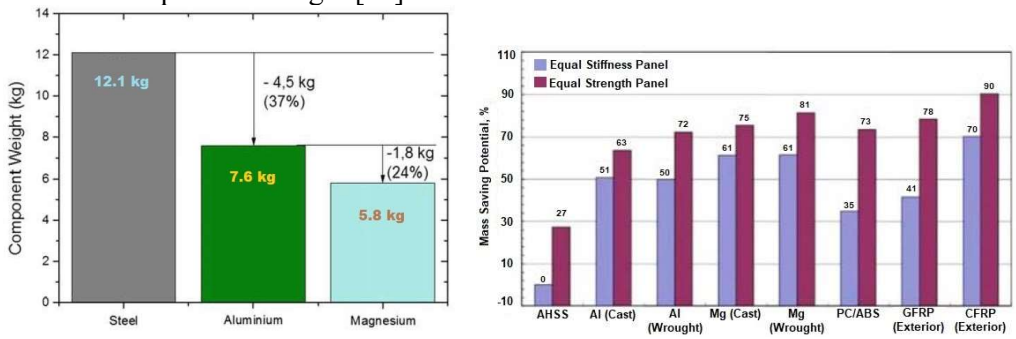

(a) (b)

Fig. 1.3 (a) Comparative weight analysis of a Volkswagen Passat boot lid across various materials [11]. and (b) Assessment of variation of mass savings potential in automobile sectors for high performance materials with mild steel in body frame panels, considering the corresponding flexural stiffness and flexural strength [5].

Majority of Mg alloys are extensively used in the cast form where its specific strength and elongation to fracture is lower than Al alloys and Steel as shown in Fig.1.1[9]. Although some of wrought Mg alloys shows specific strength and elongation to fracture is higher than Al alloys and Steel as seen in Fig. 1.1. Generally, strength of Mg alloy meant to be suitable contender for structural applications compared to other materials graphically in Fig. 1.2 (a). The specific strength and stiffness of Mg alloys compared to conventionally used as shown in Fig. 1.2

Numerous applications of Mg alloy components mostly processed by casting initially and subsequently either extrusion, rolling or even forging is employed. More than 90% of the structural parts (cars, housings, and electrical) of Mg alloy are processed by foundry route, especially by die-casting. However, inherent deficiency [9], such as gas porosity owing to splashing during mould filing and relatively coarser grains (50-200 μm) are the qualifying factors in designing the optimum properties in cast Mg alloys. The grain sizes reduced (to ~ 15-20 μm similar to that of wrought products) by alloying addition such as Li, Sc, Zr etc. in the development of cast Mg alloys. [12]. Cast Mg alloys processed by die-casting are used in automobiles as steering wheels, components for steering column, dashboard, cross beams, pedal supports, seats frames, gear boxes, air intake system, radiator braces, rear door, engine brackets, body frames and inner door panels. [5][13].

However, the wrought Mg alloys are required to develop being lower weight relative to Al and steel as shown in Fig. 1.3 (a) for the structural application desired to show greater performance in the form of extruded products, rolled sheets and forgings in comparison to cast components as shown in Fig. 1.3 (b) due to higher strength and ductility. Such wrought Mg alloys can be processed by optimum design in terms of finer grain sizes, favourable texture based on product form and correct solute elements addition in the composition. Despite promising prospect of wrought Mg alloys, industrial usage is still far below its expectation. The limited usage attributed to inevitable high temperature deformation to process the wrought products owing to poor ductility at room temperature. Consequently, relatively low-cost die-castings dominates over expensive wrought products.

Mg alloys display reduced ductility at RT attributed to deficient number of deformation components autonomous of each other for accommodating deformation about the c-axis of the *hcp* unit cell of Mg, unlike *fcc* materials bearing 12 slip systems that provides unrestricted deformation [14]. Even at 498 K, the deformation of Mg alloy is still limited because of insufficient modes of only basal and prismatic planes for slipping along with tension twinning to induce strain accommodation along the <a> axis. [15]. This kind of deformation in the Mg alloys results strong anisotropy developed due to strong textures ascribed to limited basal slip activity leading to strong yield asymmetry. Limited deformation in Mg alloy can be improvised by (i) grain refinement prevents tensile twinning and activates non-basal slip and (ii) texture weakening promotes easy slip activations.

Modification of texture introduce improvement in mechanical response of Mg alloys exploring the complex deformation behaviour. Texture in the materials is influenced by starting texture, alloy composition and processing parameters. Initial texture depends on the type of processing route, mostly it is casting process. Processing parameters generally include the operating temperature and applied strain rates. Texture weakening can be achieved by changing alloy composition, especially the role of rare earth elements (REEs) gained substantial focus recently [16][17][18]. Lower contents of REEs resulted in weaker deformation textures in wrought Mg alloys investigated in many studies. The resultant of these research proves to be suitable solute additions for developing the structural Mg alloy with better performance. Among the REEs, Cerium (Ce) addition results in homogeneous deformation at room temperature [19] weakens the deformed texture during [20][21] and improves ductility better than pure Mg [22]-[24]]. It is noteworthy that the weakening of texture, rather than the grain size [25], significantly contributes to the improvement in ductility. Additionally, the addition of Ce results in reduced yield strength, smaller grain sizes, delayed onset of instability, and enhanced work hardening. [19][23][26]. The interaction between the modified alloy composition and processing conditions is not fully comprehended. Optimization of the processing parameters like strain, strain rate, and deformation temperatures render apt hot deformation characteristics essential enough to control the desired structure-property correlation demonstrated by the processing maps [27]. At high temperature deformation, several metallurgical developments includes strain hardening, dynamic recovery, and dynamic recrystallization, might take place

concurrently [28], leading to microstructural evolution possibly with grain refinement, texture evolution and reduction in deformation resistance.

Moreover, a typical basal orientation of many grains where the c-axis aligns parallel to sheet normal accompanied by tensile twins typically develops in the conventionally rolled sheet of Mg alloys. Such intense basal orientation causes a limited deformation potential of sheet thinning [29] and a greater anisotropy [30], and consequently results in yield asymmetry. Texture softening and suppression of tensile twin by RE additions, can attained in wrought Mg alloys causes decrease in yield symmetry. [19][23][31].

The changes in the orientation can be achieved through modifying the starting microstructure or altering the processing method. A variation in strain path affects the texture formation strongly brought by cross-rolling when the direction of rolling altered examined by many researchers. [32][33]. Moreover, modification in processing conditions such as cross-rolling results into weaker basal texture in plane of sheet with considerable variation in microstructures. [34]. Such wrought products after their development, show completely different behaviour toward service environments response than compared to conventional which remain unexplored. Many studies reported the reduction in corrosion rates of hot rolled binary Mg alloys due to lowering of hydrogen evolution [35] and grain size [36]. However, the corrosion rate enhances rapidly with the presence of the twins [37]. and by increasing the amount of RE alloying addition [38]. Hence, optimization of the weight % of REEs addition is important to strike a balance between corrosion resistance and mechanical strength, essential for its successful applications.

The present work was undertaken with an aim to decrease the plastic anisotropy and yield asymmetry in the rolled sheet of Mg-0.5wt%Ce alloy by cross-rolling route and later explore its service environment behaviour. The focus was to process the rolled sheets by inducing large deformations and investigate subsequent progression in microstructure and texture.

1.2 Motivation and Objective of the Work

The deformation of the Mg alloy can be attainted effectively at high temperatures, being limited at ambient temperature because there aren't enough deformation components

without cracking because of only basal and prismatic planes for slipping along with tension twinning for strain accumulation along the <a> axis. [15]. Furthermore, only rare-earth element (Ce) addition as a solute in a binary Mg alloy has been evident of beneficial effects in same directions. However, the comprehensive picture of deformation behaviour becomes the immediate challenge for such binary Mg-Ce alloy as reported from literature review is scarce. [19]-[25].

A quest for enhancing the processing strategy for Mg-Ce alloy appears from this technical gap. This strategy made by processing temperature and strain rates as a single entity in the form of processing map. Additionally, the development of texture and microstructure along with the underlying process fills in to figure out suitable deformation parameters.

Another alluring task of deformation behaviour is to manufacture useful product forms design by the regime prescribed by processing map. Apart from product manufacturing, plastic anisotropy and yield asymmetry in the product needs to be identified and addressed, due to distinctive presence of basal texture in most of the grains parallel to sheet normal along c-axis combined with tensile twins is typically formed in the traditional rolled sheet of Mg alloys. [29]-[31] .

A change in strain path affects the texture formation strongly brought by changing the processing route studied by many researchers. [32][33]. The resultant microstructure and texture of the sheet product brings out its various properties desired for the adaptability in the given application.

Extending a step further in the challenge is the service environment response of the product manufactured through suitably modified deformation process is altogether limited for REE containing Mg alloys. Many studies reported the reduction in corrosion rates of conventional hot rolled binary REE containing Mg alloys [35]-[38] but for modified routes hardly any studies are seen.

The objective of the present work is illustrated as follows:

- A conclusive outcome drawn as a processing map from hot compressive deformation carried well above the recrystallization temperature ($T_{deformation} > 0.5T_M$) i.e., 523K to 723K, utilizing strain rates ranging from low to high low to high strain rates from 0.001 to10 s^{-1} on Mg-0.5wt%Ce alloy. The mechanical response of the starting material with respect to strain hardening and subsequent restoration mechanism leading desirable microstructure and texture evolution.

Further, the mechanism of this deformation behaviour analysed based on the understanding the developed microstructure and texture.

- The regime of manufacturing parameters of hot rolled sheet in conventional mode of UDR and modified cross-rolling route of MSCR were identified from processing map. Mechanical properties of both hot rolled sheets were determined from the ambient temperature tensile test to correlate the microstructure and texture evolved during the hot rolling processes and compared with the starting material. Additionally, mechanical properties of both sheets were utilized to establish the degree of anisotropy and asymmetry developed during hot rolling to corroborate their applicability for commercial usage.
- Finally, the response of both hot rolled sheets of UDR and MSCR subjected to two types of corrosion test electrochemical nature as polarization test and electrochemical impedance spectroscopy test using a potentiostat. The polarization test work on DC source provides overall response of both the sheets given in the form of Tafel plots. On other hand, the electrochemical impedance spectroscopy test operated on AC source furnishes minute details during electrochemical reaction occurring between the sheets and electrolyte (3.5% NaCl) in the forms of Bode plot and Nyquist plot.

1.3 Organization of Thesis

The current thesis can be categorized into 5 chapters.

Chapter 1 acquaint the topic from the perspective of present investigation and its importance.

Chapter 2 explains the essential theoretical principles relating to plastic deformation and restoration mechanisms relevant to Mg alloys, especially Ce containing Mg alloys. In addition, it dealt with the various procedures to induce large scale deformations in Mg alloy and subsequently their service response from the context of corrosion behaviour.

Chapter 3 encompasses different experimental techniques executed to initiate large scale deformation utilizing compression test on the starting material to develop processing maps to define a regime for hot rolling and subsequently tension test to figure out anisotropy. Lastly, the hot rolled sheets subjected to corrosion test as Polarization test and Electrochemical Impedance Spectroscopy test. Extensive

mechanical properties were determined from compression test, tension test, hardness test, optical profilometry and host of characterization techniques such as XRD, OM, SEM, EBSD were utilized.

Chapter 4 analyse and interprets the results of experiments in this thesis work categorize into three sub-divisions. First section interprets the outcome of compressive stress-strain curve into processing maps to identify the appropriate window of processing parameters for the hot rolling. Second section assess the hot rolled sheet manufactured by conventional route of Uni-Directional Rolling (UDR) and new improvised mode of Multi-Step Cross Rolling (MSCR) utilizing the progress of microstructure, orientation and the mechanical properties obtained from tensile, and hardness tests. Third section evaluates the response of the hot rolled sheet on Polarization test and Electrochemical Impedance Spectroscopy test.

Chapter 5 comprises the summary and conclusions of the entire thesis work.

Future Scope of Work.

Chapter 2: LITERATURE REVIEW

The materials properties governed by individual units of crystals that are characterizing the polycrystallinity. Eventually, properties defined by microstructure comprising grain size and its distribution, grain boundary and its distribution, and other microconstituents. Mere microstructural dependency for properties will not be sufficient, rather crystallographic texture (preferred orientation) needed for defining them. Such texture evolution generally occurs during solidification of primary product, deformation of crystalline nature as well as thermal treatment. The texture evolution governed by slipping and twinning during deformation, softening mechanism, and alloying addition (REE/RE texture).

Magnesium and its alloys exhibit restrictive formability yielding plastic anisotropy at room temperature because of low crystal symmetry for plastic deformation influenced strongly by processing conditions and initial texture-microstructure relationship. The present chapter provide a comprehensive outline concerning deformation and corrosion characteristics in Mg and its alloys. The mechanics of deformation in Mg and its alloys as well as the corresponding orientation development are described in Section 2.1. Section 2.2 emphasizes the need of REE addition and subsequent effect on plastic deformation. Section 2.3 propose the deformation processing map to identify the suitable region for manufacturing processes. Based on processing map, hot rolling regime and corresponding plastic deformation identified in section 2.4. The response of hot rolled products toward Corrosion behaviour highlights in section 2.5. Finally, the motivation and scope of work for the present investigation is specified in section 2.6.

2.1 Deformation Behaviour of Mg and its alloys

As seen in Fig. 2.1, magnesium and its alloys exhibit a hcp crystal structure with an atom stacking sequence of ABABAB. The unit cell shape of such *hcp* crystal structure bearing axes (a_1, a_2, and c) are parallel to the edges as seen in Fig. 2.2

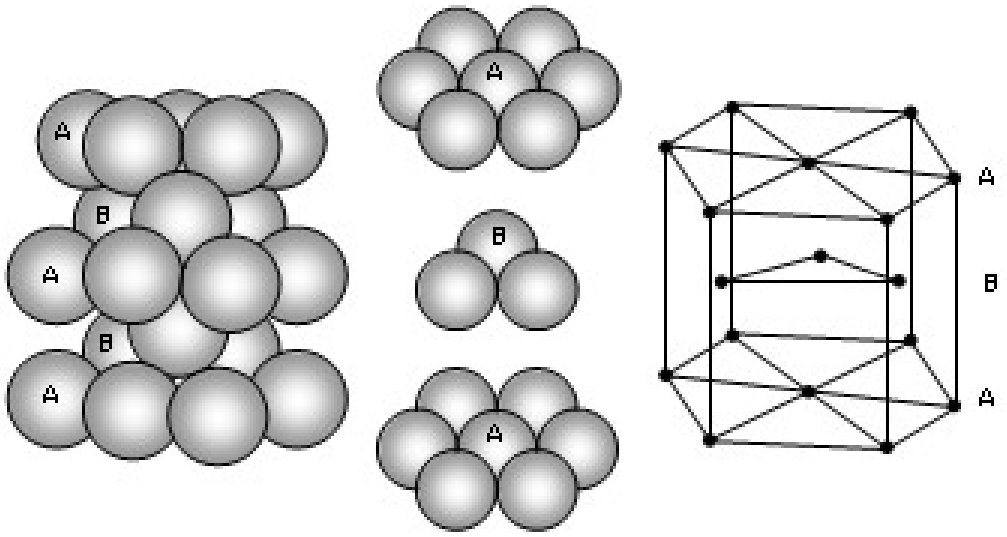

Fig. 2.1 Stacking sequence in *hcp* structure [39].

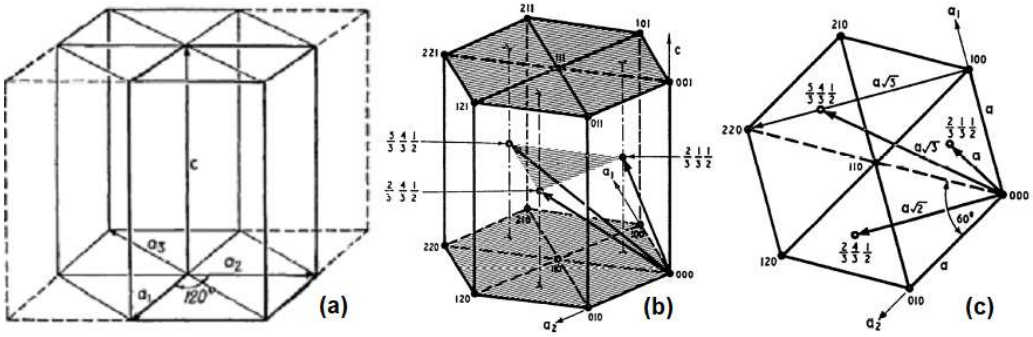

Fig. 2.2 Hexagonal prism (a) Unit cell with a_1, a_2 and c axis, (b) atomic position in special distribution and (c) in basal plane [39].

The hexagonal crystal structure is made of 4-unit cells indicated by solid and dashed lines in Fig. 2.2 (a). The primitive unit cell of hexagonal shown in Fig. 2.2 (b & c) has 2 atoms of same type located at the fractional co-ordinates 0 0 0, $\frac{2}{3}\frac{1}{3}\frac{1}{2}$, hence called double lattice structure. In ideal unit cell of *hcp* structure has 12 number of nearest – neighbouring atoms where 6 are arranged in basal plane and the remaining 6 atoms are arranged as 3 atoms above and 3 atoms below the basal plane. The shortest distance between atoms along a_1 and a_2 axes considered as '*a*' and along the c-axis as '*c*'. Then based on the atomic arrangement along *c*-axis to *a*-axis is given as $c/a = \sqrt{\frac{8}{3}}$ = 1.633 [40].

Mg being *hcp* show strong anisotropic mechanical properties due to low symmetry, unlike cubic structure metals, consequently limited deformation components cause difficulty in strain accommodation along *c*-axis. Similarly, at room temperature,

magnesium and its alloys show decreased formability and ductility. Moreover, Mg has *c*/*a* ratio = 1.624 very close to 1.633 optimum for *hcp*. On the basis of c/a ratio, the deformation mechanism in *hcp* metals can be categorize into three types [41]: (i) metals having c/a < 1.632 (Ti, Zr, Be), where deformation is assisted by slipping of basal and prismatic planes, (ii) metals having c/a ratio between 1.63 to 1.73, where the deformation is combined effect of slipping and twinning, e.g. magnesium (c/a=1.624), and (iii) metals with c/a> 1.73 (e.g. Zn, Cd), where the deformation primarily occurs through twinning mechanisms and basal slip.

2.1.1 Slip Modes of Deformation in Mg and its alloys

Plastic deformation of polycrystalline materials homogeneously as per von Mises criterion necessitate activation of at least five independent deformation components [42]. In Mg and its alloy, slip primarily occurs in basal $\{0002\}\langle 11\bar{2}0\rangle$, prismatic $\{10\bar{1}0\}\langle 11\bar{2}0\rangle$, pyramidal <a> $\{10\bar{1}1\}\langle \bar{1}2\bar{1}0\rangle$, pyramidal <a+c> type I $\{10\bar{1}2\}\langle 2\bar{1}\ \bar{1}3\rangle$ and type II $\{11\bar{2}0\}\langle \bar{2}113\rangle$ slip systems [43][44] as shown in Fig. 2.3. and Table 2.1

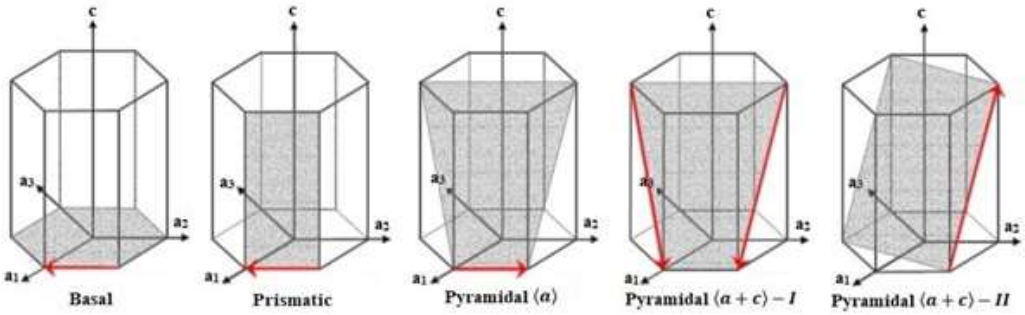

Fig. 2.3 Slip planes in *hcp* structures [43].

Table 2.1 Slip systems in *hcp* [39].

Name	Slip systems	Slip systems numbers	Independent slip systems numbers
Basal	$\{0002\}\langle 11\bar{2}0\rangle$	3	2
Prismatic	$\{10\bar{1}0\}\langle 11\bar{2}0\rangle$	3	2
Pyramidal <a>	$\{10\bar{1}1\}\langle \bar{1}2\bar{1}0\rangle$	6	4
Pyramidal <a+c> - I	$\{10\bar{1}2\}\langle 2\bar{1}\ \bar{1}3\rangle$	12	12
Pyramidal <a+c> - II	$\{11\bar{2}0\}\langle \bar{2}\ 113\rangle$	6	5

Generally, slip is mostly functional on basal plane (close-packed plane) in magnesium and its alloys. Furthermore, the activity of every slip system is determined by the *d* – spacing. As the *d* – spacing of slip-plane increases, the Peierls-Nabarro stress needed for dislocation motion will decreases. The *d* – spacing is a function of lattice constant ratio or *c*/*a* ratio, while Mg show *c*/*a* ratio 1.624 close to optimal value *c*/*a* ratio 1.633 indicating difficulty in deformation by slipping. The *d* – spacing of the prismatic planes larger than basal planes, correspondingly prismatic slip is most preferred in Zr and Ti [39], while basal slip in Mg and Co because of stable stacking faults formation on basal plane which reduces CRSS for basal slip [45]. At 25ºC, plastic deformation in Mg alloy occurs by giving strain only along the <a> = $<11\bar{2}0>/3$ axis due to four independent slip systems i.e., 2 from the slip system of basal plane (0002) $<11\bar{2}0>$ and 2 from slip systems of prismatic $(10\bar{1}0)$ $<11\bar{2}0>$. Such insufficient deformation can be added with strain given along c-axis is the $\{10\bar{1}2\}$ $<10\bar{1}1>$extension twinning which 50% of a slip mode influenced by its directional dependence.[15]

Slip trace analysis of single crystals was pioneer, [46][47] about the presence of basal slip as the effective mode of deformation in Mg and its alloys, thereafter TEM studies endorsed the existence of basal dislocation by close examination [48]. The CRSS has been estimated for the studies on slip in single crystal of a basal plane is nearly 1 MPa [49], while prismatic slip has 50 MPa [50] and pyramidal slip has 100 MPa. [51]-[53]. As the CRSS in basal slip systems are lower, hence should dominate the deformation, ironically basal slip can provide only 2 independent slip system with burgers vectors in the <a> direction indicating very poor formability. Room temperature tensile test of Mg sheet exhibits 10% elongation which is beyond expectation for basal slip [54][55].

In contrast, initiation of the off-basal slip system (means basal plane does not carry the shear direction) can provide five independent deformation modes, especially in the <c + a> directions by slip systems of pyramidal plane. Prismatic and pyramidal planes slip expected to be more energetic during deformation by Crystal plasticity modelling and experimentally endorsed by in TEM observation [54]-[56]].

Nevertheless, such activation is governed by temperature dependent deformation components as CRSS for such slip system is double compared to basal. [51]. Chances for the substantial activity of slip by prismatic and pyramidal planes considered to be unbelievable owing to their higher values of CRSS studied on single

crystal. Nevertheless, stresses developed in the microstructure are highly localize manner making them incompatible, as a result the grains well aligned for slipping on basal plane get hindered by neighbouring grains having unfavourable orientation to cause basal slip. Consequently, local stresses at grain boundaries increases by five times greater than the applied stress [57] reasonably large for non-basal slip to activate. Such incompatibility stresses can also result in higher values of CRSS than that expected by polycrystal plasticity modelling on single crystal. [44][54][56][58]. But Hutchinson et. al. [59] claimed that the comparative CRSSs of polycrystalline will coincide in Mg during deformation because the strain hardening grows greater than the proportional difference between the deformation types.

The actual CRSS's of all slip systems are also deeply related on the deformation temperature leading to lower values of yield stresses and reasonable ductility [46][47] [54][60].

Increase in higher temperature elevates the activity of non-basal slip systems by two basic effects: (i) decrease in the CRSS value required for each slip system and (ii) Reduction in the required activation energy for cross slip. This decrease in CRSS at higher temperature is because of the increased thermal energy so that dislocations can conquer energy barriers of the order ≈ kT (thermal energy) even at lower shear stress practically [45]. Increase in temperature reduces the CRSS but saturates as the energy barrier is << kT for dislocation movement. This fact is evident in basal slip owing to its lower energy barrier at lower temperature, henceforth the slip on prismatic and pyramidal planes is relatively insensitive to temperature than basal slip [61].

The slip on the planes of pyramidal and prismatic are susceptible to increase in temperature causes the activation energy to lower for the cross-slip of <a> dislocation from the basal to off-basal planes.

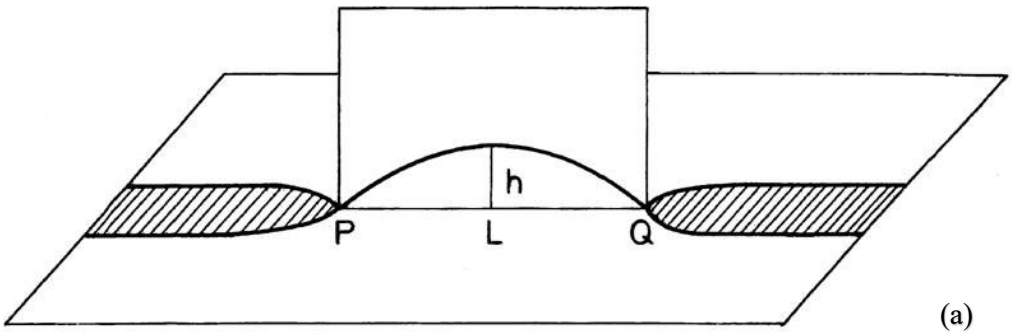

(a)

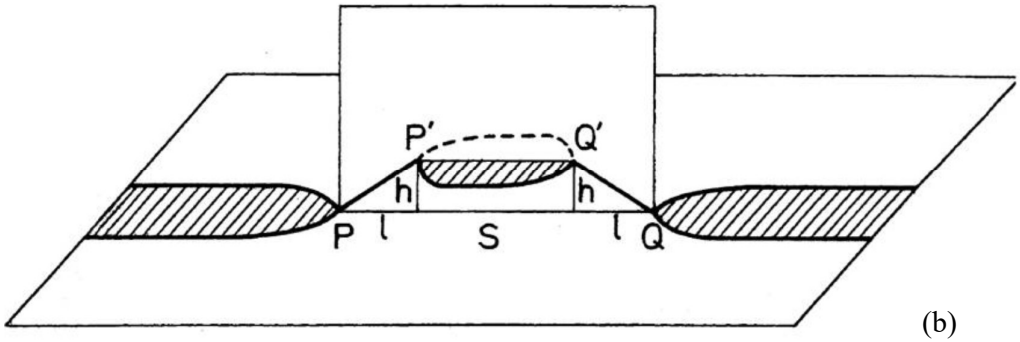

(b)

Fig. 2.4: Mechanisms of basal dislocations cross-slipping onto prismatic planes.
(a) Occurrence of cross slip at a restriction of a stacking fault on basal plane known as Friedel mechanism and (b) the double jog mechanism occurs by the prismatic dislocations as the jogs between basal planes [62].

Accordingly, the basal dislocations cross-slip from basal plane onto the prismatic plane forming prismatic dislocations based on the temperatures of deformation occurs by two mechanisms:

(i) at T<400K, the basal dislocation gets extended during cross-slip may pinned at two points such that it bends on the prismatic plane as observed in Fig. 2.4 (a) [62]-[65]]

(ii) at T>400K, the basal dislocation cross-slip onto the prismatic plane on which the prismatic dislocation undergoes further dissociation back to basal plane such that dissociation occurs parallel to the original prismatic plane is observed in Fig. 2.4 (b) as Friedel-Escaig, jog or kink pair mechanism [62]-[64]].

These pair of jogs from the prismatic dislocations are located at midway of two stacking fault of basal plane. Subsequently, the jog pairs decide the cross slip by nucleating and propagating on the prismatic plane based on the activation energy [64].

In comparison to the prismatic dislocations, the formation of pyramidal dislocations is poorly understood still pyramidal slip is heavily influenced by temperature [52] and also the mechanism of cross-slip. [66][67]. The nucleation source of pyramidal dislocations being suggested by two cross slip mechanism:

(i) As basal <a> dislocations after cross-slipping onto the prismatic plane forms prismatic <a> dislocations, which in turn combine with a sessile <c> dislocation developing <c+a> dislocation which gets cross-slip onto the plane of pyramidal [67].

(ii) The formation of pyramidal dislocations is proposed free of cross-slip from the basal plane. After the formation on the pyramidal I $(10\bar{1}1)$ plane, then the pyramidal dislocations cross slip onto the pyramidal II $(10\bar{2}2)$ plane [66].

The deciding factor for both the activity of pyramidal slip in Mg and its alloys is determined by cross-slip of dislocations. In Mg, the <*c*+*a*> type of deformation for the pyramidal slip type II occurs by slip system $(11\bar{2}2)$ $<11\bar{2}3>$. The slip system, having the largest burgers vector as $<11\bar{2}3>/3$ and the lowest interplanar spacing, considered as the most retarded for gliding due to largest Peierls stress for the dislocation mobility. The microscopic processes following generation and movement of non-basal dislocation slip is not fully understood. The CRSS for <*c* + *a*> slip needs to be assessed based on the dislocation nucleation mechanism or its subsequent movement [15][67] [68].

Since <*c*+*a*> dislocations are linked to huge burgers vectors, hence it appears in a separate arrangement and core structures of non-planar type. Minonishi et al. [69] suggested the dislocation dissociation that initiate the faults in stacking sequence in pyramidal <*c*+*a*> type II slip systems as,

$b \rightarrow \alpha b + (1-\alpha)$ ----------(2.1)

$<11\bar{2}3>/3 \rightarrow \frac{1}{2} <11\bar{2}3>/3 + (1 - \frac{1}{2}) <11\bar{2}3>/3$ ----------(2.2)

where $b = <c+a> = <11\bar{2}3>/3$ is the Burgers vector

$\alpha \approx 1/2$ for symmetric dissociation.

The pyramidal <*c*+*a*> type II slip potentially nucleates at the neighbourhood of grain boundaries or adjacent to twin boundaries with incoherence present within the grains. Such nucleation sites generate the complete dislocation in single step due to high stacking fault energy or in two steps brings out partial dislocations one after another with stacking fault strip in between [68].

Some experimental outcomes confirm such nucleation of partial dislocations <*c*+*a*>/2 adjoining the twin boundaries [52][70]. Transmission electron microscopy studies by burger vector analysis reports the mechanism of nucleation for such pyramidal <*c*+*a*> dislocations are combined with <c> and <a> types of dislocations. The screw orientation of <*c*+*a*> dislocation shows stable nature but unstable in edge orientation. The edge orientation so splits into dislocations of the <c> and <a> types. Thus, the association of <c> and <a> dislocations cause origination of <*c*+*a*>

dislocations. The mechanism of creation of <c+a> slip rely on the intersections of sessile <c> prismatic dislocations and the slip <a> basal dislocations as observed in Fig. 2.5 [67].

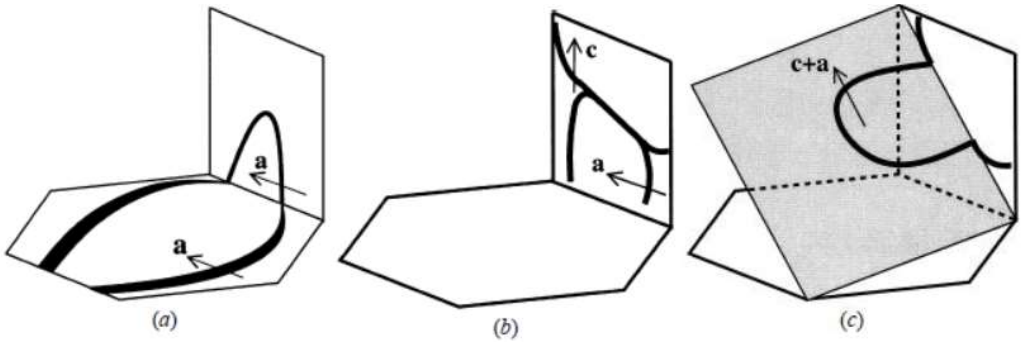

Fig. 2.5 Progression of the start of <c+a> dislocation in pyramidal slip system [67]

The basal dislocation's screw portion first cross slips energetically favoured to the prismatic plane because of the elastic connections of the screw type basal <a> dislocations and the edge type <c> dislocations as shown Fig. 2.5a. The parameter = 1/ (1−ν) (where ν = Poisson ratio) determines the magnitude of elastic interaction of an edge with screw component of a dislocation [52]. For pure Mg, Yoo [52][67] the value of ν = 0.29 implies that the strong desirable force drags out the <a> type dislocation from the plane of basal. This screw <c+a> dislocation cross slip to the $(11\bar{2}2)$ planes of pyramidal to produce the <c+a> dislocation on the plane of the pyramidal as observed in Fig. 2.5 (c). But this cross slip is energetically hostile in Mg from prismatic planes to pyramidal <c+a> type II planes even at high temperatures [71]. These scrutinization contradicts the anticipated nucleation mechanism. Besides, the generation of <c+a> dislocations by associating <a> and <c> dislocations, results in less than five independent slip system from <c+a> dislocations because independent slip system requires an independent dislocation nucleation source [15].

Atomistic studies [69][72] suggest that the screw dislocations have a strong likelihood of cross slipping on pyramidal planes as the cores of screw dislocations can dissociates on multiples along with $\{11\bar{2}2\}$ and $\{10\bar{1}1\}$ of pyramidal planes II and I order respectively. Besides, the dissociation of dislocation in creating partials based on the reduction in overall free energy ($\Delta G_{reduction}$) because of similar amount of the stacking fault energies for $\{11\bar{2}2\}$ and $\{10\bar{1}1\}$ of pyramidal planes II and I order respectively.

$\Delta G_{reduction} = \Delta G_{total\ dislocation} - \Delta G_{partials}$ ----------(2.3)

where $\Delta G_{total\ dislocation}$ = the undissociated state free energy and

$\Delta G_{partials}$ = total energy of the partial dislocations

Accordingly, the dissociation of pyramidal slip (type I to II) is dependent on temperature i.e., dissociation of the pyramidal plane at low temperature is favoured by one of the types and later at higher temperature dissociation will shift to active other type [67].

2.1.2 Deformation Twinning

Besides slip, twinning is crucial for accepting deformation in magnesium systems. Twinning is a shear deformation of the crystal such that a part of the crystal reorients exhibiting mirror symmetry in relation to the adjacent un-twinned host crystal along mirror plane as demonstrated in Fig. 2.6

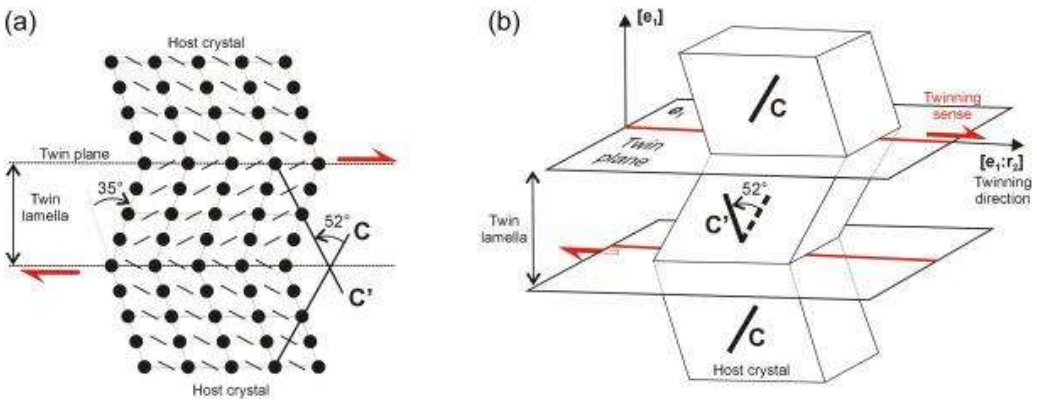

Fig. 2.6 Twinning of the host crystal (a) Atomic reorientation in twinned and host crystal and (b) Part of twinned and host crystal arranged on same twinned plane called habit plane [73].

The direction along with the atoms move microscopic step is stated as the twinning direction and the part of twinned and host crystal arranged on same mirror plane, is called the twin plane, also known as habit plane.

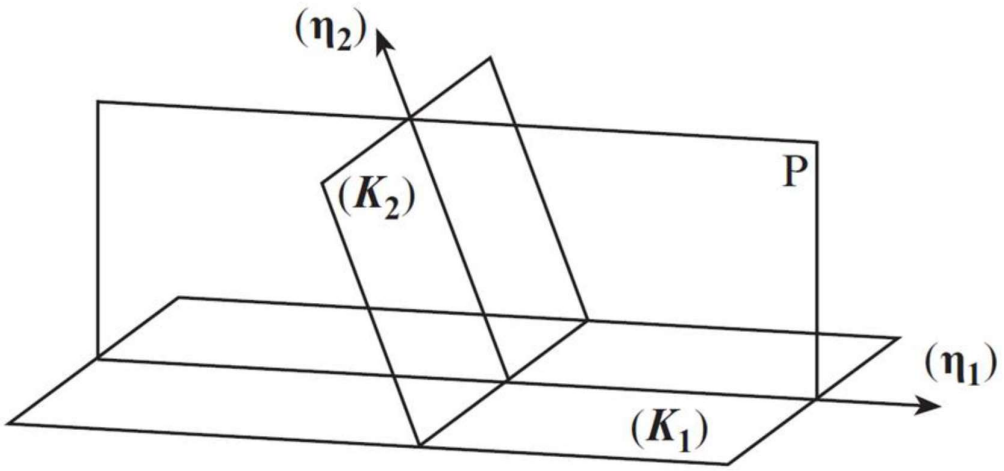

Fig. 2.7: Planes and directions within a twin. K_1 represents the twinning plane also called habit plane and K_2 is the reciprocal twinning plane, P is the shear plane. η_1 and η_2 are the twinning and reciprocal twinning directions [74].

In slip, each atom on the slip plane moves forwards or backwards whereas in twinning, simultaneous motion of a huge number of atoms along η_1 direction on the shear plane (P) as shown in Fig. 2.7. In twinning, atoms rearrange within the twin to produce the accurate twin structure inside the twin [75]. The twin plane K_1 clearly determines the association between host grain and twin such that it remain constant for twinned and un-twinned crystals and the shear direction η_1. There are different twinning modes in Mg, given in Table 2.2, where individual twin classified based on misorientation about $<11\bar{2}0>$ axis rotation between the twin and un-twinned crystal. Since c/a < 1.732 in Mg, hence during tension along c-axis, tension twins of $\{10\bar{1}2\}$ type form and during compression along c-axis, compression twins of $\{10\bar{1}1\}$ and $\{10\bar{1}3\}$ type form. [76]. Two generally double twin systems spotted in Mg is also outlined in Table 2.2 [77].

Table 2.2 Various twinning modes in Mg, in terms of misorientation about $<11\bar{2}0>$ axis rotation between the twin and un-twinned crystal [77].

Twin Plane	Misorientation	Shear
$\{10\bar{1}2\}$	86º	0.131
$\{10\bar{1}1\}$	56º	0.138
$\{10\bar{1}3\}$	64º	0.138

$\{10\bar{1}1\}$ - $\{10\bar{1}2\}$	38º	0.208
$\{10\ \bar{1}\ 3\}$ - $\{10\bar{1}1\}$	22º	0.192

At low temperatures, deformation brought by twinning plays a substantial role in magnesium due to the greater activation stresses required for non-basal slip modes. These deformation twins form as embryos at grain boundaries or other locations where source defects and stress concentrations are most prevalent [78]. Deformation twin is a key mode, particularly in Mg as the $\{10\bar{1}2\}$ tension twin has a CRSS of approximately 33 MPa [56] (according to polycrystal plasticity modelling), making it the most easily activated deformation mode after basal slip. Such tension twin is activated along c-axis producing low yield stress because of high Schmid factor and low CRSS in this orientation. Usually, compression twins are very hard attributed mostly to active aspects of atomic rearrangement, more nucleate than tension twins [79][80].

Deformation twinning usually includes,

i) twin initiation and

ii) twin development. Thompson and Millard proposed the dislocation model using the pole mechanism for $\{10\ \bar{1}\ 2\}$ twinning [81], where twinning initiation site emerges from a pole formed by dislocation reaction given as

$$[0001] \rightarrow \alpha\,[10\bar{1}1] + [10\bar{1}0] \qquad (2.4)$$

where α value lies between 1/12 and 1/4.

However, above suggestion only justifies for twin growth in contrary to deformation twin nucleation and growth for bcc system using the pole mechanism. Orowan [82] instead proposed a homogeneous twin embryo nucleation from the vicinity of elevated stress concentration in the homogeneous lattice shear. Bell and Cahn [83] gave backing to Orowan's proposition, with their experimental results on $\{10\bar{1}2\}$ twin in Zn (*hcp* system) based on the concept of homogeneous nucleation. Nucleation of twin arises from the concentration of stresses caused by sessile dislocations as a result of basal and pyramidal slip interaction. In addition, Price, [84] proposed the twin nucleation on Zn whisker which are free of dislocation at the corners of the specimen and the specimen grips proving the mechanism of homogeneous twin nucleation. In contrast, Mendelson [85], projected that nucleation of twin urging for slip of non-planar dissociation. Consequently, heterogeneous nucleation of twin occurs

at pre-existing dislocation or phase to boundaries of grain or intersection of twins. Such inhomogeneous initiation of twin usually entails the evolution of twin seed and later dislocation glide of zone. This sort of situation is energetically favourable owing to lesser nucleation stresses analogous to a state of equal shear involving all planes.

The occurrence of deformation twinning process includes two important operations i.e., atomic re-arrangement and shearing. $\{10\bar{1}2\}$ tension twins work mainly by re-arranging mechanisms, while $\{10\bar{1}1\}$ compression twins are controlled by shearing. Generally, on nucleation additional stress increment promotes twin growth, but exclusively in $\{10\bar{1}2\}$ tension twins, twin growth occurs with a drop in stress. Growth of Twin needs much smaller activation stresses, prolonged through (i) growing process along the perpendicular to the plane of twin and (ii) growth along twin length. The mechanism of localized dislocations stated above facilitates the twin growth process of regional dislocations [15][67][86].

In the process of twin growth along length wise twin increment rely on the motion of $\{10\bar{1}2\}<10\bar{1}1>$ twinning dislocations. However, the $\{10\bar{1}1\}$ compression twins that are actively unsuitable for rearranging atoms liable to create abundant parallel strips, slender lamellae having 0.1 – 1 μm thickness, devoid of exhibiting a decrease in stress. Subsequently, the stress increases continuously during strong interaction of the twin bands with pyramidal <c+a> dislocations. Hence, growth of $\{10\bar{1}1\}$ compression twins lengthwise is determined by the motion of $\{10\bar{1}1\}$ $<10\bar{1}2>$ twinning dislocations. Shear failure occurs because the slip becomes unsuitable beside Compression twin boundaries originating from their growth resistance.

In polycrystalline Mg, compression twins show no change in texture during deformation owing to their low volume fraction, but very evident with tension twins. In comparison to tension twins, compression twins are not liable to twin growth. Correspondingly, compression twins are thin and sharp while tension twins are thick and has wavy structure. On the other hand, twins with compression can acquaint softening of texture whereby they can lessen the real work hardening within the twinned material and the flow stress.

Smaller degree work hardening occurs immediately after yielding because such twins accommodate most of the strain. But the moment twinning gets exhausted substantial work hardening appears as slip operation takeover the deformation modes. However, compression along c-axis accommodated most of the strain by slip showing

hardening behaviour anticipated for deformation mainly by dislocation slip than by compression twins because of its high CRSS. Such anisotropic behaviour of flow stress as a function of twins is validated by crystal plasticity modelling similar tom slip, where the twin activity is controlled by Schmid factor and a distinctive CRSS [56][87][88] [89].

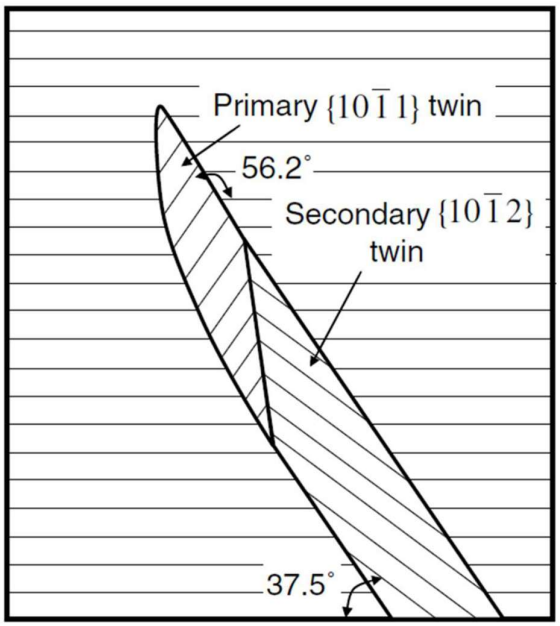

Fig. 2.8 Representation of {10$\bar{1}$1} - {10$\bar{1}$2}double twin along the <11$\bar{2}$0> axis in the basal planes [90].

Most of the twinning events in Mg is primarily assessed by Schmid factor values [80]. But the formation of double-twin variants with a deviation in Schmid factor, increases the strain compatibility with the adjoining matrix as shown in Table 2.2 and in Fig. 2.8 [90][91]. This concludes that the twinning is understood thoroughly from macroscopic effects, but the full conceptual understanding of twinning remains partially known [86].

2.1.3 Detwinning

Deformation in Mg and its alloys exhibit detwinning in a twinned material apart from dislocation slip. Detwinning can be described using microstructures based on receding of the existing twin bands or thinning down under reverse loading. Barnett et. al. [92], observed that during loading and unloading twins appear and disappear using in-situ tension test investigation of twinning behaviour. The microstructure shown in

Fig. 2.9 discuss various loading states. Twin disappears from grain 3 with increase in a strain of ~5% and new twins forms in grain 2. On further unloading causes twins to reappear and disappear slightly, while a new twin is also formed.

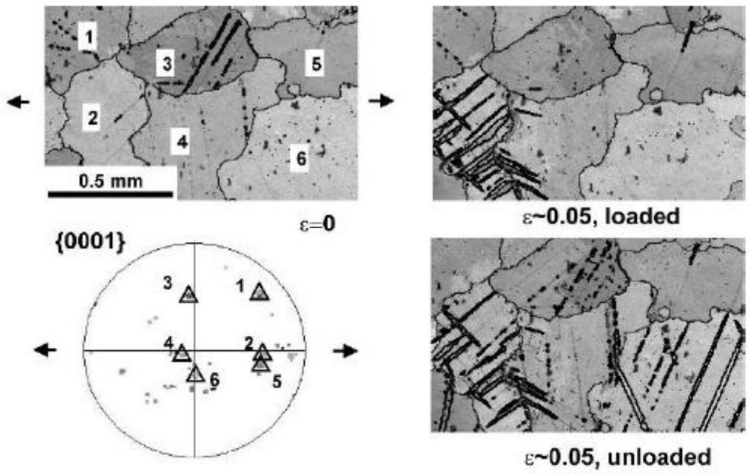

Fig. 2.9 Microstructures acquired in the course of an in-situ tensile test in various stages of loading with direction indicated by arrows [92].

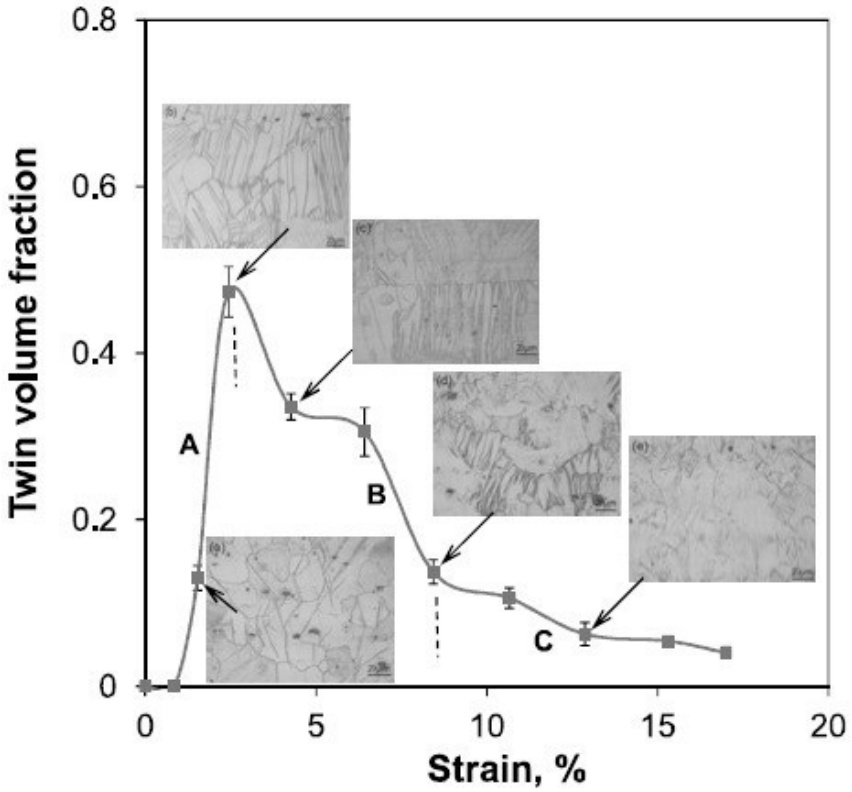

Fig. 2.10 Variation of twin volume fraction and microstructural progression of Mg-Al-Mn alloy during plastic deformation [93].

Extruded Mg alloy AZ31B is evident of twinning and de-twinning through at least 250 cycles in compression-tension cyclic loading [94]. In this case, the initial texture resulting from extrusion is unsuitable for twin formation in tension. Eventually, on compression the grain gets twinned such that optimum orientation achieved for twinning or de-twinning during plastic deformation by tensile mode because the basal planes after initial compression are parallel to the tensile axis. The stress needed for detwinning is more than twin growth but less than twin nucleation.

Sarkar et. al. [93] observed de-twinning effect from microstructure through plastic deformation of Mg-Al-Mn (AM30) alloy after extrusion . The deformation led to the progression of twin volume fraction and subsequent microstructural changes shown in Fig. 2.10 as three simple steps:

(I) as twin formation begins strain hardening decreases.

(II) higher the volume fractions of twins, drastic rise in the strain hardening due to strong interactions of dislocation and twin.

(III) These interactions successively initiated the events of de-twinning causes the twins to disappear resulting low strain hardening regime.

2.1.4 Shear Band Formation

Shear bands are areas of high strain localization, frequently crossing many grains. The shear bands formation in Mg alloys occurs during compression and double twinning modes of deformation [95][96]-[99]. Generally, shear band forms during plane strain compression (highest shear stress plane) at 45º to compression direction but also examined at angles less than ±35º to the RD [100]. Shear bands are predicted as the primary indication of localized strain and the precursor to failure.

In Mg alloys, undergoing hot rolling or cold rolling shear bands generally be seen and degrade the formability, even at elevated temperature. Deformation mechanisms, recrystallization, and texture are significantly influenced by the strain localization in shear band. Mostly, the microstructure of heterogeneous nature initiated by shear bands cannot be removed entirely after formation. Enhancement in rolling capability can be accomplished by realization of the shear bands formation mechanism and microstructure. Microstructurally, shear bands appear as colonies where the slip planes within the band readjust themselves by shear direction. As a result, within the shear band a localize plastic instability occurs exhibiting as strain softening activity.

Accordingly, shear bands initiate from mainly three techniques:

(i) gathering of slip bands (specifically in HSFE materials) [101].

(ii) localized DRX nearby grain boundaries resulting in clusters of strain free smaller grains that can slip freely than the matrix hardened under strain [102].

(iii) clusters of tiny-twin strip formation (generally in LSFE materials) [101] [103].

Mechanisms (ii) and (iii) are seen in Mg and also strongly related to the working conditions.

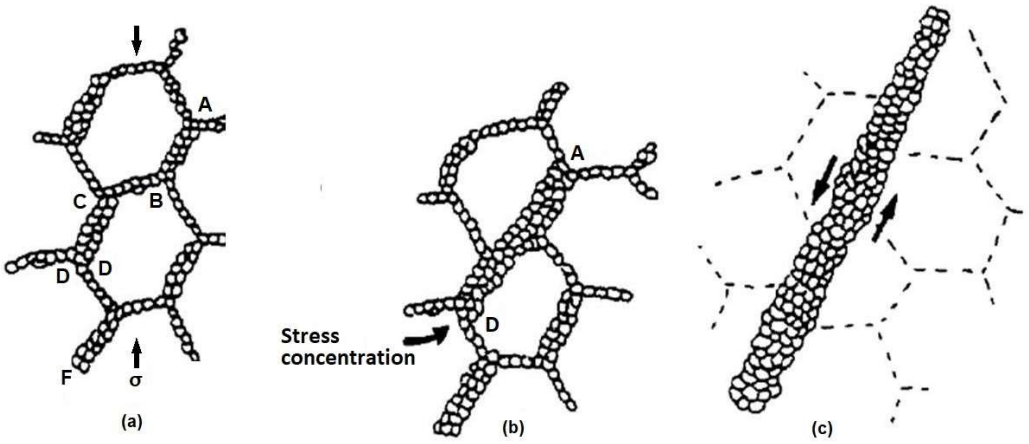

Fig. 2.11 Shear band formation from the clusters of recrystallized grains [102].

Ion et. al [102], identified the mechanism (ii) in shear band formation during high temperature deformation attributed to DRX at Mg grain boundaries owing to unavailability of slip systems. Fig. 2.11 shows schematic procedure for shear band formation. Fig. 2.11(a) dynamically recrystallized regions at the grain boundaries are liable to basal slip being favourably oriented for it. Still shear along AB grain boundary cannot occur because of restrictions from adjoining grains A and B. Subsequently, the grain boundaries AB and CD may get broaden and unite to form single potential band for easy slip-on additional extension in strain as shown in Fig. 2.11 (b). On further continuous deformation causes the single potential band creates shear zones as seen in Fig. 2.11 (c).

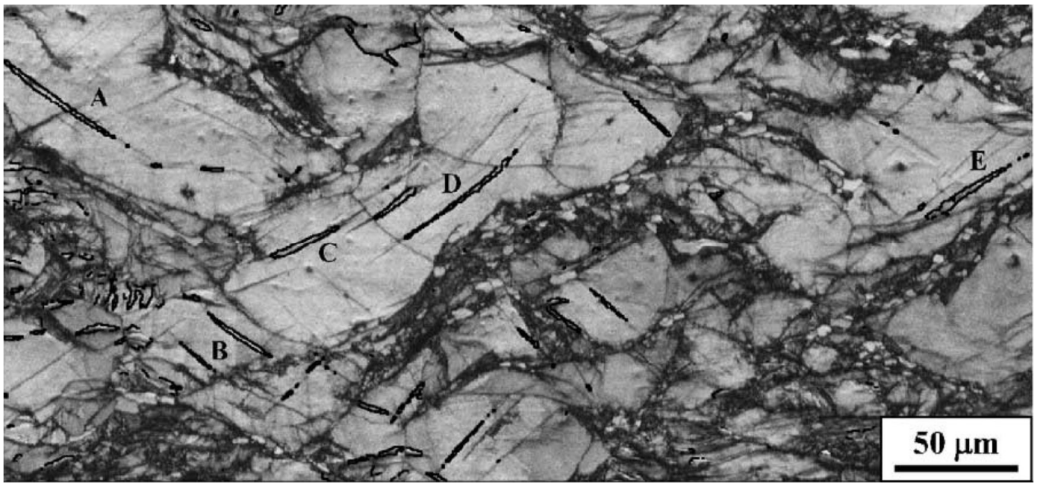

Fig. 2.12 Shear band structure and $\{10\bar{1}2\}-$ twins in 30% reduction during cold rolling of pure Mg shown in EBSD Kikuchi band contrast map [104].

Couling and Pashak et. al. [103], pioneer in identifying (iii) mechanism of shear band formation in Mg alloys in cold rolled condition which are soft and deformable. Accordingly, they proposed the evolution of shear bands owing to grouping of compression and double twins. Such clustering of twins in shear band formation often noted in Mg-RE alloys. Barnett et. al. [104], stated such shear band formation track in cold rolled Mg, Mg-Ce and AZ31 alloys and labelled such behaviour especially for Mg-Ce alloy as a texture softening process.

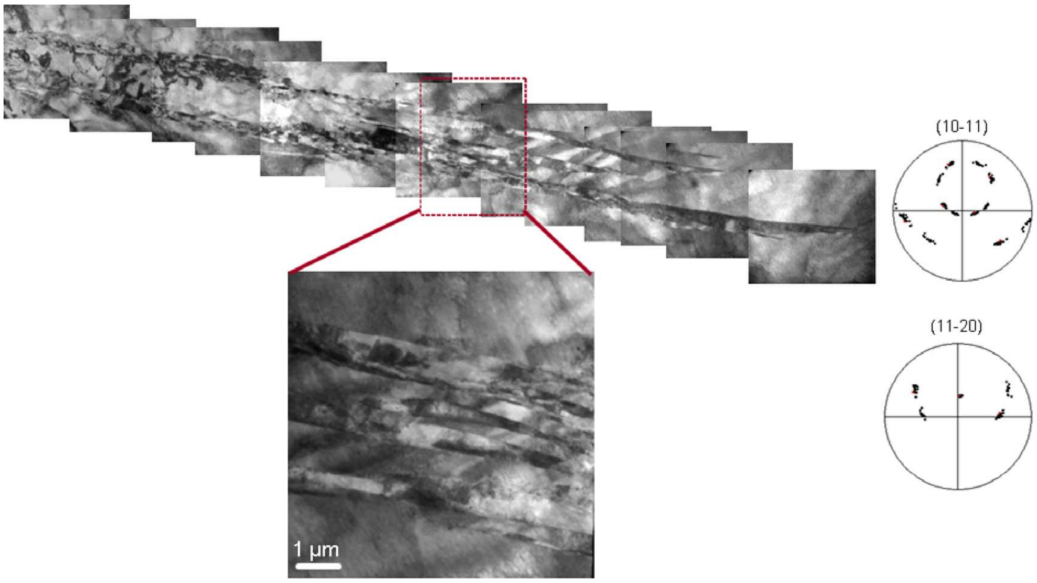

Fig. 2.13 Shear band observed in a deformed Mg alloy with 3 wt.% Y taken from TEM-BF images along with corresponding pole figures [96].

Sandlöbes et. al. [96], reported that shear bands constitute narrows bands with higher density having $\{10\bar{1}1\}$ - $\{10\bar{1}2\}$ orientation revealed by TEM – BF investigation as shown in Fig. 2.13

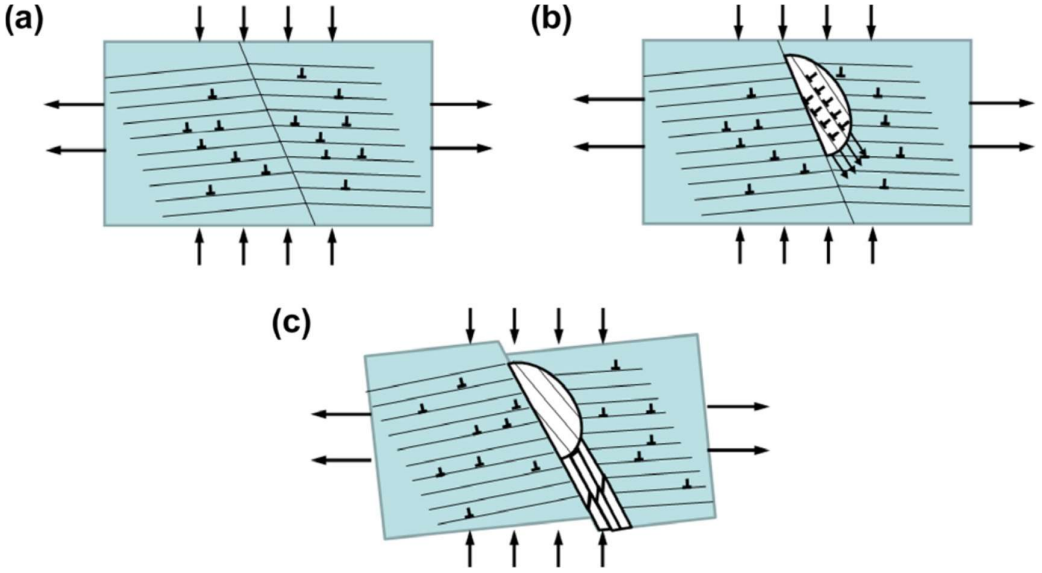

Fig. 2.14 Shear band formation model in pure Mg and Mg-Y alloys [96]

Sandlobes et. al. [96], identified that the shear band comprise of fine twins that are triggered due to strain localization as depicted in the shear band formation model in Fig. 2.14 [96]. Sandlobes et. al. claimed that increased ductility in Mg-RE alloys can be justify partially using a fine distribution of fine shear band in the deformed microstructure [96]. In specifically, smaller accommodation of strain occurs in low intensity shear band distributed finely leads to higher strain just before failure, compared to strain accommodated with very large shear band in less number. Spatial distribution of shear band is notable in estimating the ductility in Mg alloys.

The crucial parameters overseeing the mechanism of shear band are the critical strain hardening value and suitable orientation of slip planes for shear band formation. Coarse grained materials predicted to have higher shear band illustrating the impact of grain size influence on the shear band formation. Shear banding is less likely when the Zener-Holloman parameter (Z) is less in value. Tendency for shear band formation may favour due to presence of solutes and particles [101].

2.1.5 Effect of Grain Size

The tensile elongation to failure has pronounced effect of grain size described by Yamashita et al. [105], where grain size reduction from 400 μm to 17 μm, increases the elongation to failure up to 15%. The ductility increases up to 55% at room temperature during ECAP of AZ61 alloys reported by Kim et al. [106]. Annealing treatment after ECAP technique observed increases the ductility more than 40% in Mg at room temperature by Mukai et al. [9]. Plastic deformation carried out only by basal slip system and twinning mechanism, then such larger values of elongation not possible to achieve.

Mg alloy bearing coarse grain have a off-basal CRSS of nearby 1.1–2.5 times more compared to a basal slip [55]. Rolled AZ31 alloy possess a CRSS ratio of 2–2.5 and around 14 μm grain size observed by Agnew and Duygulu [54][107] established the prismatic plane's slip system's CRSS ratio in relation to basal slip system to be nearly 1.5 according to the Schmid factor in relation to the loading direction. The CRSS ratio of the prismatic slip system to that of basal slip system around 1.5 based on Schmid factor as a role of loading direction established by del Valle et al. [107].

Both grain size and texture influence the ductility of Mg. Koike et al. [55] observed that grain size decides the ductility as very low stress is required for basal slip to enable microscopic yielding in a large size grain. Hence, activation of other slip systems is necessary for any additional deformation. Moreover, grain boundaries and triple junctions [108] experiences the stress concentration due to inhibition for slipping by many basal dislocations as Mg possess strong plastic anisotropy. As a result, small grains experiences activation of off-basal slip system and bigger grains twin formation. In Mg alloys, reduction in the grain size decreases activity of twins owing to reduction in work hardening was identified by Barnett et al. [109]. Strain suitability (numerous microns from GB) at grain boundary could be liable for the improved cross-slip from plane of basal to non-basal observed by Koike et al. [55]. Sliding of grain boundaries at room temperature could be additional feasible mechanism for improving ductility in Mg alloys reported by Hauser et al. [110] in for 1mm grain. Further, Koike et al. [111] reported that the sliding by grain boundary adds around 8% of strain relating to total strain.

2.1.6 Evolution of Texture

To explore deformation mechanisms, texture evolution and reproduction of the stress-strain behaviour could be authoritative means. Simulations on the experiment carried out in uniaxial tension and compression deformation behaviour [112][113] to show the movements of off-basal slip systems. The rolled Mg alloy under uniaxial deformation reported that The off-basal to basal slip's CRSS ratio was 5 – 6 [112] and 2 – 3 [113].

The variation in strain as a function of orientation can be used for evaluating the deformation mechanisms by neutron diffraction [112]. The variation in experimental strain could be repeated by the activation of <*a*> slip of prismatic along with existing the predominant basal <*a*> slip under tension was shown with the findings of Hauser et al. [110]. Likewise, activation of <*c*+*a*> slip of pyramidal in compression in spite of smaller contribution [112].

Simulation of Viscoplastic self-consistent (VPSC) modelling [114] was executed by Agnew et al. [88], on casted Mg alloy under the plane-strain compression. In this simulation, the movement of <*a*> slip of basal, <*c* + *a*> slip of pyramidal and twin formation modes of potential deformation mechanisms were assessed by matching the investigational stress–strain curves and X-ray pole figures [114]. Correspondingly, the activity of basal slip in relation to the off-basal slip was 3-17, indicating utter need for the beginning of <*c*+*a*> slip in the given deformation components. Moreover, twinning mode of deformation was primarily active but subsequently restored with pyramidal <*c*+*a*> slip. This pyramidal <*c*+*a*> slip activities increase with alloying additions, conforming with the CRSS determined for single crystal Mg–Li alloys [115]. Perez-Prado et al. [116], expressed that the hot rolled AM60 alloy displays the texture progression in line with the findings observed by Agnew et al. [88], Visco-plastic Taylor model [117], used to identify the deformation modes accountable for the texture development in wrought AZ31 alloy during cold rolling by Styczynski et al. [118]. This simulation derives the CRSS ratio value 3 for the ratio of non-basal slip to the basal slip. In addition, prismatic <*a*> slip and pyramidal <*a*> slip was incorporated during the simulation in contrary to the simulation by Agnew et al. [88].

The CRSS ratio value off-basal slip to basal slip in the above simulations for identifying the deformation mechanisms accountable for the evolution of texture remarkably smaller than already investigated single crystal CRSS ratio (100:1). The relative simulated activities of slip systems were conforming to the experimental data

in Mg alloys [46][53]. The polycrystalline Mg alloys bearing coarse grain (>6.5μm) have the CRSS ratio of the slip of non-basal to basal slip about 1.1 – 2.5 [55]. The CRSS ratio of about 2 – 2.5 determined for the deformed samples of AZ31 alloy having 14 μm grain size under cold rolling by TEM analysis executed by Agnew et al. [54]. Ruano et. al. [107], confirmed the CRSS ratio value obtained from division of that for the prismatic slip by the basal slip nearly 1.5 depends on the Schmid factor along the loading direction.

2.2 Restoration Mechanisms

Deformation of a materials causes to increase the numbers of defects especially dislocations in the crystal structure such that the stored energy of the system increases steadily. The driving forces required to reduces this free energy done by specific process such that the defects eliminated. These processes are referred to as restoration mechanism and are classified as recovery, recrystallization, and grain growth. The restoration processes are termed as dynamic, when occur simultaneously with the deformation and as static, when occur during annealing treatment [119]. These softening mechanisms cause substantial change in the behaviour of deformed materials. During deformation of materials such softening mechanism exhibits the dynamic processes in the flow curves.

Recovery: Recover process shows many dislocations rearrange themselves along low energy configurations such that annihilation occurs reducing the stored energy of the system [119]. This rearrangement usually forms cell or sub-grain walls.

Recrystallization: Recrystallization leads to forms completely new grains enclosed by HAGBs and consisting of a low defect density [119]. Recrystallization occurs due to various nucleation mechanism of new strain free grains.

Grain growth: Grain boundaries are considered as defects and more the grain boundaries fractions more will be defects thereby increasing the stored energy of the materials. Grain growth acts as a driving force to decrease the number of grain boundaries fractions generating larger grain size. Grain growth is followed once complete recrystallization occur and hence considered as less prominent than recovery and recrystallization. [119].

The tendency of most materials goes through restoration mechanism either recovery or recrystallization generally based on the stacking fault energy (SFE). High SFE materials experience recovery extensively because of easy movement of

dislocation (climb and cross-slip) e.g., Al or ferritic steels and even eliminate maximum stored energy to halt recrystallization. Low SFE materials experience less recovery and high level of recrystallization due to delay in dislocation climb or cross-slip e.g., Cu or Ni [119]. But the SFE values for Mg most cited as 78 mJ/m^2 and 125 mJ/m^2 [120] such that Mg has regions with low SFE and medium to high SFE respectively. Correspondingly, it becomes doubtful whether Mg should go through recrystallization or recovery. Somekawa et al. [121] stated that additions of solute to Mg alloy reduce the SFE effectively from 78 mJ/m^2 to 5.8 mJ/m^2 for Mg-9wt.%Al alloy. But similar tendency with other solutes in many of Mg alloys, may or may not impact on the SFE. The mechanisms of recovery supplement the process of recrystallization by reducing the stored energy which helps in emerging the potential nuclei and also enhances the nucleation as it reduces the growth rate. [122]

2.2.1 Recovery in Mg alloys

As the dislocations density and the temperature are adequately high, then recovery occurs. Koike et al. [55] reported that DRV observed in AZ31 alloys during deformation at room temperature, usually should appear at higher temperature deformation. Accordingly, many investigations on various Mg alloys reported about the recovery and formation of sub-grain boundaries during and after higher temperature deformation [102][116][123][124]. The density of dislocations within the grains increases during deformation, thereby the stored energy increases. Thereafter recovery proceeds by rearranging dislocations in low energy configurations causing annihilation of dislocations resulting in the stored energy reduction. The mobility of dislocations during recovery process proceeds by glide, climb or cross-slip varying based on the material type and temperature. Dynamic recovery especially is based upon the stress conditions. Every dislocation is exposed to stresses arising from adjoining dislocations but in dynamic recovery due to the applied stress. Consequently, these dislocations traverse through the structure, they encounter other dislocations of opposite sign resulting in annihilating each other. Accordingly, the overall dislocation density will be reduced, left out with a smaller number of dislocations. Such dislocations continue to travel through the materials to obtain the potential lowest energy configurations. As a result, the dislocations appear at LAGBs such tilt boundaries, while in other complex polycrystalline, the dislocations will generate sub-grain boundaries and cell walls. On further recovery, cell walls lose the entanglement of dislocations causing decline in

dislocations inside the cells, transforming into more distinct sub-grain boundaries comprising of regular arrangement of dislocations [119][125].

The sub-grains formation at the grain boundaries results into serrated grain boundaries in the final microstructure. However, Mote and Dom [126] identified that the serration in grain boundaries are the resultant of slip on basal planes having regular spacing observed in Mg-3wt.%Nd alloy. Hence, the existence of serrated grain boundaries is not a symbol of recovery initiated sub-grain formation.

2.2.2 Recrystallization in Mg alloys

Recrystallization phenomenon is a process of regenerating microstructure by nucleating strain free grain in a distorted matrix and subsequently grows at the cost of the adjoining matrix being completely exhausted. The stored energy in the matrix due to dislocations pile-up during deformation is the driving force for recrystallization. After deformation or during deformation causes recrystallization to appear. Recrystallization after deformation may occur owing to annealing of cold deformation (also called static recrystallization (SRX)) or due to cooling of hot-deformed product (after DRX). DRX stands for dynamic recrystallization, which is the occurrence of recrystallization during deformation. These DRX categorize as discontinuous and continuous. Discontinuous DRX (DDRX) initiated at localized manner near the deformation characteristics such as shear band, grain boundaries, second phase particles etc. Continuous DRX (CDRX) occur throughout the microstructure in homogeneous manner, as if recovery effectively being extended. Generally, DRX in Mg is observed very commonly rather at low deformation temperatures $T > 400^{o}K$. The activation energy of DRX is dependent on stacking fault energy (SFE) of a material. High rate of DRX decided by low SFE of a material owing to easy dissociation of dislocations into partials that prevents cross-slip. As the cross-slip hindered recovery becomes difficult, consequently DRX occur due to availability of high stored energy.

Despite similar SFEs in Mg and Al [119], DRX is very frequently observed in Mg than in Al. Stress concentration in the materials is mainly responsible for DRX in Mg due to strong crystallographic textures along with anisotropies in slips and twins. Consequently, the degree of dislocations and stored energy enhances in the microstructure especially at grain boundaries where opposing stress values are highest between adjoining grains. Such sites permit the occurrence of DRX at relatively low temperatures due to high stored energy. On contrary, in Al the strain concentration is comparatively lower and subsequently the deformation roughly uniform along with

high SFE that avoids DRX. Most of the Mg alloys that processed in industries experiences substantial DRX which encompasses the growth of nuclei or grain. The deformation mechanisms are crucial in producing the stored energy in the deformed microstructure that help DRX to arise and subsequently the DRX mechanism controls the nucleation of texture components. Therefore, clear understanding of the nucleation mechanisms of DRX along with corresponding texture evolution becomes critical.

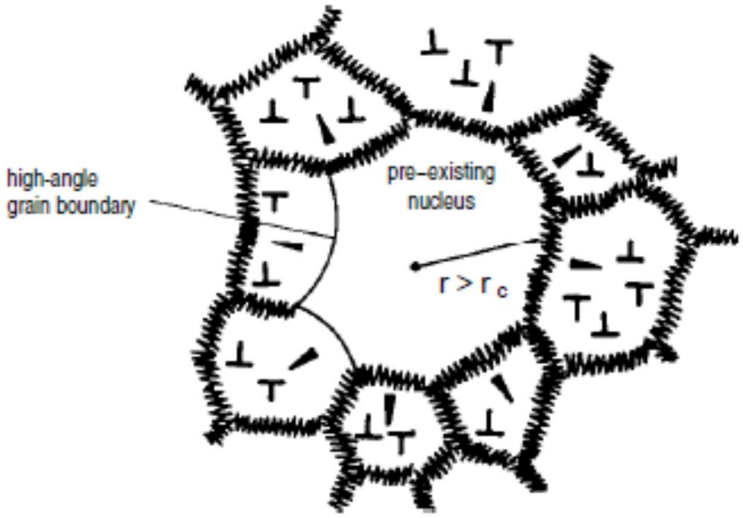

Fig. 2.15 **G**rowth potential of a recrystallization nucleus within a deformed structure [41].

On contrary to solidification, recrystallization ideally does not include the nucleation conventionally but can be explained by a process of continuous growth in grain size in which the nucleating embryo for recrystallization remains stable in relation to adjoining in all steps of growth. This indicates that the deformed substructure already contains the nuclei. Nevertheless, the possibility of attaining critical size for recrystallized embryo so as grow as desired grain depends on 3 main instability criteria [41][127] as seen in Fig. 2.15

(i) *The thermodynamic instability criterion*: Despite growing larger, the nucleus's Gibbs free energy is seen to decrease as it gets bigger. Mathematically, the critical size of the recrystallization nucleus that introduce instability; $r_c = 2\gamma/\rho G b^2$, where γ = surface energy, ρGb^2 = the stored energy of dislocations

(ii) *The mechanical instability criterion*: The driving force behind the grain boundary's movement in a particular direction depends on localize disparity arising due to heterogeneous dislocation densities and variations in sub-grain sizes.

(iii) *The kinetic instability criterion*: The nucleus definitely should have high angle boundaries i.e., difference in the orientation in relation to its adjoining is greater than 10°- 15°, so that it remains mobile during the growth process.

A nucleus cannot progress into the typical growth regime unless the aforementioned three requirements are met.

2.2.2.1 Recrystallisation Mechanisms of Nucleation

Several nucleation mechanisms of recrystallisation in Mg alloys bring about variations in recrystallization textures and microstructures. In the following we consider each mechanism and the texture components they nucleate.

2.2.2.1.1 Grain Boundary Nucleation

Activation of non-basal slip mechanism accommodate substantial extent of plastic strain in localize manner at grain covered regions beside the grain boundaries causing new fine grain nucleation surrounding the original grain boundaries, as shown in Fig. 2.16 [102]

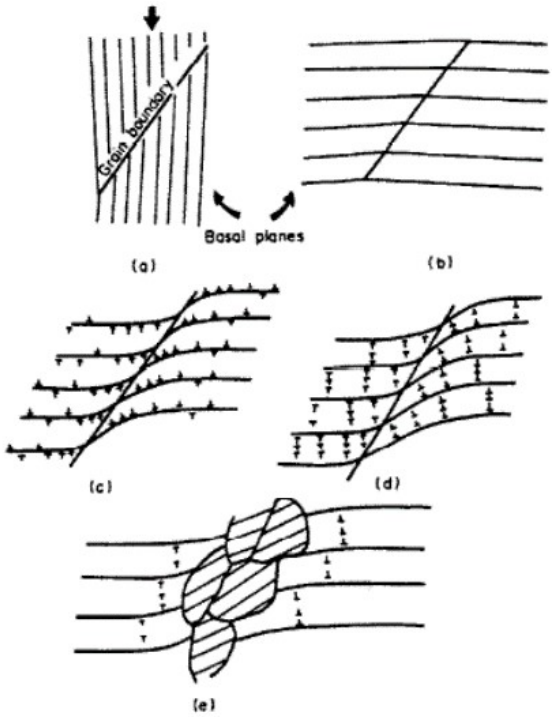

Fig. 2.16 DRX at grain boundaries after deformation [102]

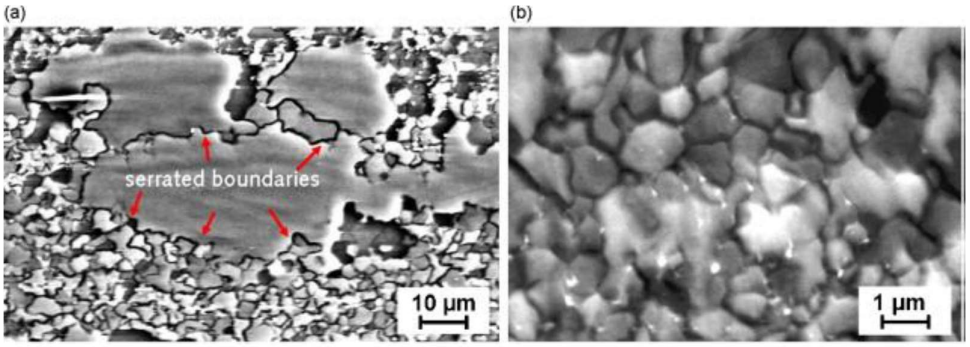

Fig. 2.17 (a) DRX process shows serration at grain boundaries resulting in (b) smaller stress free grains [128].

Generally usual wrought alloys experience such dynamic mechanism of recrystallization. Such nucleation of recrystallization at grain boundaries is of sporadic nature initiated by bulging mechanism of grains. As the deformation increases, fluctuations along the grain boundary become evident resulting in serrations and bulges that alter into strain free new grains as seen in Fig 2.17.

Al-Samman et. al. [128], identified a necklace structure at grain boundaries due to bulging phenomenon of highly deformed grains in AZ31 alloy exploring DRX mechanism. Such necklace structure formed newly around grain boundaries are having 5° to 20° of misorientation. Necklace formation during recrystallization is evident by other mechanism in addition to bulging, mainly due to substantial incoherency in the orientation of recrystallized and parent grains. The primary mechanism for necklace formation was ascribed to rotational DRX (RDRX) [129], due to high localized lattice rotations in the regimes of grain boundaries.

Rotation of lattice generally develops from the sub-grain formation near pre-existing grain boundaries during deformation resulting into a constant rise in the disorientation till a HAGB is achieved.

At some point, a certain orientation shows a stronger propensity to rotate in relation to their grain boundary. The majority of polycrystal grains exhibited tilt or twist grain boundary characteristics, but when external force was applied, the grains concurrently rotated their twist characteristics and migrated their tilt character impacts. Depending on the angle formed by the stress direction and the normal of the grain boundary plane, the degree of grain rotation may increase or decrease. Such events can also occur during static annealing using movement of high angle boundaries.

2.2.2.1.2 Sub-Grain Boundary Migration

The recrystallization nuclei forms attributing to sub-grain boundary movement via deformation zone along with pile-up of misorientation or merging of sub-grains resulting in high angle grain boundaries formation [130]. These mechanisms of nucleation are occurred with extensive recovery and formation of sub-grain. Galiyev et.al.[123] identified that during deformation of ZK60 alloy at lower temperatures (higher Zener (Z) values) above types of recrystallization gets activated.

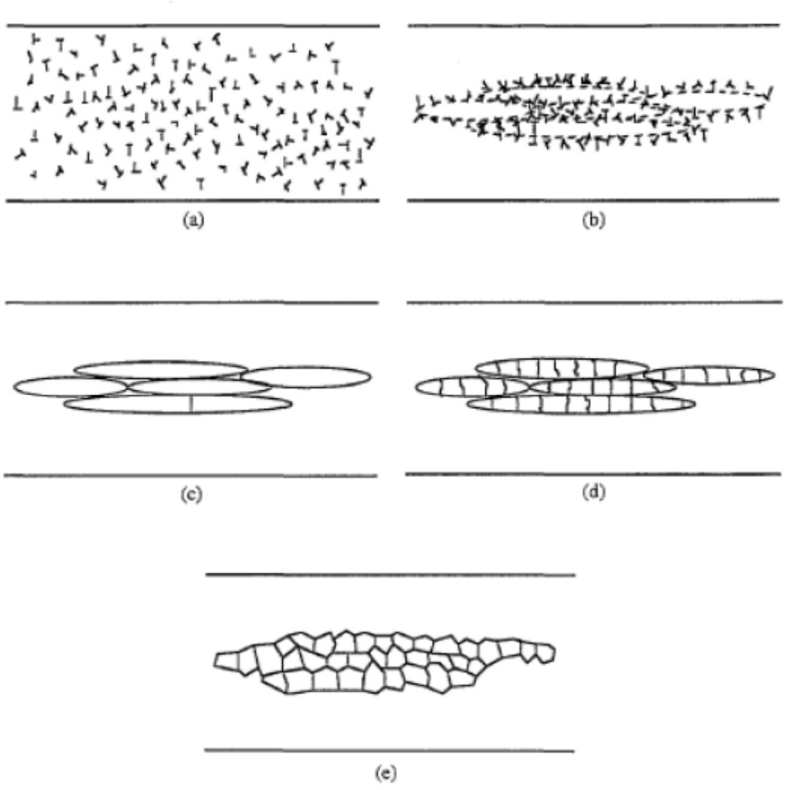

Fig. 2.18 Meyers et. al [129] model of rotational DRX (RDRX) mechanism

Al-Samman et. al. [131] additionally reported the occurrence of such recrystallization based on recovery in single crystals of Mg. The recovery develops by two mechanisms viz. migrational and rotational depending on both static and dynamic circumstances. These mechanisms of recrystallization usually result in retaining of the deformation texture and takes place regularly in pure Mg. This mechanism designated as rotation recrystallization mechanism as shown on Fig. 2.18, similar to grain boundary nucleation mechanism for recrystallization. Occurrence of such rotation recrystallization mechanism necessitate the presence of non-homogeneous deformation to develop essential orientation gradients such that part of the parent grains rotated creates new grains.

2.2.2.1.3 Shear Band Nucleation (SBN)

Different types of shear band nucleation sites are observed in Mg for recrystallization. Kink bands are one of relevant type formed in the grains which are weakly oriented for slip of basal plane [102], and the twin shear bands occur in the regions experiencing twinning phenomenon [132] or double twinning [103].

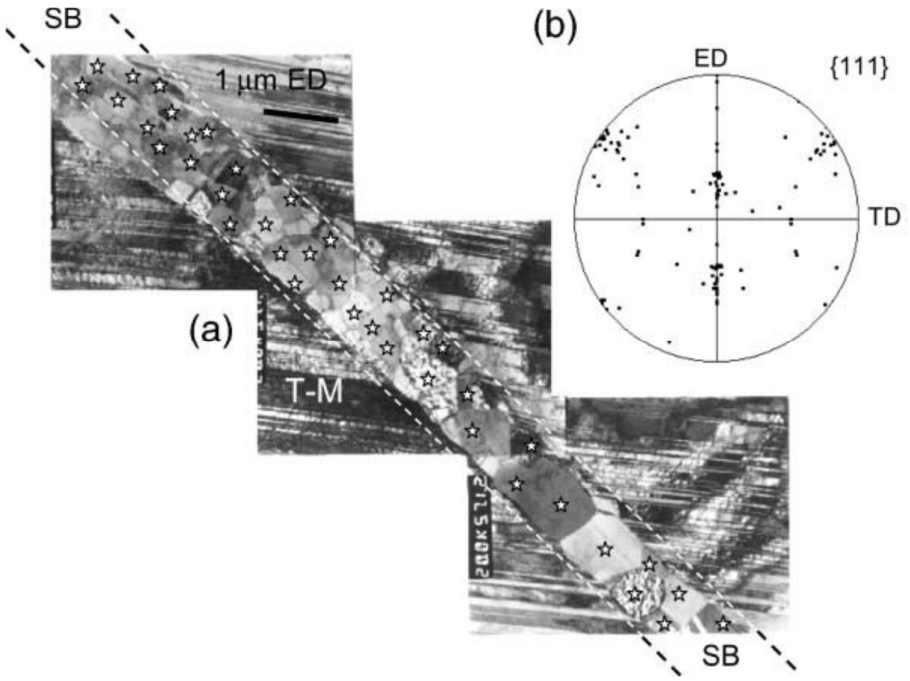

Fig. 2.19 Nucleation of recrystallized small grains inside shear bands in the TEM micrograph [133]

Generally, the microstructures of shear band are very heterogeneous showing huge spread of internal orientation. As seen in Fig. 2.19, this heterogeneous dispersion is what creates new grain nucleation sites across a wide range of orientations, with just a small number deforming differently from the typical texture. Shear band mechanism of recrystallization nucleation has critical role in Mg-REE alloys [98] [134].

2.2.2.1.4 Deformation Twinning Nucleation (DTN)

Deformation twins are appearing as nucleation sites for recrystallization having substantial potential to adjust the recrystallization texture. This happens because of more rotations related with fresh orientations corresponding to the orientation of matrix of deformed structure brought by using different range of primary and secondary twinning. These recrystallizations are studied extensively which nucleate inside the

deformation twin and at the intersections of twin-twin or twin-grain boundaries. [46] [99][128][131][135][136].

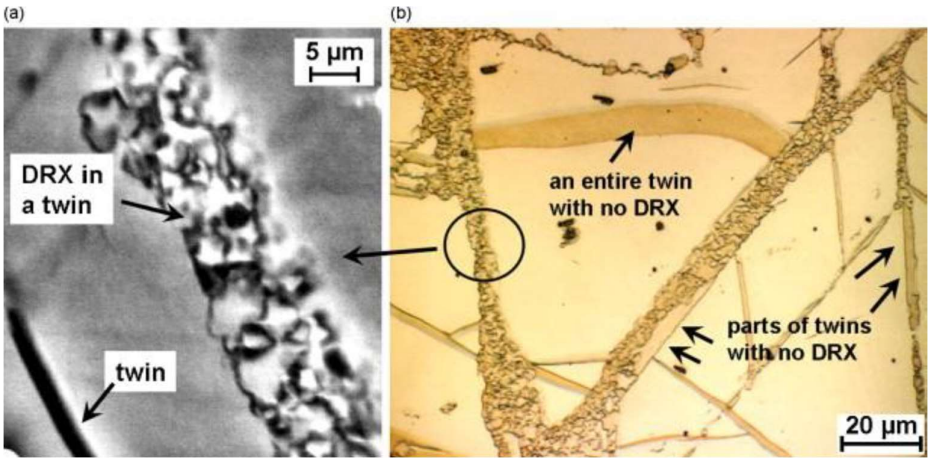

Fig. 2.20 DRX inside twins in AZ31 alloy in (a) SE mode of SEM and (b) Optical images [128]

AZ31 alloy shows an example of DRX within twins as in Fig. 2.20. Few studies [99][135] outcomes on the effectiveness of nucleation sites within twins for recrystallization and their nature of twin is either tensile or contraction and twin generation of either primary or secondary determines the contribution for texture evolution

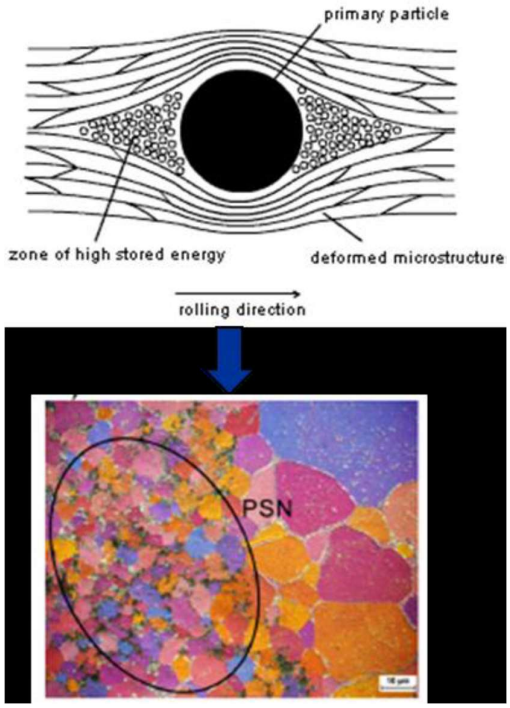

Fig. 2.21 (a) Zone of Deformation around the particle [120]; (b) finely recrystallized grains forming next to the particles [137]

2.2.2.1.5 Particle Stimulated Nucleation (PSN)

Particles of actually small size in large quantity can pin grain boundaries and impede recrystallization, However, as Fig. 2.21 illustrates, particles in a different phase that are larger than about 1 μm can actually act as nucleation starting sites for recrystallization. [119]. PSN has been regularly recognized in Mg alloys present large number of nuclei oriented discontinuously such that poor recrystallization textures [138][139]. PSN recrystallization mechanism is in race with other mechanisms in Mg alloys. Contribution of PSN to the recrystallized microstructure is usually less in reference to the volume fraction. In few situations, PSN recrystallized grains fully affect the bulk texture and manage the microstructure. Even though PSN grain growth usually has a negligible volume fraction contribution to the microstructure of recrystallized material, there are situations in which it becomes dominant and greatly affects the bulk texture as a whole. [137]. Robson et.al [140] presented studies broadly carried out on recrystallization due to the particle effects in Mg-Mn alloys such that PSN appeared prominently along clusters of particles rather than coarse particles seen as individual. Such PSN of recrystallization behaviour ascribed to higher misorientation on cumulative basis along clusters of particles in comparison with individual coarser particles. Further, the recrystallized grains nucleated by PSN mechanism are smaller in sizes while from other mechanism e.g., HAGB nucleates coarser grains. The effectiveness of PSN on weak random textures during static recrystallization is evident, but not seen in dynamic conditions. Ultimately, the potential for weak texture during static annealing was linked to the mechanism of strain-induced boundary migration, and PSN's influence on the final texture is negligible.

2.2.2.2 Microstructure Evolution during Recrystallization in Mg alloys

Hot processing of most viable Mg alloys manufactured to semi-finished products can be interpreted by the texture evolving mechanisms. Consequently, major studies in the literature are more focussed on recrystallization and grain growth to interpret the DRX behaviour and the corresponding texture evolution in wrought Mg alloys. Barnett et. al. [141] a studied wrought AZ31 alloy and reported on recrystallization in static and dynamic conditions on the subsequent grain size distribution and evolution of texture. This study identified that the kinetic of DRX were driven by the deformation condition rather than the starting texture. DRX would be incomplete at higher Z (*Zener-Holloman parameter*) values, but entirely recrystallized

microstructure was attained at lower Z values. A complicated relationship involving the Z value and the size of final grain achieved during the annealing of partially DRX samples. The resulting observations and corresponding conclusions were initiated:

a) **Low Z values:** The influence of Z on the microstructure was not significant, hence the initial grain size during DRX is slightly smaller than the final one. As a result, the specimens go through grain growth after experiencing full DRX.
b) **Intermediate Z values:** Abnormal grain growth is generally evident generating the coarsest grains. Around ~80%-95% grain in the microstructure attained DRX, while the remaining not yet undergone DRX before annealing process. Later static annealing causes desirable recrystallized grains to grow beside the deformed regions and in-turn consume these deformed grains for the growth of recrystallized grains. The moment recrystallized grains growth is interrupted, then abnormal grain growth occurs for the newly grown grains.
c) High Z values: Considerable amount of non DRX regions available prior to annealing and hence go through static recrystallization on resultant heat treatment. As the Z value increases, then the overall number of sites for nucleation increases, subsequently size for final grains would continue decreasing.

The annealing treatment shows negligible response qualitatively toward deformation texture except texture weakening.

Cottam et. al. [142] reported comparable interpretations studied on pure Mg and Mg-Y alloys regarding DRX texture reduced the intensity of texture but no effect on deformation texture. The deformation conditions control the evolution of DRX texture in place of special circumstances of nucleation or growth.

Gottstein et. al. [143] also reports similar analogy of no effect of static recrystallization on deformation texture but decreases the texture intensity in pure Mg and AZ31 alloy. The recrystallization process considered as continuous usually where extended recovery occurs because of no qualitative changes in the crystallographic texture as compared to deformation texture. The progression of recrystallization during annealing process is discontinuous in Mg alloys shown by nucleation and growth in the microstructural evolution like *fcc* metals. (0001) fibre texture occurs due to the activity of two basal slip system mainly i.e., $<11\bar{2}0>$ (0001) and $<10\bar{1}0>$ (0001) systems. Since the basal plane show 6-fold rotation symmetry, then the changes in texture due to recrystallization are very tough to examine by macrotexture analysis.

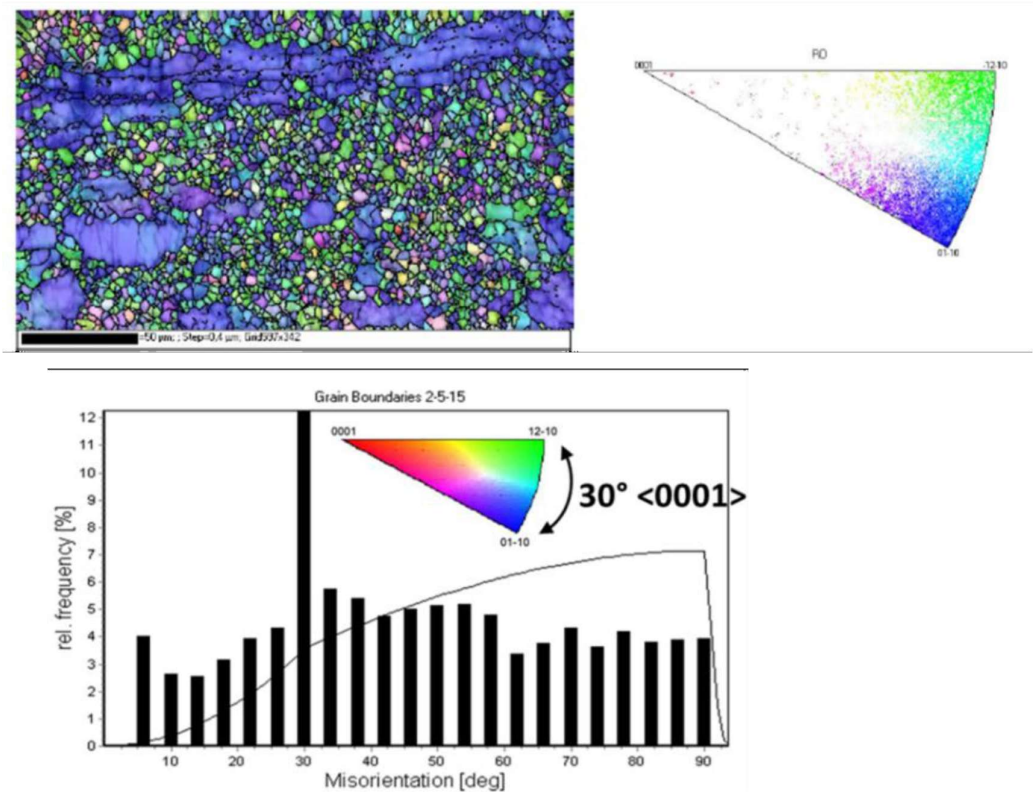

Fig. 2.22 (a) Together with IPF scatter data, green recrystallized grains predominate over blue deformed grains with a misorientation of 30^ <0001> in magnesium. The distribution map of grain boundary misorientation (b) displays the maximum misorientation at 30˚. [143].

The discontinuous behaviour of recrystallization in magnesium with a misorientation of 30° <0001> connection involving the recrystallized and deformed grains is validated by the EBSD study shown in Fig. 2.22. Lücke et. al. [144] reported similar results earlier regarding nucleation of recrystallized grain boundaries having misorientation of 30° <0001> with deformed grains preferentially in pure Mg. Nevertheless, such preferred orientation was unpredictable either because of preference in oriented nucleation or during oriented growth develops at competitive stage.

The annealing procedure was carried out on rolled AZ31 alloy at temperatures of 200° C, 300° C, and 400° C by Jäger et al. [137]. Incomplete recrystallization resulted in very low fraction at 200° C that probably nucleating at the neighbourhood of twins and twin intersections. Within the first two minutes of the annealing process, the AZ31 alloy achieved complete recrystallization at 300° C. Grain growth then started, with the triple junctions progressing to the equilibrium order of 120°. Grain

growth is influenced by the twins in a way that makes growth at the twin boundaries more stable than elsewhere.

The twin boundaries most likely act as preferred sites to nucleate recrystallize grains, accordingly despite being low temperature ~ 150°C - 200°C twin boundaries are first to recrystallize. Annealing process at 400° C results into complete recrystallized microstructure developed at a holding time of 60 seconds. After static recrystallization at 400°C, the texture revealed of huge spread of asymmetric and significantly weaker intensities. The initial texture along basal plane in as-received specimen exhibit along TD while the recrystallization texture display along RD predominantly.

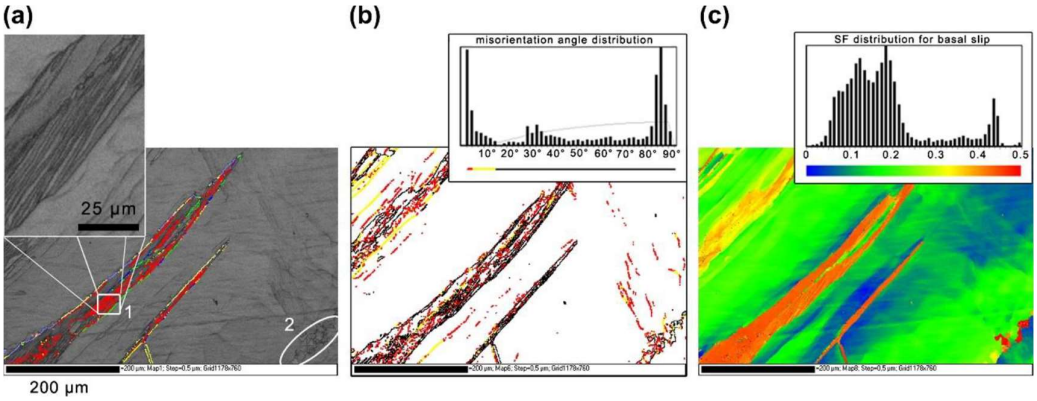

Fig. 2.23 Twinning behaviour in Mg single crystals at 200 °C [131].

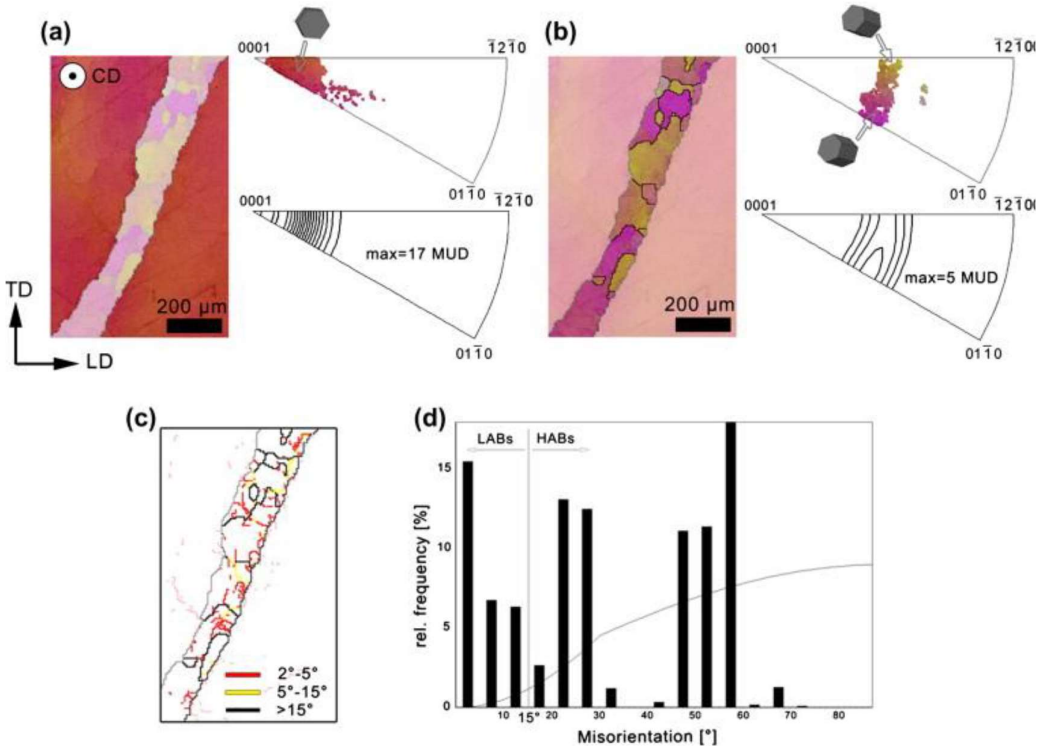

Fig. 2.24 At 370°C, single crystals of magnesium exhibit distorted and double DRX textures. [131].

Al-Samman et. al. [131] examined the DRX activities under c-axis compression in single crystals of magnesium. Around 200°C, there was a lot of twinning in the deformation microstructure, with main $\{10\bar{1}1\}$ and $\{10\bar{1}3\}$compression twins passing through secondary $\{101\bar{2}\}$ tension twinning as noticed in Fig. 2.23(a) generate preferential orientation for basal slip as seen in Fig. 2.23(c). The misorientation relationship between LAGB and HAGB being in the range of 80° - 90°.9 as depicted in grain boundary maps in Fig. 2.23 (b). The HAGB related to the double twinned regions generally made of primary compression twins and secondary tension twin having misorientation relationship. These twinned regions go through recrystallization completely, where the new grain maintain the orientation of parent compression twin about c-axis having misorientation angle of ~56°±5° with the host grain along the [0001] direction as seen in Fig. 2.24 (a)-(c). The DRX mechanism within the twins pursued the continuous recrystallization process, where intense recovery causes HAGB formation so that strain free new grains are generated as seen in Fig. 2.24 (d) & (e). The DRX grains within the twins exhibited their c-axes rotation randomly developing fibre spread involving $[\bar{1}2\bar{1}0]$ and $[01\bar{1}0]$ axes.

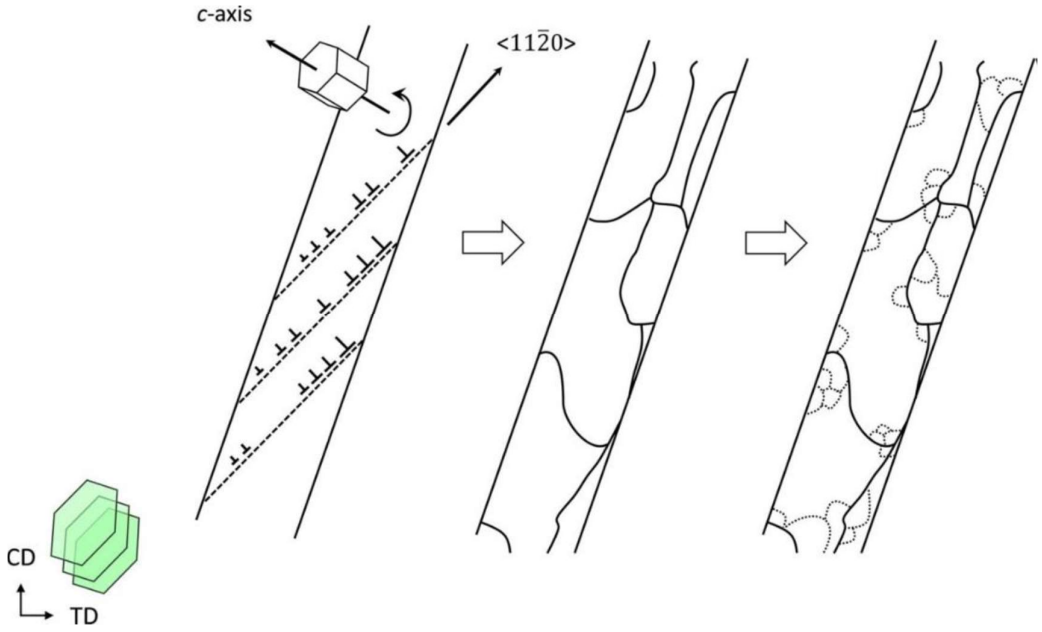

Fig. 2.25 Representation of immediate slip instigated lattice rotation and break up while DRX in twins of compression and double respectively [145].

Further investigations by Molodov et. al. [145] reported the activity of prismatic slip responsible for the DRX in twins causes simultaneous fragmentation of twin and rotation of the lattice surrounding the grain c-axes, as depicted in Fig. 2.25

2.2.2.3 Progression of Textures of Recrystallization

The texture of recrystallization mainly based on (i) the orientations of the new nuclei or sub-grains, and (ii) the relative nucleation and growth rates of the newly formed grains. Accordingly, two main possible models for the estimation of texture development during recrystallization [127].

Theory of orientation-based nucleation:

A particular orientation intensifies for nucleation quicker than other orientations and hence control the orientation distribution finally. Consider P as preferred orientations for the nuclei fraction and R as random orientations (except the preferred orientations) for the nuclei fraction, then for orientation-based nucleation will have P/R>> 1. Moreover, the abovementioned principle is similar to grain frequency parameter provides the most repeatedly appearing orientation required for nucleus. Difficulty in predicating the nucleating orientations appears as a limitation of this model [127].

Theory of orientation-based growth:

Some orientations of recrystallized exhibit a distinct relationship of misorientation referring to the deformed host grains which devour the matrix quicker than others so that the selection of growth mechanism conforms to grain boundaries with ~ 40°<111> as seen in *fcc* systems regularly [146].

Similar analogy applied to *hcp* systems where the recrystallized grains experience misorientation of 30°<0001> or 90°<10$\bar{1}$0> with the deformed host grains are recognized to grow preferentially than the others [144]. This theory states as a grain size effect. Consider 'Ps' and 'Rs' as the average grain size pertaining to Preferred orientation and non-preferred orientation respectively, then Ps/Rs >> 1 [127]. Efforts have been made to hypothesise the essential mechanisms that evolve in a situation where the criterion, Ps/Rs >> 1 is met.

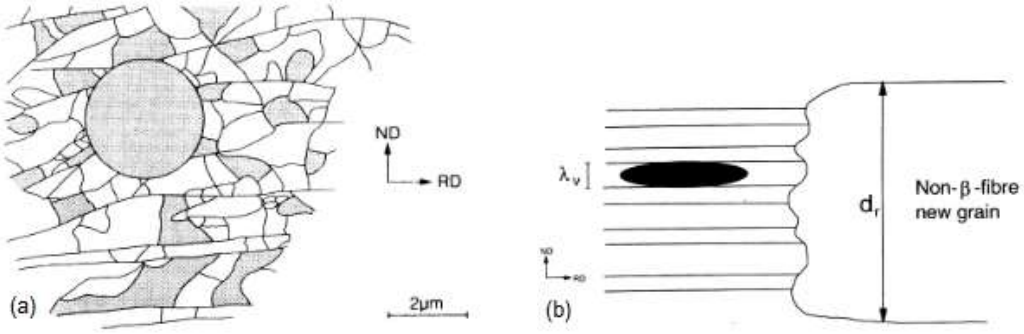

Fig. 2.26 Pinning and variant inhibition [127].

Pinning based Orientation: As the grain grows, then it starts meeting numerous grain boundaries having different values of misorientation as showed in Fig. 2.26 (a). In this process suppose a grain encounters a region having similar orientation, then it will form LAGB in the deformed materials and consequently its movement will be significantly reduced, thus slow down its growth. On the contrary, some of the orientations meet very few similar orientations and consequently such grains orientation grows relatively quicker than other grains [147].

Types of Inhibition: The deformation of grains takes place parallel to extrusion direction in plane strain deformation conditions so that deformation bands of stable orientation initiate along processing direction as observed in Fig. 2.26 (b). The resultant microstructure illustrated by LAGB between adjacent deformed bands. Such components of deformation texture initiate the grains that are not capable of thickening and cause strong inhibition for growth across normal directions. Many nuclei grow in

a single deformed orientation despite having diverse orientations, hence the growth rates are determined by the misorientation brought on by the deformed matrix and the stored energy. On contrary, the nuclei growth rates consist of variation in misorientation with the deformed grains depicted as compromise growth because the nuclei growth occur in number of deformed grains. Both competitive and compromise types are furthermost growth types. In actuality, the first growth stage is identical to the competitive type, and the growth stage shifts to resemble a compromise growth as soon as the nucleus develops beyond the deformed grains (i.e., when the diameter of the nucleus is equal to the smallest grain deformation dimension). Identifying growth based on orientation from oriented based nucleation is difficult in practical scenario. Besides, the preferred orientation relationship develops a temporary parameter as the grains continues to grow in new adjacent regimes [148].

2.2.2.4 Grain Rotation during Recrystallization

The recrystallization texture in *hcp* metals is associated with rotations of ~30º about the <0001> axis and ~90º about $<10\bar{1}0>$ [149]. Gottstein et al. [150] identified that the recrystallization texture in Mg alloys sample is same to the deformation texture. Such predominant texture remains unchanged even though some other components are developed during annealing at temperature greater than 400ºC. Suwas et al. [151] and Wagner et al. [152] independently made similar interpretations on Ti_3Al and Ti respectively, wherein the texture development during static recrystallization appears rather slow. Based on these findings Biswas et al. [153] reported that during static recrystallization the deformation texture remain unchanged for pure Mg processed by ECAE. The texture of recrystallization is determined by the orientation of the newly produced grains and the relative speeds of their nucleation and development. Retaining of the texture of deformation can be done either by substantial recovery and polygonization process or by the nucleation process of grains that gets oriented afresh during deformation. Gottstein et. al. [150] identified that during annealing of AZ31 and AZ61 alloys, growth occur preferentially by rotation at 30º along {0002} axis from $<2\bar{1}\bar{1}0>$ to $<10\bar{1}0>$. Since the texture components shift from $\varphi_2 = 0°$ or 60º to $\varphi_2 = 30°$ and finally $\varphi_1 = 30°$, then 30º rotation observed in the ODF plot in $\varphi = 90°$ section of the Euler space.

2.3 Magnesium Rare Earth (RE) alloys

Mg alloyed with rare earth (RE) elements usually incorporate La, Ce, Nd, Eu, Gd, Yb and Y. Primarily Mg with added RE elements impart strengthening through solid solution and creep resistance at elevated temperatures [154][155]. Poor textures and decreased yield anisotropy of RE alloys were initially informed by Ball and Prangnell [139], following studies have explained substantial enhancements in ductility also appear with RE addition [17][18][156]. RE elements belonging to lanthanide group elements having alike physical and chemical properties bearing atomic numbers (Z) from 57 to 71. They are classified into mainly two subgroups such as (i) Light REs include all the elements beginning with Lanthanum (La, Z=57) to Europium (Eu, Z=63) and (ii) Heavy REs involving Gadolinium (Gd, Z=64) to Lutetium (Lu, Z=71) along with Yttrium (Y, Z=39). A typical thumb rule about REs in Mg says that 'light' REs usually exhibits low solubilities, while the 'heavy' REs displays high solid solubility. The solid solubility of REs can be explored by heat treatment such that Mg-Nd alloys exhibit huge reciprocation to age hardening succeeding by Mg-Ce alloys, while Mg-La alloys display nearly no response to age hardening owing to the less solubility of La in Mg [154].

2.3.1 Phase Transformations in Mg-REs alloys

There are number of variety of phases in Mg–RE elements alloys potentially formed common to all such as $Mg_{12}RE$, $Mg_{17}RE_2$, Mg_3RE or Mg_2RE phases. Nevertheless, the clarity about such phases in terms of type or form possibly nucleating under a particular solidification condition. e. g., in the Mg–Nd system, speculation about the phase $Mg_{12}Nd$ is either an equilibrium or metastable phase. Similarly, in Mg-La system the phase $Mg_{12}La$ forms oppositely to $Mg_{17}La_2$. Therefore, to identify the influence of RE element adding on the properties and processing of these alloys necessitate the urgency to obtain a few backgrounds about the phase transformations arising in such alloys. In this section, the phase transformations of binary Mg-Ce alloys will be represented. An extensive information on the Mg-RE element alloy system pertaining to their physico-chemical properties is reported for further reference [154].

2.3.2 Mg-Ce Phase Diagram

The Mg-Ce phase diagram as seen in Fig. 2.27 is characterized by presence of six intermetallic systems such as $Mg_{12}Ce$, $Mg_{17}Ce_2$, $Mg_{41}Ce_5$, Mg_3Ce, Mg_2Ce and

MgCe phases. Majority of the phases are formed by peritectic reaction except Mg_3Ce, which is consistently melting compound. Eutectic transformations of two occur on both the Mg-rich and Ce-rich ends, along with these eutectoid transformations showing as $Mg_2Ce \rightarrow \alpha\text{-Mg} + Mg_{12}Ce$ and $\delta\text{-Ce} \rightarrow \gamma\text{-Ce} + MgCe$

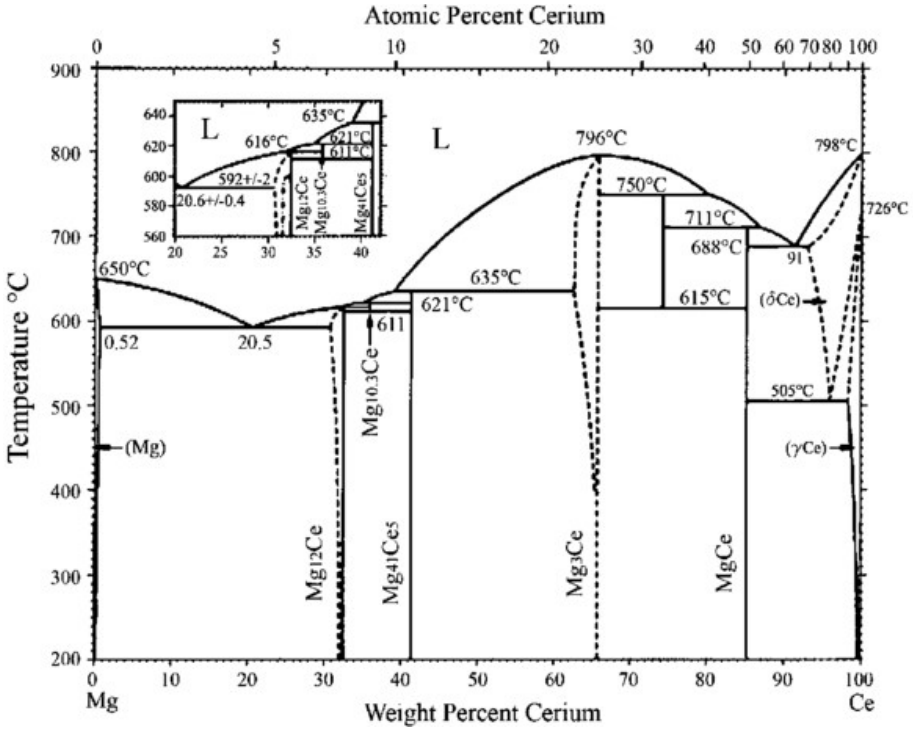

Fig. 2.27 Mg-Ce phase diagram [157]

According to the literature, the two compounds Mg_3Ce, Mg_2Ce and MgCe are very clear effectively. $Mg_{12}Ce$ displays true orthorhombic crystal structure [158]. At the eutectic temperature of 590°C in the Mg-rich side displays Ce to 20.5 wt% at the eutectic point. From the resistivity experiments, the solubility of Ce solid in Mg found to be maximum of 0.74 wt.% at 590°C but decreases lowest about 0.04wt.% at 200° C. The solid solubility of Ce in Mg is 0.06 wt. % and 0.08 wt. % at 300° C and 400° C [154].

2.3.3 Texture Alteration in Mg alloys: Effect of RE Element addition

During deformation and recrystallization alteration in textures is acknowledged to RE elements addition in Mg alloys. Such changes in textures due to RE element during deformation is primarily noticed in along with simultaneous DRX. The intention of RE element addition in Mg for the first time was primarily required to enhance solid

solution strengthening and impart creep resistance in the system. The development of weak textures and decreased plastic anisotropy in RE element added alloys containing Y reported 3 decades before. Similarly, in another RE element i.e., Nd addition induced large random type textures in contrary to usual Mg alloy during extrusion deformation process. Enhanced texture randomization effectively decreases the large asymmetry occurs during tension – compression which essential for improvement in formability by controlling the texture. Recrystallization based on PSN was attributed for the randomized texture exhibited in these WE alloys loaded by large addition of Y and RE elements. [139][159]. Enhancement of PSN for recrystallization due to addition of RE element is not yet established. Nevertheless, the contribution of PSN mechanism for recrystallization is comparatively very low (~1%) to the overall texture usually contemplated as negative feature as a sole mechanism. Even though PSN mechanism of recrystallization induced weakening of texture was ascribed to suitable growth of PSN orientations [137].

During deformation and recrystallization alteration in textures is acknowledged to RE elements addition in Mg alloys. Such changes in textures due to RE element during deformation is primarily noticed in along with simultaneous DRX. The intention of RE element addition in Mg for the first time was primarily required to enhance solid solution strengthening and impart creep resistance in the system. The development of weak textures and decreased plastic anisotropy in RE element added alloys containing Y reported 3 decades before. Similarly, in another RE element i.e., Nd addition induced large random type textures in contrary to usual Mg alloy during extrusion deformation process. Enhanced texture randomization effectively decreases the large asymmetry occurs during tension – compression which essential for improvement in formability by controlling the texture. Recrystallization based on PSN was attributed for the randomized texture exhibited in these WE alloys loaded by large addition of Y and RE elements [139][159]. Enhancement of PSN for recrystallization due to addition of RE element is not yet established. Nevertheless, the contribution of PSN mechanism for recrystallization is comparatively very low (~1%) to the overall texture usually contemplated as negative feature as a sole mechanism. Even though PSN mechanism of recrystallization induced weakening of texture was ascribed to suitable growth of PSN orientations [137]. Texture modification also identified even though for a very small addition of RE element (~1wt.%) both in term of quantitative and qualitative aspects in later studies. Bohlen et al. [17], studied variations in the additions of Zn and

RE element in six Mg alloys. According to their studies, RE element containing alloys has lower levels of total textural intensity and the strength of basal pole aligned with ND of sheet compared to conventional alloys. Moreover, this investigation also revealed that the anisotropy got reversed for the yield strength and consequently the planar anisotropy decreased to $r \sim 1$ than compared with the conventional Mg alloy sheets.

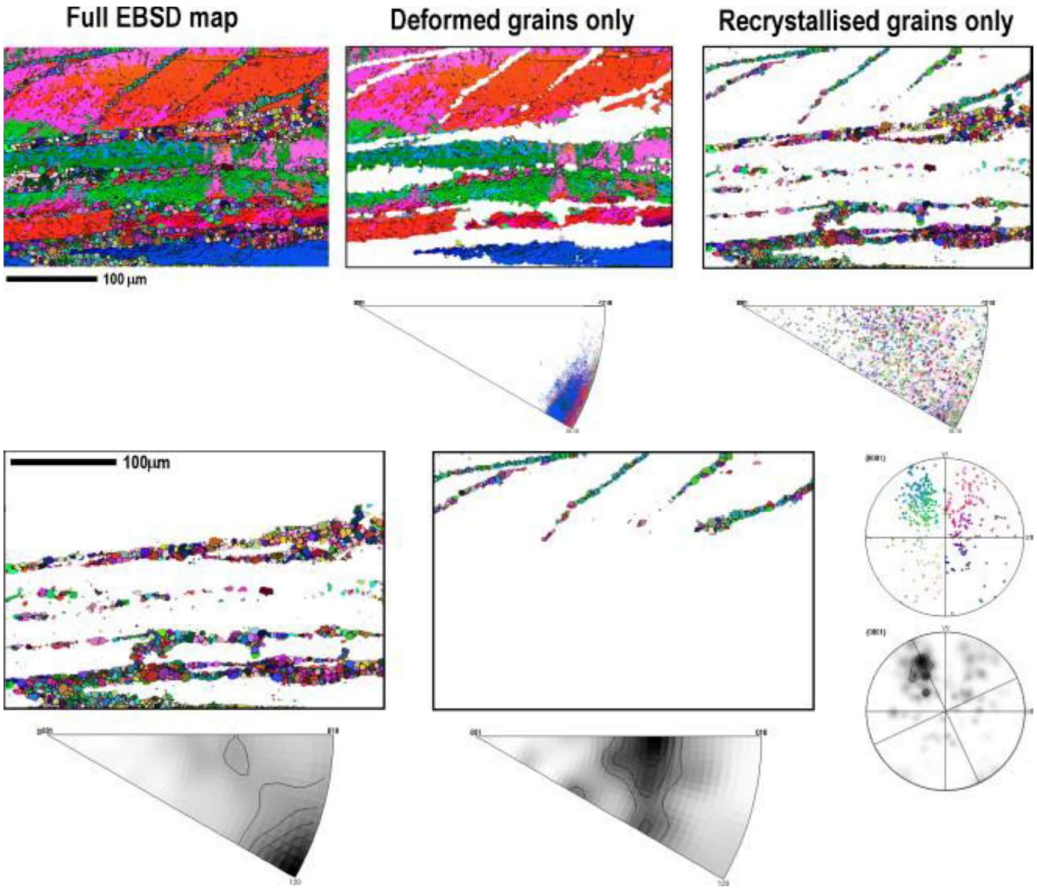

Fig. 2.28 The <11$\bar{2}$1> directions of shear band orientations parallel to ED in Mg-REs [98].

Both features modify the texture in the Mg–Zn–RE alloys, where large number of grains are placed in suitable orientations to be slipped in basal plane and tension twins. Stanford and Barnett carried an extensive investigation [98], where it was revealed that the RE element additions resulted in specific texture component along the <11$\bar{2}$1> directions parallel to ED in hot extruded Mg alloys as observed in Fig. 2.27 The texture component was conceived as '*RE-texture*'. Emergence of then *RE-texture* was ascribed to collective effects of oriented nucleation in kinetics of retarded

recrystallization and in shear bands. In contrast, texture alteration in Mg-Zn-Ce (ZE10) hot-rolled alloys [134] during recrystallization by shear band was ascribed to suitable growth of texture features rotated by ~45° in TD shown by the pole figure data in Fig. 2.28

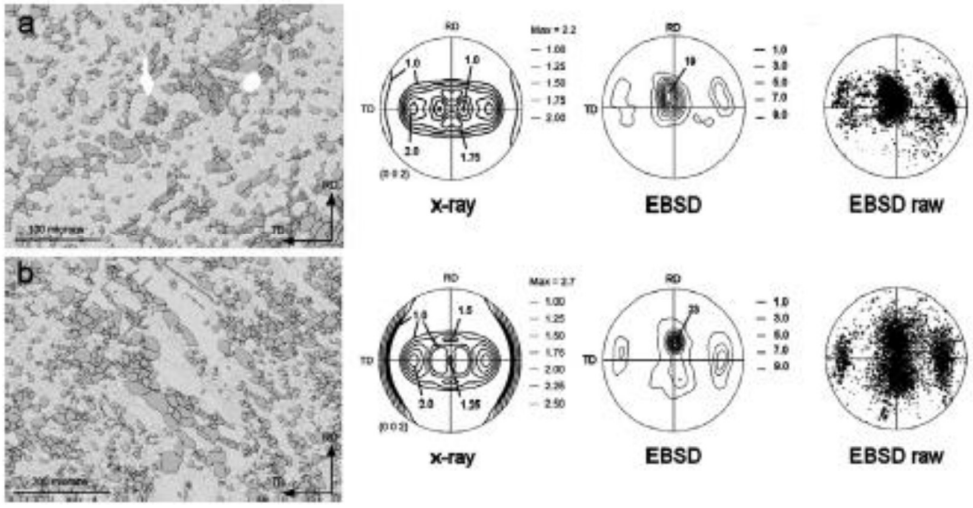

Fig. 2.29 ZE10 alloy, Recrystallization by shear band in the hot rolled after annealing at 400˚C for (a) 60s and (b)180s, induces suitable growth of texture features rotated by ~45˚ in TD [134].

Hantzsche et al. [160], reported the investigation of the Mg alloys sheets revealed that sheet textures get weaken due to enhancing the content of Ce, Nd, and Y such that shear bands appears consisting of double twins and compression and the constraint of grain growth through annealing latterly. Nucleation within compression and double twins deviated primarily from basal orientations stimulate alteration in texture potentially during subsequent recrystallization. Finally, the inclusion of RE elements in wrought Mg alloys provide an opportunity to control the textures.

The manifestation of the literature recommends weakening of texture in Mg alloy ascribed to following main roles of REs:

(i) Changes in the SFE of the Mg matrix features rotated by ~45° in the TD shown by the pole diagram data in Fig. 2.28

(ii) Produces particle pinning or solute drag effects during deformation and recrystallization.

However, the definite character of interaction involving RE elements during deformation and annealing activities in Mg alloys yet remains disguised area. From this

perspective, systematic investigations insisted to address specifically the following concerns:

(a) Critical impact of alloying content and choice of RE element needs clarity in specific.

(b) Moreover, additional investigation required to check the impact of the processing parameters of both crystallographic deformation and annealing treatment on the above conditions.

Finally, the further role of non-REEs in helping REE – associated texture alteration has to be recognized.

2.3.4 Recovery in Mg-RE alloys

The softening mechanism of deformation attributed to process of recovery and recrystallization. Both recovery and recrystallization behaviour are changed due to presence of non-basal slip systems. Recovery mechanisms, which annihilate dislocations and realign them into sub-grain boundaries, reduce the collected energy of a microstructure during deformation [119]. Many Mg alloys shows formation of sub-grains that arises through continuous RDRX (Rotational Dynamic Recrystallization) mechanism [102][123]. RDRX is a quasi-recovery process where representative of recrystallization, nucleation and growth occurs along with formation of sub-grain at grain boundaries. Activation of many slip systems are required for sub-grain formation [161], which happens especially at superior temperatures with the activation of non-basal slip system [102]. Hadorn et.al. [161], claimed that sub-grain formation in Mg-RE alloys occurs at low temperatures due to increase in prismatic slip such that RE texture nucleate within RDRX grains. Prismatic slip mainly responsible for sub-grain formation and thereafter texture weakening within a contraction twin in CDRX grains observed in the study of a single crystal [145]. Nevertheless, apart from prismatic slip, effective pyramidal slip can also increase the sub-grain formation, as both provide the additional slip systems required for easy sub-grain formation.

Since the recovery rates decides the stored energy in deformed grains depending on recrystallisation rate, then the recovery rates result in the formation of RE texture [119]. Fazadfar et.al. [162] suggested prospective forming of RE textures as grains with RE orientation recrystallizes quicker than others due to initiation of SRX at different rates based on different grain orientations having differences in stored energy. The

variations in the stored energy between orientations depending on dissimilarities in recovery rate between grains causes faster recovery by the non-basal slipping.

Fazadfar et.al. [162] reported that the stored energy in RE orientation grains along ND-TD is 20 times less than in grain oriented along basal plane in Mg-0.81at%Y alloy at 50% reduction during hot rolling at 350ºC in a single pass. Very finer substructure is noticed in the basal grain due to higher stored energy than the relatively in the ND-TD grains with low stored energy. Anyway, such huge variations in stored energy and substructure occasionally stated in alloys bearing low intensity RE textures. Stanford et. al. [163] reported that the variations in stored energy using grain orientations in Mg-Gd alloy is not substantial in plane strain compression at 400ºC operated in wide strain rates. Y Chino et. al. [19] identified the recovery process in Mg-0.2wt%Ce alloy attributed to Ce addition that causes suppression of DRX and low diffusion.

2.4 Processing Maps

The processing maps are formulated based on the principles of Dynamic material modelling (DMM) [164] outlined by Wellstead was founded upon the important principles of continuum mechanics involving huge plastic flow, physical systems modelling, and irreversible thermodynamics [165].

In this model, the workpiece was conceptualized as a body dissipating power.

Briefly, they are derived as follows:

$$P = \overline{\sigma}\dot{\overline{\varepsilon}} = \int_0^{\dot{\varepsilon}} \sigma \, d\dot{\varepsilon} + \int_0^{\sigma} \dot{\varepsilon} d\sigma \quad \text{---------- (2.5)}$$

where P = the overall power dissipated by the workpiece, often rewritten as $P = G + J$

The power contribution in the workpiece was followed in the following two corresponding parts during plastic deformation: the visco-plastic heat (the rate of production of internal entropy) induced by plastic deformation, denoted as G, and the internal energy alteration in the material due to microstructural changes, denoted as J. The constitutive equation dictates the comparative values of power dissipation through heat conduction and microstructural dissipation as the origin of visco-plasticity lies is in the microstructural dissipation. For materials deforming plastically, the power law:

$$\overline{\sigma} = K(T, \overline{\varepsilon}, \dot{\overline{\varepsilon}})\dot{\overline{\varepsilon}}^{m(T,\overline{\varepsilon},\dot{\overline{\varepsilon}})} \quad \text{---------- (2.6)}$$

Is extensively utilized to establish a constitutive relation, where T = temperature and $\overline{\varepsilon}$= the effective strain. At a particular T and $\overline{\varepsilon}$, and within small variations of $\dot{\overline{\varepsilon}}$, $\Delta J/\Delta G$

and $\Delta J/\Delta P$ display the alterations in the dissipative mechanism. For smaller values of K, m, and $\dot{\bar{\varepsilon}}$, the instant values of $\Delta J, \Delta G$ and ΔP, are given as

$$\Delta J/\Delta P = m/(m+1) \quad \text{---------- (2.7)}$$

Strain rate sensitivity (m) is considered a power dividing factor. The sensitivity index (m) of strain rate of flow stress can be computed based on the strain rate by establishing a linear correlation between ln(σ) and ln(ε̇) through fitting (as seen in Fig. 2) using a cubic spline function from Eq. (8) for the given range of temperatures [166]

$$\eta = \frac{\partial ln(\sigma)}{\partial ln(\dot{\varepsilon})} \quad \text{---------- (2.8)}$$

The power dissipation efficiency $\boldsymbol{\eta}$ in relation to the linear dissipator is expressed as

$$\eta = \frac{\nabla J/\nabla P}{(\nabla J/\nabla P)_{linear}} = \frac{m/(m+1)}{1/2} = \frac{2m}{(m+1)} \quad \text{---------- (2.9)}$$

where $\boldsymbol{\eta}$ is a variable associated with temperature of deformation, strain, and strain rate.

For a particular strain, the correlation among η (efficiency), deformation temperature (T), and strain rate (ε̇) can be illustrated through three-dimensional graphs drawn as a processing map. The variations of the power dissipation efficiency with temperature and strain rate in each processing map, shows distinct zones that may be associated with particular microstructural processes. The zone of dynamic recrystallization (DRX) is selected for the hot working of metals because this process results in suitable formability and a defect-free microstructure without instabilities. But the high values of power dissipation may not always be beneficial for material workability, since they are generally high in the unstable domains [167]. These power dissipation maps are employed alongside instability maps, that identify domains of flow instabilities depends on extreme principles of irreversible thermodynamics as applied to extensive plastic flow stress suggested by Ziegler, [168].

Ziegler observed that stable flow occurs when,

$$\frac{dD}{d\dot{\varepsilon}} > \frac{D}{\dot{\varepsilon}} \quad \text{---------- (2.10)}$$

is satisfied, where D $(\dot{\varepsilon})$ represents the dissipative function of the material. Since metallurgical stability is of interest, assessing microstructural stability involves substituting J for D.

In accordance with the criterion established by Prasad, [169] flow instability will occur if:

$$\xi\ (\dot{\varepsilon}) = \frac{\delta ln\left[\frac{m}{m+1}\right]}{\delta ln[\dot{\varepsilon}]} + m < 0 \quad \text{---------- (2.11)}$$

This instability criterion physically suggests that when entropy creation rate of a system is lower than the strain rate, localized plastic flow will ensue, leading to flow instability. The domains where the parameter $\xi(\dot{\varepsilon})$ is less than zero were indicated on the two-dimensional temperature–strain rate map leading to the instability map.
The fluctuation of $\xi(\dot{\varepsilon})$with temperature and strain rate forms the instability map which may be overlapped on the power dissipation efficiency map to delineate instability regions characterized by negative $\xi(\dot{\varepsilon})$values. This procedure has been employed to optimize the hot workability of a variety of metals and alloys [170] such as Mg–Li–Al alloys in their as-cast state, [171] and rolled conditions [172]. The processing maps for Mg alloys through low stacking faults energy exhibit dynamic recovery (DRV) that occurs when efficiency of power dissipation (shown by contour lines), η<30%, can enhance the thermal processing effectiveness by its softening and thus stabilization functions on flow [173].

The processing map depicts that, there is a higher power dissipation efficiency zone under the comparatively high-temperature and low-strain rate, because the elevated deformation temperature accelerates atomic diffusion, facilitating the occurrence of DRV, thereby improving the driving force for flow softening reported by Deogade et. al. [174].

2.5 Numerical Methods for Constitute Analysis

Several constitutive models, for instance empirical, semi-empirical, phenomenological, and physically based models, are proposed to describe deformation of alloys as a function of the flow behaviour and establish constitutive equations under diverse hot deformation conditions [175][176][177]. Amid of the suggested models, the Johnson–Cook (JC) [178] and Zerelli–Armstrong (ZA) [176] models are the utmost popular for studying the deformation behaviour of alloys. The constitutive model of Johnson–Cook (JC) is the most extensively known model that incorporates phenomenological flow stress based on forming temperature, strain, and strain-rate. This model had been successfully employed on various materials exhibiting diverse arrays of temperature of deformation and strain rate. The Zerelli–Armstrong (ZA) model is developed cantered on dislocation mechanisms, which perform a prominent task in controlling the inelastic behaviour of a metal and its associated flow stress underneath various loading conditions. The flow behaviour of the metals and alloys

determined by the results of strain hardening, strain-rate hardening, and thermal softening are considered. Sellars and McTegart [179] recommended a hyperbolic sinusoidal Arrhenius-type equation tailored to a large extent of flow stresses. Later, Arrhenius-type equations were initiated with the Zener-Hollomon parameter to communicate the relation between the strain rate and the temperature. The flow stress values can be properly predicted by these Arrhenius-type hyperbolic sinusoidal constitutive equations throughout a wide range of high temperature working circumstances.

Gao et al. [180] used the Arrhenius-type statements to get the constitutive equations of Mg alloy WE43. Changizion et al. [181]. utilized the hyperbolic sinusoidal Arrhenius-type equations to find the constitutive equations along with error analysis but without correlating with the processing map for commercially applicable Mg alloy AZ81. Hadadzadeh et al. [182]. developed the constitutive model in conventional and as well as modified hyperbolic sine expressions in view of the outcome of strain, strain rate, and temperature-dependent material parameter for a well-known Mg alloy ZK60, by dividing hot deformation conditions into 4 regimes based on high and low temperatures and strain rates. Another commercial Mg alloy AZ31 was used by Hamed Mirzadeh et al. [183] to describe the peak stress under hot conditions of compression, torsion, and tension tests using hot working activation energy as a task of Arrhenius-type hyperbolic sinusoidal equations.

2.5.1 Hyperbolic Sine Arrhenius Model

Arrhenius-type sinusoidal hyperbolic equation determines the hot deformation flow stress**,** so as to establish the constitutive equations [177]. This deformation at high temperatures is based on temperatures and strain rates examined by applying the Zener-Holloman parameter, Z also called as temperature-compensated strain rate [178].

The corresponding constitutive equations stated as

$$Z = A.[\sinh(\alpha\sigma)]^n = \dot{\varepsilon}.\exp(Q/RT) \text{---------- (2.12)}$$

This Equation (2.12) can be noted as

$$\dot{\varepsilon} = A.[\sinh(\alpha\sigma)]^n.\exp(-Q/RT) \text{----------(2.13)}$$

$$\dot{\varepsilon} = A.\sigma^{n'}.\exp(-Q/RT) \text{ where } (\alpha\sigma) < 0.8 \text{----------(2.14)}$$

$$\dot{\varepsilon} = A.\exp(\beta\sigma).\exp(-Q/RT) \text{ where } (\alpha\sigma) > 1.2 \text{----------(2.15)}$$

$$\dot{\varepsilon} = A.[\sinh(\alpha\sigma)]^n.\exp(-Q/RT) \text{ for all } (\alpha\sigma) \text{---------- (2.16)}$$

where A, α, and n = materials constants self-reliant of temperature, R = the universal gas constant, T = absolute temperature (K), and Q = the apparent activation energy needed for deformation (J/mol), $\dot{\varepsilon}$ and σ are strain rate (s^{-1}) and true stress (MPa) respectively.

As per the flow stress, σ levels, 3 distinct forms of Equation (2.13) given as: Equation (2.14) for low flow stress, σ as power function; Equation (2.15) for high flow stress, σ as exponential function; and Equation (2.16) for any flow stress, σ as hyperbolic sine function.

Equations (2.14 – 2.16) can be modified as

$$ln\dot{\varepsilon} = n'.ln\,\sigma + ln\,A_1 - Q/RT \text{ where } (\alpha\sigma) < 0.8 \quad \text{----------(2.17)}$$

$$ln\dot{\varepsilon} = \beta.\sigma + ln\,A_2 - Q/RT \text{ where } (\alpha\sigma) > 1.2 \quad \text{----------(2.18)}$$

$$ln\,\dot{\varepsilon} = ln\,A + n.ln[\sinh(\alpha\sigma)] - Q/RT \text{ for all } (\alpha\sigma) \quad \text{----------(2.19)}$$

where A_1 and A_2, are MC, and n, β, n' are associated to m indicator.

The apparent activation energy, Q required for plastic deformation in hot compression test is determined by Equation (2.20)

$$Q = R.\left[\frac{\partial ln\dot{\varepsilon}}{\partial ln[\sinh(\alpha\sigma)]}\right]_T.\left[\frac{\partial ln[\sinh(\alpha\sigma)]}{\partial(1000/T)}\right]_{\dot{\varepsilon}} = R.n.S \quad \text{---------- (2.20)}$$

where $S = \left[\frac{\partial ln[\sinh(\alpha\sigma)]}{\partial(1000/T)}\right]$, a linear fit slope from ln[sinh($\alpha\sigma$)] vs 1000/T and (stress-exponent), $n = \left[\frac{\partial ln\dot{\varepsilon}}{\partial l\ [\sinh(\alpha\sigma)]}\right]$, a linear fit slope from ln$\dot{\varepsilon}$ vs ln[sinh($\alpha\sigma$)].

2.5.1.1 Temperature-Strain rate compensation to calculate predicted flow stress

Taking logarithm on both side of Equation (2.12), we get Equation (2.21) illustrating the relation between flow stress, σ and Zener-Holloman parameter, Z.

$$ln\,Z = ln\,A + n.ln[\sinh(\alpha\sigma)] \quad \text{---------- (2.21)}$$

The σ can be determined by the MC (n', β, α, n) and Q in the CE as a function of Z, thereby taking the Equations (2.12) and (2.16) as follows:

$$\sigma = \frac{1}{\alpha}.ln\left\{\left(\frac{Z}{A}\right)^{\frac{1}{n}} + \left[\left(\frac{Z}{A}\right)^{\frac{2}{n}} + 1\right]^{\frac{1}{2}}\right\} \quad \text{---------- (2.22)}$$

2.5.1.2 Strain-compensation to calculate predicted flow stress

The computed values of the materials constant (α, β, n, A) and Q obtained from equations (2.17 – 2.19) varied with 0.1 to 0.5 strain. The corresponding curves

pertaining to each constant were subjected to polynomial fitting resulting in the corresponding equations of each materials constant. In these equations, the value of strain ranging from 0.1 to 0.5 is being introduced, then subsequently, new set of material constants will be obtained. Consequently, new set of material were replaced in Equation (2.16) establishing new constitutive equation at various strain rates from Equation (2.16) and then flow stress from Equation (2.22) evaluated with new set of materials constants.

2.5.1.3 Strain rate-compensation to calculate predicted flow stress

The accuracy of constitutive equation achieved by strain rate-compensation to modify the *Z*. This modification was done by changing the exponent of strain rate, $\dot{\varepsilon}$ in Zener-Holloman parameter, Z equation (2.21) [184] [185]. An exponent of 0.85 was noticed to be best for the strain rate-compensation for this alloy. The modified Zener-Holloman, Z parameter ($\grave{Z}$) obtained on multiplying Eq. (2.12) with $\dot{\varepsilon}^{-0.15}$ is given as,

$$\grave{Z} = \dot{\varepsilon}^{0.85}.\exp(Q/RT) \quad \text{----------(2.23)}$$

The correlation between Zener-Holloman parameter, Z and modified Zener-Holloman parameter, $\grave{Z}$ may be stated as:

$$ln(\grave{Z}) = ln\,(Z) - 0.15\,ln(\dot{\varepsilon}) \quad \text{----------(2.24)}$$

Therefore, the flow stress, σ needs to be modified using constitutive equation (2.22) as:

$$\sigma = \frac{1}{\alpha}.ln\left\{\left(\frac{\acute{Z}}{A}\right)^{\frac{1}{n}} + \left[\left(\frac{\acute{Z}}{A}\right)^{\frac{2}{n}} + 1\right]^{\frac{1}{2}}\right\} \quad \text{---------- (2.25)}$$

2.5.2 Verification of the constitutive equation accuracy

The reliability of the constitutive equation on the experimental data was quantified by employing the basic statistical entities stated as the average absolute relative error (AARE),

$$AARE = \frac{1}{N}\sum_{i=1}^{N}\left|\frac{E_i - P_i}{E_i}\right| \quad \text{----------(2.26)}$$

and the correlation coefficient (R),

$$R = \frac{\sum_{i=1}^{N}(E_i - \bar{E}).(P_i - \bar{P})}{\sqrt{\sum_{i=1}^{N}(E_i - \bar{E})^2.\sum_{i=1}^{N}(P_i - \bar{P})^2}} \quad \text{----------(2.27)}$$

where E and P are experimental and predicted flow stress, σ values respectively; $\overline{E}$ and $\overline{P}$ = average E and P values, respectively, N = number of selected quantities.

2.6 Rolling

Forming of Mg alloys being *hcp* system at room temperature results in limited ductility due to highly anisotropic behaviour of basal slip [39] where (0002) basal planes of many grains are close to plane of the sheet. Accordingly, many grains are in unsuitable orientation where resolved shear stress value is nil for the basal plane resulting in stress concentration and premature failure [54][113]. Formation of basal texture can be avoided by rolling at elevated temperatures results in enhanced formability and decreases in-plane anisotropy representative of Mg sheet product [186]. Generally, hot deformation of Mg alloys carried out at and above 200ºC ($T_{deformation} > 0.4T_m$) [54] i.e., recrystallization temperature results no grain refinement adequately. [187]. Coarser grains resulting from high temperature and constraint in room temperature processing limit wrought products including sheets as inevitably increase in the cost of production.

On other hand, basal slip orientation causes {1012} tensile twinning to control during compression in orthogonal direction to the main c-axis orientation, which is comparatively easy to activate than the tensile mode of deformation, resulting in yield asymmetry. Accordingly, both anisotropy and yield symmetry in Mg alloys can be addressed by four aspects i.e., texture softening, solid-solution strengthening, refinement of grain sizes and precipitation strengthening [188].

The strategy needed for sorting both anisotropy and yield symmetry in Mg alloys. Texture softening and suppression of tensile twin by RE additions, can attained in wrought Mg alloys causes decrease in yield symmetry [19][23][31][98][139]. The sheet forming is related with the evolution of crystallographic texture and has important effect on its properties. The texture can be modified either by altering the initial microstructure or by changing the processing route. During texture evolution, dislocation substructure develops on plastic deformation, where dislocations organize in low energy configurations. [189]. Both texture evolution and dislocation substructure are correlated with each other. Increase in texture intensity and reduction in dislocation cell size with enhancement in strain provided dynamic recovery or recrystallization mechanism should not step-in. Nevertheless, change in the strain path would create deviation in the above tendency when presumed boundary conditions were modified.

[190][191] The extent of change in strain path described by a scalar parameter anticipated by Schmitt et al. [192]

This parameter is expressed as $\theta = (\varepsilon_p : \varepsilon)/(||\varepsilon_p||||\varepsilon||)$ ----------(2.28)

where ε_p = the strain tensor prior to strain path and

ε = the strain tensor in the succeeding strain path

The value of θ = 0 and 1 corresponding to no change in strain path and orthogonal change in strain path respectively.

A change in strain path affects the texture formation strongly brought by cross-rolling where the of change of rolling direction studied by many researchers. [32][193] [33][191] In cross-rolling operation, rotation of the sample in terms of the first rolling direction in turn rotates the substructure along new rolling direction. Such change in the strain path causes disruption of the substructure formed by changing the complete configurations of dislocations during previous rolling and the moment of dislocations network gets hindered during the slip process. Simultaneously, these modifications affect the evolution of deformation texture and in-turn also influence the recrystallization texture.

These findings involved the understanding of microstructure and texture through unidirectional rolling, two-step and multi-step cross rolling. Cross rolling (CR) deviates from the conventional unidirectional rolling (UR) by involving two rolling directions (RD1 and RD2), i.e., on completing individual rolling step (e.g., RD1), the sample rotated by 90º keeping the normal direction constant that means rolling direction changed (RD2).

2.6.1 Anisotropy Calculation

Plastic anisotropy known as the property values of plastic deformation of materials will be different in different directions. Majority of the polycrystalline materials demonstrate anisotropy behaviour. During material processing, preferred orientation (textures) developed in the materials and thereby improves the anisotropy. The degree of deformation and its type decides the formation of textures; accordingly, the level of anisotropy fluctuates. Rolling forms more intense textures in the direction of rolling resulting variation in the property values in the RD and TD.

Lankford coefficient, R, gives a value for plastic anisotropy, mathematically expressed as the ratio of strain in width direction (ε_w) to the strain in thickness direction (ε_t) in the uniaxial tensile test. Higher the R value, higher will be opposition of the

material to thinning, therefore the materials can be drawn into larger height. Lankford coefficients rely on the orientation of tensile axis with respect to the rolling direction, in the rolling plane and defined by the angle (α) and R= Rα.

$$R = \left\{\frac{ln\,[w_f/w_o]}{ln[t_f/t_o]}\right\} = \left\{\frac{ln[w_f/w_o]}{ln[(l_o*w_o)/(l_f*w_f)]}\right\} \text{----------(2.29)}$$

where w_f and w_o are final and initial width respectively and t_f and t_o are the final and initial thickness respectively.

R = 0 shows no widening,

R = ∞ indicate no thinning and

R = 1 meant for isotropic materials.

Subsequently, overall resistance to thin down a sheet will be measured by taking an average value of R in three α angles generally determined by Normal anisotropy. Generally, the anisotropy in the materials is defined by average $\bar{R}$ according to ASTM E 517, also known as Normal Anisotropy

$$\bar{R} = \frac{1}{4}[R_{0^0} + 2R_{45^0} + R_{90^0}] \text{----------(2.30)}$$

Any $\bar{R}$ value more than 1 shows more contraction of the sheet than its thinning during the elongation, indicating of better formability [194].

Similarly, the amplitude of the in-plane anisotropy is measured by taking difference in the R values given as variation of Rα becomes crucial in the plane of the sheet, expressed as coefficient of Planar anisotropy,

$$\Delta R = \frac{1}{2}[R_{0^0} - 2R_{45^0} + R_{90^0}] \text{----------(2.31)}$$

Planar anisotropy corresponds to the formation of ears during deep drawing operation.

(i) ΔR>0, then formation of ears occurs at 0º and 90º along RD and

(ii) ΔR<0, ears forms at 45º

Crystallographic texture decides both Normal and Planar coefficients [195].

2.7 Corrosion behaviour of hot rolled Mg alloy

Corrosion occurs in various substances such as natural minerals, polymers, and ceramics. Broadly defined as, “The deterioration of a substance (usually a metal) or its properties because of a reaction with its environment”[196]. This indicate that corrosion changes the properties of the materials from such deterioration. However, *deterioration* do not illustrate all events related to corrosion. Under certain conditions in metallic

corrosion, the creation of an oxide layer on the metal surface acts as a protective shield, preventing the material from undergoing deterioration. Therefore, a definition based on the comprehension of the "interaction between material and media and transformation of properties" might be more than adequate.

As engineering materials, during service, are in contact with the corrosive environments like moisture, different aqueous solutions including sea water, Corrosion of these materials, the electrochemical interaction of materials with materials, is a main concern.

This section provides fundamentals of electrochemical theories of metal and environment interaction that controls the metallic corrosion shown in many literatures. [197][196][198][199][200] The conceptual understanding of electrochemical behaviours of materials is applied to understand the Corrosion behaviour and the rate of Mg alloys by electrochemical corrosion testing methods.

2.7.1 Fundamentals of Metallic Corrosion

Metal corrosion resulting from exposure to an aqueous solution can be elucidated by invoking the Second Law of Thermodynamics. The state of ordered atoms forming metals is not considered the most stable, as substances tend to strive for maximum disorder. In order to reduce chemical potential, atoms at the metal surface deviate from the crystalline structure and transition into the solution as ions, leaving electrons on the metallic surface until the chemical potential (or free energy) of both states reaches equilibrium. [199]

2.7.1.1 Electrochemical characteristics of Corrosion

Metallic corrosion arises from two or more electrochemical reactions occurring on the metal surface. These electrochemical reactions are influenced by four essential factors: an anode (where the oxidation of an atom on the metal surface results in the release of electrons with a negative charge, while the positively charged ion of this atom enters the solution, known as the anodic reaction), a cathode (where the electrons released during the anodic process are consumed by a species in the solution and undergo reduction, known as the cathodic reaction), an electrolyte (the liquid conductor responsible for the movement of ionic species between two electrodes when a potential difference is applied), and a DC power source (to maintain the required potential difference between the two electrodes).

The spontaneous occurrence of corrosion process relies on two electrochemical reactions (that brings change in the *valence* or *oxidation state* of the species) need take place at the same time and the same number of electrons must be exchanged between anodic and cathodic processes. i.e., rate of oxidation should be equal to the rate of reduction.

When positive ions migrate from the metallic surface into the solution, the surface is left with an excess of negative charges, creating an electric field that influences the surrounding solution. This results in the establishment of an electrode, a surface formed between the metal and the ion-containing solution. The reactions taking place at the electrode can be classified into two categories: oxidation and reduction reactions.

These reactions proceed through their following partial equation reactions:

$M \rightarrow M^{+n} + ne^-$ (Anodic reaction or Oxidation reaction) ----------(2.32)

$2H^+ + 2e^- \rightarrow H_2$ (Cathodic reaction of Acidic sol.) ----------(2.33)

$O_2 + 4H^+ + 4e^- \rightarrow 2H_2O$ (Cathodic of Acidic sol. with dissolved O_2) -------(2.34)

$O_2 + 2H_2O + 4e^- \rightarrow 4OH^-$ (Cathodic of Acidic sol. with dissolved O_2) --------(2.35)

$M^{+n} + e^- \rightarrow M^{+n-1}$ (Cathodic of higher to lower oxidation state) ------(2.36)

$M^{+n} + e^- \rightarrow M$ (Cathodic reaction of metal reduction) ----------(2.37)

As positive ions from the metallic surface penetrate the electrolyte, the negative charge of the electrons on the metallic surface attracts them, leading to the formation of a double layer. This developed potential pertaining to double layer is called H_2 electrode potential and can be measured. In such a system, when H2 gas is evolved through 1M HCl at a pressure of 1 atm, the electrode formed is referred to as the Standard Hydrogen Electrode (SHE). The magnitude of the SHE potential is conventionally considered as zero. SHE is employed to ascertain the electrode potential of metal-electrode systems and the pH of the solution.

Generally potential measurements are not done by using the *Saturated Hydrogen Electrode* (SHE) because of certain limitations: (i) difficult to build and control the pressure of H_2 gas to be accurately at 1 atm pressure throughout the experiment. (ii) challenging to sustain the concentration of HCl at 1M during the excessive evolution of H_2 gas carries a small amount of HCl with it and decreases the H^+ concentration. (iii) cannot be used in the solution containing oxidising and reducing agents. (iv) impurities in hydrogen and HCl destroy the ideal platinum electrodes and

reduce the life of SHE. (v) difficult to obtain pure hydrogen gas and an ideal platinum electrode.

The measurement of potential is typically carried out using liquid (secondary) electrodes aligned with the Standard Hydrogen Electrode (SHE), whose potentials are established and constant, allowing easy conversion to an equivalent relative to the SHE. Commonly employed liquid (secondary) electrodes include the Saturated Calomel Electrode (SCE), Silver-Silver Chloride Electrode, and the Copper-Copper Sulphate Electrode, with relative potentials to the SHE of +0.241 V, +0.235 V, and -0.318 [[198]] respectively.

2.7.1.2 Thermodynamics of Corrosion

The Standard Electrode Potential (Eº) designates the potential of a particular electrode reaction. Various factors impact the electrode potential, including temperature, partial pressure, and the concentration of chemical species. The Nernst equation can be employed to calculate the potential variation due to concentration changes.

(1) $$E = E^0 + \frac{RT}{nF} ln \frac{[ox]}{[red]}$$

where E =the electrode potential, E^o = the standard electrode potential, R = the gas constant, T = the absolute temperature, F = the Faraday constant, n = the number of moles of electrons exchanged in the half-cell reaction, and [*ox*] and [*red*] are the activities of the oxidized and reduced species, respectively.

In electrochemical corrosion experiments, *Three-Electrode Electrochemical Cell* is generally used as seen in Fig. 2.30. The potential of a system at the start can be measured for such experiments when the currents are typically null, called as *open circuit potential – OCP*. In this condition, an electrical contact will be maintained only with two necessary components i.e., *a reference electrode and test electrode*.

Conversely, if an electric current freely flows through a galvanic cell established between two dissimilar metals or is externally imposed, the resultant cell potential deviates from its equilibrium potential. The determined potential encompasses two overpotentials from the electrodes, rendering it impossible to measure the potential of the test electrode independently.

To measure the potential accurately, a third electrode, known as the auxiliary electrode, is introduced. The reference electrode is connected to a high-resistance

voltmeter in this configuration. In such an arrangement, the current only flows through the test and auxiliary electrodes, not through the reference electrode. This setup ensures the stability and unpolarized state of the reference electrode during potential measurement.

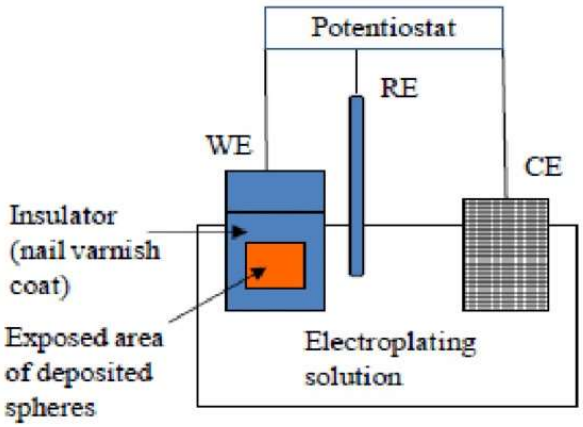

Fig.2.30. Schematic of a three-electrode electrochemical cell setup. [[201]]

The evolution of potential concerning pH gives rise to the development of the Potential-pH diagram (E-pH), commonly referred to as the Pourbaix diagram. Determined by the Nernst equation, as outlined in Equation 7 and involving standard chemical potentials, the Pourbaix diagram is a graphical representation that delineates the zones of stability for Immunity, Corrosion, and the passive state in water. These zones are depicted as a function of potential (on the y-axis) and pH (on the x-axis), as illustrated in Figure 2.31.

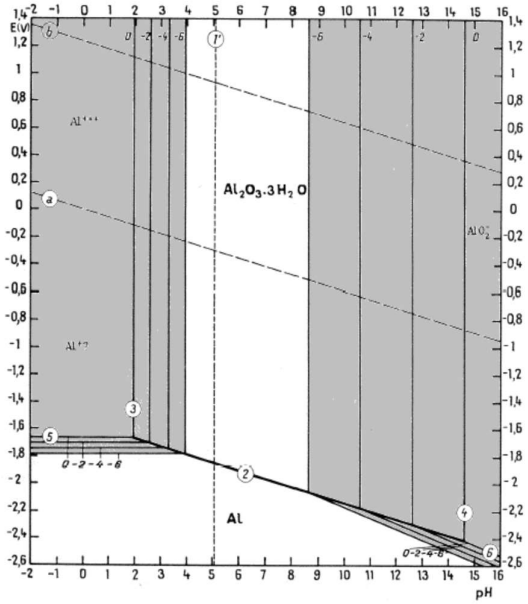

Fig. 2.31 Pourbaix diagram of pure metals (aluminium). [[202]]

2.7.1.3 Kinetics of Corrosion

An electrochemical reaction inherently involves the generation or consumption of electrons. The overall current (I), referred to as the exchange current, represents the flow of electrons during both anodic and cathodic reactions on the anode and cathode, respectively. The exchange current serves as an effective means for measuring the corrosion rate, being equivalent to the weight of metal dissolution during the anodic reaction. Faraday's law establishes a relationship between the measured current and the mass of corroded metal, expressed as:

$$m = \frac{tIM}{nF} \text{ ----------(2.39)}$$

Where, F = the Faraday constant, t (s) = the time elapsed, I (A) = the current generated, M (g/mol) = the atomic weight, n = the number of electrons exchanged in a reaction and m (g) = the mass that reacted.

The occurrence of cathodic and anodic reactions, resulting from multiple electrode processes, requires identification. In such scenarios, the sum of the rates of all partial reactions within the anodic process should equal that of the cathodic process.

The electrode area is another critical factor in corrosion kinetics. A current density (i) with units in A/cm² is assigned to electrode processes. In uniform corrosion, the anodic and cathodic areas, along with their respective current densities, are considered equal. Regardless of the corrosion type, the anodic and cathodic currents should be equal. In cases of localized corrosion, if the cathodic area is greater, demanding more current while the anodic area must supply it, pitting corrosion results in more localized damage.

Determining exact current densities is not as straightforward as it may seem. In uniform corrosion, the cathodic and anodic areas may be too small to differentiate, and the availability of surface for an electrode process cannot accurately predict active participation in an electrochemical reaction.

Changes in the overall surface reaction led to alterations in the electrode potential of a half-cell. Such changes induce polarization (η) or overpotential at the surface. Excessive electrons provided by the surface make the overpotential more negative, resulting in cathodic polarization (η_c) and a negative η_c. Conversely, removing electrons from the surface triggers a positive overpotential or anodic polarization (η_a). These polarizations occur due to slow reaction rates and are controlled by two

mechanisms: activation control (known as activation polarization) or mass transport control (known as concentration polarization), where one is the limiting factor.

The delay in the cathodic reaction, resulting from activation energy at the electrode surface, gives rise to activation polarization. Likewise, the sluggishness is attributed to the migration of ionic species from the bulk of the solution to the electrode surface, leading to concentration polarization.

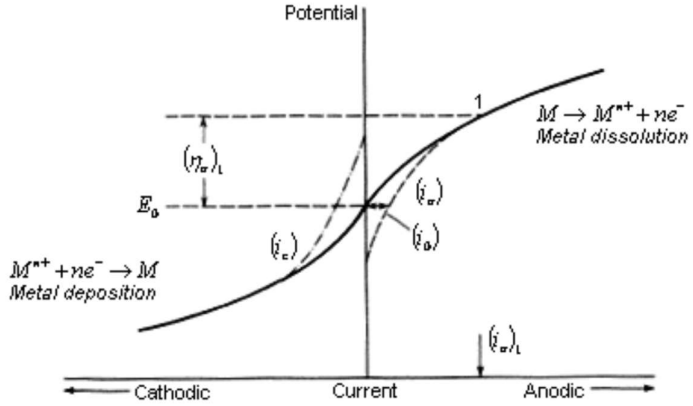

Fig. 2.32 Theoretical current – potential diagram for a metallic electrode [[196]]

2.7.1.4 Passivation Behaviour of Metals

The concept of passivation has been introduced earlier in this discussion, albeit without delving into the intricacies of the phenomenon. Passivity is evident in metals and alloys capable of forming an oxide layer, providing resistance against corrosion. Certain metals and alloys exhibit corrosion resistance due to the presence of a surface film. These films develop under highly oxidizing conditions or with high anodic polarizations. This significance distinguishes metals possessing a simple barrier film with reduced corrosion at an active potential and minimal anodic polarization. Furthermore, insoluble compounds formed through dissolution and reprecipitation offer less protection compared to oxide films that form in-situ on the metal surface. This is a crucial characteristic observed in various structural metals such as Fe, Cr, Ni, Ti, and Al, with their specific alloys, notably exemplified by stainless steels.

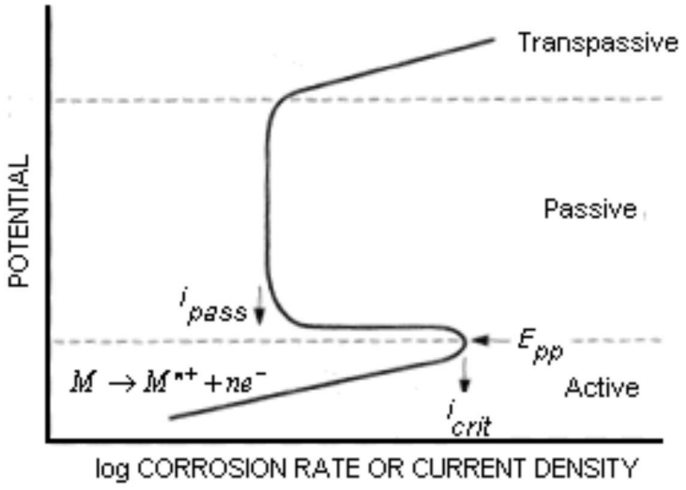

Fig. 2.33 Polarization diagram exhibiting transitions from active corrosion to passive behaviour and to the transpassive state. [198]

Metals and alloys exhibiting passive behaviour exhibit a distinct trend in anodic polarization, as illustrated in Figure 2.33. As the potential increases from the corrosion potential, the current rises until reaching a critical value (icrit) in accordance with typical dissolution behaviour, marking the initiation of stability for passive films that form at potentials higher than the primary passive potential (*Epp*).

Subsequently, the measured current decreases to a residual current (ipass) by multiple orders of magnitude. At higher potentials (E_t), when the metal enters the transpassive state, the passive film disintegrates with an increase in anodic reactions. Conversely, self-passivation can occur when the potential of the cathodic reaction is nobler relative to the anodic reaction, surpassing the primary passive potential (*Epp*).

2.7.2 Electrochemistry of Mg and Mg Alloys

Enhancement in the properties of Mg alloys is the real challenge, especially corrosion resistance is the major weakness and hence actively researched. Despite the much research on the corrosion mechanism of Mg and its alloys, which remain still unclear, justifying the efforts to increase more on understanding the process. The electrochemical corrosion of Mg and Mg alloys is being dealt extensively. However, the electrochemical behaviour of Mg in passivating media [203][204] or the characteristics of the passive layer that forms at the surface [205] (spontaneously or in alkaline solutions) are poorly researched.

2.7.2.1 Corrosion behaviour of Pure Magnesium

The stability of magnesium bearing negative corrosion potentials, relies on the disposition of a surface film capable enough to restrain the attack on the surface following exposure to a corrosive atmosphere. The corrosion of pure Mg deals with reactions that adheres the overall equation:

$$Mg + 2H_2O \rightarrow Mg(OH)_2 + H_2$$ ----------(2.49)

This above equation can be divided into the partial reactions of cathodic (Eq. 2.50) reaction and anodic (Eq. 2.51) reaction:

$$2H^+ + 2e^- \rightarrow H_2$$ ----------(2.50)

$$2Mg \rightarrow 2Mg^+ + 2e^-$$----------(2.51)

The hydrogen evolution is very critical in the corrosion mechanism of Mg. H_2 molecules can be release in the reduction reaction (Eq. 2.50) and by a chemical reaction between Mg and water:

$$2Mg^+ + 2H_2O \rightarrow 2Mg^{2+} + 2OH^- + 2H_2$$----------(2.52)

$$Mg^{2+} + 2OH^- \rightarrow Mg(OH)_2$$ ----------(2.53)

The major corrosion product yielded is magnesium hydroxide {Mg $(OH)_2$} (Eq. 22). Nevertheless, variety of conditions and solutions will yield other sorts of corrosion byproducts including carbonates and hydrated carbonates (in the existence of carbonic acid or CO_2 dissolved in water) or sulphites and sulphates (in the existence of diluted sulphuric acidic or sulphur comprising impurities) [[196].

Analysis of the above equations concludes:

(i) Mg corrosion will not display a major dependency to oxygen concentration in the electrolyte. [196], [[206]], [[207]]

(ii) Major alkalinization of the media occur in the existence of small volume of electrolyte.

Mg has a highly active standard potential of -2.37 V (SHE) [[197], [196], [206], presuming direct contact and equilibrium between the uncovered metallic surface and the divalent ion. However, the standard potential is much less active in 3% NaCl solutions -1.63 V (SCE), or -1.38 V (SHE) [[197]], which implies the formation of a hydroxide layer when the metallic surface is in no direct contact. The covering of a hydroxide layer on the metallic surface indicates about the protection against corrosion in alkaline solutions.

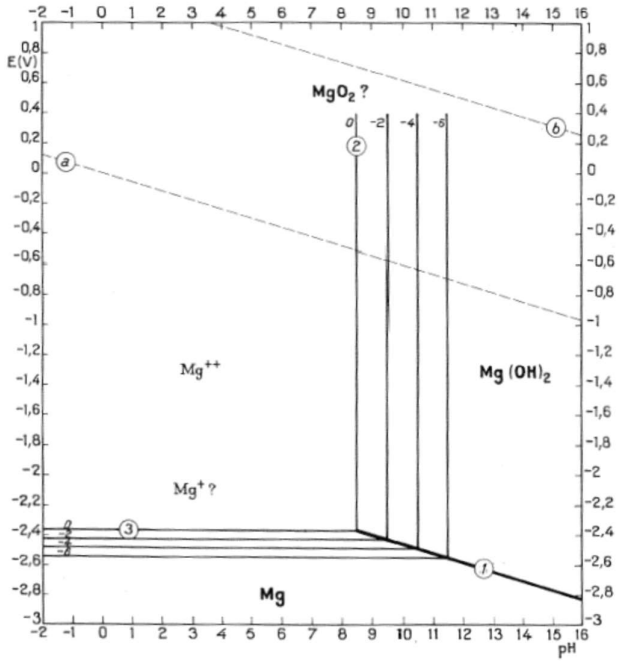

Fig. 2.34 Pourbaix Diagram of pure Mg [202]

The Pourbaix diagram shown in Fig. 2.34 illustrates the thermodynamics of aqueous solution. As the pH value of the solution exceeds 11, then Magnesium hydroxide Mg $(OH)_2$ develops the stable species but below 11, the divalent ion remains unchanged in solutions. In pure magnesium, the corrosion processes are usually accompanying with Localized Corrosion [206]. This corrosion process is the special grade planned to distinguish from other types of localized corrosion such as pitting as it develops quite distinctly.

The magnesium hydroxide {Mg $(OH)_2$} film covering metallic surface of Mg is metastable and somewhat protective. As a result, Mg appears to have free corrosion potential (E_{corr}) less negative than a pitting potential (E_{pit}). The corrosion process starts with the formation uneven and shallow pits. These pits covering the entire metallic surface extending laterally rather growing in depth as seen in the behaviour of other systems such as stainless steels or aluminium. This behaviour is result of the alkalinization of the electrolyte brought about by the cathodic reaction. The magnesium hydroxide Mg $(OH)_2$ becomes more stable with an increment in pH value and retards the dissolution process within the pit. But the attack in the form of anodic dissolution continues at the edges of the pits due to low value of pH. Such corrosion process is comprising a self-limiting nature. On other hand, other pitting mechanism are self-catalytic in character and usually speed up the corrosion action. Since the corrosion

process extend laterally, it causes the second phase particles in the microstructure get undermine from their matrix and pops out from the surface. Such process of second phase particles getting pop out during undermining is usual in Mg alloys.

2.7.3 Electrochemical Techniques

Electrochemical techniques are very dynamic method to examine the corrosion behaviour using DC or AC source of applied potential. Accordingly, the electrochemical techniques using DC source in the potentiodynamic polarization test can investigate the thermodynamic and kinetic of corrosion reactions, including the corrosion rate, assessment of passivity and hydrogen evolution. On other hand, the AC source electrochemical methods most extensively used techniques is electrochemical impedance spectroscopy which investigates the corrosion behaviour from its mechanism taking part and formation of surface film in the aggressive environment. The electrochemical impedance spectroscopy can also measure the rate of corrosion and ability to protect from corrosion [208]

2.7.3.1 Potentiodynamic Polarization Test

The Potentiodynamic Polarization (PDP) test yields a graphical representation of the variation in current density concerning an applied potential, illustrated in Evans plots. The electrochemical principles necessary for comprehending this method have been elucidated in Section 2.6.1.3 (Kinetics of Corrosion). The polarization curve reveals the behaviour of electrode processes at anodic potentials (more positive than Ecorr) and cathodic potentials (more negative than Ecorr).

Potentiodynamic Polarization tests can be conducted in two types:

(i) Fast polarization scan: The polarization rates are approximately 60V/h.

(ii) Slow polarization scan: The polarization rates are about 1V/h. [Baboian [14]]

High polarization rates are employed to assess whether surface films are thin or absent, and to estimate high anodic action. Slow polarization rates are necessary to investigate the film formation processes and assess film stability. For this study, the slow scan rate is selected. Analysing a polarization graph yields various parameters such as Ecorr and icorr, identified by two intersecting tangents on cathodic and anodic curves in the Tafel region (The Tafel Slope Extrapolation method) or the kinetics of the anodic and cathodic activities. This analysis reveals the system's behaviour, including passivation and its breakdown phenomena.

2.7.3.2 Open Circuit Potential

In an electrochemical system many reactions occur on an electrode, exhibiting an intermediate potential amongst the equilibrium potentials of cathodic and anodic reactions. Such potentials obtained by the intersection of polarization curves corresponding to anodic and cathodic reactions. This potential is known as mixed potential in electrochemistry, whereas in certain case of corrosion it is described as the corrosion potential. The actual equilibrium potential is measured as the potential for the non-corroding metal. The open circuit potential (OCP) is calculated through experiment by making precise evaluation of the electrode potential in association to a reference electrode.

2.7.3.3 Potentiodynamic Polarization (PDP) measurement of Mg alloys

The electrochemical techniques of potentiodynamic polarization measurement on pure Mg immersed in 3.5wt. NaCl as shown in Fig. for 1h and for 1 day reported by A Pardo et.al. [209] showed higher rate of dissolution due to less protective oxide layer unable to defend the progression in corrosion.

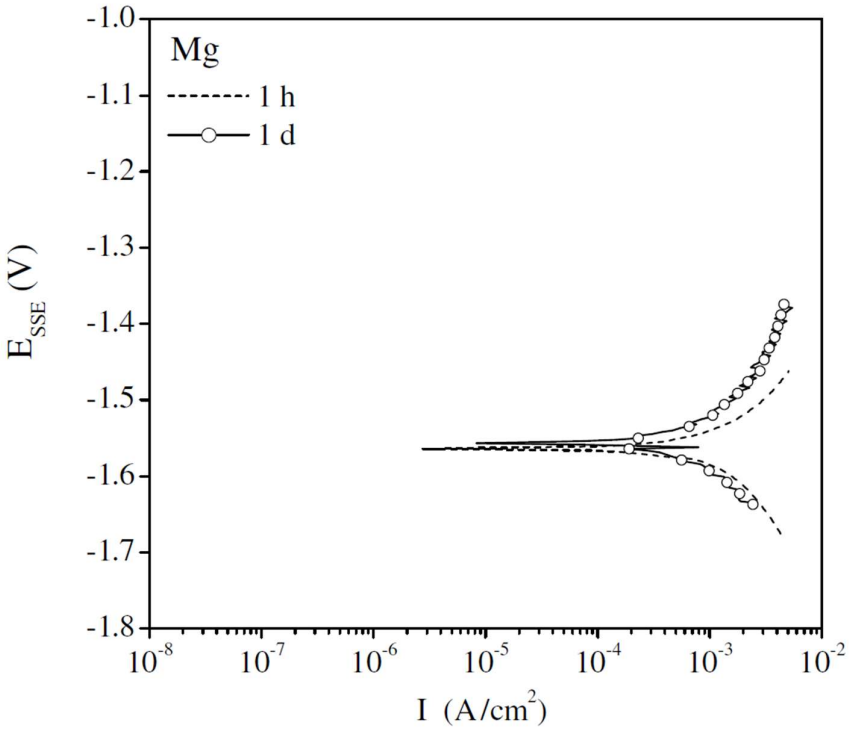

Fig. 2.35 Potentiodynamic polarization curve of pure Mg in 3.5wt.% NaCl solution [209]

Corrosion resistance of Mg alloys can be improved by deformation is reported in limited cases. [35][36] [210][211] and addition of alloying elements of Mg. Gu et. al. reported the reduction in corrosion rates of hot rolled binary Mg alloys due to lowering of hydrogen evolution when immersed in Hank's solution as well as simulated bodily fluid. Wang et. al [36] reported the enhancement in corrosion resistance of hot rolled Mg alloy in Hank's solution due to grain refinement. Corrosion resistance of several binary Mg-X alloys (X: Gd, Al, Sn, La, Ca, Mn, Sr, Nd, Ce, *etc*.) have shown improvement by hot rolling. Hot rolling not only involves grain refinement but also leads to twin generation. [211][212]. Birbilis et. al [38]reported that increasing the amount of RE (Ce, La, and Nd) alloying addition consistently accelerated the corrosion rate and yield strength of the alloy. Hence, optimization of the wt.% of rare earth metal addition is important to strike a balance between corrosion resistance and mechanical strength which is essential for its successful applications. The effect of lower concentrations (i.e.,<0.5 wt.%) of RE additions recognizes a lower limit threshold to avoid degradation of corrosion properties significantly. [213].

2.7.3.2 Electrochemical Impedance Spectroscopy

Electrochemical Impedance Spectroscopy (EIS) is a highly dynamic technique for acquiring kinetic and mechanistic data across an extensive range of frequencies through electrical means in electrochemical systems. In EIS measurements, a small amplitude AC signal is introduced into the system, making it a non-destructive method suitable for assessing various materials, including coatings, anodized films, and corrosion inhibitors. The EIS technique explores surface morphology involving two or more electrode processes with distinct kinetics occurring simultaneously. Comprehensive evaluations under EIS examination encompass corrosion rates, dielectric properties, the impact of composition on solid conductance, mass transport, electrochemical processes, localized corrosion detection, and reaction kinetics [Hamdy, El-Shenawy [23], Macdonald [24]. EIS measurements are easily conducted, and the obtained data requires analysis using suitable software.

The concept of impedance is comprehended by establishing a correlation between resistance and electrical current flowing through a circuit element, as given by Ohm's law (Eq. 2.54).

$$R = \frac{V}{I} \text{ ----------(2.54)}$$

where R= the electrical resistance, V = the potential applied and I = the electrical circuit

The resistance shown in Eq. 2.54 is independent of the voltage value and remains unaffected by frequency, continuing in phase with an applied AC voltage signal, as Ohm's law is applicable to ideal resistances. This leads to a simplified model of impedance (Z) (Eq. 2.55), which is unaffected by the same constraint as electrical resistance:

$$Z = \frac{V(t)}{I(t)} \text{----------(2.55)}$$

A minor perturbation made to the system in the EIS technique yields a potential in sinusoidal wave signal form given by

$$V(t) = V_0 \sin(\omega t) \text{----------(2.56)}$$

where V_0 = the signal amplitude and ω = angular frequency

The corresponding current of the system is then recorded as

$$I(t) = I_0 \sin(\omega t + \delta) \text{----------(2.57)}$$

where I_0 = amplitude of the current signal and

δ = difference in phase angle between the two signals.

The overall impedance of the sytem is provided by the following equation:

$$Z = \frac{V(t)}{I(t)} = \frac{V_0}{I_0} \frac{\sin(\omega t)}{\sin(\omega t + \delta)} \text{----------(2.58)}$$

The two signals can be indicated as sinusoidal waves with the corresponding amplitudes, $V_0$and I_0 having the same frequency, but out of phase by δ angle. In other word, the two signals can be denoted by two vectors revolving at the same frequency with δ shift in the phase. This suggests, the impedance of a system can be described by a vector that relates ratio of the other two vectors:

$$|Z| = \frac{|V|}{|I|} \text{----------(2.59)}$$

and a phase angle

$$\theta = (\omega) - (\omega t + \delta) = -\delta \text{----------(2.60)}$$

The impedance vector can moreover be represented as a complex number with real and imaginary components:

$$Z = Z_{real} + j\, Z_{imaginary} \text{----------(2.61)}$$

with the common treatment for vector module and angle

$$|Z| = \sqrt{Z_{real}^2 + Z_{imaginary}^2} \text{----------(2.62)}$$

$$tan\theta = \frac{Z_{imag}}{Z_{real}} \text{----------(2.63)}$$

Impedance spectra can be demonstrated through Nyquist plots and Bode plots. A Nyquist plot displays Cartesian coordinates expressed by Zreal and Zimaginary, providing information to evaluate polarization resistance and some kinetic data directly. In Nyquist plots, the Y-axis is often inverted to facilitate understanding, as many electrochemical systems exhibit a specific type of capacitive behaviour, resulting in points appearing in the 4th quadrant. To transport these points to the 1st quadrant, axis inversion is necessary.

The precise analysis of a Nyquist plot is challenging due to the wide range of magnitudes of impedance values and frequencies of electrode processes, making electrochemical systems complex. Bode plots illustrate the variation of log |Z| or phase angle (θ) with log (ω), where (ω) is the angular frequency. Each electrode reaction is displayed as a maximum in the phase angle plot, known as the absolute value, as phase angle values are usually negative, hence the Y-axis is inverted.

Other types of illustration are utilized for narrower applications, such as: Z_{real}vs $log(\omega)$, Z_{imag}vs $log\ (\omega)$ and Z_{real}vs ω Z_{imag}. Using the features of Admittance (Y), the inverse of impedance (Y=1/Z). The electrochemical system exhibits a response similar to that of passive constituents of an electric circuit such as resistors, capacitors, and inductors, to the potential perturbation applied while an EIS experiment.

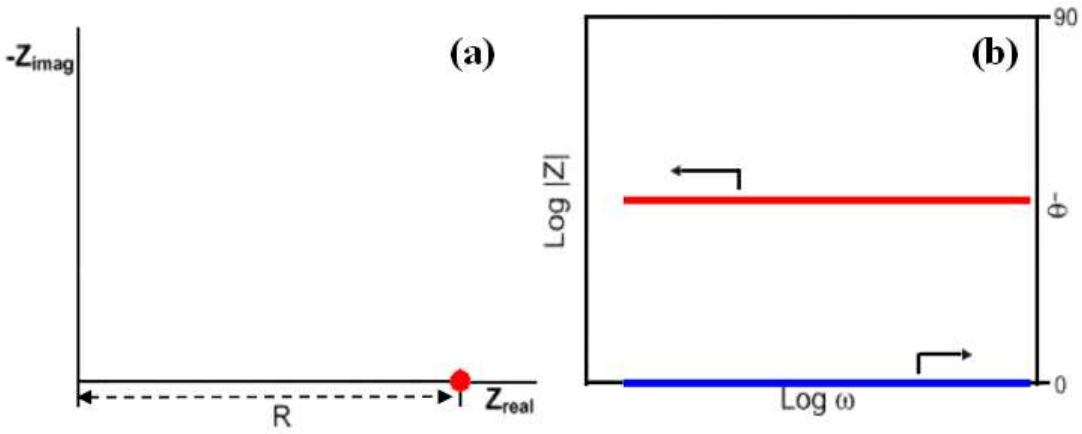

Fig. 2.36 Schematic illustration of (a) the Nyquist plot and (b) the Bode plot for a resistor [214][215]

Since the Ohm's law is precisely applicable for a pure resistance and the conditions associated with it already discussed earlier, therefore a resistor's impedance and resistance are directly proportional.[214][215].

$Z_R = R$ ----------(2.64)

The Nyquist plots shown in Fig. 2.36 (a) illustrate the variation of constant values (Z_{real} and Z_{imag}) of impedance |Z| and Fig. 2.36 (b) describes the variation of the absolute value of impedance |Z| and phase angle with the frequency for a resistor.

A capacitor is characterized by constant capacitance (C) can be identified as the ratio of the charge (positive or negative) Q on each conductor of the parallel plate to the voltage V between them.

$C = Q/V$ or $Q = CV$ ----------(2.65)

The equation for the impedance of a capacitor can be obtain after few mathematical simplifications:

$Z_c = \frac{1}{j\omega C} = -\frac{1}{\omega C}$----------(2.66)

The capacitor possesses only the imaginary component and furthermore, the impedance (Z) is inversely proportional to the frequency (ω), and the capacitance (*C*). On the Nyquist plot, a capacitor in the is depicted by a straight-line coinciding with the origin and in Bode plot a line with a slope of -1 showing inverse ratio with log |Z| and log (ω).

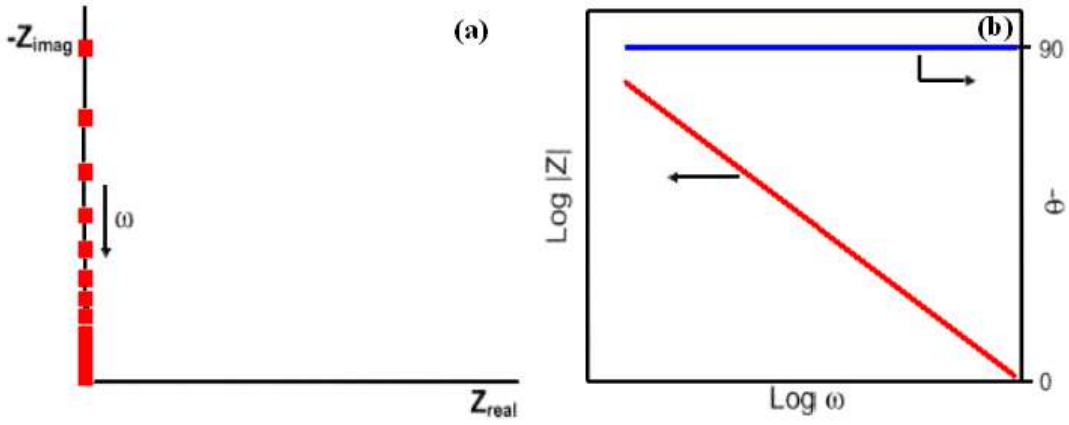

Fig. 2.37 Schematic illustration of (a) the Nyquist plot and (b) the Bode plot for a capacitor [214][215]

The response of a capacitor to perturbation with a -90º phase delay is evident from Fig. 2.37. An inductor, similarly, having only an imaginary component, exhibits impedance (Z) directly proportional to the frequency (ω) of the perturbation and the inductance (L).

$Z_L = j\omega L$ ----------(2.67)

The Nyquist and Bode plots for an inductor are the opposite of the capacitor plots. The impedance (Z) increases with frequency (ω) where the log |Z| plot has slope of 1, with a phase angle of +90º. The analogy of the simple examples mentioned above can be augmented to the analysis of complicated electrochemical systems only by connecting several resistors and capacitors in series.

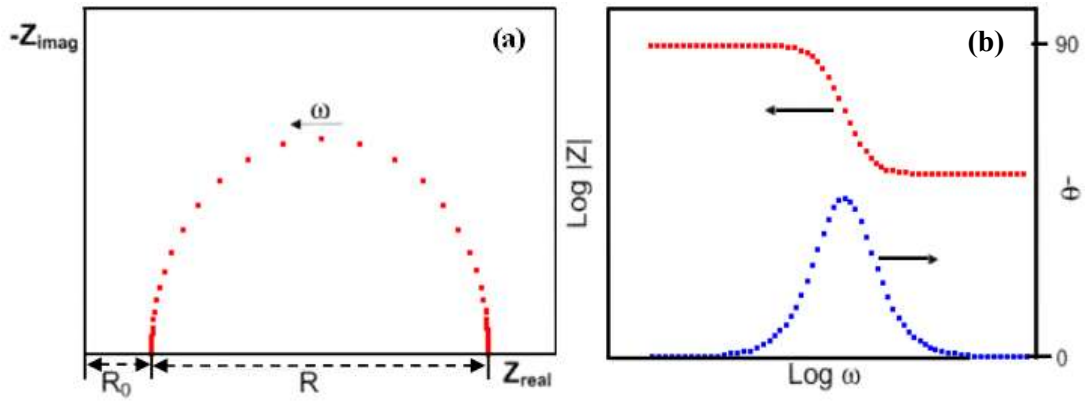

Fig. 2.38 Nyquist and Bode plots for a R (RC) circuit. [[216], [215]

This kind of analysis is very simple for the impedance data that would only fit for very simple systems. Extremely complicated systems will have many processes with fluctuating and superimposing in the working range of frequency meant for investigation. For these cases, many available software using different algorithms can be utilize for the fitting procedures following deconvolution of the various superimposing curves, thereby automatically calculate the electrical circuit parameters.

The principal challenge in the fitting procedures of an electrochemical system is to identify an optimum equivalent electrical circuit so as to characterize the system accurately in terms of circuit elements. The accuracy of characterization depends on the requisite experience and thorough understanding of electrochemical reactions taking place at the electrode surface.

The analysis of the impedance spectrum data becomes more difficult due to deviation from ideal behaviour. The semi-circle appeared in the Nyquist plot in an impedance experiment for the overall frequency range is rarely ideal as in Fig. 2.38 which usually appears depressed as described in Fig. 2.39. The extent of depression differs depending on the system.

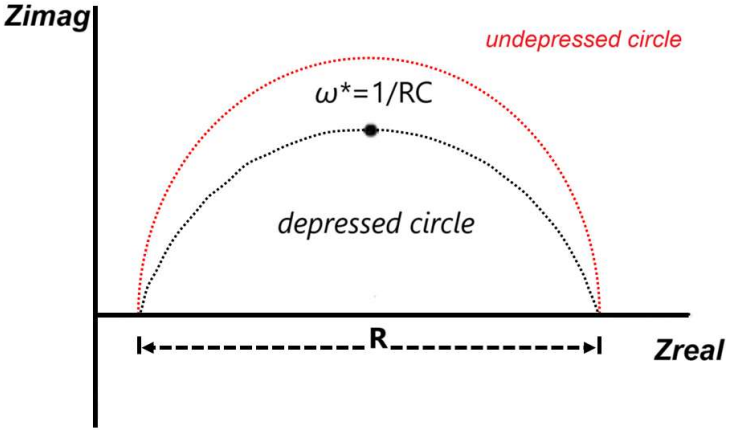

Fig. 2.39 Nyquist plot with and without depression [214], [215]

The phenomenon of depression, initially identified by Cole and Cole [217]in their study of dielectric constants using complex graph, is referred to as the Cole-Cole Depression. This concept was later adapted to electrochemical systems by various authors [214][215].

The impedance spectra represent a single electrochemical system modelled by the equivalent circuit. The time constant (τ) for this system can be defined as:

$$\tau = R_{ct}C_{dl} \quad \text{----------(2.70)}$$

The depression in the semi-circle is explained by assuming that the time-constant τ of the process has a varying value scattered around an average value, τ_0. This scattering of time-constants has been associated with the inconsistency in the electrode surface, considering it as a grouping of nearby tiny electrodes carrying their individual values of R_{ct} and C_{dl}, accordingly individual value of τ [214][215].

The semi-circle depression in the EIS results can be addressed by another approach known as the Constant Phase Element (CPE). A Constant Phase Element is analogous to a capacitor but differs in phase angle by 90°. The application of CPE is empirical, lacking theoretical justification. This model operates on simple mathematical concepts and is recognised for fitting the experimental data.

The conclusion for the depression in the semi-circle provided by the above two approaches is equivalent. This outcome can be confirmed by solving the equations for the impedance of a R(RC) circuit taking the Cole-Cole depression in account(depicted in Eq. 2.71) substituting the capacitor by a CPE (given by Eq. 2.72)

$$Z_{Cole} = R_{\Omega} + \frac{R}{1+(j\omega\tau_0)^{1-\alpha}} \quad \text{----------(2.71)}$$

$$Z_{CPE} = R_{\Omega} + \frac{R}{1+RY_0(j\omega)^n} \quad \text{----------(2.72)}$$

where α differs between 0 and 1 and the n=1-α can be assume any value approximately above 0.75 and up to 1 lies in the interval of -1 to 1.

Experimental results can be fitted by using the CPE but with careful consideration. Since the CPE is used as a replacement for a capacitor, it does not represent true capacitance but signifies the property of admittance.

The circuit element becomes very versatile since the phase of a CPE can be altered to replicate the behaviour of any other passive component in an electrical circuit. If the value n =1, then the CPE will respond as a capacitor.

n =0, then the CPE will behave as a resistor.

n =-1, then the CPE will simulate as an inductor.

A diffusion-controlled processes can also be simulated by the CPE when $n=0.5$, using an element called *Warburg diffusion elements*, fitted with electrical circuit. An equivalent circuit consisting of CPEs only can also be developed, providing a flawless mathematical result for any electrochemical system but with no physical understanding.

Although the CPE lacks physical understanding of the Cole-Cole depression, the mathematical outcome for both remains unchanged. This versatility of the CPE and its ability to be included in majority of fitting algorithms make the CPE an essential tool for impedance analysis but needs to be used with caution. Hence, the use of CPE should be considered as starting step of fitting to identify which circuit elements should be incorporated in the model.

The information collected in EIS scanning across a wide range of spectra can be challenging to analyse the complex systems, especially to establish the accuracy between an authentic result and an outcome from experimental error. The validity of EIS measurements will depend on four conditions: [216][218] (1) Causality, (2) Linearity , (3) Stability and (4) Impedance . If the above conditions are not validated the outcomes may not be authentic resulting in misinterpretation of the physical processes and mechanisms at the interface.

2.6.3.3 Electrochemical Impedance Spectroscopy of Mg and its alloy

The electrochemical impedance spectroscopy measurement of pure Mg and alumina coated Mg metal showed depressed semi-circle with inductive tail for pure Mg smaller than that of coated samples reported by I B Singh et.al. [219]. This indicates that pure Mg is showing less resistance toward corrosion as its real impedance value is very low than both coated samples. Faster diffusion rates of oxidized Mg^{2+} ions at the

interface of metal oxide and solution, resulted in low charge transfer resistance R_{ct} responsible for yielding protective films. Similarly, lower Rs for pure Mg than the coated samples indicated its poor resistance toward corrosion attack, which in agreement with the polarization curve.

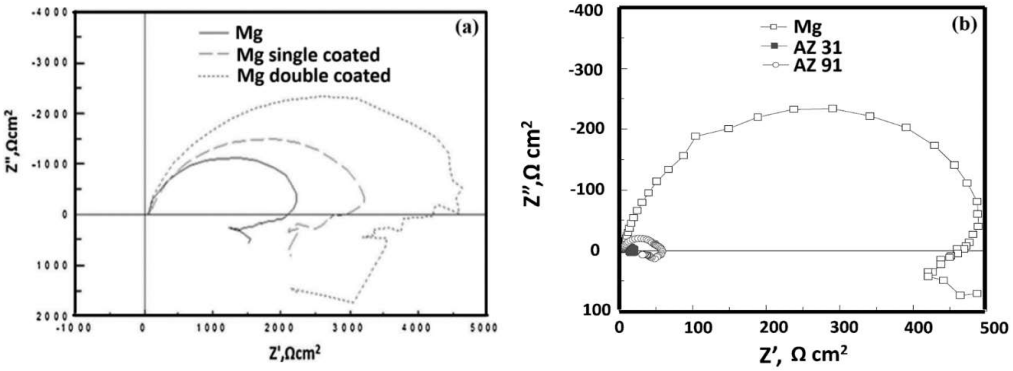

Fig. 2.43 Electrochemical Impedance Spectroscopy – Nyquist plot for (a) pure Mg and Alumina coated Mg metal in 3.5wt.% NaCl [219] and (b) for pure Mg, AZ31 and AZ91 alloys in 3.5wt.% NaCl after 1 ½ h of exposure.[220]

The electrochemical impedance spectroscopy measurement resulted in Nyquist plot as shown in Fig. 2.43 (b) for pure Mg , AZ31 and AZ91 alloys contradict to that of as discussed above in Fig. 2.43 (a). Here, pure Mg has bigger semi-circle than AZ31 and AZ91 indicating pure Mg to be better corrosion resistance. Here all the samples are observed to form protective oxide film but in pure Mg shows better capacitive behaviour than its alloys AZ31 and AZ91 and hence shows better corrosion resistance. AZ31 and AZ91 showed low frequency capacitive loop corresponding to Faradaic process i.e., diffusion process at the metal/solution interface. Moreover, Cl^- anions adsorption increases due to relaxation of absorbed anion on metallic surface occurring at low frequency inductive loop. This causes oxidation of metals to increase by consuming electrons at the adsorbed sites of oxidized metal, subsequently inevitable beginning of correction reaction particularly at adsorbed sites. While pure Mg has lower magnitude of inductive loop represents low vulnerability for Cl^- anion adsorption resisting corrosion attack.

Chapter 3: EXPERIMENTAL DETAILS

An overview of the various experimental techniques is provided in this chapter performed to accomplish the objectives of this work are presented. Section 3.1 outlines the relevant material used. Section 3.2 describes the procedures of the material processing and testing methods. Section 3.3 discuss the electrochemical testing and characterization on the processed material. Section 3.4 exhibit the relevant metallographic practices whereas, Section 3.5 explains the analysis techniques of materials characterization techniques.

3.1 Materials used

The binary Mg-0.5wt.% Ce alloy (Test material) is chosen as the experimental material in this study. Test material was received as a semi-finished cast billets and extruded product in rod shape from the M/s General Motors, Warren, USA. The reason for the selection of this binary alloy of Mg-RE system was to know the effect of RE on the material behaviour. The criteria for restricting the composition of 0.5wt% Ce is based on the solubility up to about 0.52wt% as a terminal phase the eutectic composition with 20.5wt.% Ce is also observed at temperature 590ºC as binary phase and decreases *to* 0.04wt.% as the temperature lowers down to 200°C in the form of solute and precipitate as in Fig. 2.26 Mg-Ce phase diagram [157]

3.2 Material Processing and Testing Methods

3.2.1 Hot Compression Test

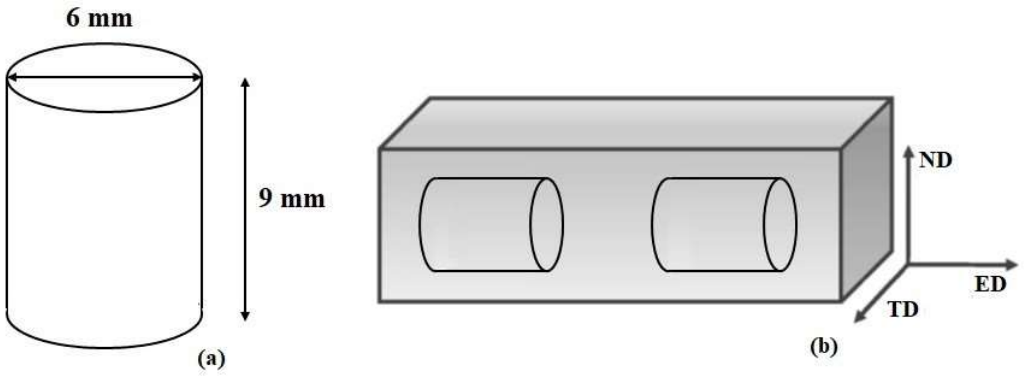

Fig. 3.1 Compression test material (a) sample with dimension and (b) test samples extracted from extruded rod.

In the hot compression test, Mg - 0.5 wt.% Ce alloy is chosen as the experimental material. The Test material was received in the form of extruded rods from the M/s General Motors, Warren, USA. Cylindrical specimens of 6 mm diameter and 9 mm height were machined from the as-extruded rod via electrical discharge machining (EDM) such that their faces were parallel during hot compression test. The specimen edges were chamfered during machining to prevent fold over during the starting stages of compression. Molybdenum disulphide–graphite paste was applied on both the faces of the specimen as a lubricant. Uniaxial compression tests were performed at true strain rates and temperatures using a computerized servo-hydraulic machine (DARTEC, Stourbridge, West Midlands, UK). The resistance furnace bearing Kanthal heating element was used for conducting the Isothermal tests of hot compression. The temperature tolerance limit in the furnace was within ± 3 K. Specimens were subjected to 50% height reduction during hot compression. Five different combinations of true strain rates from 0.001 s^{-1} to 10 s^{-1} and five different temperatures from 523 K to 723 K in 50 K increments were employed to assess the deformation behaviour. The compressed samples were air cooled.

The load versus elongation curves developed from the raw data obtained from the compression tests at a specific temperature and strain rate were transformed to engineering stress versus strain curves and finally true stress versus strain curves. The aforementioned curves provided the flow stress data based on temperature, strain rate, and strain. The log(flow stress) versus log(strain rate) data were fitted by a cubic equation and the strain rate sensitivity was calculated at various true strain values. The of strain rate sensitivity was then utilized to develop the power dissipation maps and the instability maps, which were superimposed to give the processing maps.

3.2.2 Hot Rolling

Test material was received in the form of extruded square rod of 16 x 16 mm^2 dimension. Square rod of the as-received materials was hot extruded at 400˚C.
Two modes of hot rolling at 450˚C and ε = 0.1 per pass using a single stand Two-High Reversing Rolling Mill till a true strain of 2.0 (total 20 passes) were employed viz.

(i) Uni-Directional Rolling (UDR)
(ii) Multi-Step Cross Rolling (MSCR)

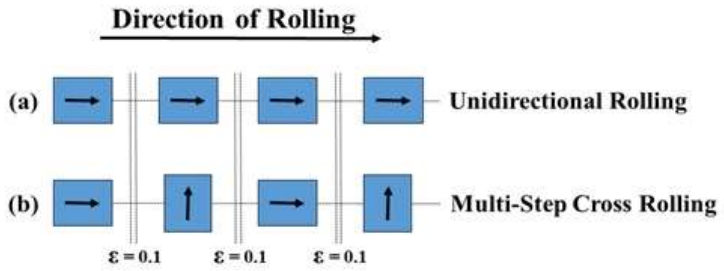

Fig. 3.2 Simple representation of the strain paths in rolling routes: (a) UDR and (b) MSCR

In UDR, Rolling Direction (RD), Transverse Direction (TD), Normal Direction (ND) are all constant at each pass as shown in figure 1a. The starting sample has rectangular shape with 43 mm length, 16 mm width and 8mm thickness was initially soaked for 45min and subjected to rolling with a ε = 0.1 per pass and later intermittent soaking between two passes was given for 3 min. This cycle repeated till total 20 passes, where sample attains a true strain, ε = 2.

In MSCR, ND remain constant while RD and TD keep on changing after each pass as shown in figure 1b. The starting sample has cubical shape with 16 mm length, 15 mm width and 7 mm thickness were initially soaked for 45min and subjected to rolling with a ε = 0.1 per pass and later intermittent soaking between two passes was given for 3 min. This cycle repeated till total 20 passes, where sample attains a true strain, ε = 2.

3.2.3 Room Temperature Uniaxial Tensile Test

Mechanical properties of Mg-0.5wt%Ce alloy hot-rolled sheet samples processed in different mode carried out by using miniature tensile testing specimens. Tension test was carried out to measure the ductility, ε_f and strength (YS, UTS) of the rolled sheet samples. Each test repeated at least 3 times to confirm the recurrence of similar the stress – strain curves. Tensile test samples were cut using EDM wire machine in dog-bone shaped with dimension as shown in Fig. 3.3 (a). All the tensile test samples were taken from rolled sheet of UDR and MSCR after 20^{th} pass along final RD at 0°, 45°, 90° as shown in the Fig. 3.3 (b).

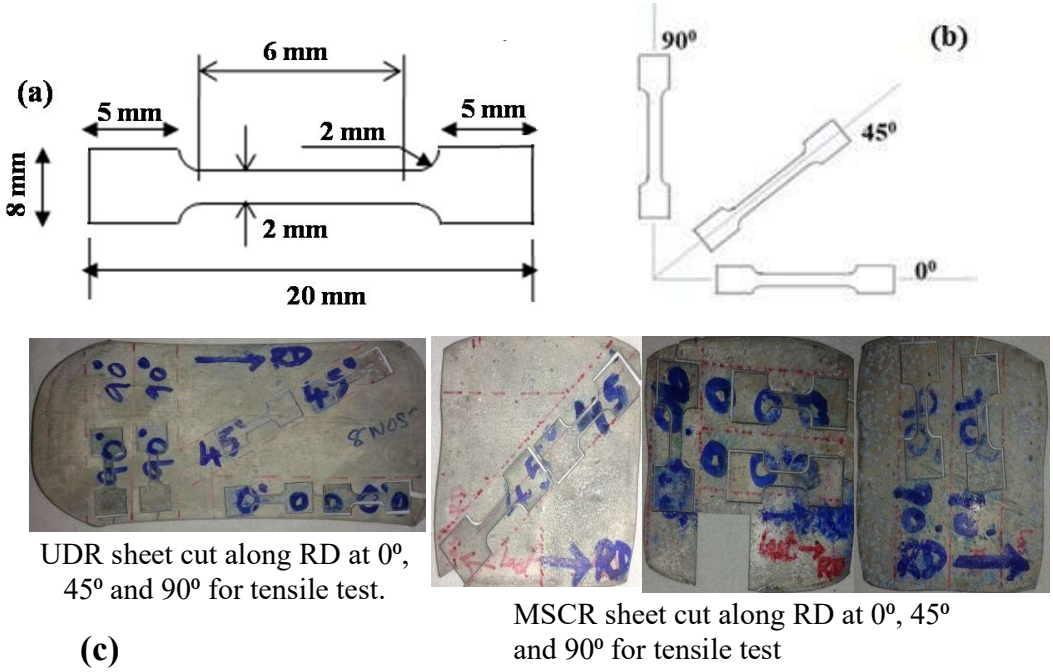

Fig. 3.3 Tensile test samples: (a) Tensile test sample dimension, (b) UDR and MSCR rolled sheets cut along final RD at 0°, 45°, 90°, and (c) UDR and MSCR rolled sheets cut along marked directions.

Tensile test was carried out at room temperature and at a constant strain rate of 10^{-3} s^{-1} using Instron 5967 testing machine.

3.2.4 Room Temperature Vickers Hardness

Vickers hardness testing were conducted with the help of Shimadzu HMV Vickers hardness tester worked under 1N (kgf) load. Vickers hardness test was carried out on as-extruded samples, UDR and MSCR rolled sheets with a dwell time of 10s at room temperature. Vickers hardness tester operated by square shaped pyramidal indenter having an angle 136˚ between opposite faces made of diamond. Before hardness measurement, each sample was cleaned by 1000 and 2000 grit size SiC polishing papers followed by cleaning using ultrasonicator stirrer for less than 2 min. Vickers hardness values are measured using following equation,

$$HV = \frac{Load}{Area} = \frac{F\ x\ 2\ sin\left(\frac{136^0}{2}\right)}{d^2} = 1.854\left(\frac{F}{d^2}\right)\ approximately$$

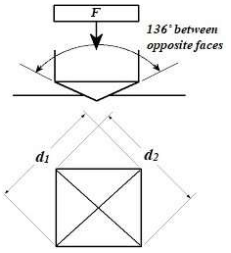

Fig. 3.4 Vickers hardness measurement on the sample using diamond indenter having squared-shaped pyramidal.

3.3 Electrochemical Testing and Characterization

Samples were section from the two modes of hot-rolled sheets of Test material with respect to final RD. Accordingly, samples to be tested are (i) Extruded sample, (ii) UDR and (iii) MSCR. Specimen cut in the square dimension of 7 mm x 7 mm from extruded sample and hot rolled sheets of UDR and MSCR. These samples as seen in Fig. 2 were soldered with pure copper wire so as to make them conduct during Polarization and Electrochemical Impedance Spectroscopy test. Copper-wire is insulated to avoid any metallic interaction during these tests. The soldered specimen surface was cold mounted using cold setting solution leaving the other surface NOT to be exposed during the corrosion test. Later specimens were polished till 3000 SiC paper and followed by diamond paste of ½ μm for mirror-finish polishing. Such mirror-finish polished cold mounted specimens were applied with enamel on the edges to avoid crevice corrosion during the corrosion test.

3.3.1 Potentiodynamic Polarization (PDP) Test

Potentiodynamic Polarization (PDP) test was conducted using Potentiostat-Galvanostat equipment of AUTOLAB 302N model. Software used for the measurement of Potentiostatic and Potentiodynamic behaviour is General Purpose Electrochemical System (GPES) Manager. Type of normal measurement is Linear Sweep Voltammetry (Staircase). Polarization curves studies of the samples after immersion test to find their potentiodynamic polarization and potentiostatic behaviour.

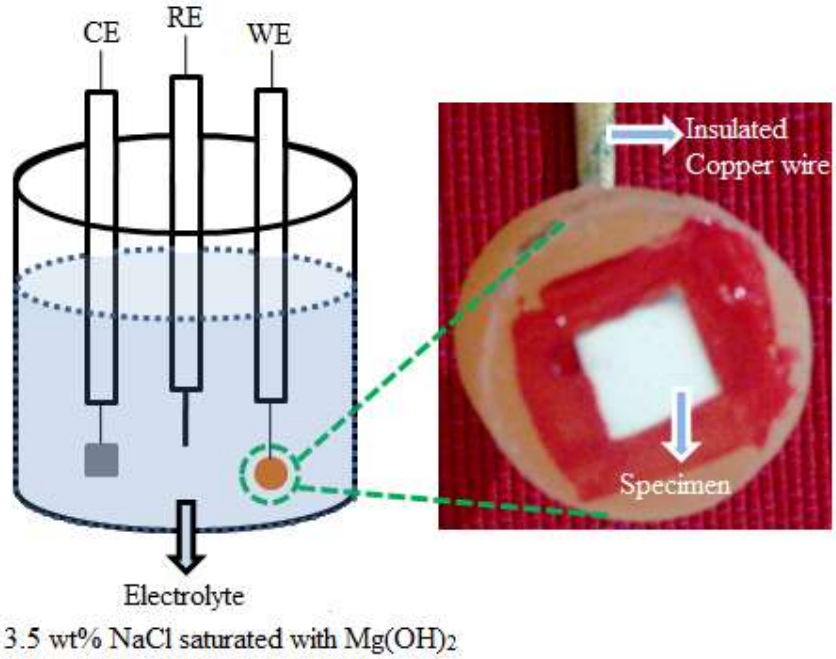

Fig. 3.5: Specimens of extruded rod, UDR and MSCR sheet prepared for corrosion test

Prior to potentiodynamic polarization testing, samples were immersed in the same electrolyte for 15 minutes at 25 ± 1°C to steady the open-circuit potential (OCP). PDP testing was done with 3 electrodes in an electrolytic solution. Reference Electrode: Ag/AgCl (Saturated Calomel Electrode). Counter Electrode: Pt. Working Electrode: Specimen. Electrolytic solution: 3.5 wt% NaCl solution saturated with $Mg(OH)_2$ in distilled water. The potential of the electrodes was swept through an electrolyte cell at a rate of 0.1mV/s in the range from initial potential of -250mV versus E_{corr}.

3.3.2 Electrochemical Impedance Spectroscopy

Electrochemical Impedance Spectroscopy (EIS) testing was carried out by the same Potentiostat-Galvanostat equipment of AUTOLAB 302N model. Software used for the Electrochemical Impedance measurement is GPES (General Purpose Electrochemical System) Manager. The sinusoidal perturbation amplitude employed was -10mV. The frequency range covered 0.1 kHz- 10 kHz. Prior to EIS testing, samples were immersed in the same electrolyte for 15 minutes at 25 ± 1°C to steady the OCP. Electrochemical Impedance measurement was done with 3 electrodes in an electrolytic solution. Reference Electrode: Ag/AgCl (Saturated Calomel Electrode).

Counter Electrode: Pt. Working Electrode: Specimen. Electrolytic solution: 3.5wt.% NaCl solution saturated with $Mg(OH)_2$ in distilled water.

3.4 Metallography Practices

In this topic of metallographic practices covers different characterization techniques both microstructural aspects and structural composition to set up the structure-property co-relationship. The working principle and different parameters in the operations of characterization equipment are presented so that the structural and mechanical properties are evaluated in the subsequent chapters.

3.4.1 Optical Microscopy: Metallurgical Microscope

In this current research, the initial microstructure of as-received (extruded form) samples and experimentally deformed (compressed and rolled) observed using M/s. OLYMPUS make BX-51 upright Metallurgical microscope with Polarising and Differential Interference Contrast. The samples for Metallurgical microscope observations were prepared by standard procedure of paper polishing using 1000, 2000, 3000, 4000, grit size paper with distilled water. Consequently, cloth polishing carried by using chemical i.e., Glycol-Etch Solution to obtain mirror finish. Glycol-Etch Solution contains 75ml of Ethylene Glycol, 24ml of Distilled water and 1ml of Nitric acid. Thereafter the samples were cleaned by methanol for 2 minutes using stirrer of ultrasonicator type without heating just to remove chemical solution and other contaminates. Manual etching was carried on by using etchant solution having composition 1:1:7 ratio of acetic acid: distilled water: 6% picral solution. 6% picral solution is made by dried 6 g of picric acid and 100 ml of methanol. Samples were dipped in the etchant for 3 seconds. Subsequently, the samples were cleaned by methanol for 2 minutes using stirrer of ultrasonicator type without heating just to remove chemical solution and other contaminates.

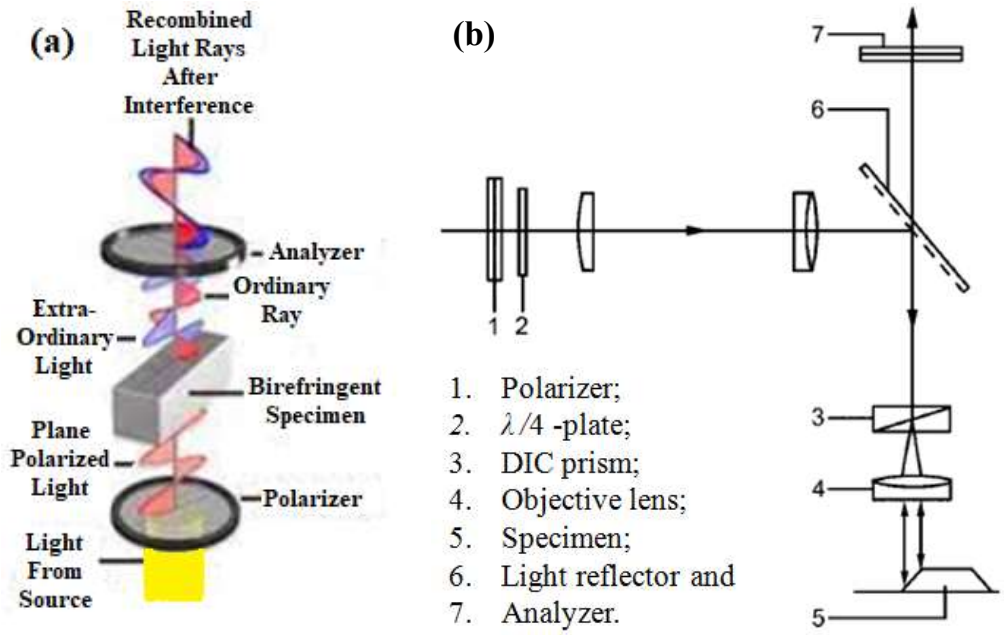

Fig. 3.6 Optical arrangement of (a) Polarized Light microscopy and (b) DIC microscopy in reflected light illumination.

Metallurgical microscope with Polarizing mode creates contrast in microstructure of the samples having little or less contrast in brightfield microscopy. Polarized light vibrates in a specific plane, rather than randomly and such property reveals the contrast in the microstructure. Polarizing microscope additionally consist of two filters namely, polarizer and analyzer oriented perpendicular to each other. Light rays from the source gets linearly polarised after passing through a polariser. This linearly polarized beam after passing through the specimen generates two rays, ordinary and extraordinary, perpendicular to each other moving in two different refractive indices and thereby exhibits phase difference. As a result of the phase difference, the resultant ray can form elliptical, or spiral or spirally ellipse is allowed from the filter analyzer but blocks no phase difference resultant rays.

Metallurgical microscope with Differential Interference Contrast (DIC) mode also introduces contrast in microstructure of the samples having little or less contrast in brightfield microscopy. Light rays from the source gets linearly polarised after passing through a polariser. This linearly polarised light ray enters the first DIC prism that generates two parallel polarized beams vibrating perpendicular to each other. These two beams are then reflected from the specimen which is having variations in thickness and refractive indices such that interfere coherently in the image plane and generate two

slightly displaced images with a phase difference, thereby creating height contrast.. Whereas with no path difference, the resultant light rays will be linearly polarized beam, showing no contrast at all. The analyzer located after second DIC prism, blocks the linearly polarized beam but allows the elliptically polarized beam introduces deceptively 3D images. [221].

3.4.2 Scanning Electron Microscopy

Scanning electron microscopy utilizes electrons beam as an incident radiation provides huge spatial resolution unlike metallurgical microscopy that uses visible light source. The wavelength of the electrons is related to their energy E by the equation, $\lambda \approx 1.22/\sqrt{E}$, where E = electron energy in eV and λ = wavelength of the electron. The electron beam will penetrate the sample deeper as its wavelength being shorter, consequently, more will be the resolution for SEM than compared to optical microscope. In addition, SEM also provide greater depth of field and depth focus even on a higher magnification and most widely used for fractography.

During operation of SEM, electron beam as a probe scans the specimen to form a rectangular raster region with the help of scan coils.. Secondary electrons are loosely bound electrons knocked out from specimen atomic orbital shell due to inelastic scattering between incident electron and the specimen, whereas the backscattered electrons are the primary incident electrons that interacts with specimen elastically loosing very less energy and scattered backside from nucleus of the specimen atom. Third type of electrons are characteristics X-rays, emitted from the deeper specimen atoms particularly the inner most orbital shell electron knocked out creating vacancy which is occupied by adjacent shell electron in the same atom. The excess amount of electron energy emitted is the characteristic of that atom only that are dispersed in various channels to stored based on energy. Secondary electrons are used primarily for topographic contrast imaging, while backscattered electrons are utilized give rise to variation in density contrast imaging. While EDX gives information regarding composition of the sample under investigation.

In this current study, SE mode was used for imaging the rolled samples. Fracture studies of rolled samples after tensile test and also after electrochemical corrosion test. EDX mode used to examine the chemical composition of the Mg-Ce alloys under investigation. Scanning electron microscopy (HITACHI S-3400N with Tungsten

filament) is used to characterize the microstructures of Mg-0.5wt%Ce alloys for all failure analysis.

3.4.3 Electron Backscattered Diffraction (EBSD)

EBSD technique was employed to acquire the microstructure of the materials in the present investigation. The SEM model FEI Quanta 200 equipped with EBSD detector was used. The TSL OIM version 6.0 software was used to collect and analyze the data. Using a pre-tilted sample holder, the samples were angled 70° to the horizontal plane. 20 kV of acceleration voltage was employed for the SEM operation. Electro-polishing method was used to prepare the EBSD samples after standard metallographic polishing. The electrolyte for electro-polishing contains ethanol and ortho-phosphoric acid 3:5 ratio in volume. Electro-polishing was conducted at 3 V for 30 sec and 1.5 V for 2 minutes at less than 5°C temperature.

The area for scanning on the prepared samples were based on deformation conditions given as:

(i) For compressed samples, sectioning was done along compression axis in the centre of the cylindrical samples such that the scanning of the microstructural features occurs at the compression plane perpendicular to the compressive axis. Scanning for EBSD sample done at different step size varying from the 0.3 – 0.5 μm based on grain size at different stages.

(ii) For rolled samples EBSD measurements was done along rolling direction (RD) of sectioned samples using the step size of 0.4 – 0.6 μm.

TSL OIM EBSD software was used for microstructural characteristics such as grain size distribution and grain boundary character distributions. TSL-OIM version 6 data analysis software was used for detailed investigation of the scan images.

In this investigation, the average grain orientation spread (GOS) values obtained for different deformed conditions from the microstructures. The grain orientation spread (GOS) is determined using the average orientation of each grain. The average GOS value is used to distinguish the microstructures as softened grains having less GOS value than average, while deformed grains have larger GOS values.

Such distinction of grains in the microstructures based on following conditions:

(i) Softened grains should be equiaxed, while elongated morphology is seen for deformed grains.

(ii) Deformed grains contain large fractions of LAGB, while softened grains have HAGB in large fractions.

(iii) Softened grains show rotation of grains around c-axis by 10 - 30° relative to deformed grains, denoted by $\varphi = 90°$ Euler space where rotation of 30° of maxima along φ_2 axis.

3.4.2.3 Surface Profilometer

Surface profilometer are interference microscopes usually used to determine height differences such as surface roughness with utmost precision as the light wavelength is considered as the ruler. The path difference of the light rays emerging from a test surface and a reference surface is generally compared. A light beam divides into two rays such that one ray reflected from the reference surface (mirror) and other ray travel through the focal plane of objective lens of the microscope. These two rays form constructive interference provided when the sample surface and the reference surface are equally spaced from the beam splitter. On contrary, if the beam splitter is at varying distances between both the surfaces, then the two reflected beams emit dark and light bands called as interference fringes. Profilometer employs these fringes for estimating surface finish and surface roughness, until the large quantity of light ray is reflected back into the objective from the surface. [222]

In the current investigation, the surface roughness (any defect formation and surface roughness) of Test material samples in different deformation conditions i.e., as-extruded, UDR and MSCR were measured. The surface roughness was measured on an area of $963 \times 722\ \mu m^2$ at the centre of the samples utilizing the non-contact mode of a Bruker optical surface profiler (Model: Contour GT-K0).

3.4.3 X-Ray Diffraction

In this study, the phases of Test material were identified from the crystallographic features point of view using X-Ray diffraction (XRD) techniques. X-ray diffraction is primarily used as a quantitative technique for material characterization. As the X-rays are strike on a crystalline material made of periodic array of atoms, then waves scattered by individual electrons present in each atom will emit in a phase forming a constructive interference. The Bragg's Law gave a condition $n\lambda = 2d\sin\theta$ for the formation of this constructive interference and called as diffracted X-rays. 2θ is the only measurable entity during X-ray diffraction techniques. Amongst methods of diffraction, only

diffractometer is most widely used as a versatile method. [40]. The operating parameters of X-ray diffractometer are shown in Table 3.2

Table 3.1 Details of operating parameters followed in XRD

X-ray source	**Cu -Kα**
Wavelength	1.54 Å
Voltage	40 kV
Current	30 mA
2θ	10° - 120°
Step size	0.02°
Time/step	0.5 second
Geometry	Bragg-Brennato
Model	Bruker D8 Advance

Chapter 4: RESULTS AND DISCUSSIONS

This chapter outlines the results obtained from experimental techniques to evaluate the deformation and the corrosion behaviour as discussed in chapter 3 for the Mg-0.5wt% Ce alloy. Subsequently, complete correlation of test results was established with materials characterization after the analysis for both behaviours.

Section 4.1 describes the results of deformation conditions during compression test are being represented by flow curves and subsequently generate processing maps and establish the constitutive equation in accordance with the deformation behaviour. A detailed analysis of flow curves, processing maps and constitutive equations identified by using related microstructures and texture development.

Section 4.2 explains the outcome of processing maps reveals the regime of processing the Test material using hot rolling method performed in two routes viz. UDR and MSCR. Subsequently, tension test was performed on the hot rolled sheets. The materials characterization is conducted on hot rolled sheet before and after tension test describes the deformability of the Test material.

Section 4.3 discusses the response of the rolled sheets in the environment of applications identified by corrosion test done by Potentiodynamic polarization test and electrochemical impedance test. Microstructural analysis pertaining to the findings of both electrochemical test outlines the mechanism proceeding in the corrosion behaviour of the Test material.

4.1 Hot Deformation Behaviour of Mg-0.5wt% Ce alloy

4.1.1 Starting material

In the present investigation, Test material is chosen as the starting experimental materials for all types of deformation conditions. Mg-0.5wt% Ce alloy received in the form of extruded rods from M/s General Motors, Warren, USA. The initial microstructure of as-extruded specimen of Test material is shown in Fig. 4.1. The microstructure exhibits average grain size of 25-35 μm in well-defined recovered grain structure. Few grains are extended in the extrusion direction, while majority are equiaxed, consequently in-homogeneity in the material increases. Presence of many second phase ($Mg_{12}Ce$) particles was confirmed by the SEM-EDS elemental mapping

and are observed both at grains and grain boundaries and thus $Mg_{12}Ce$ phase in microstructure validates the Mg-Ce phase diagram. These precipitates reveal random

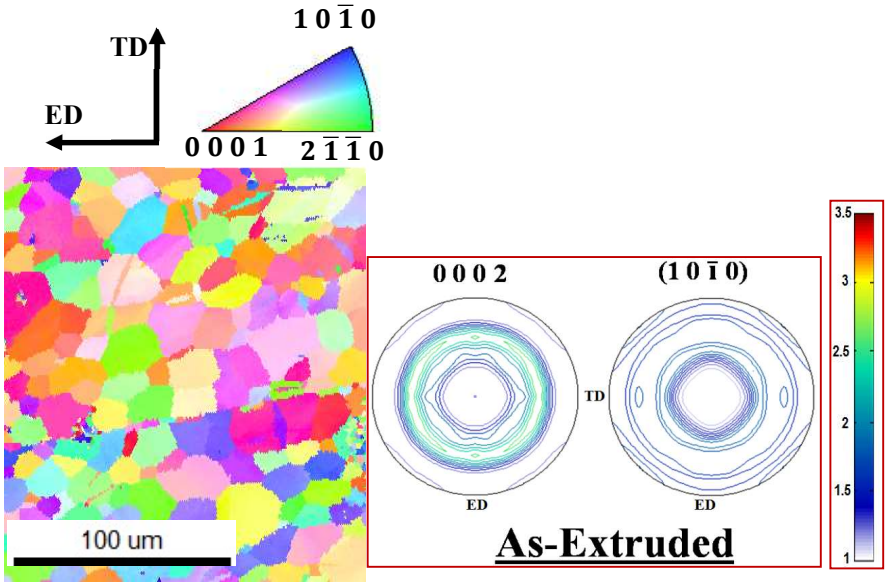

(a) IPF Map (b) (0002) and (10$\bar{1}$0) Pole Figure Map

Fig. 4.1 Inverse Pole Figure (IPF) (a) and Pole Figure Map of As-extruded samples from EBSD image.

distribution throughout the microstructure either in elongated rod-shaped or globular morphologies. The volume fraction of these precipitate very low less than 2% and the size of precipitates range between 2.58 to 14.00 μm while average size is 4.2 μm. The basal plane inclined at an angle of 40-50º to extrusion axis as seen in fig. 4.1 (b) (0002) and (10$\bar{1}$0) pole figures, indicating more suitable orientation for huge numbers of grains. [22].

4.1.2 Hot Compression Test

The selected material for hot compression test was extruded rod of Test material as the experiment procedure.

4.1.2.1 Stress- Strain Curves

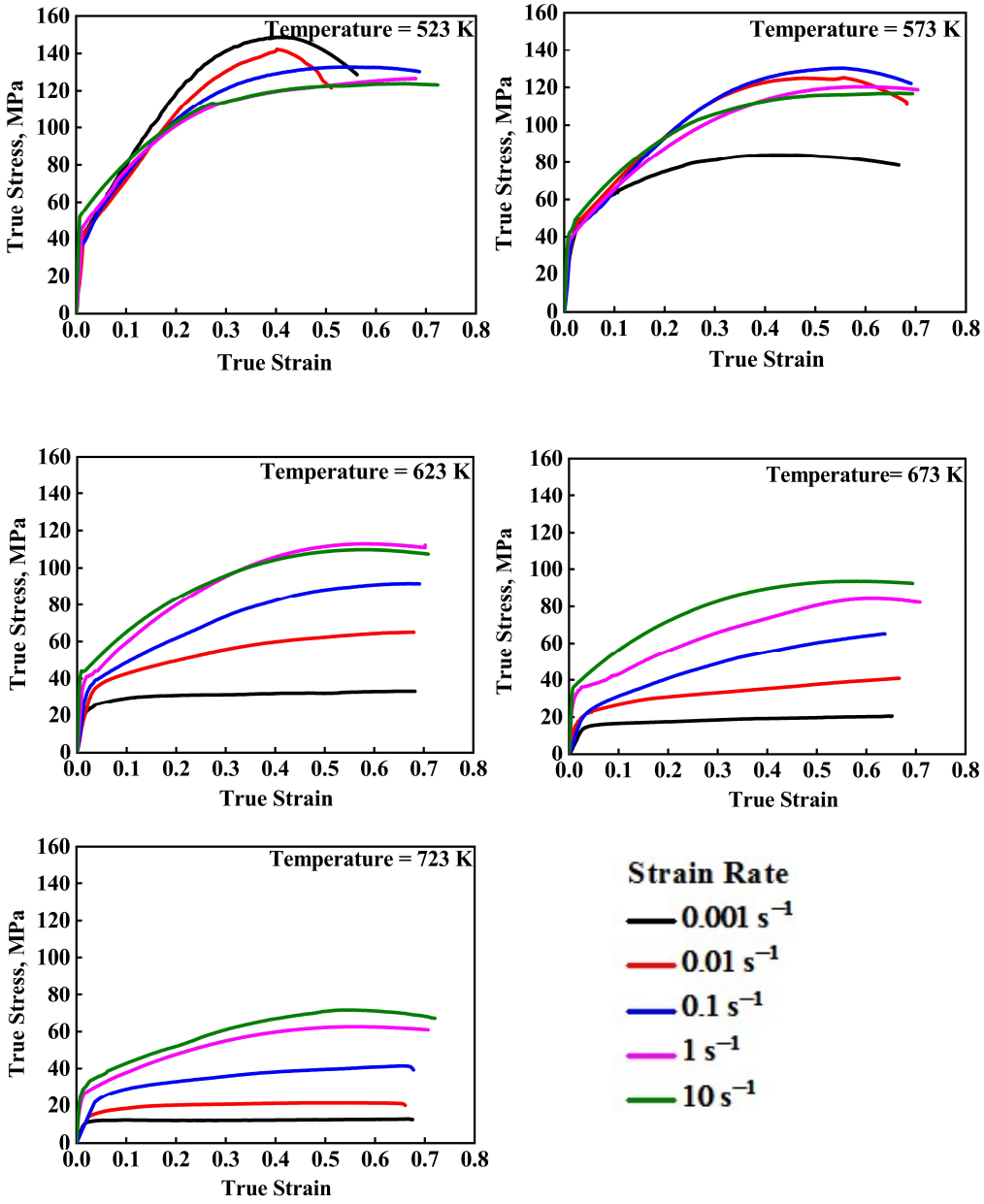

Fig. 4.2 True stress–true strain curves obtained for Test material in hot compression at 5 different temperatures and 5 different strain rates as indicated in each curve.

The true stress–strain curves are developed typically in flow curves nature based on hot compression test parameters of five distinct temperatures and five different strain rates as observed in Fig. 4.2.

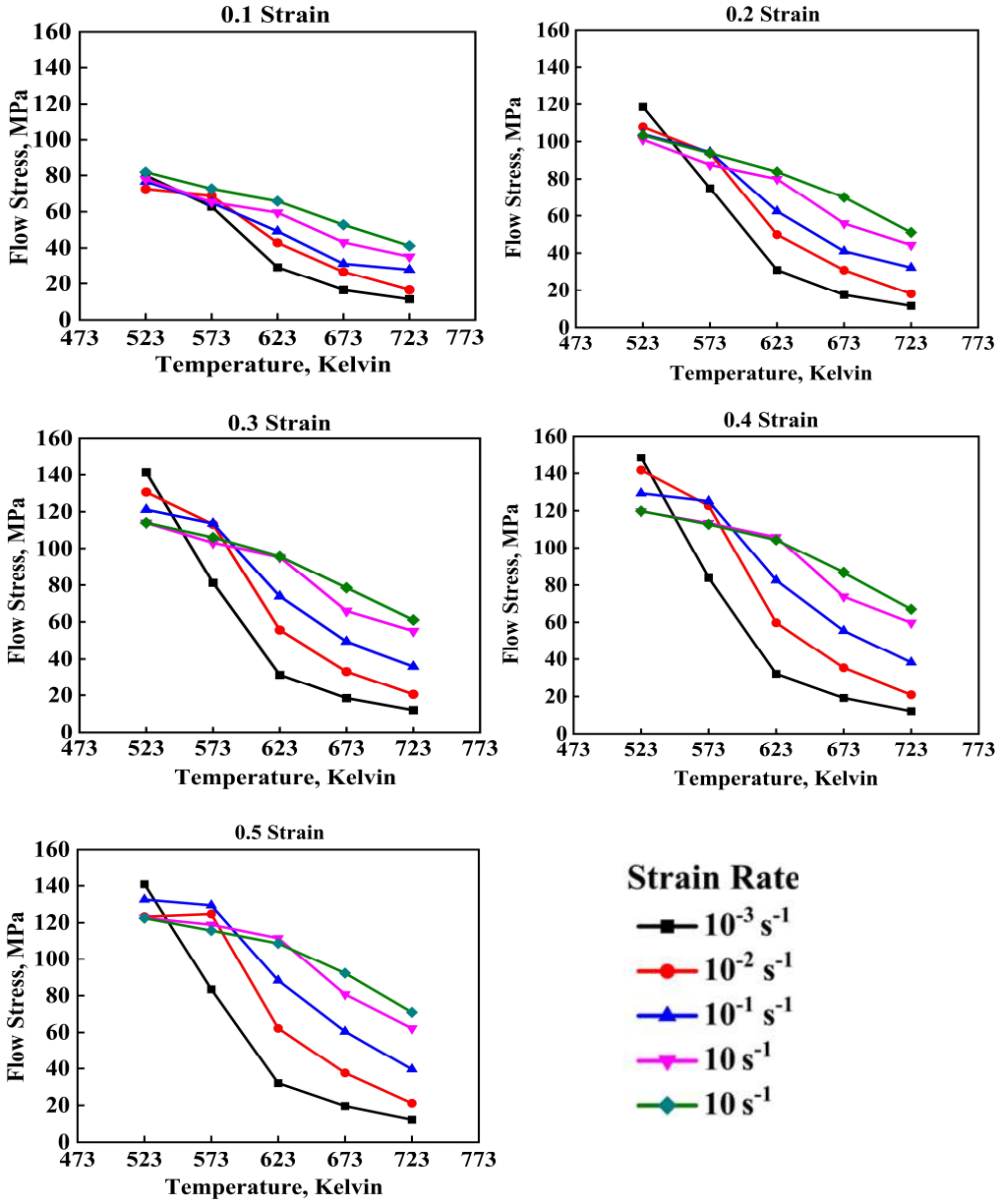

Fig. 4.3 Variation of flow stress with temperature from 0.1 and 0.5 strains

Now these true stress-strain curves are employed to establish the variation in flow stress with the temperature of hot compression as seen in Fig. 4.3. It can be observed that flow stress reduces with rise in the deformation temperature and decline in the strain rate. But this fact is true at 623 K, 673 K and 723 K.

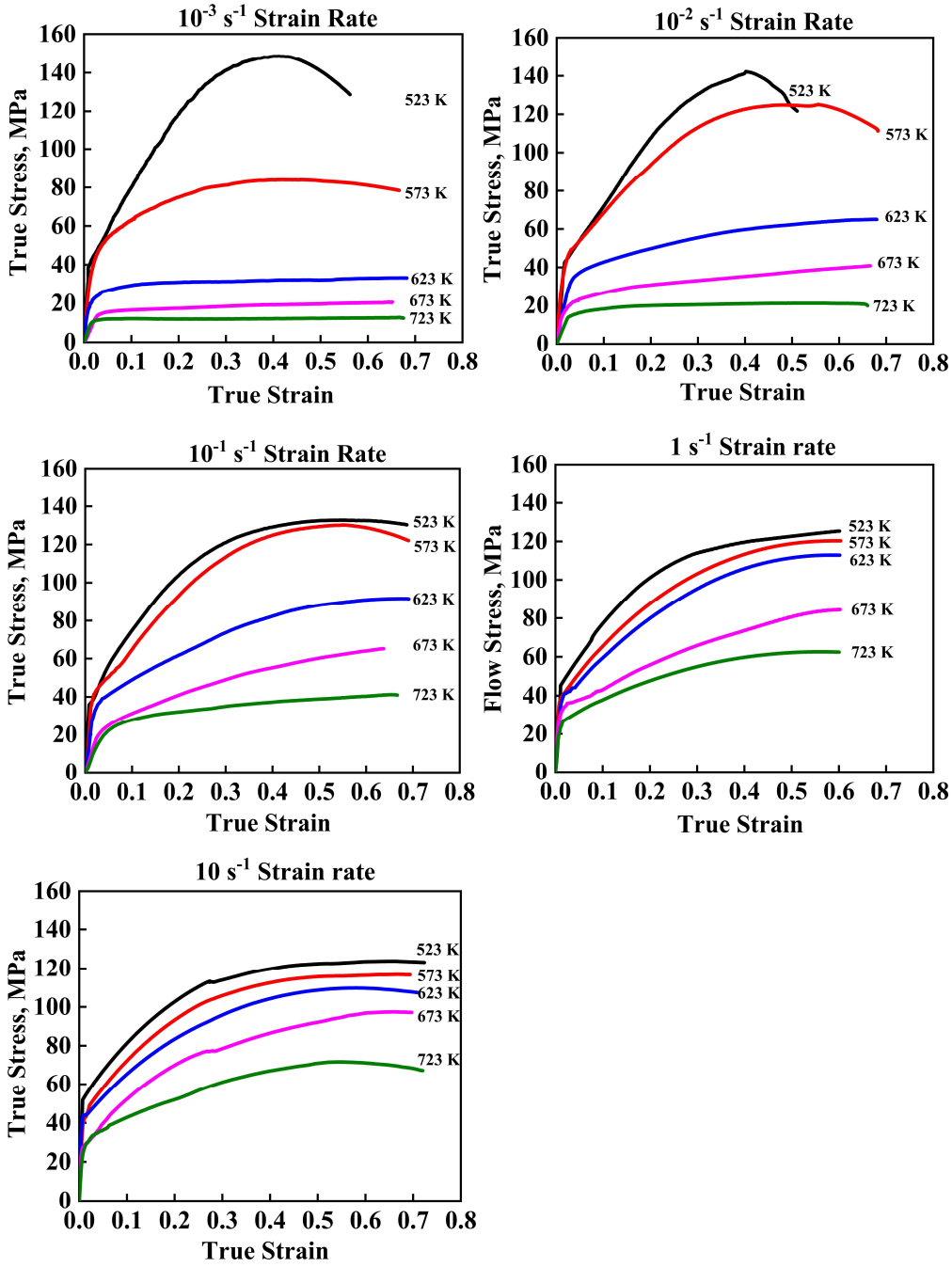

Fig.4.4 True stress–true strain curves obtained for Test material in hot compression at 5 different temperatures and 5 different strain rates as indicated in each curve.

For all the test temperature, the true stress-true strain curves at strain rates of 10^{-1} s^{-1}, 1 s^{-1} and 10 s^{-1} exhibited strain hardening, whereas at lower strain rates (10^{-3} s^{-1}, 10^{-2} s^{-1}) flow softening of recovery was observed as shown in Fig. 4.4. The peak stress at 0.4 strain for lowest strain rates 10^{-3} s^{-1} occurs slightly above the remaining strains, followed by 0.01 s^{-1} at lowest temperature of 523 K. This deformation in occurs

by giving strain only along the <a> = <11$\bar{2}$0>/3 axis due to four independent slip systems i.e., 2 from the basal slip system (0002) <11$\bar{2}$0> and 2 from prismatic slip systems (10$\bar{1}$0) <11$\bar{2}$0>. Such inadequate deformation leads to strain given along c-axis by {10$\bar{1}$2} <10$\bar{1}$1> extension twinning brings about half of the slip mode based on direction. [15]. Later, the peak stress shifts to 0.5-0.6 strain for 10^{-2} and 10^{-1} s^{-1} with increase in temperature at 573 K. However, the onset of flow softening occurs at the lowest strain rate 10^{-3} s^{-1}. This occurs because of either reduction in critical resolved shear stress (CRSS) of basal slip system or decrease in activation energy required for cross slip, causing other slip systems (prismatic and pyramidal) to activate. [54]-[56]]. Such activation is driven by temperature dependent deformation components because prismatic and pyramidal slip systems has the CRSS value double that of basal. [51].

The flow curve shows steady state behaviour upto 0.7 strain for deformation temperature of 623 K to 723 K for the highest strain rate of 10 s^{-1}. But at 1 s^{-1} strain rate exhibits onset of steady state behaviour at 673 K and get stabilize steady state at 723 K. The flow stress reduces with increase in temperature from 673 K and 723 K for all the strain rates. The deformation temperature decides the CRSS of slip system that causes lower stresses and considerable ductility. [54] [47][60]

The samples cracked for the temperature below 523 K because of highly localize incompatible stresses are developed in the microstructure that causes the grains oriented properly for basal slip get obstructed from the adjoining grains not oriented suitably for basal slip. Subsequently, the stress concentration increases more at the grain boundaries than the applied stress and high enough even to activate non-basal slip. [57]

The choice of deformation temperature is based upon strain accumulation in the materials and subsequently restoration of this accumulation. Hence, the selection of deformation temperature decided by recrystallization temperature considering the phase diagram of the material under investigation. Simultaneously, the range of strain rate is estimated by strain accumulation controlled by stacking fault energy of the materials and an industrial choice between accomplishment of materials processing with complete structure-property relationship and cost of production. Therefore, this alloy was tested at a temperature from 523 K, 573 K, 623K, 673 K and 723 K and strain rates applicable over the range of 10^{-3} s^{-1} to 10^{1} s^{-1} to obtain sufficient deformation processing data. . The flow stress values taken at 0.6 strains in all the cases, are

exhibiting more pronounced strain hardening as it enhances with increase in strain rates but declines with increase in temperatures.

4.1.2.2 Processing maps:

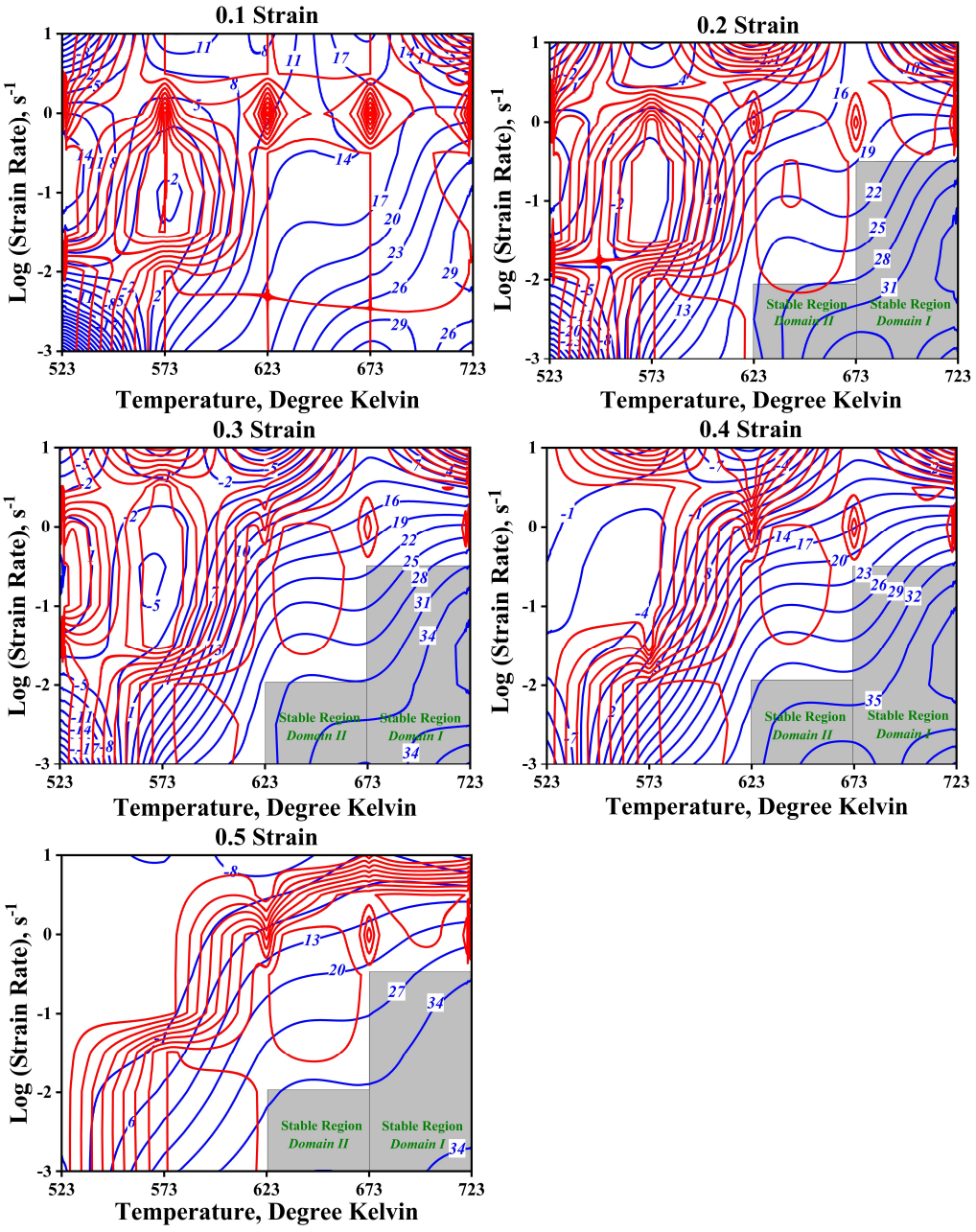

Fig. 4.5 Processing maps for Test material at 0.1 to 0.5 strain

Processing map overlapping of efficiency of power dissipation map on instability map. Fig. 4.5 shows contours lines (blue and red) in a temperature–strain rate frame for 0.1 to 0.5 strain. The blue coloured contours lines shows constant efficiency

as a percentage. The number on each blue contour line indicate the efficiency of power dissipation in percentage. The red contour line shows the instability in the flow stress for Test material.

In processing maps, the efficiency of power dissipation value at 0.1 strain exhibit very low, while gradual increment is observed from 0.2 to 0.5 strains. The processing map at 0.2 strains corresponds to the extensive strain subjected on the experimental Test material in the vicinity of critical strain for majority of strain rates and same is also being depicted in the processing map at 0.3 strain. The map at 0.4 and 0.5 strains correlates to the steady state condition.

The processing map demonstrates of two distinct domains:

Domain I: Occurring at 723 K and 10^{-3} s^{-1} to $10^{-0.5}$ s^{-1} (10^{-3} s^{-1} to 0.316228 s^{-1}) with a peak efficiency of around 40% - 30%.

Domain II: Occurring at range of 623 K – 673 K and 10^{-3} s^{-1} - 10^{-2} s^{-1} (10^{-3} s^{-1} - 10^{-2} s^{-1}) with a peak efficiency of about 50% - 35%.

These maps are unlike to that attained on as-cast magnesium [223], as the first domain occurred at 698 K and 0.3 s^{-1}, whereas the second domain was more evolved as testing was continued to 823 K, a higher temperature.

In general, the power dissipation efficiency rates of 30% and greater are regarded safe for processing. Domain 1 in Mg-0.5wt% Ce alloy appears to be a stable domain as the concerned efficiency value is above 30%. The region identified as domain 2 also shows a zone of safer area. However, due to significant grain coarsening, the effect of deformation heating should not be overlooked at low strain rate and high temperature regime.

The domain around lower strain rates changes narrowly with increasing strains and corresponds to higher value of power dissipation efficiency. Processing maps are 2D descriptions of topographic maps in 3D, where the domains represent peaks or maxima of efficiency, and the contours lines are comparable to the lines of equal height along the peak. The quantification of shift from stable to unstable zones or vice-versa cannot be done by number in fraction or percentage of efficiency but needs to detect a valley. Therefore, the deviation from the optimum value of safe zone by the changes in processing parameter manifests the gradual decrease in the efficiency points to the closed contour lines. [26]

The red contour lines of instability map overlap on the blue contour lines of power dissipation efficiency map developing the processing map observed in Fig.4.5. The

regime of instability inside the efficiency contour lines shows negative value of $\xi(\dot{\varepsilon})$ as given by equation (2.11) and exhibits flow instability.

Therefore, the material flow is unstable manner at strain rates greater than $0.1s^{-1}$ regime that is manifested in the microstructural evolution. The instability maps at 0.1 and 0.2 strains are partially developed than compared to 0.3, 0.4, and 0.5 strains. The demarcation of unstable and stable regimes shown by region of red coloured contour lines over blue ones and only blue contour lines respectively.

Lower values of power dissipation efficiency at 523 K – 573 K, irrespective of the strain rates implies unsuitability for the hot working conditions. However, higher efficiency values obtained in the 0.001 s^{-1} to below 1 s^{-1} strain rate region is apt for hot working of Mg-0.5% Ce alloy.

4.1.2.2.1 Stability Domain

Fig. 4.5, domain I is marked in the range of 10^{-3} to $10^{-0.5}s^{-1}$ and 673 to 723K, while domain II is marked within 10^{-3} to $10^{-1.5}s^{-1}$ and 623 to 673K. Domain I represents steady state stress due to DRV, while domain II corresponds to recrystallized regions. Generally, stable domains characterized by DRV are observed at a maximum power dissipation efficiency η<30% based on stacking fault energy of the materials [170].

4.1.2.2.2 Instability Domain

Between 523–623K and 10^{-3} – 1 s^{-1} instability domain is observed with an efficiency of 25% indicating a larger fraction of power being utilized in heat generation rather than microstructure refinement. As a result, insufficient DRV occurs at grain boundaries which are high energy state, and further increase in strain tends to be localized deformation in terms of deformation bands or shear bands. Higher strain rates promote the occurrence of such localized deformation resulting in earlier failure [224].

Instability domain at 623–723K/1–$10s^{-1}$ strikingly identifies high deformation temperature suitable for DRV or DRX, however, high strain rate restricts uniform deformation. Simultaneously, the presence of original coarse grain and deformation induced fine grains will trigger instability extending it to nucleate cracks. At higher strain rates, the deformation induced heat generation is concentrated along the grain boundaries resulting in the occurrence of adiabatic shear bands. At high strain rate and high temperature, the plastic deformation work energy will be transferred to heat energy

resulting inadequate recrystallization and excessive softening causing reduction in grain boundary strength. Sometimes, high dislocation density and stress-accumulation along grain boundary leads to localized flow stress instability which should be avoided in hot processing. [225].

4.1.3.3 Microstructure evolution:

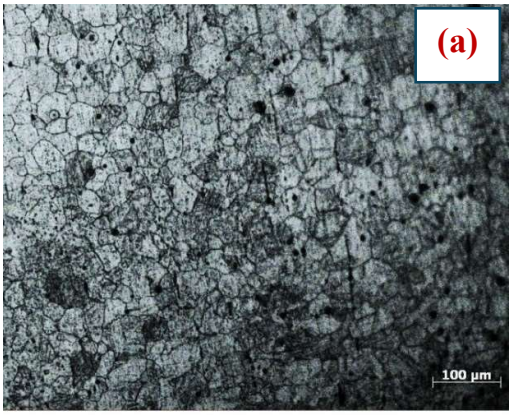

As-extruded 100X

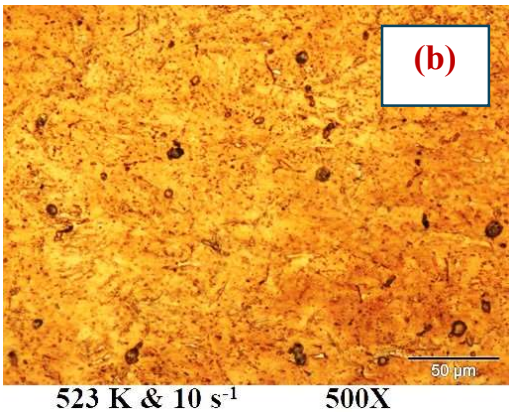

523 K & 10 s^{-1} 500X

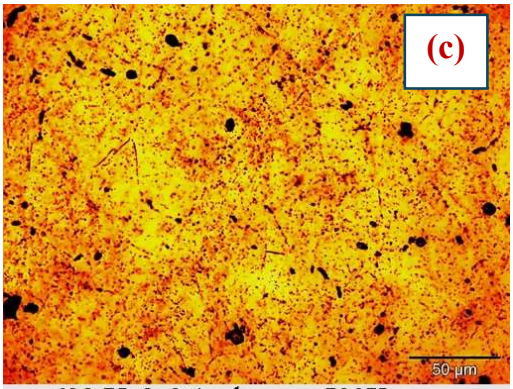

623 K & 0.1 s^{-1} 500X

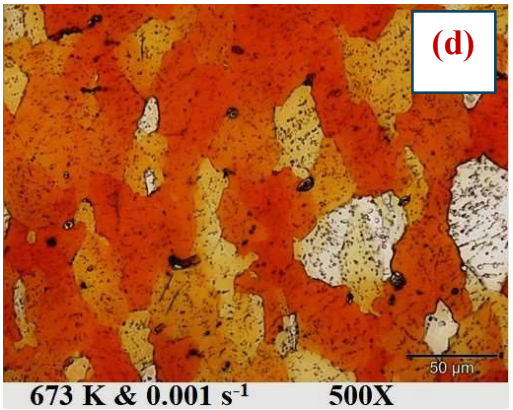

673 K & 0.001 s^{-1} 500X

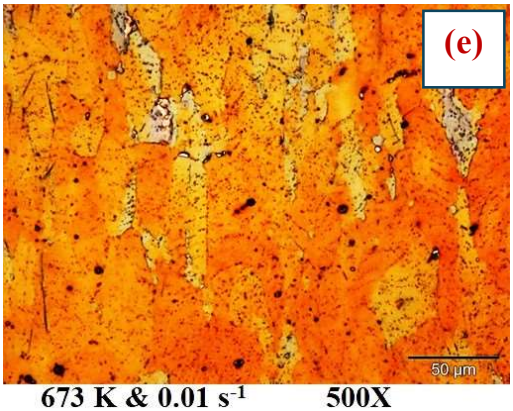

673 K & 0.01 s^{-1} 500X

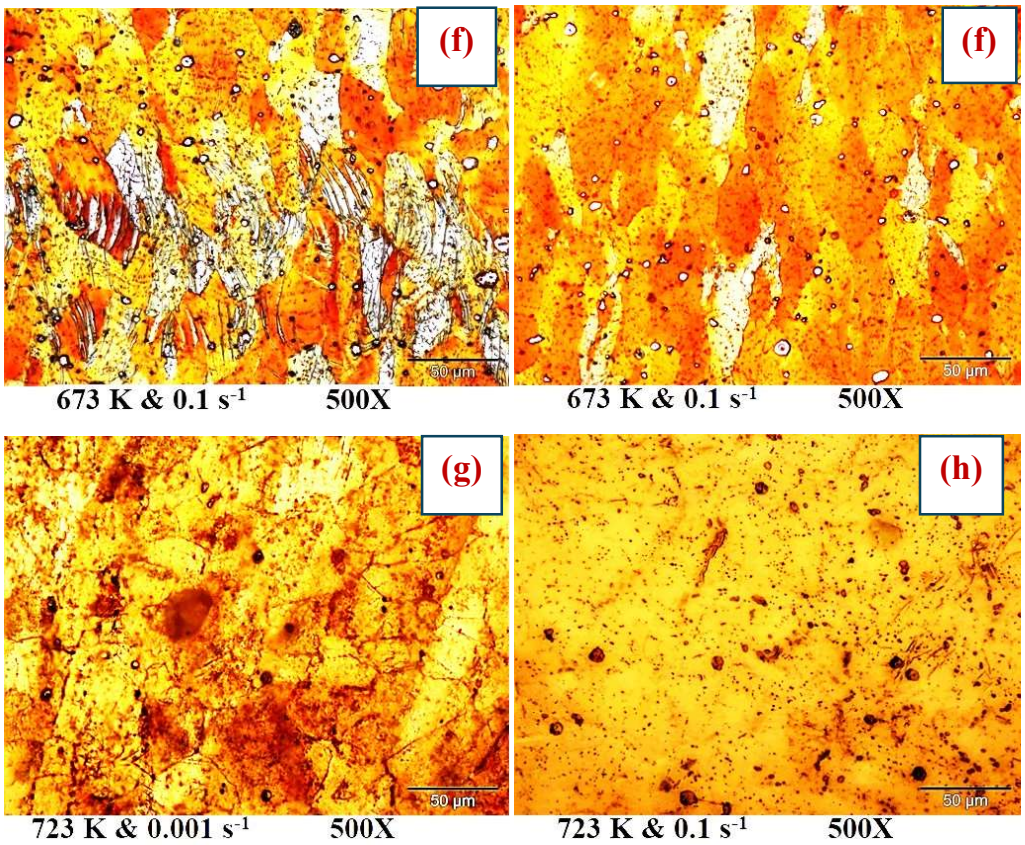

Fig. 4.6 Optical microstructures of As-extruded specimen at 100X and 500X of compression tested specimen of Test material.

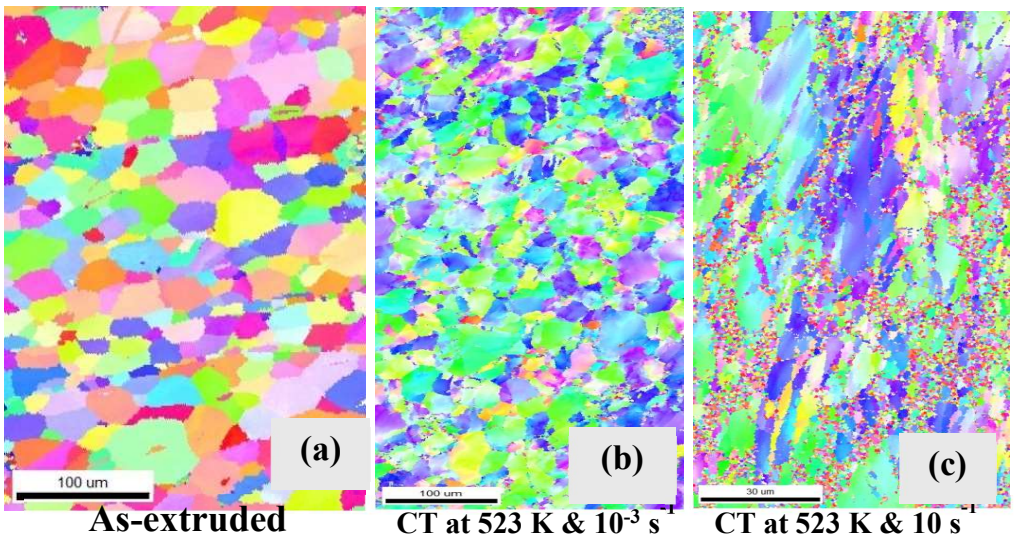

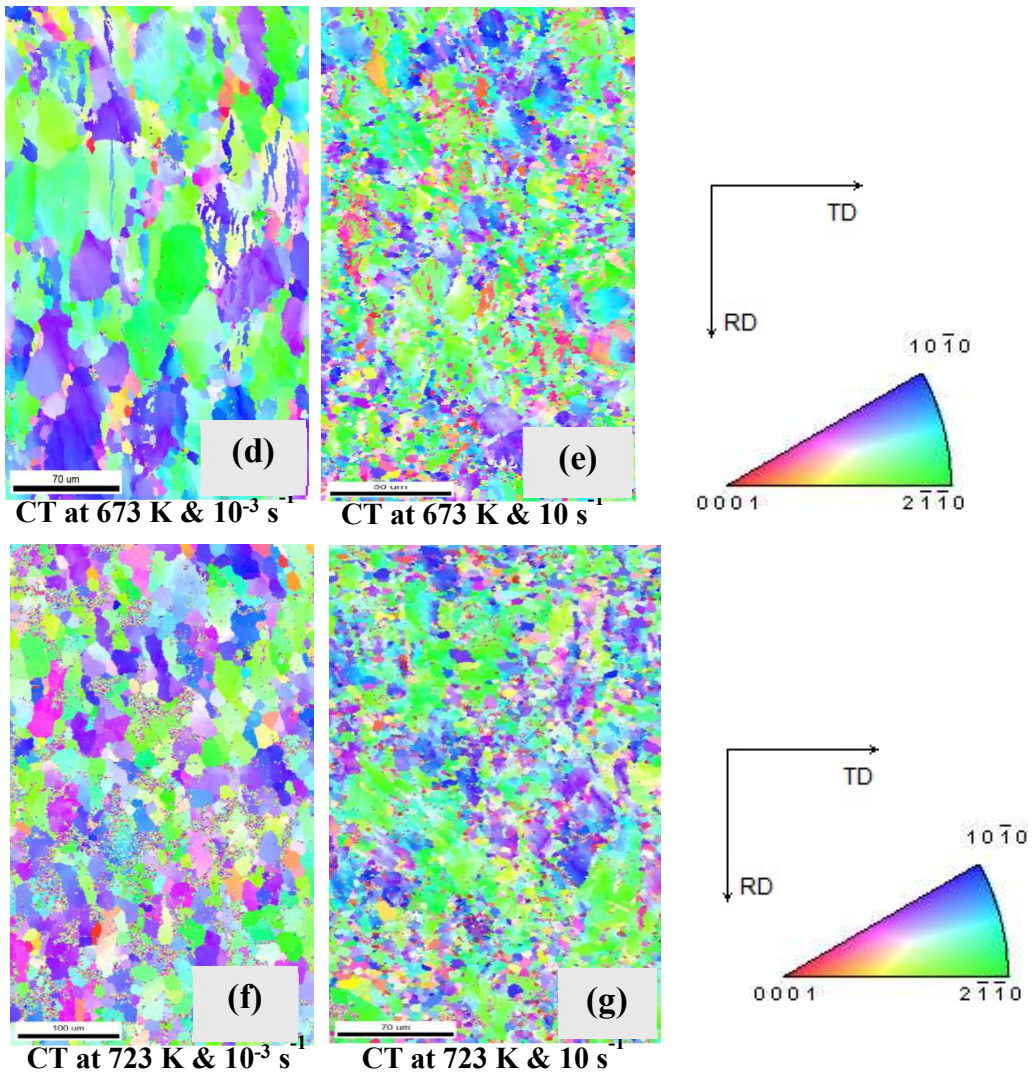

Fig. 4.7 EBSD Inverse Pole Figure (IPF) of (a) As-extruded specimen and (b-e) Compression tested specimen of Test material.

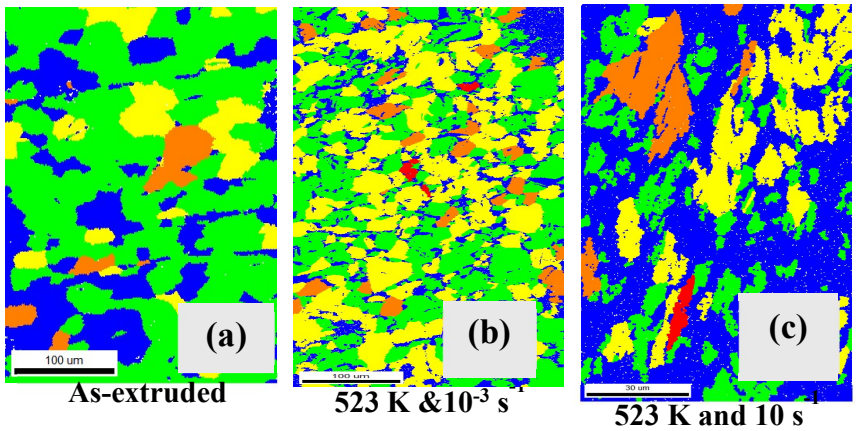

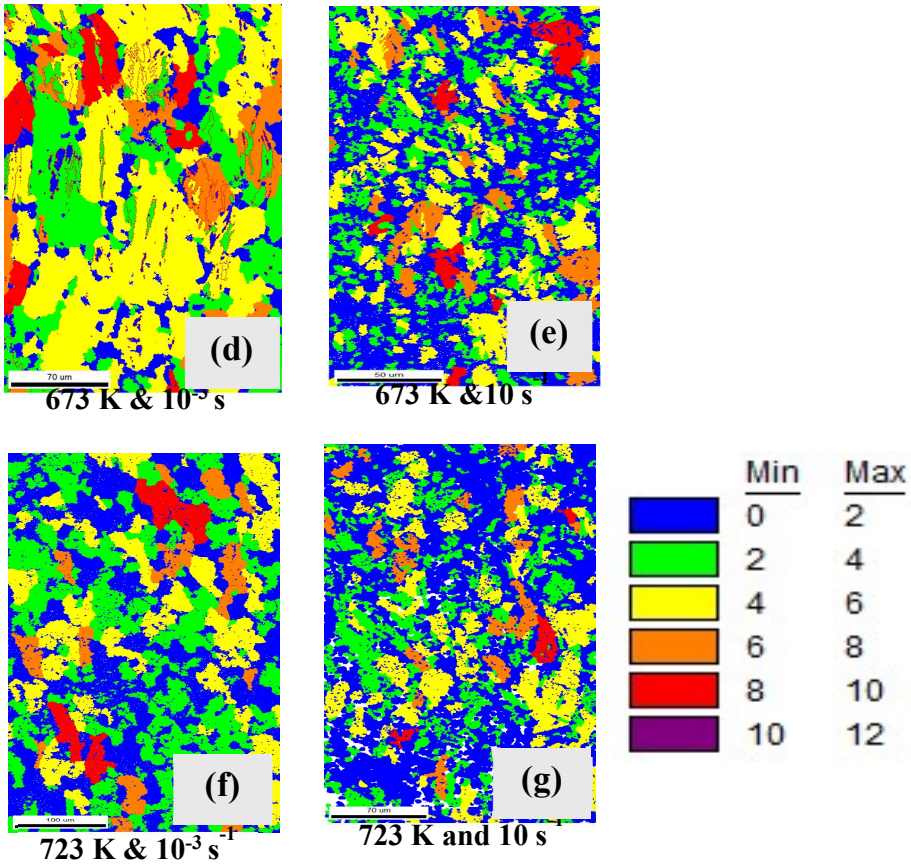

Fig. 4.8 EBSD Grain orientation spread (GOS) microstructures of (a) As-extruded specimen and (b-g) Compression tested specimens of Test material.

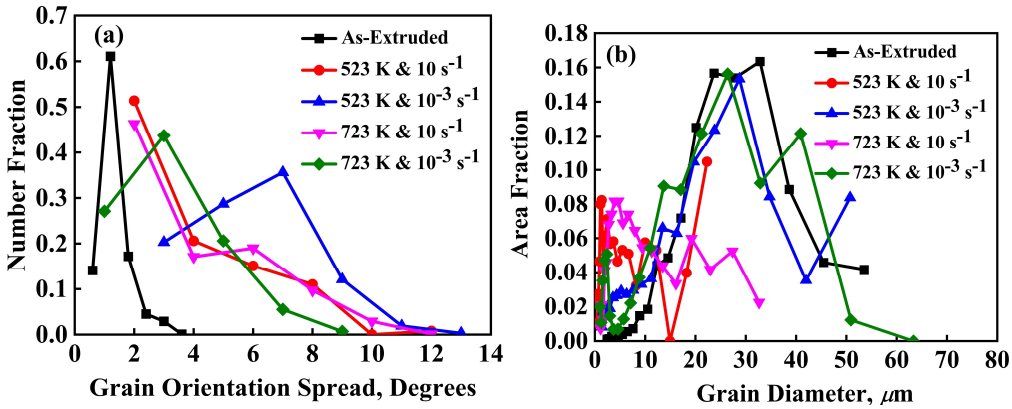

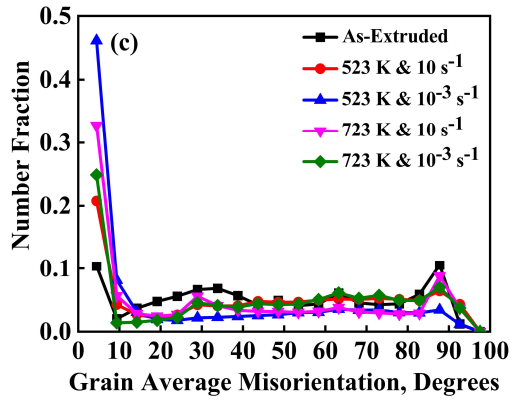

Fig.4.9 Quantification of EBSD data with (a) Grain orientation spread (GOS), (b) Grain Size distribution and (c) Grain Mis-orientation Angle of as-extruded specimen and compression tested specimens of Test material.

During hot working the dynamic restoration process is extremely vulnerable to deformation conditions in Mg alloy because non-basal slip system has strong dependency on temperature and strain rate. Plastic deformation is carried out by basal slip (0001) <11$\bar{2}$0>, prismatic slip {10$\bar{1}$0} <11$\bar{2}$0>, and pyramidal I-type {10$\bar{1}$1} <11$\bar{2}\bar{3}$>, and pyramidal II-type {$\bar{1}\bar{1}$22} <11$\bar{2}$3> system along with tensile twin {10$\bar{1}$2} <10$\bar{1}$1>, and compression twin {10$\bar{1}$1} <10$\bar{1}$2>. The non-basal slip system activates system during hot deformation relies on the union cross slip of glissle screw <a> basal dislocation with the sessile edge <c> dislocation on the prismatic plane generating screw type <c+a> dislocation easy to cross slip on the pyramidal plane. [67]. The microstructures obtained from EBSD are evaluated through IPF and GOS. Fig.4.7 shows IPF images of (a) As-extruded specimen and (b-e) Compression tested specimen of Test material.

At 523 K, Mg-Ce alloy exhibit poor ductility than the pure Mg which contains dislocations nearly parallel to each other resulting parallel slip-band. [19]. The slip banding in Mg-Ce alloy shows wavy lines indicating of cross slip at 523K due to non-basal dislocations slips [226]. Many dislocations in Mg-Ce alloys are not parallel indicating different orientations and activity viz, basal <a>, prismatic <a> at room temperature as proposed by Koike et. al. [55]. The non-basal slips activate dominantly at higher temperatures as reported by Reed-Hill et. al. [50], such as prismatic slip at 83-298 K and pyramidal slip at 423-559 K. This confirms that pyramidal slip is responsible for deformation at 523 K [19].

Generally, $\{10\bar{1}2\}$tensile twins are more commonly observed during compression, but even $\{10\bar{1}1\}$compression twins are formed. These compression twin initiates (i) local shear deformation inside twin volume and (ii) crack at their boundaries, consequently, leads to failure. [227] [86]. Compression twins nucleate at larger grain size at lower strains, while nucleation of tensile twin is not strongly dependent on grain size above 15-30 μm. Mg-0.5wt% Ce alloy has grain size above this value. Sometimes, smaller grains twin observed even at higher stress levels. [24]. Double twins when grouped with compression results into shear bands formation generally observed in Mg-RE alloys (especially in Mg-Ce alloy leading to texture weakening). [104]

Formation of extensive shear band occurs at highest strain rates and at 523 K , whereas small fraction of shear bands are formed at 673 K and 723 K. Shear bands are basically areas of high strain localization appears to be frequently crossing many grains. The shear bands formation in Mg alloys occurs during compression and dual twinning modes of deformation. [95][96][98][99]. Generally, shear band forms during compression at 45º to the compression direction as seen in Fig. 4.7 (c) at 523K and 10 s^{-1}. Such shear bands are projected as the fundamental demonstration of strain localization and the indication of damage. During hot rolling or cold rolling in Mg alloys shear bands are generally observed and depreciate the formability, even at above room temperature. A heterogeneous microstructure develops due to the shear bands which cannot be removed completely once formed. In such microstructures, shear bands occur as areas of slip plane segregation (High SFE) reorienting toward shear direction or grouping of micro-twin band formation (Low SFE).[101]

Still there is decrease in the ductility at 523 K, attributed to the spatial distribution of shear bands. Larger size shear bands extending along many grains can accommodate less amount strain accumulation than compared to smaller size shear bands distributed finely throughout grains within the microstructure [96] Such larger size (both width and lengthwise) of shear bands is distinctly seen in the IPF microstructure of 523 K compressed at 10 s^{-1}, where strain accumulation is less and hence ductility decreases accordingly. Similar trend of shear band formation leading to flow localization continues even at lower strain rates such as 1 s^{-1}, and 10^{-1} s^{-1}, when tested compressively at 573 K and 623 K. Such kind of shear band formation attributed

to flow localization resulting in instability zone for these deformation parameters as seen in processing map shown by red colour lines.

However, narrow size of shear band formation is a resultant of larger amount of micro-twin bearing $\{10\bar{1}1\}$ - $\{10\bar{1}2\}$ orientation disclosed by TEM – BF [96]. Accordingly, smaller size of shear bands is observed in the IPF microstructure of 673 K, and 723 K compressed at 10 s^{-1}, having smaller fraction distributed finely. Smaller extent of strain accommodation occurs in low intensity shear bands in large numbers resulting in high strain prior to failure. Therefore, the stress – strain curve shows better ductility for 673 K and 723 K compressed at 10 s^{-1}, even at higher strain rate. Similar, precedence is followed for lower strain rate of 1 s^{-1} at 673 K and 723 K. These shear band formation even though accommodating large strains resulting better ductility comparatively but still flow localization persisting. Hence, microstructure with flow localization results into a regime of instability zone, as depicted in the processing maps for 673 K and 723 K compressed at 10 s^{-1}, and 1 s^{-1}, strain rates. Thus, at high strain rates, extensive shear band formation is prevalent.

At 723 K and 10 s^{-1}, the accumulation of dislocation is high due to strain hardening. Fraction of high angle grain boundaries (HAGB) is significant for specimens deformed at higher strain rates. Specimen deformed at highest strain rate shows large fraction of fine grains corresponding to sub-grain formation. This indicates the characteristic of dynamic recovery revealing the onset of flow restoration mechanism. This fact is also validated by the steady state nature of the stress-strain curve.

At lowest strain rates, grain sizes of the deformed samples are comparable with as-extruded samples as dynamic recovery occurs without dynamic recrystallization. At 523 K and 10^{-3} s^{-1} to 10^{-2} s^{-1}, parameters show heterogeneity of deformation gradient inside the grains, more strain at the grain boundaries and less in the centre of the grain. The variation in this deformation gradient is attributed to activity of numerous slip system along grain boundaries compared with central region of grain where only basal plane is active [102]. This development is demonstrated by formation of smaller fraction of fine equiaxed grain but not recrystallized at the grain boundaries. The remaining grains stays bigger in size due to larger concentrations of dislocation density and presence of tensile twins. At lower temperature, fraction of dynamic recovered grains is lower due to insufficient thermal driving force. Similarly, compression at 573 K and 10^{-3} s^{-1} to 10^{-2} s^{-1} also shows same behaviour of insufficient dynamically recovered grains. The microstructures at 523 K and 573 K compressed at lower strain

rates shows smaller fraction of sub-grains formation appearing as fine grains along boundaries of bigger grains. On these compression test parameters of 523 K and 10^{-3} s^{-1}, the specimens are observed to have high GOS values as shown by Fig. 4.8 EBSD – Grain Orientation Spread images and Fig. 4.9 (a) GOS value.

At 673 K and 10^{-3} s^{-1} to 10^{-1} s^{-1}, the thermal energy is utilized in dynamic recovery rather than dynamic recrystallization as indicated by steady state flow curve. The grains in the microstructures shown by Fig. 4.6 (d to e) for this regime shows completely restored from deformed state. As grain interior and grain boundaries both are well defined to prove the same. As Test material contains very weak texture initially leading to considerable tensile twinning during hot compression deformation along with non-basal oriented twinning. Presence of double twins and other twin activity is observed in the GOS map for 673 K and 10^{-3} s^{-1}. The soft oriented grains and twins were not recrystallized reveals the fact of unable to attain sufficient energy of strain hardening for recrystallization at this deformation parameters. Consequently, the microstructure evolved has sub-grain formation due to low deformed region during dynamic recovery process. Alike, 723 K and 10^{-3} s^{-1} to 10^{-1} s^{-1}, same trends follow as above parameter except that of temperature increment makes the grain sizes recovered dynamically. This type of microstructure evolution represents the steady state behaviour of stress-strain curve considered as stable zone from the viewpoint of processing map of this material.

4.1.3.4 Constitutive Equation Analysis: Hyperbolic Sine Arrhenius Model

The hot deformation behaviour of flow stress during compression test analysed by constitutive equations based on Arrhenius-type sinusoidal hyperbolic equation [177]. In this study, flow stress behaviour at low strain (0.2 strain) and high strain (0.4 strain) are considered. The constitutive equations are established using three ways i.e.,

(i) by applying the Zener-Holloman parameter, *Z* also called as temperature-compensated strain rate [178]. Temperature-Strain rate compensation used to calculate predicted flow stress.

(ii) the strain – compensation to calculate predicted flow stress**.**

(iii) strain rate – compensation to calculate predicted flow stress.

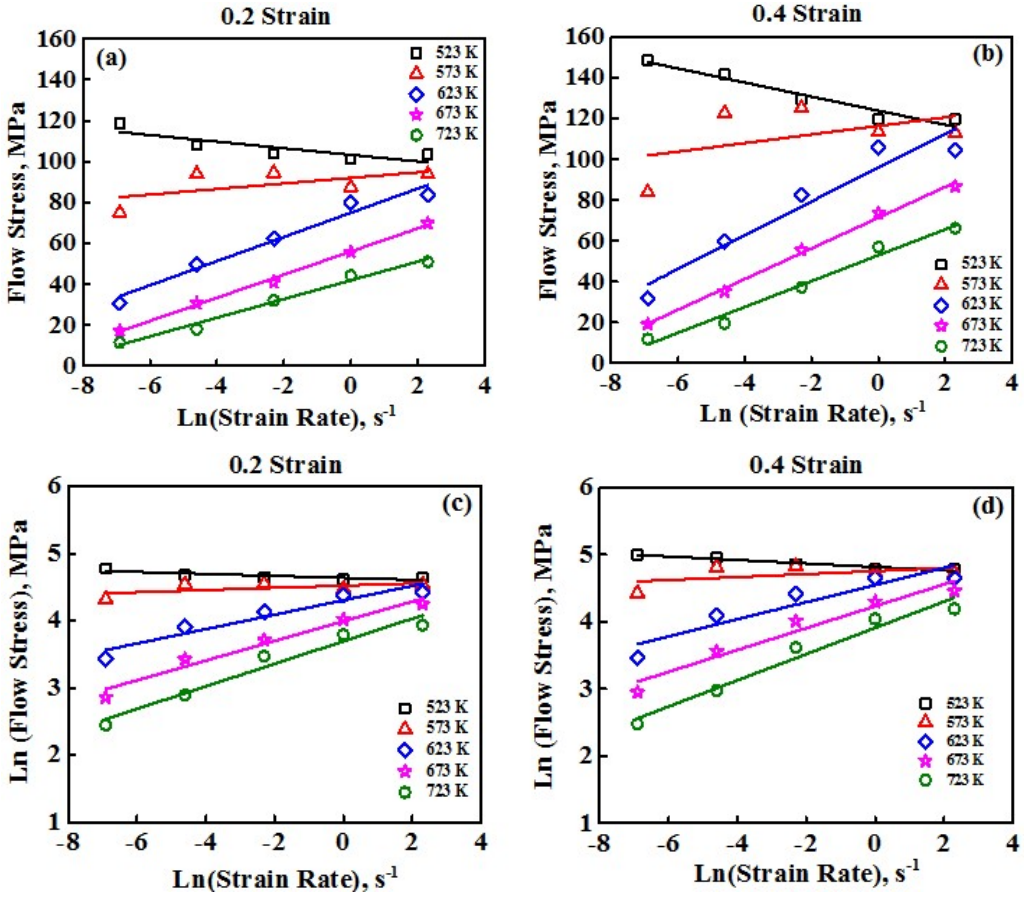

Fig. 4.10: Estimation of materials constants, (flow stress) vs Ln (strain rate) at (a) 0.2 strain and (b) 0.4 strain and Ln (flow stress) vs Ln (strain rate) at (c) 0.2 strain and (d) 0.4 strain

Fig. 4.10 (a-d) displays the flow stress as a part of strain rate at 0.2 strain and 0.4 strain. MC, $\alpha = \beta/n'$, wherein average of the slope values of n' and β are secured by Fig. 4.10 (a & b) and Fig. 4.21 (c & d) respectively found by Equations (2.17) and (2.18) at various strain. The β value obtained as 0.27 MPa^{-1} and 0.19 MPa^{-1} at 0.2 strain and 0.4 strain respectively. Similarly, the n' value obtained as 7.11 and 6.17 at 0.2 strain and 0.4 strain respectively. These n' and β are taken to compute the α value as 0.04 and 0.03 at 0.2 strain and 0.4 strain respectively.

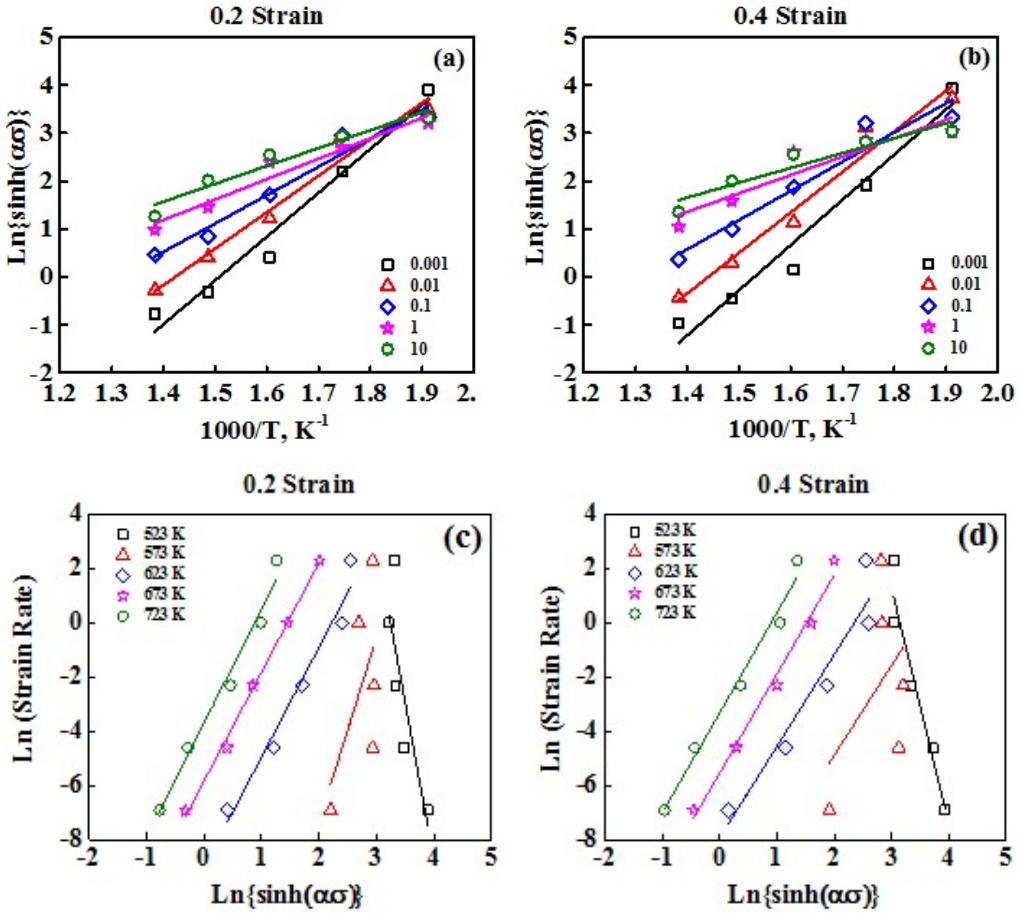

Fig. 4.11: Determination of apparent activation energy, Q estimated by material constant from Ln (sinh (ασ)) Vs 1000/T at (a) 0.2 strain and 0.4 strain and Ln (strain rate) Vs Ln (sinh (ασ)) at (c) 0.2 strain and 0.4 strain.

Fig. 4.11 (a–b) estimates materials constants, $S = \left[\frac{\partial ln[\sinh(\alpha\sigma)]}{\partial(1000/T)}\right]$ from ln[sinh($\alpha\sigma$)] vs 1000/T and Fig.4.11 (c–d) determines stress-exponent, $n = \left[\frac{\partial ln\dot{\varepsilon}}{\partial ln[\sinh(\alpha\sigma)]}\right]$ from ln$\dot{\varepsilon}$ vs ln[sinh($\alpha\sigma$)] where both are linear fit slopes. The apparent activation energy, Q required for plastic deformation in hot compression test is determined by Equation (2.20)

$$Q = R.\left[\frac{\partial ln\dot{}}{\partial ln[\sinh(\alpha\sigma)]}\right]_T.\left[\frac{\partial ln[\sinh(\alpha\sigma)]}{\partial(1000/\ )}\right]_{\dot{\varepsilon}} = R.n.S$$ ----------from (2.20)

The calculated average apparent activation energy, Q is 332 kJ/mol and at 0.2 strain and 0.4 strain are 360 kJ/mol and 335 kJ/mol respectively, while stress-exponent, n has values 7.06 and 6.52 at 0.2 strain and 0.4 strain respectively.

Spigarelli et.al. [228] proposed several deformation mechanisms based on different stress-exponent, *n* values, such as sliding by grain boundary (*n*=2), dislocation glide (*n*=3), climb-controlled dislocation recovery (*n*=5) and cross-slip of dislocation (*n*=>6). In Mg-0.5wt%Ce alloy, the stress-exponent, *n* values are between 6 and 7, demonstrating that the hot deformation mechanism is governed by dislocation cross slipping and partially by climb-controlled dislocation creep.

Increase in strain rate leads to higher dislocation density resulting in higher activation energy, Q as the strain hardening makes deformation more challenging. The calculated activation energy, Q values (360 kJ/mol and 335 kJ/mol at 0.2 strain and 0.4 strain respectively) for Mg-0.5wt%Ce alloy are considerable higher than those for self-diffusion through grain boundary (92kJ/mol) [171] and lattice-diffusion (135 kJ/mol) [229]. Such larger activation energy, Q in hot deformation is attributed to dynamic precipitation, second phase particles volume fraction and the pinning effect. The dissolved Ce in Mg induces the pinning of dislocations, with Ce-rich precipitates acts as barrier for dislocation slip.

4.1.3.5.1 Temperature - Strain rate compensation to calculate predicted flow stress

As discuss in the chapter 2 section 2.5.1, taking logarithm on both side of Equation (2.12), we get Equation (2.21) illustrating the relation between flow stress and Zener-Holloman parameter, *Z*.

$ln\ Z = ln\ A + n.ln[\sinh(\alpha\sigma)]$----------{taken from equation (2.21)}

The flow stress, σ can be determined by the materials constants (n', β, α, n) and Q in the constitutive equations as a function of Zener-Holloman parameter, *Z*, thereby taking the Equations (2.12) and (2.16) as follows:

$$\sigma = \frac{1}{\alpha}.ln\left\{\left(\frac{Z}{A}\right)^{\frac{1}{n}} + \left[\left(\frac{Z}{A}\right)^{\frac{2}{n}} + 1\right]^{\frac{1}{2}}\right\}$$----------taken from equation (2.22)}

The flow stress, σ based on the constitutive equations established by Equation (2.22) at 0.2 strain and 0.4 strain can be determined after calculating all the parameters described above stated as

$$\sigma_{0.2} = \frac{1}{0.04}.ln\left\{\left(\frac{Z_{0.2}}{1.78*10^{28}}\right)^{\frac{1}{7.00}} + \left[\left(\frac{Z_{0.2}}{1.78*10^{28}}\right)^{\frac{2}{7.00}} + 1\right]^{\frac{1}{2}}\right\}$$ ----------(4.1a)

$$\sigma_{0.4} = \frac{1}{0.03}.ln\left\{\left(\frac{Z_{0.4}}{2.93*10^{26}}\right)^{\frac{1}{6.52}} + \left[\left(\frac{Z_{0.4}}{2.93*10^{26}}\right)^{\frac{2}{6.52}} + 1\right]^{\frac{1}{2}}\right\}$$ ----------(4.1b)

but the Z at 0.2 strain and 0.4 strain can be stated as

$$Z_{0.2} = \dot{\varepsilon}.\exp\left(\frac{360\ x\ 10^3}{RT}\right)$$ ----------(4.2a)

$$Z_{0.4} = \dot{\varepsilon}.\exp\left(\frac{335\ x\ 10^3}{RT}\right)$$ ----------(4.2b)

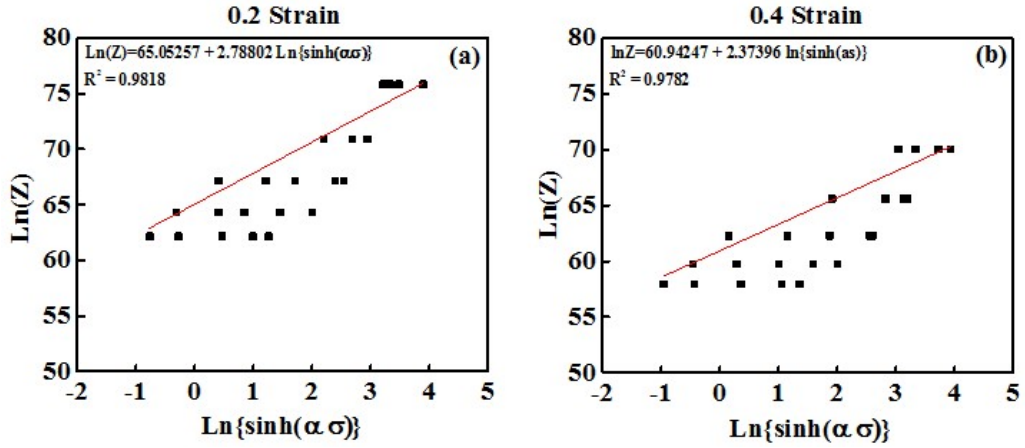

Fig. 4.12: Estimation of materials constants ln(A) using ln(Z) vs ln (sinh ($\alpha\sigma$)) at (a) 0.2 strain and (b) 0.4 strain.

Consider y-intercept of linear fit as ln(A) value [184] [185] from above Fig. 4.12, constitutive equations are established as per strain, temperature and flow stress by replacing the materials constants (α, n, A) and Q values in Equation (2.16)

$$\dot{\varepsilon} = 1.78 * 10^{28} * [\sinh(0.04 * \sigma_{0.2})]^{7.06} \exp\left(\frac{360\ x\ 10^3}{RT}\right)$$ ---------- (4.3a)

$$\dot{\varepsilon} = 2.93 * 10^{26} * [\sinh(0.03 * \sigma_{0.4})]^{6.52} \exp\left(\frac{335\ x\ 10^3}{RT}\right)$$ ---------- (4.3b)

Equation (4.3) work only at 0.2 strain and 0.4 strain.

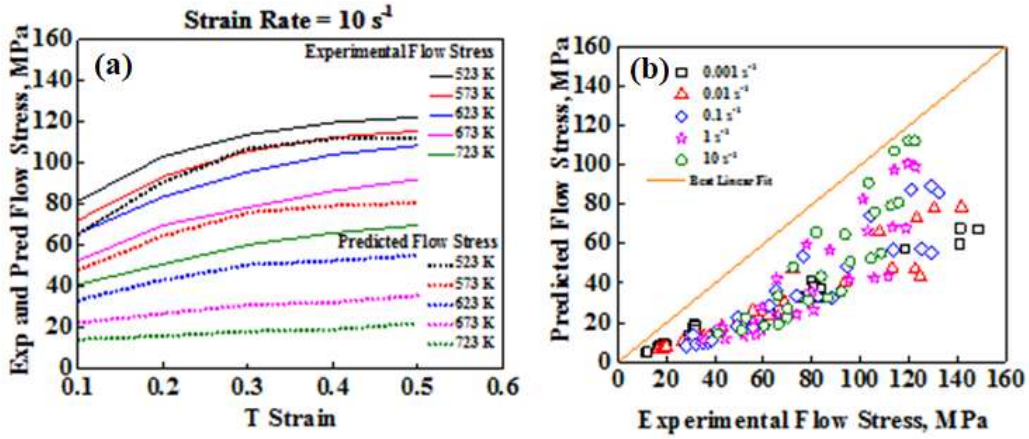

Fig. 4.13: Comparison of true stress - strain (a) Experimental flow stress and Predicted flow stress modified constitutive equation by Temperature-Strain rate compensated and (b) Consolidated comparison.

The developed constitutive equation was evaluated by comparing predicted values with experimental findings using materials constant values across different strain rates and temperature regimes (Fig. 4.13). This comparison ratifies fairly for the strain rate $10s^{-1}$ but depicts distinctive errors for the other strain rates, as observed in Fig. 4.13a and 4.13b respectively. Consequently, modifications are required in the form of strain-compensation and strain rate-compensation to improve the predictability of constitutive equations.

4.1.3.5.2 Strain-compensation to calculate predicted flow stress

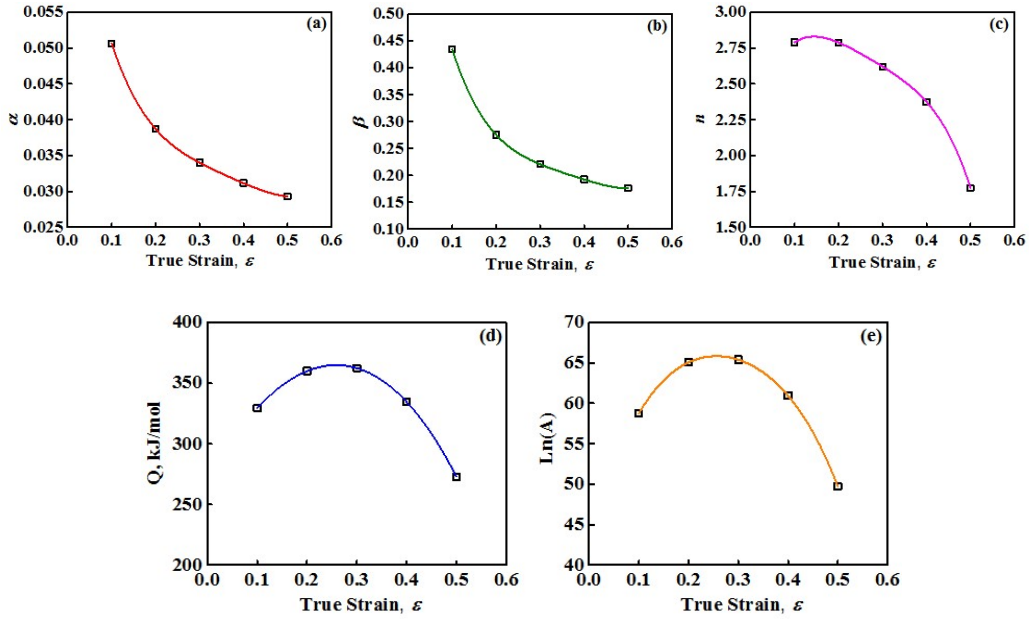

Fig. 4.14: Variation of materials constant (a), (b), (c), (d), and (e) with strain fitted by 4^{th} degree of polynomial.

The computed values of the materials constants (*α, β, n, A*) and *Q* obtained from equations (2.17 - 2.19) varied with 0.1 to 0.5 strain as seen in Fig. 4.14. The corresponding curves pertaining to each constant were subjected to polynomial fitting as shown by Fig. 4.14 (a to e). The corresponding equations of materials constants are,

$$\alpha = 0.07 - 0.42.\varepsilon + 1.56.\varepsilon^2 - 2.78.\varepsilon^3 + 1.89.\varepsilon^4 \text{----------(4.4)}$$

$$\beta = 0.83 - 5.90.\varepsilon + 22.26.\varepsilon^2 - 39.47.\varepsilon^3 + 26.50.\varepsilon^4 \text{----------(4.5)}$$

$$n = 7.71 - 5.42.\varepsilon + 15.13.\varepsilon^2 - 20.38.\varepsilon^3 - 5.56.\varepsilon^4 \text{----------(4.6)}$$

$$Q = 272.14 + 705.01.\varepsilon - 1333.93.\varepsilon^2 + 102.13.\varepsilon^3 - 499.64.\varepsilon^4 \text{----------(4.7)}$$

$$lnA = 42.07 + 241.32.\varepsilon - 886.11.\varepsilon^2 + 1536.83.\varepsilon^3 - 1337.69.\varepsilon^4 \text{----------(4.8)}$$

Thereafter, materials constants (*α, β, n, A*) and *Q* are recalculated based on polynomial regression analysis by substituting 0.1 to 0.5 strain values in Equations (4.4 – 4.8) for strain-compensation. Consequently, their values were replaced in Equation (2.16) establishing new constitutive equation at various strain rates from Equation (2.16) and then flow stress from Equation (2.2) was evaluated with recalculated materials constants. The coefficients of materials constants and strain fitted by 4^{th} order polynomials are presented in Table 4.1.

Table 4.1: 4^{th} order polynomials coefficients for the fitted materials constants and strain curves

α		***β***		***n***		***Q kJ/mol***		***lnA***	
A_0	0.07	B_0	0.83	C_0	7.71	D_0	272.14	E_0	42.07
A_1	-0.42	B_1	-5.90	C_1	-5.42	D_1	705.01	E_1	241.32
A_2	1.56	B_2	22.26	C_2	15.13	D_2	-1333.93	E_2	-886.11
A_3	-2.78	B_3	-39.47	C_3	-20.38	D_3	102.13	E_3	1536.83
A_4	1.89	B_4	26.50	C_4	-5.56	D_4	-499.64	E_4	-1337.69

The strain-compensation α-values are narrow-ranging from 0.05 to 0.003, while stress-exponent, n-values are wide-ranging from 7.30 to 5.89 relating to 0.1 to 0.5 strain. These values decrease with increase in strain. Apparent activation energy, Q-values are varying from 272 kJ/mol to 362 kJ/mol at 0.1 to 0.5 strain. The ln(A)-values are fluctuating from 65.05 to 60.94 at 0.1 to 0.5 strain. These strain-compensation values of α, n, Q, $ln(A)$ at 0.2 strain is 0.04, 7.07, 360, 65.05 and at 0.4 strain are 0.03, 6.52, 345, 60.94 respectively.

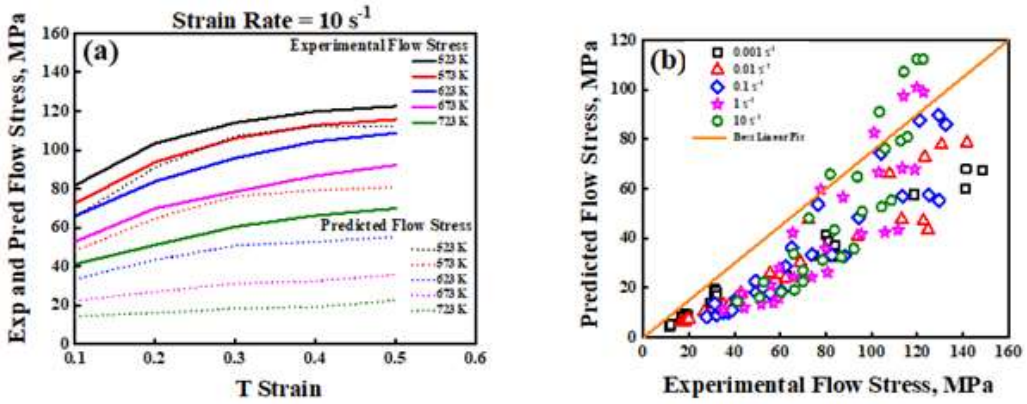

Fig. 4.15: Comparison of true stress-strain curves (a) Experimental flow stress and Predicted flow stress modified constitutive equation by strain-compensated and (b) consolidated comparison.

In Fig. 4.15, the strain-compensated modified predicted data is compared to experimental findings, showing qualitative agreement with a few deviations under specific conditions. At lower strain rate significant deviations are observed in the stress values across different temperatures. These differences arise due to the material constants (n' and β values) in Equations (2.17) and (2.18). Such tiny deviations ultimately influence the values calculated by the Equations (4.4 – 4.8) decreasing the accuracy of the constitutive equations [230].

4.1.3.5.3 Strain rate-compensation to calculate predicted flow stress

The accuracy of constitutive equations achieved by strain rate-compensation to modify the Z. This modification was done by changing the exponent of strain rate in Z equation [184] [185]. An exponent of 0.85 was noticed to be best for the strain rate-compensation for this alloy. The modified Z parameter ($\grave{Z}$) obtained on multiplying Eq. (2.12) with $\dot{\varepsilon}^{-0.15}$ is given as,

$$\grave{Z} = \dot{\varepsilon}^{0.85}.\exp(Q/RT) \quad \text{---------- (20)}$$

The correlation between Z and $\dot{Z}$ may be stated as:

$$ln(\dot{Z}) = ln\,(Z) - 0.15\,ln(\dot{\varepsilon})\text{----------} \quad (21)$$

Therefore, the flow stress, σ needs to be modified using constitutive equations (2.22) as:

$$\sigma = \frac{1}{\alpha}.ln\left\{\left(\frac{\acute{Z}}{A}\right)^{\frac{1}{n}} + \left[\left(\frac{\acute{Z}}{A}\right)^{\frac{2}{n}} + 1\right]^{\frac{1}{2}}\right\}\text{----------} \quad (22)$$

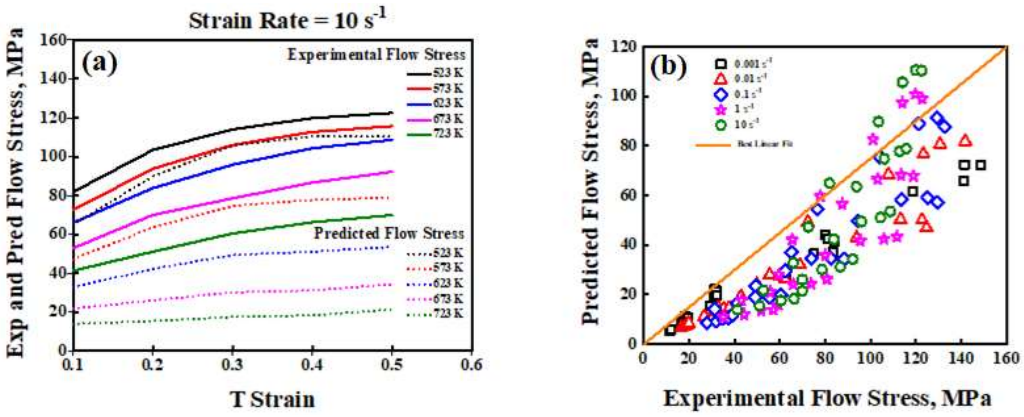

Fig. 4.16: Comparison of true stress - strain curves (a) – Experimental flow stress and Predicted flow stress using modified Zener-Holloman parameter, Z by 0.85 strain rate compensated and (b) Consolidated comparison.

Fig. 4.16 symbolizes strain rate-compensated modified predicted data and experimental findings shows considerable agreement observed with few deviations to verify the modified constitutive equations. At lower strain rate demonstrates sizeable deviations in the flow stress observed at many temperatures.

4.1.3.6 Verification of the constitutive equations' accuracy

The reliability of the constitutive equation on the experimental data was quantified by employing the basic statistical entities stated as the average absolute relative error (AARE) as discussed in chapter 2 section 2.5.2,

$$AARE = \frac{1}{N}\sum_{i=1}^{N}\left|\frac{E_i - P_i}{E_i}\right| \text{----------\{taken from (2.26)\}}$$

and the correlation coefficient (R),

$$R = \frac{\sum_{i=1}^{N}(E_i-\bar{E}).(P_i-\bar{P})}{\sqrt{\sum_{i=1}^{N}(E_i-\bar{E})^2.\sum_{i=1}^{N}(P_i-\bar{P})^2}}$$ ----------{taken from (2.27)}

where E and P are experimental and predicted flow stress, σ values respectively; $\overline{E}$ and $\overline{P}$ = average E and P values, respectively, N = number of selected quantities.

At 0.4 strain showed 15.16% peak value of AARE at 723K and $1s^{-1}$ strain rates and the corresponding R is 0.89. The cumulative values of AARE at 0.2 strain and 0.4 strain is 10.18% and 10.56% respectively indicate substantial fitting of the constitutive equation established with the experimental data. The correlation coefficient (R) is 0.95 applying least square fitting line with various data, showing a linear relationship between values of experimental and predicted -flow stress, despite its fluctuation.

4.2 Effect of Strain Path on Anisotropic Behaviour of Hot Rolled Mg-0.5wt% Ce alloy

The processing maps for the Test material provides insight into the potential for producing various wrought products, including plates and sheets as detailed in section 4.1. Based on the power efficiency obtained from the processing maps, the hot rolling parameters for the extruded rod of Test material, was carried out using through two routes: UDR and MSCR. Subsequently, the hot-rolled sheet specimens underwent various characterization, including X-ray Diffraction, Hardness testing, Microstructural analysis, Tensile testing, Fractography, etc. The results of these studies are elaborated in the following sections.

4.2.1 X-Ray diffraction (XRD)

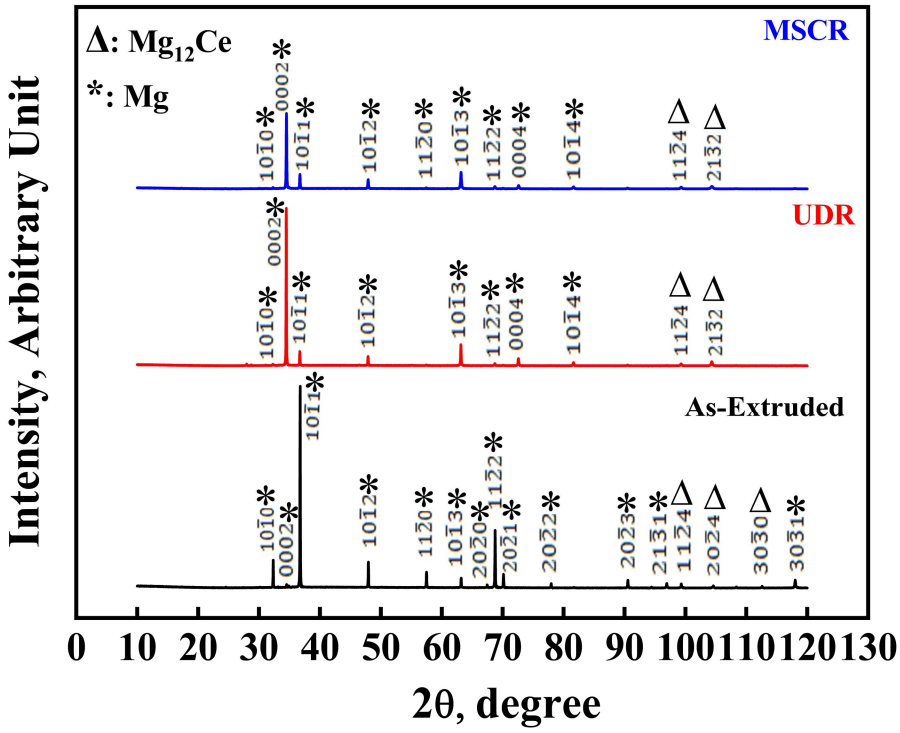

Fig. 4.17: XRD of As-Extruded rod, UDR and MSCR sheet specimens

The XRD patterns of extruded, UDR and MSCR samples of Mg-0.5wt.%Ce alloy is illustrated in Fig. 4.17. The XRD pattern reveals the presence of $Mg_{12}Ce$ as a minor phase along with Mg as the major phase. $Mg_{12}Ce$ phase has body centred tetragonal lattice of t126 crystal structure bearing lattice parameters a=10.33 Å and c=5.96 Å and density of 2.25 (g/cm^3) [157]. Significant changes in the intensity of

{0002} peak could be observed for samples processed under different conditions. The lowest intensity is observed for the extruded sample and increases in MSCR condition, and the intensity becomes maximum for the UDR samples.

XRD pattern of extruded, UDR and MSCR samples unveil slight deviation from the XRD pattern of pure Mg with reference from Powder Diffraction File (PDF) database. (PDF No. 65-3365) [231]. Ce has a minimal solubility in Mg. Therefore, apart from the peak shift arising from the solid solution, a significant contribution could be arising from the residual stresses due to the processing.

4.2.2 Microstructural Analysis

The hot rolled sheets of UDR and MSCR were characterized by SEM in SE mode for topographical images and Energy Dispersive Spectroscopy mode for elemental mapping. In addition, dedicated SEM – EBSD (Electron Backscattered Diffraction) mode was also utilized for both qualitative and quantitative analysis of the experimental alloy specimens.

4.2.2.1 SEM and SEM-EDS analysis

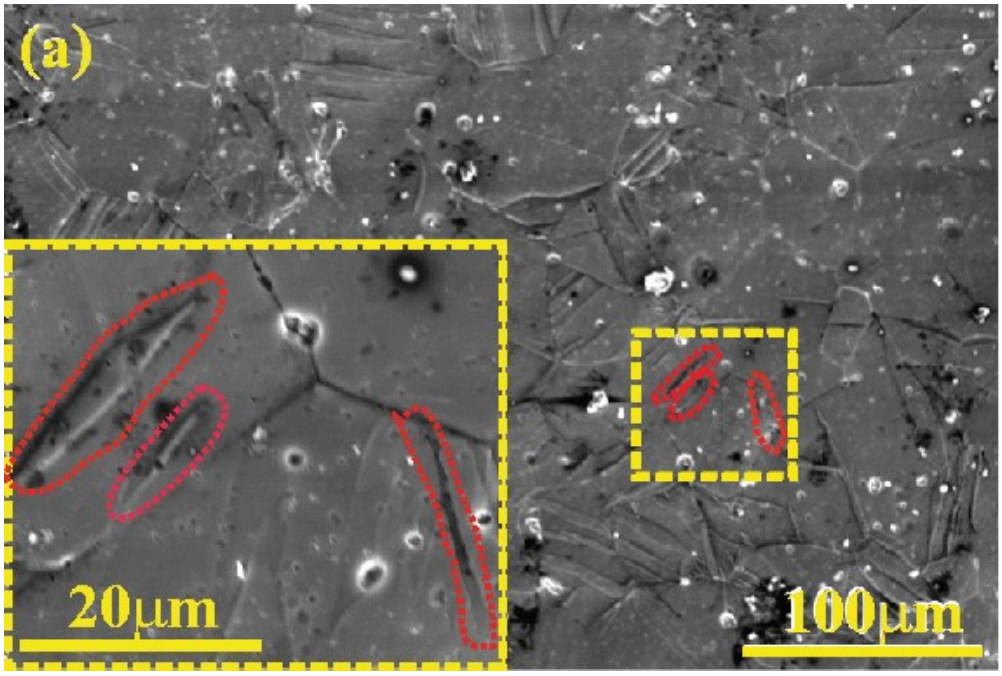

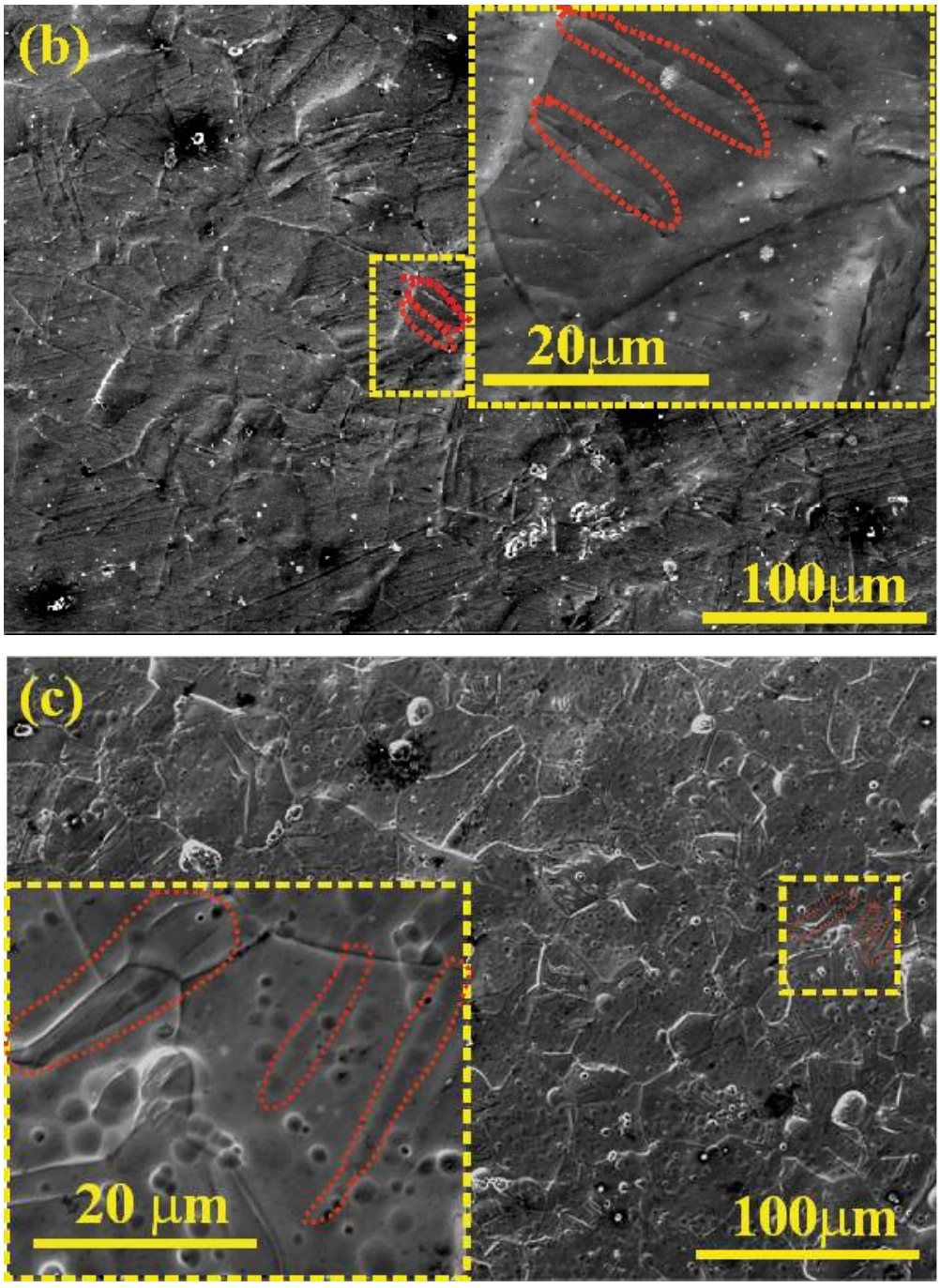

Fig. 4.18: FESEM images at 1000X and 5000X of (a) As-Extruded rod, (b) UDR and (c) MSCR sheet specimens after 20th pass.

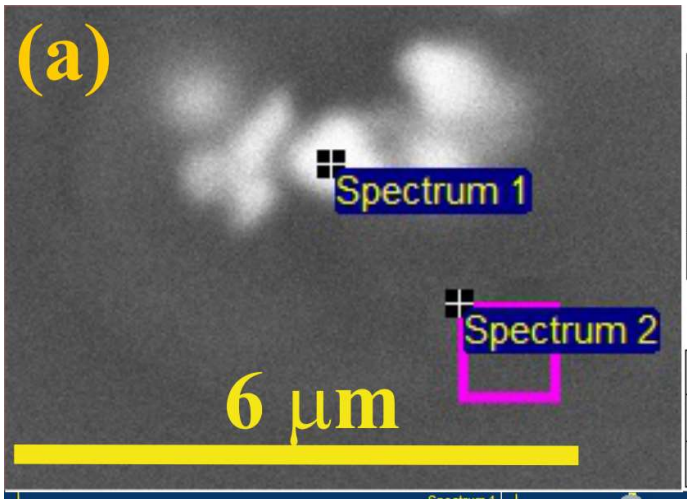

Spectrum 1:

Element	Weight%	Atomic%
O K	8.38	15.58
Mg K	64.26	78.61
Ce L	27.36	5.81
Totals	100.00	100.00

Spectrum 2:

Element	Weight%	Atomic%
Mg K	100.00	100.00
Totals	100.00	

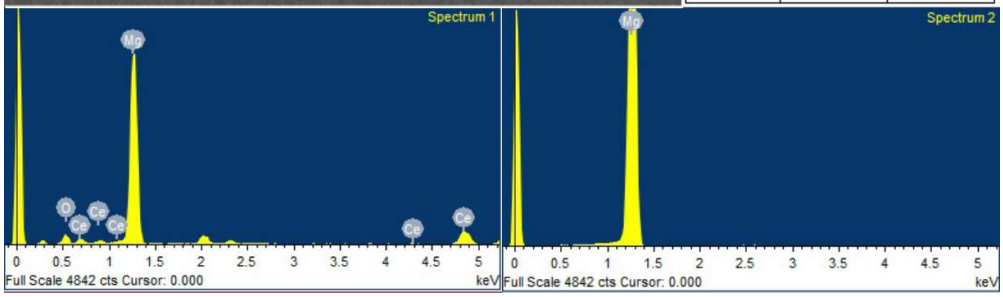

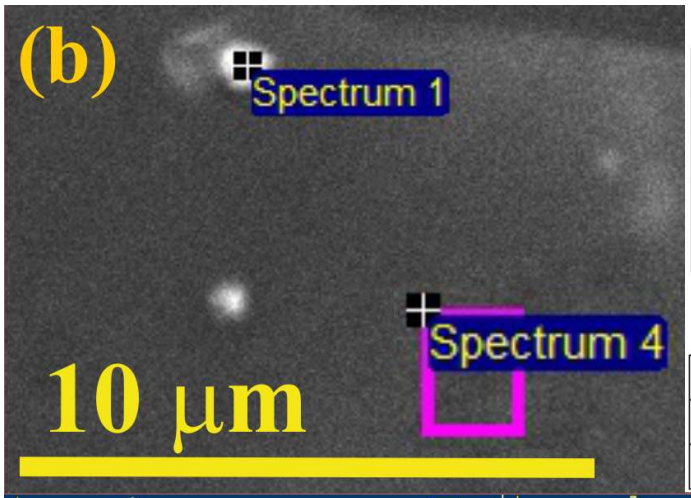

Spectrum No.1

Element	Weight%	Atomic%
O K	11.94	20.01
Mg K	69.30	76.41
Ce L	18.75	3.59
Totals	100.00	

Spectrum No. 4

Element	Weight%	Atomic%
Mg K	100.00	100.00
Totals	100.00	

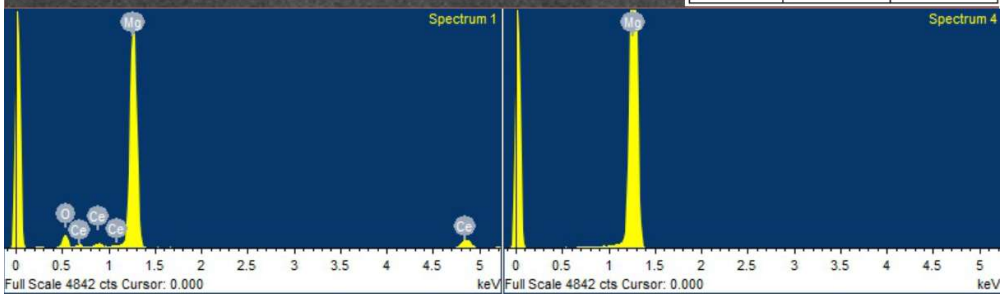

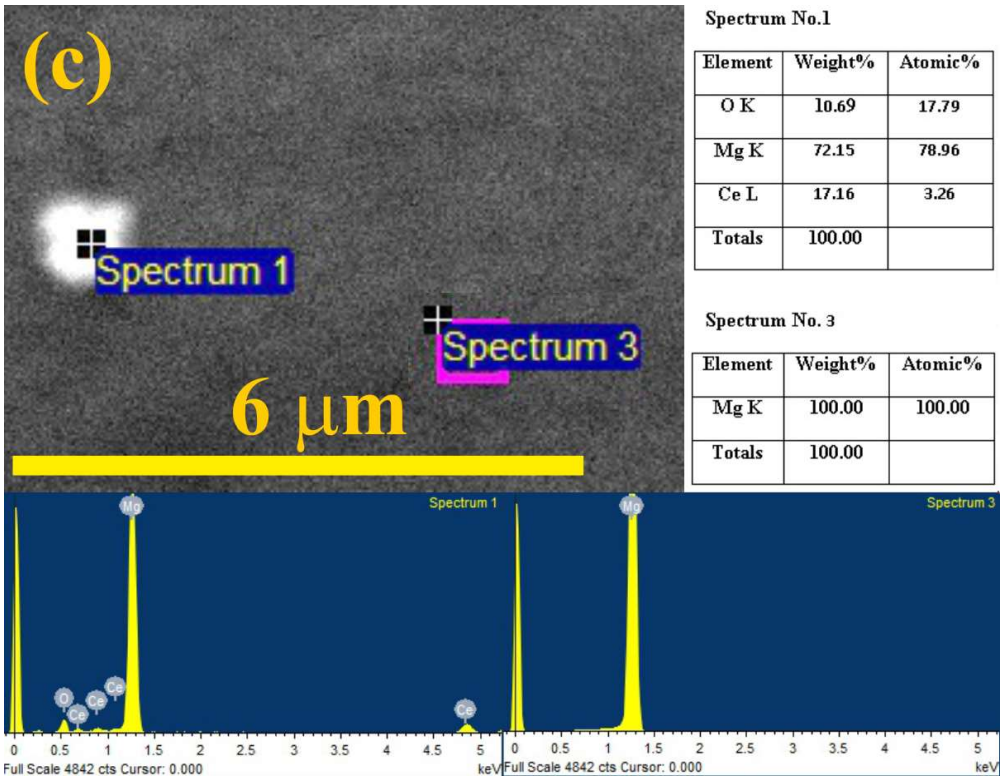

Fig. 4.19: SEM-EDS elemental mapping of (a) extruded rod, (b) UDR and (c) MSCR sheet specimens.

The FESEM microstructure of the Test material samples in different conditions of extruded, UDR and MSCR is illustrated in Fig. 4.18. The FESEM microstructure of extruded and hot-rolled UDR and MSCR shows mixed distribution of deformed grains mostly twinned grains; along with some original grains, smaller grains, along with sub-grain formation and limited amounts of $Mg_{12}Ce$ precipitates ($Mg_{12}Ce$ as per Mg – Ce phase diagram shown in Fig. 2.26) randomly distributed in its matrix phase. As shown in Fig. 4.19(a), the elemental mapping of spectrum 1 in SEM EDX images gives the ratio value of $\frac{MgK}{CeL} \approx 28.18$, which is exactly the matches with the maximum composition limit of $Mg_{12}Ce$ precipitates at 590ºC. The microstructure of as-extruded materials shows well defined recovered grains in the order of 25-50 μm and some twins within the grains as shown in Fig. 4.18(a). The extruded sample microstructure reveals coarser size of the precipitates scattered in a highly disproportionate manner. Many particles are located within the grain, but very few of the precipitates are also seen at grain boundaries.

Precipitates appeared within the grains and at the grain boundaries are of different size ranging from 4 μm to 9 μm with a volume percentage of 1.5% for as-

extruded sample, while UDR sample has narrow range of 4.5 μm to 5.6 μm with a volume percentage of 1.6% and 3.4 μm to 8.2 μm with a volume percentage of 1% for MSCR sample.

The microstructure of UDR referred in Fig. 4.18(b) shows more homogeneous distributions of 35-55 μm grains. $Mg_{12}Ce$ precipitate particles are coarser and are ineffective in pinning the grain boundaries. The precipitate sizes in UDR are in close range compared to MSCR sample.

In Fig. 4.18(c), the microstructure of MSCR indicates relative grain growth having grain sizes 40-90 μm. Since there is no evidence for the formation of dynamically recrystallized nuclei near the grain boundaries or flow localized areas, the grain growth has occurred possibly following dynamic recovery. The precipitate particles in MSCR are relatively finer than extruded and located within grains but a few of them could be noticed along the grain boundaries.

4.2.2.2 EBSD Analysis:

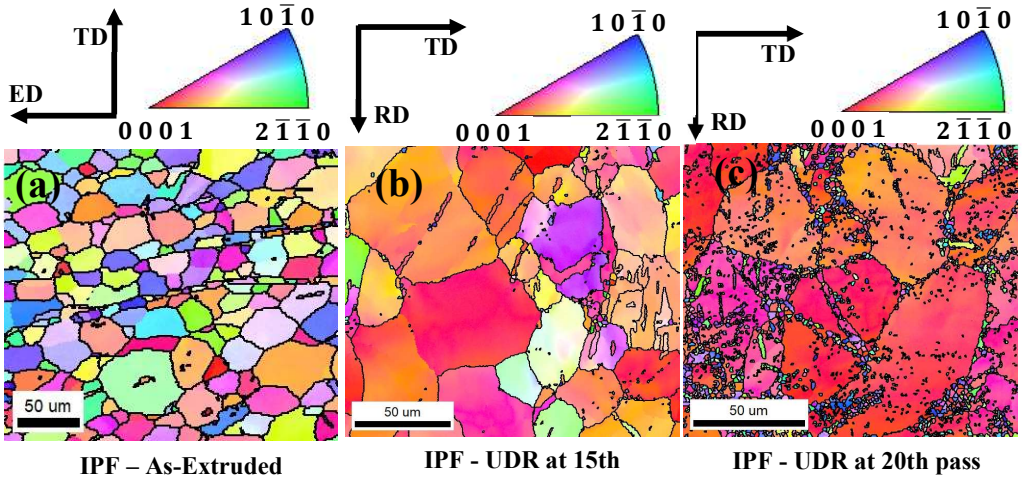

Fig. 4.20 EBSD – Inverse Pole Figure maps for (a) As Extruded, (b) UDR at 15th pass and (c) UDR at 20th pass.

With increasing the deformation strain, the microstructures of the starting materials (i.e., As-Extruded) develops progressive changes. The microstructures are characterized with the presence of twinning and in some grains multiple variants of twins are noticed. Apart from twins, the microstructure also reveals non-indexed areas because of macro shear bands, where the deformation is localized, possibly due to the less availability of slip systems. Such localized deformation may also give rise to

residual elastic stresses in the sample. The elongated extruded grains, mostly having non-basal orientation rotates along basal planes but not strongly. The grain sizes in UDR 20th pass are very similar to the as-extruded microstructure. The microstructure of UDR 15 in Fig. 4.20(b) shows comparatively coarse grains (45-75 µm) than UDR 20 (35-55 µm), due to smaller deformation strain and are strongly oriented towards basal planes. During these 20 passes of UDR, Test material subjected to very strain of 2.0, assuming reasonably that the precipitates $Mg_{12}Ce$ phase will be severely fragmented. As a result, the sizes of these particles fall in the narrow range of 4.5 to 5.5 μm than compared to the As-Extruded in order 4.0 μm to 9.0 μm. Moreover, the number fraction of these precipitates increases marginally over the As-Extruded microstructure indicating of more likelihood of particle pinning the grains and thereby retarding their coarsening.

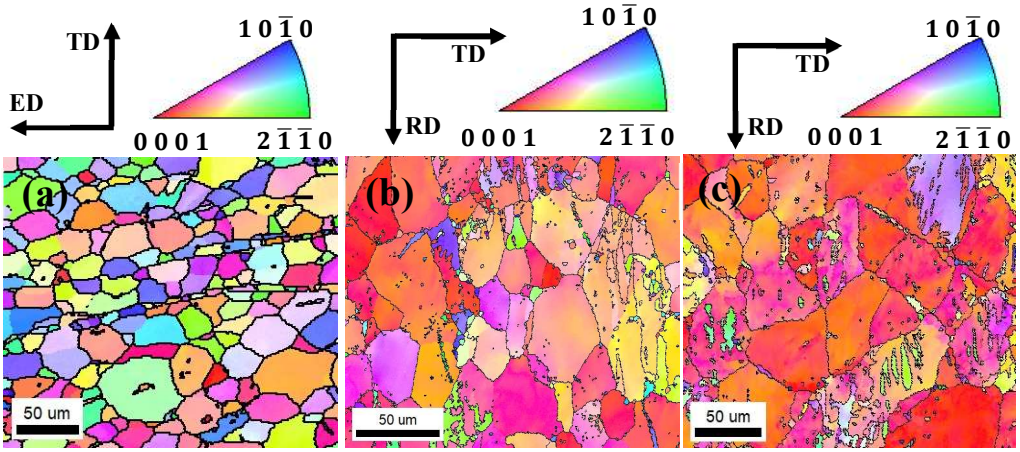

Fig. 4.21 EBSD – Inverse Pole Figure maps for (a) As Extruded, (b) MSCR at 15th pass and (c) MSCR at 20th pass.

The EBSD generated microstructures in terms of inverse pole figures (IPF) maps are depicted in Fig. 4.21 for As-Extruded sample along with MSCR after 15th pass and at 20th pass. The microstructures were examined on RD-TD planes of the sheets.. The grains (40-90 µm) of MSCR 20th pass microstructures are coarser than the MSCR 15th pass (25-45 µm) and As-Extruded (25-50 µm) indicating the possible grain growth during high temperature rolling. The microstructures of both MSCR shows weak basal orientation as subjected to changes in rolling plane after each pass compared to the as-extruded. The size of the second phase precipitates $Mg_{12}Ce$ phase sizes are remains nearly similar to that of as-extruded condition, but their number fraction decreased to a greater extent in MSCR 20th pass microstructure. These $Mg_{12}Ce$ precipitates are likely to align themselves with shear band planes with basal orientation becomes

unaccountable. Consequently, the assumed pinning effect of the precipitates lowers down leading to coarsening of grains in the MSCR 20th pass.

Majority of the grains aligned them along shear band in the basal orientation. However, at 20th pass in both UDR and MSCR are exhibiting basal plane orientation for most of the grains with small amount tilt roughly 10º -15º away from ND of the rolled sheet in the rolling direction, indicating of basal texture weakening in the final sheet sample. Both the type of rolling UDR and MSCR exhibited substantial spread of basal poles in the TD from completely non-basal orientations of the grains in the As-Extruded rod sample. Additionally, microstructures of UDR and MSCR also shown the entire network of shear bands distributed uniformly over the RD-ND plane. These shear bands are wavy extending for a large distance in the microstructure accommodating the strain accumulation during rolling.[[20]]

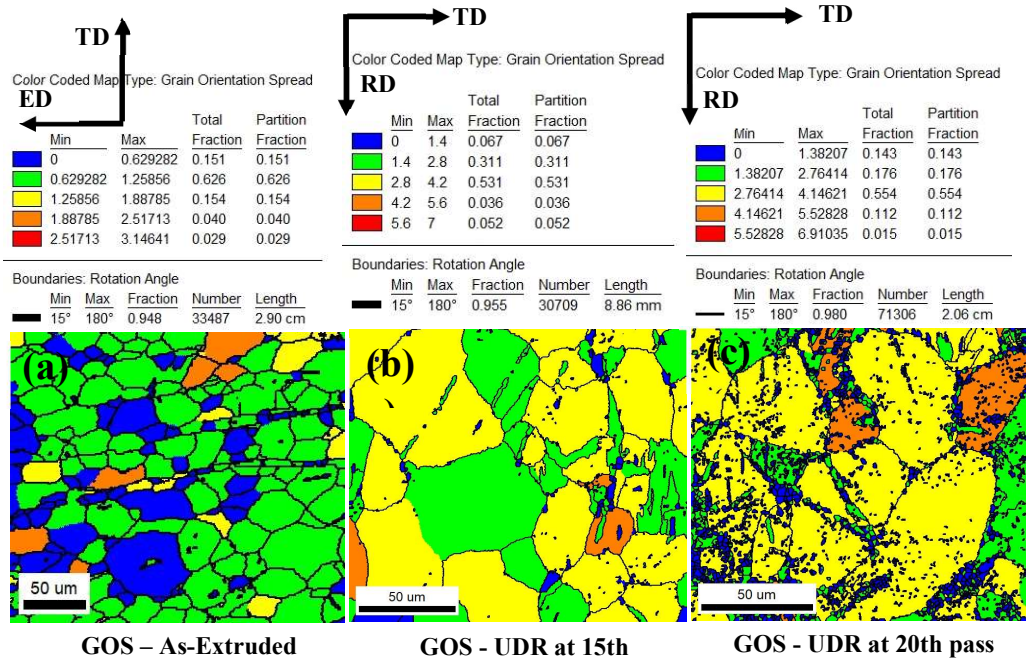

Fig. 4.22 EBSD – Grain orientation spread maps for (a) As Extruded, (b) UDR at 15th pass and (c) UDR at 20th pass.

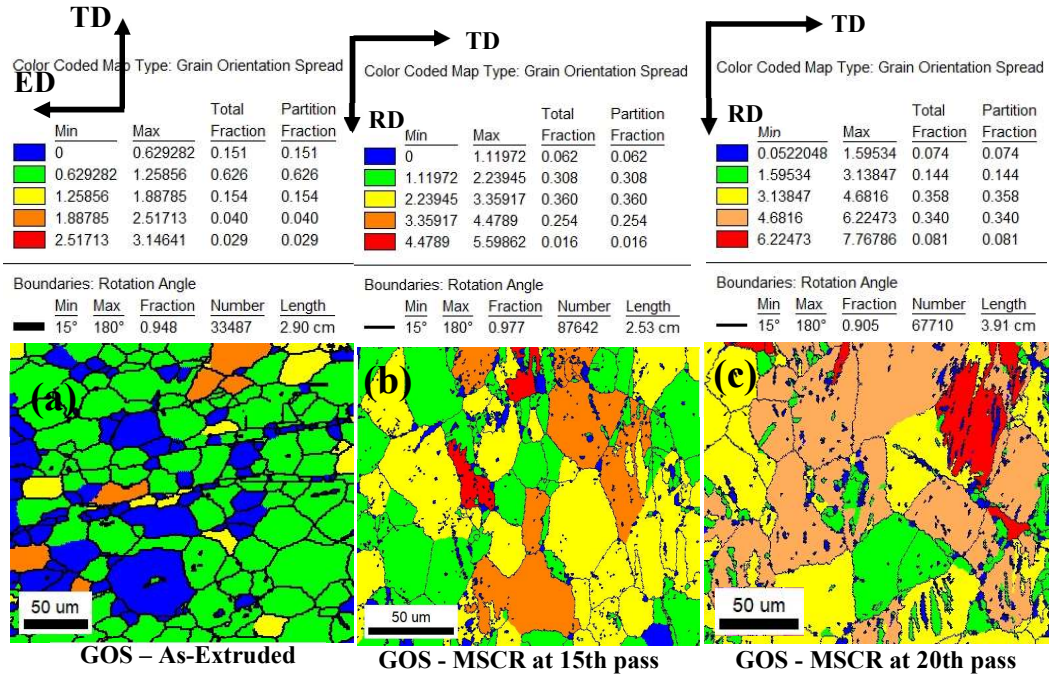

Fig. 4.23 EBSD – Grain orientation spread maps for (a) As Extruded, (b) MSCR at 15th pass and (c) MSCR at 20th pass.

The EBSD generated grain orientation spread (GOS) maps of as-extruded, UDR and MSCR deformation conditions are reported in Fig. 4.22 and Fig. 4.23 respectively. GOS relates to the deviation in the grain orientation to average grain orientation. A higher value of GOS indicates a deformed microstructure, while a lower value indicates recrystallized or extensively recovered microstructure.

The intra-grain misorientation generation in UDR 20th pass is observed to be more than MSCR 20th pass. This could be attributed to the fact that the changes in the strain path during MSCR activated multiple slip systems and therefore, the chance of dynamic recovery is high due to the possibility of cross-slip, whereas in UDR since the strain path is kept constant, the same set of slip systems could be activated for a larger deformation strain leading to higher orientation gradient.

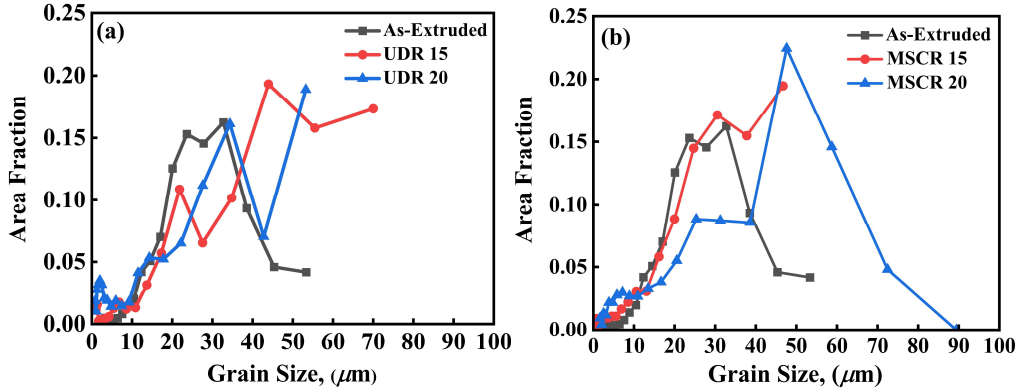

Fig. 4.24 EBSD microstructures statistics as Grain Size Distribution of As-Extruded compared with (a) UDR 15 and UDR 20 and (b) MSCR 15 and MSCR 20

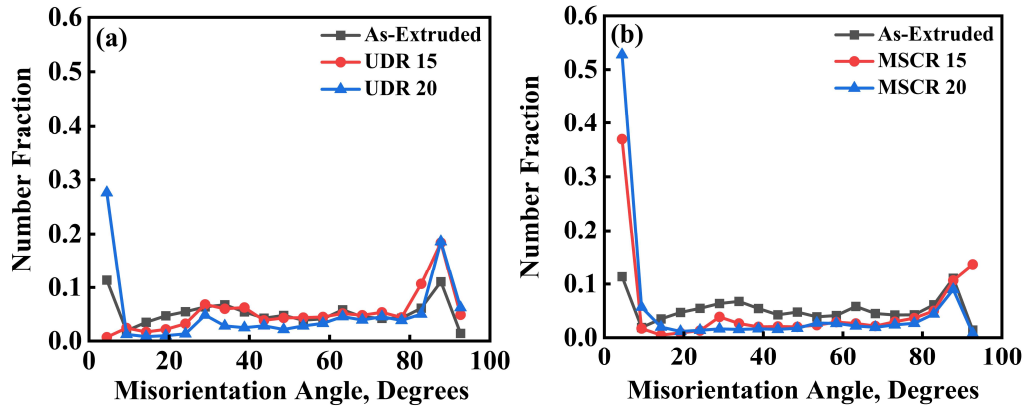

Fig. 4.25 EBSD microstructures statistics on Misorientation Angle of As-Extruded compared with (a) UDR 15 and UDR 20 and (b) MSCR 15 and MSCR 20

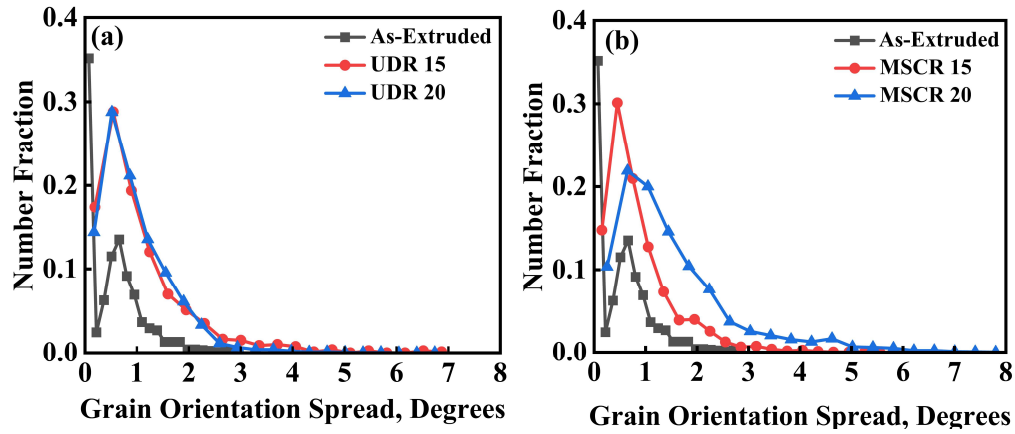

Fig. 4.26 EBSD microstructures statistics on Grain Orientation Spread of As-Extruded compared with (a) UDR 15 and UDR 20 and (b) MSCR 15 and MSCR 20

Grain size distribution in Fig. 4.24 displays the grain size distribution in the range of 40-60 μm for the hot rolled Test material. In Fig. 4.24 (a), UDR 20 is observed to exhibit a larger variation in grain sizes compared to other conditions, whereas As-

extruded appears to have well defined average grains in size of 30 μm, but with grains getting coarsen upto 55 μm. UDR 15 and MSCR 20 shows more pronounced coarsening of the grains compared to all other as shown in the Fig. 4.24.

The grain boundary misorientation angles distributions of hot rolled samples are exhibited in Fig. 4.25. As-extruded samples shows small proportion low angle grain boundaries (LAGBs). UDR 15, UDR 20 and MSCR develops equal amount of LAGBs, indicating a possible similarity in the grain splitting mechanism. MSCR 20 develops the largest proportions of LAGBs. High angle grain boundary (HAGBs) fraction for all the rolled and extruded samples is varying between 0.05 to 0.1.

4.2.3 Texture evolution: Local Texture

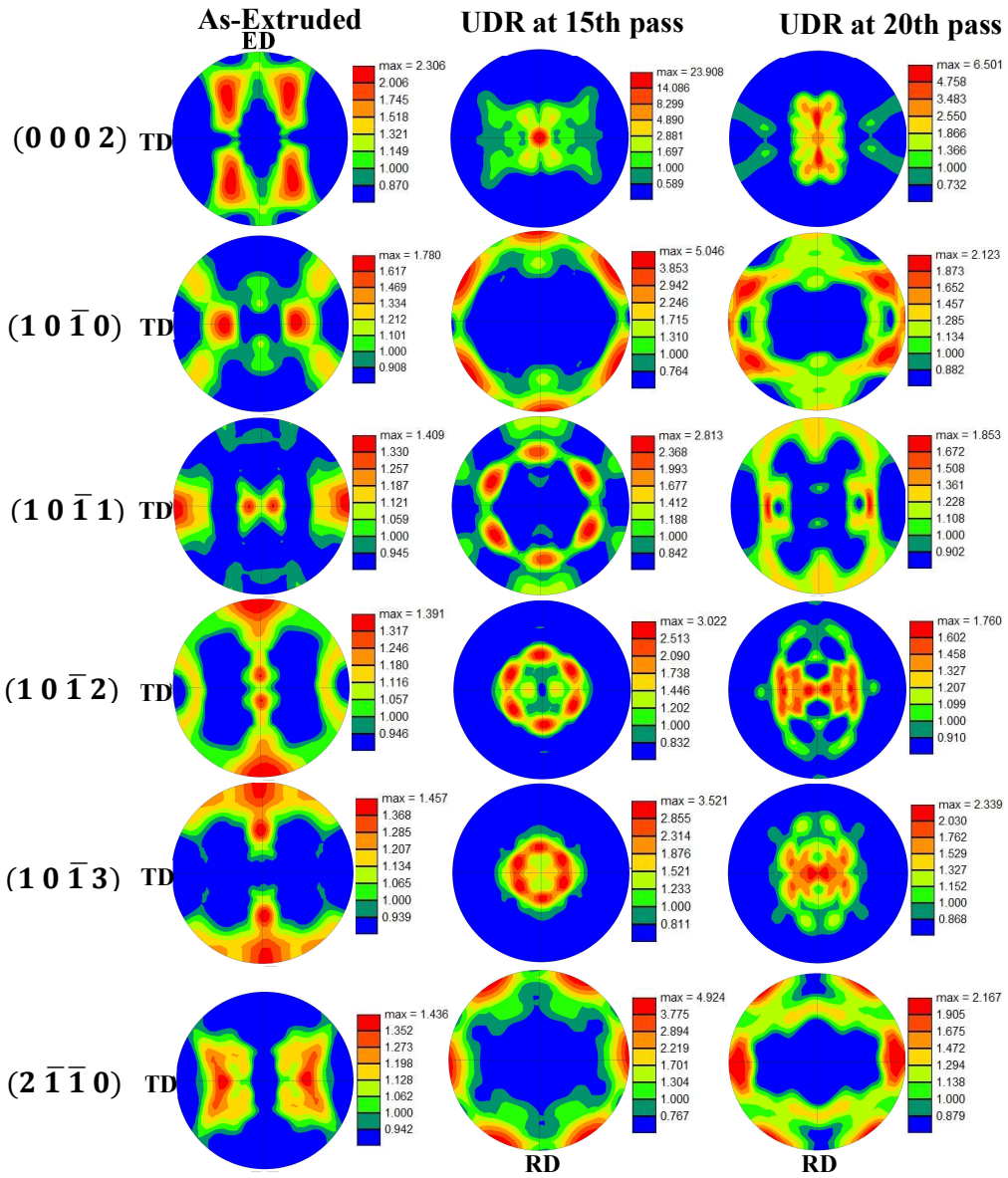

Fig. 4.27 Comparison of EBSD - Pole figures at different planes for As-Extruded with hot rolled sheet specimens of UDR at 15th pass and UDR at 20th pass.

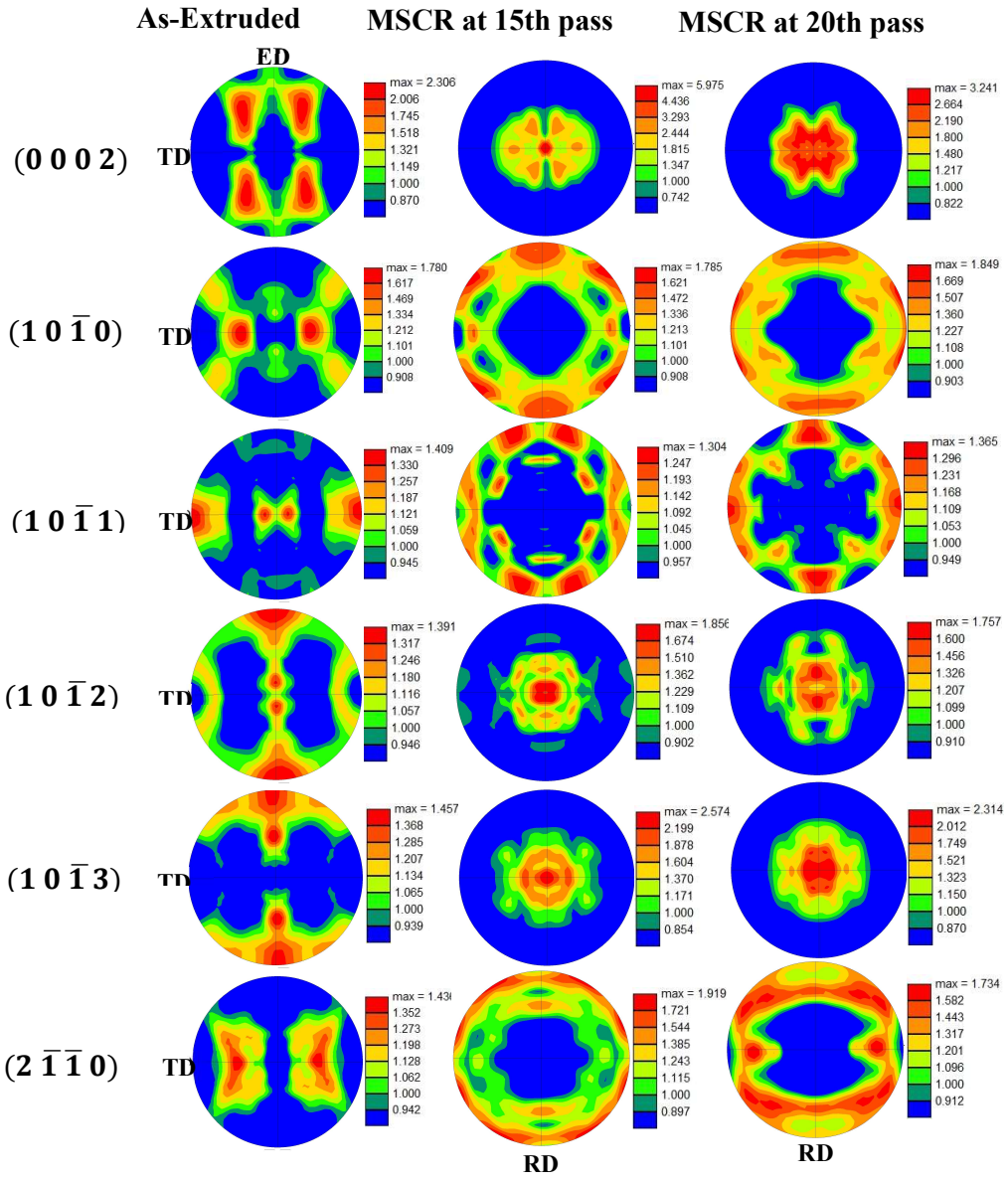

Fig. 4.28 Comparison of EBSD - Pole figures at different planes for As-Extruded with hot rolled sheet specimens of MSCR at 15th pass and MSCR at 20th pass.

The micro texture obtained from EBSD scan are plotted in Fig. 4.27 in terms of for the basal plane (0002), $(10\bar{1}0)$ and $(2\bar{1}\bar{1}0)$ pole figures of as-extruded compared with hot rolled sheets after UDR 15th Pass and UDR 20th Pass. The (0002) pole figures of as-extruded sample show deviation of poles from the ND to the ED resulting from the extrusion process. Thus, the basal plane are inclined to the extrusion axis makes the

large numbers of grains in a more suitable orientation as reported by Raja K Mishra et.al. [22] The multiples of random distribution for the shifted basal pole are roughly 7.8, indicating a favourable orientation for the ease of deformation. The (0002) basal pole figure indicates a split of basal poles towards ED and the deviation is nearly 15-20^{o} in both modes of rolling, similar to the rolled magnesium as reported by Huang et.al. [232].

Primarily, the basal pole splitting is more prominent in UDR than in MSCR. The maximum value of m.r.d. observed for UDR 20 sample is ~ 6.5, while for the MSCR 20 sample the corresponding value is ~3.2, revealing a much weaker texture generation for the MSCR process. The significant difference in the intensity of the (0002) basal texture between the two types of rolling processes is attributed to the changes in the activated slip systems associated with the strain path changes. In UDR process, as the rolling reduction continuously increases, then the strength of the basal poles reduces by a factor of 4. In Fig. 4.27, UDR 15 and UDR 20, the basal poles are tilted to a same degree towards TD and have a maximum m. r. d. 23.9 and 6.5 respectively. On other hand, for the MSCR sample, while the observed texture weakening is maximum, the strength of basal poles reduces by a factor of 2. Fig. 4.28 shows movement of (0002) away from ND towards TD in progressive manner as denoted by maxima of m.r.d. 5.9 for MSCR 15 and 3.2 for MSCR 20.

The $(10\bar{1}0)$ pole figure indicate an axial symmetry of the texture component through the presence of high intensity rings along the perimeter of the stereogram. This represents the development of a fiber texture. Along the fiber textures, certain orientations appear in high intensity. The $(10\bar{1}0)$ pole figures display high intensity orientation for UDR 15 with a maximum value of m.r.d. ~5.0, while UDR 20 shows ~ 2.1. However, in Fig. 4.28, MSCR 15 and MSCR 20 showed similar maximum m.r.d. ~ 1.8, indicating that the MSCR leads to a saturation in texture development.

The $(2\bar{1}\bar{1}0)$ pole figures for as-extruded sample are characterized by a presence of weak basal texture, spreading along TD-RD plane. In the UDR process a maximum m.r.d. value of 4.9 is observed for the UDR 15 sample, and this value decreases to 2.1 for the UDR 20 sample. The corresponding values for MSCR 15 and MSCR 20 samples are 1.9 and 1.7 respectively. The observed differences in the generation of rolling textures due to the changes in the strain path from UDR to MSCR is similar to the results reported by [233].

4.2.2 Hardness Test of As-Extruded, UDR and MSCR

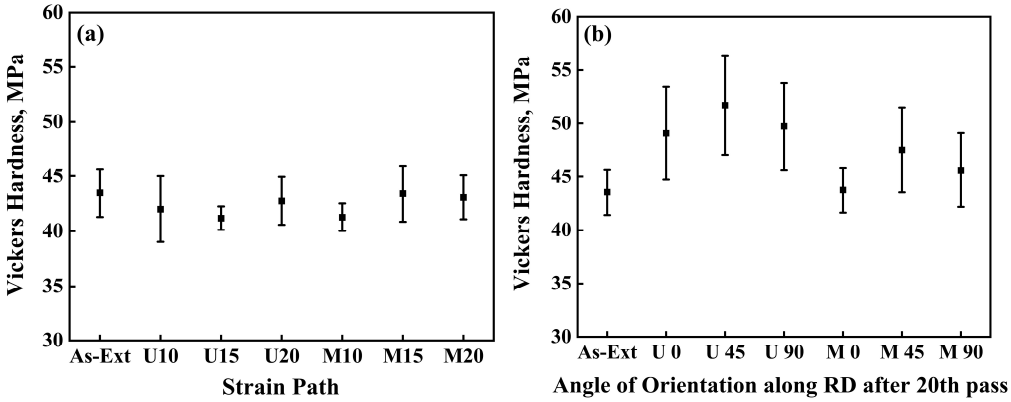

Fig. 4.29: Variation of Vickers Hardness values with As-Extruded rod, and (a) based on change in strain path of UDR and MSCR sheet specimens and (b) based on angle of orientation along RD of UDR and MSCR sheet specimens.

Fig. 4.29 shows graphical representation and the micro-hardness values of the extruded material and hot rolled UDR and MSCR sheet samples obtained from Vickers hardness tester respectively. The Vickers hardness value of UDR is higher with large deviation in individual values than both extruded and MSCR samples. But the hardness value of extruded samples in comparison to MSCR varies slightly in fraction only. During UDR, the number of passes (20 passes of 0.1 strain) on the same plane (where RD, TD, and ND are constant) increases, then strain hardening occurs leading to increased hardness. For UDR samples, increasing the number of passes (20 passes of 0.1 strain each) on the same plane (0002) (where RD, TD and ND is constant) of applied compressive stresses during rolling, strain hardening of the grains take place. Conventionally rolled (UDR) samples indicate formation of (0002) basal plane (*c*-axis parallel to ND) as shown in XRD pattern Fig. 4.17 typically present with strong intensity as that of magnesium. S. Biswas et al. [234] reported that at higher temperature of 450° C, occurrence of dynamic recovery (DRV) grains in discontinuous manner attributed is to (0002) basal plane having low stacking fault energies. Consequently, the ductility of UDR samples being slowed down only to result higher hardness.

In MSCR, the plane of applied compressive stress during rolling were changed after each pass (i.e., RD becomes TD and TD becomes RD where ND is constant) and thereby planes are alternately work hardened during rolling. Low fraction of various microstructural constituents within grains and higher fraction of grain boundaries leads

to lower micro-strain. Moreover, as strain path are changed in MSCR a greater number of slip systems gets activated [233]. Consequently, the preferred basal plane gets weaken shown by its decreased intensity in SEM-EDS elemental mapping Fig. 4.19 compared to UDR. This combined effect of microstructural changes along with activation of off-basal plane causes improvement in ductility during rolling thereby decrease in hardness. Hence, MSCR has lower hardness than UDR at the end of 20 passes bearing 2.0 strain.

4.2.3 Tensile Test

4.2.3.1 True Stress-Strain curve

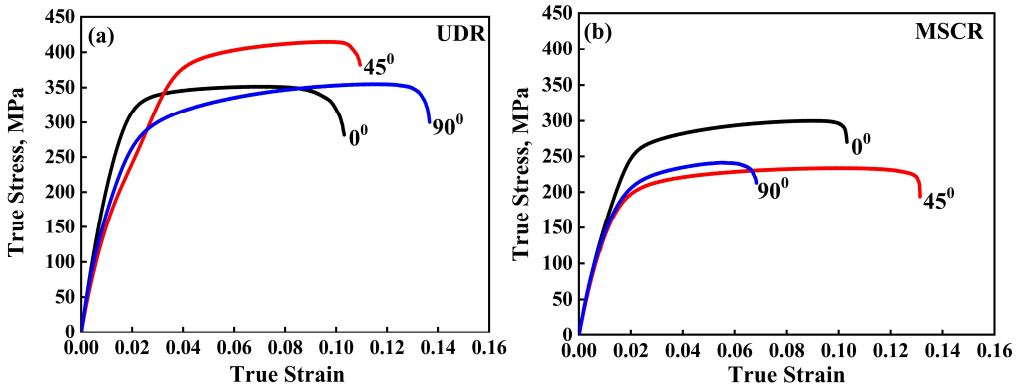

Fig. 4.30 True Stress-True Strain curves of Tension test of (a) UDR and (b) MSCR rolled sheets cut along final RD at 0º, 45º, 90º.

The true stress- strain curve as function of the sheet orientation for UDR (a) and MSCR (b) after 20th pass of rolling as shown in Fig. 4.30. In both the Fig. 4.30 (a) and Fig. 4.30 (b) shows merely two stages i.e., (i) strain hardening and later (ii) steady state behaviour in UDR and MSCR curves. UDR shows pronounced strain hardening effect as strain path remain unchanged and finally the sheet obtained with 2.0 strain with 0.1 strain per pass given upto 20 passes. During hot rolling of UDR process, the second phase precipitates $Mg_{12}Ce$ undergoes fragmentation decreasing their sizes and subsequently dispersed both within the grains and also along the grain boundaries. Such precipitates $Mg_{12}Ce$ having spheroidal morphology under pinning effect of the grains [235]. Therefore, the strain accumulation in most of grains having basal orientation will occur at each pass, but unable to compensate. Simultaneously, profuse twinning activity appears leading to formation of shear band, further causing strain concentration. The inherent heterogeneity of shear bands causes continuous increase in strain hardening effect. As the twinned regions reorient their basal poles consistently along shear

direction. Moreover, splitting basal poles occurs toward TD and non-basal planes orient themselves along RD. Such reorientation provides shear bands suitable for slip leading to plastic flow and finally into dynamic recovery.

On other hand, in MSCR process of cross-rolling allows the strain accumulation to get compensated by tensile stress and compressive stress due to continuous interchanging of rolling plane and introduces variety of twins that reorients the basal poles. Accordingly, the strain hardening effect is lower, whereas the elongation is more. As the strain path is changing alternately during MSCR causes the basal poles to reorient and get split-up toward TD. This brings in the activity of off-basal planes and decreases the internal misorientation than UDR. Compensation of the strain accumulation during MSCR relates to dynamic recovery caused by constant change in strain path [34]

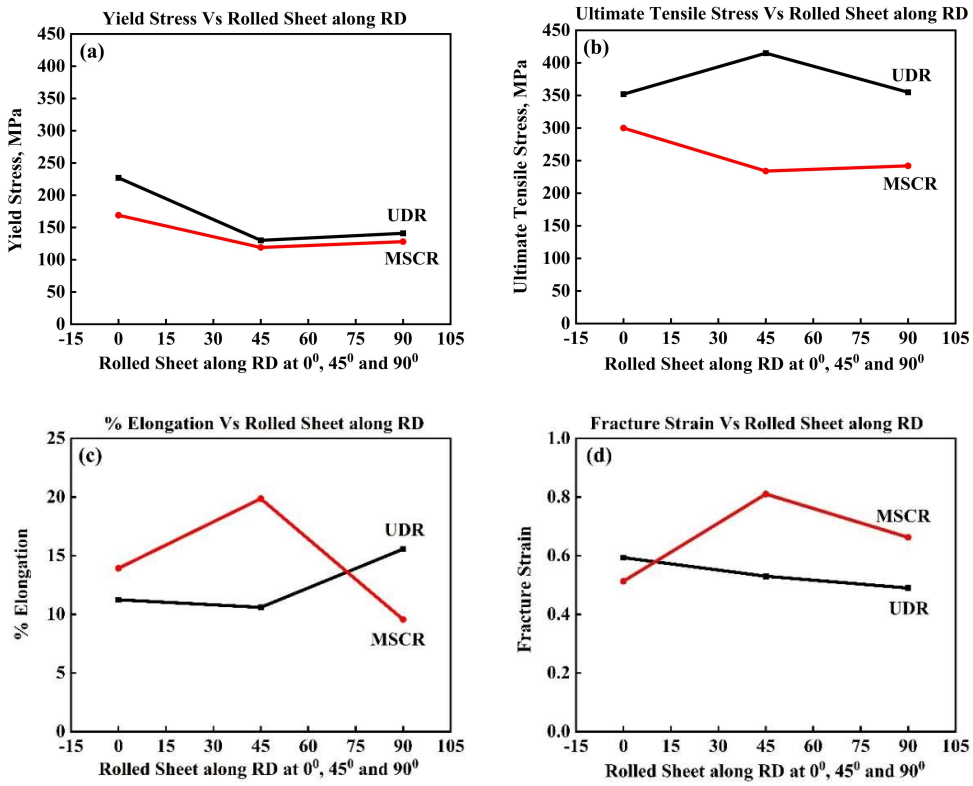

Fig. 4.31 Rolled Sheet along RD at 0º, 45º, 90º Vs (a) Yield Stress, (b) Ultimate Tensile Stress, (c) % Elongation (d) Fracture Strain

The tensile test of hot rolled sheet specimens of UDR and MSCR renders mechanical properties summarized in Table 4.2.. The yield stress (YS) in Fig. 4.31 (a) and ultimate tensile stress (UTS) values in Fig. 4.31(b) is lower for MSCR samples

compared to UDR samples. Hence, UDR exhibits more strength (YS and UTS) than compared to MSCR. However, the anisotropy in strength (YS and UTS) values is less for MSCR than compared to UDR. UDR exhibits less ductility and fracture strain than compared to MSCR, whereas the anisotropy in ductility as seen in Fig. 4.31(c) and in Fig. 4.31(d) fracture strain is less for UDR than MSCR. This anisotropic behaviour in ductility and fracture strain of UDR is a consequence of the basal (0002) texture splitting by 15 -20^{o} along RD and towards TD, thereby weakening of the basal texture. On the other hand, the anisotropic behaviour in strength is lower in MSCR than in case of UDR due to continuous interchanging of rolling plane uniformly distributes the stress accumulation. The yielding difference in MSCR is 41 MPa, while in UDR it is 86 MPa between rolling direction (0^{o}) and transverse direction (90^{o}). In general, MSCR samples are expected to show less anisotropy, but needs to be evaluated.

Table 4.2 Mechanical properties from tensile test on hot rolled UDR and MSCR samples

Specimen Orientation	***Yield Stress, MPa***		***Ultimate Tensile Strength, MPa***		***Elongation %***		***Fracture Strain***	
	UDR	***MSCR***	***UDR***	***MSCR***	***UDR***	***MSCR***	***UDR***	***MSCR***
0^{o}	227	169	352	300	11.23	13.92	0.5929	0.5127
45^{o}	130	119	415	234	10.59	19.85	0.5295	0.8098
90^{o}	141	128	355	242	15.55	9.55	0.4894	0.6623

4.2.3.2 Anisotropy Calculations

The variation of mechanical properties pertaining to plastic deformation starting with Vickers hardness value, tensile yield stress and ultimate tensile stress, % elongation and fracture strain shows certain level of anisotropy, which needs to be investigated by anisotropy calculations.

In anisotropy calculations, the variation in gauge length width and thickness is measured before and after the tensile test. Following the collection of width and thickness data from the tensile test sample, and then calculated plastic anisotropy compared with the plastic strain experienced during the tensile test. Based on these data, the plastic anisotropy calculated as *Lankford parameter – 'R' value*, expressed from the equation (2.29)

(2.29)

$$R = \left\{\frac{ln\,[w_f/w_o]}{ln[t_f/t_o]}\right\} = \left\{\frac{ln[w_f/w_o]}{ln[(l_o*w_o)/(l_f*w_f)]}\right\}$$

where w_f and w_o are final and initial width respectively and t_f and t_o are the final and initial thickness respectively.

Table 4.3 Plastic anisotropy values of hot rolled sheet in UDR and MSCR modes of rolling.

Specimen Orientation	***Plastic Strain***		***Lankford parameter – 'R' value***	
	UDR	***MSCR***	***UDR***	***MSCR***
0º	0.05744	0.07492	0.201529814	0.199553502
45º	0.07239	0.09137	0.222241507	0.197165838
90º	0.10087	0.04322	0.203756883	0.180242711

The Lankford parameter ('R' value) as depicted in Table 4.3. The R value of UDR samples at 0º (RD) and 90º (TD) are nearly same but the relative plastic strain experienced by the tensile specimen is 50% at 0º (RD) compared to 90º (TD). Hence, the anisotropy in UDR samples at 0º (RD) and 90º (TD) is negligible. On the other hand, the 'R' value in MSCR is decreasing gradually from 0º (RD) to 90º (TD), where corresponding plastic strain introduced in the tensile specimen of MSCR shows higher value at 45º followed by 0º (RD) and 90º (TD). Anisotropy in MSCR shows higher at 0º (RD) and lowest at 90º (TD). The MSCR samples have the lowest anisotropy values because to their huge grain size of 90 μm and split in the basal pole distribution is observed. Strain hardening effect in UDR is prominent as discussed in section 4.2.3.1, causes higher R value at 45º. Eventually, as seen in Fig. 4.32 (a) the R value is ranging from 0.1802 (MSCR) to 0.2222 (UDR) depicts that anisotropy is more in UDR than in MSCR with marginal widening of the sheets.

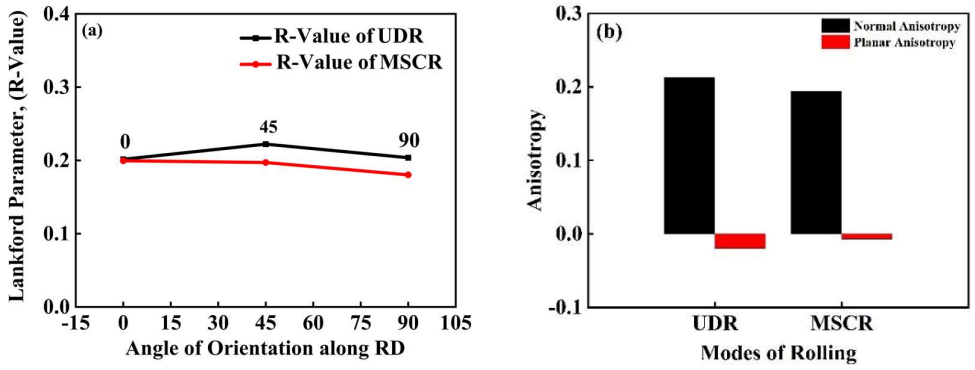

Fig. 4.32 Anisotropy calculation give (a) Variation of Lankford parameter (R-value) for hot rolled UDR and MSCR sheet specimens with the angle of specimen orientation along RD and (b) Variation of Normal and Planar anisotropy parameters with modes of hot rolling (i.e., UDR and MSCR)

Subsequently, overall resistance to thin down the sheets (both UDR and MSCR) also measured by taking an average value of R in three α angles (0º, 45º, 90º) generally determined by Normal anisotropy expressed from equation (2.30)

$$\textit{Normal Anisotropy}, \bar{R} = \frac{1}{4}[R_{0^o} + 2R_{45^o} + R_{90^o}]$$

Normal anisotropy value in UDR is 0.212442428 and in MSCR is 0.193531972. Any $\bar{R}$ value more than 1 shows more contraction of the sheet than its thinning during the elongation, indicating of better formability. But in both the cases of UDR and MSCR hot rolled sheets, as the $\bar{R}$ value range between 0 to 1 indicating of restricted formability. Contraction of sheet was observed preferentially than thinning in UDR, but in MSCR contraction and thinning of sheet occurs simultaneously.

Similarly, the amplitude of the in-plane anisotropy also determined by taking difference in the R values given by Planar anisotropy shown from equation (2.31)

$$\textit{Planar Anisotropy}, \Delta R = \frac{1}{2}[R_{0^o} - 2R_{45^o} + R_{90^o}]$$

Planar anisotropy ΔR, value in UDR is -0.019598159 and in MSCR is -0.007267731. As ΔR<0, then probability of ears formation will occur at 45º [194]. Consequently, sheet formation at 0º (RD) and 90º (TD) will not show formation of ears (as ΔR is not greater than 0) which is most desirable from formability point of view. However, ΔR value along 45º is approaching to 0 value as shown in Fig. 4.32 (b) and can be considered very low. The possibility of negative deviation of ΔR value along 45º rely

on shear texture created by dense network of shear bands where localized softening in the form of dynamic recovery is insufficient than compared to 0º (RD) and 90º (TD).

4.2.3.3 Fractography:

The fractured samples from the tensile test were carried out on hot rolled of UDR and MSCR sheet specimens observed under SEM having tungsten filament-based electron gun.

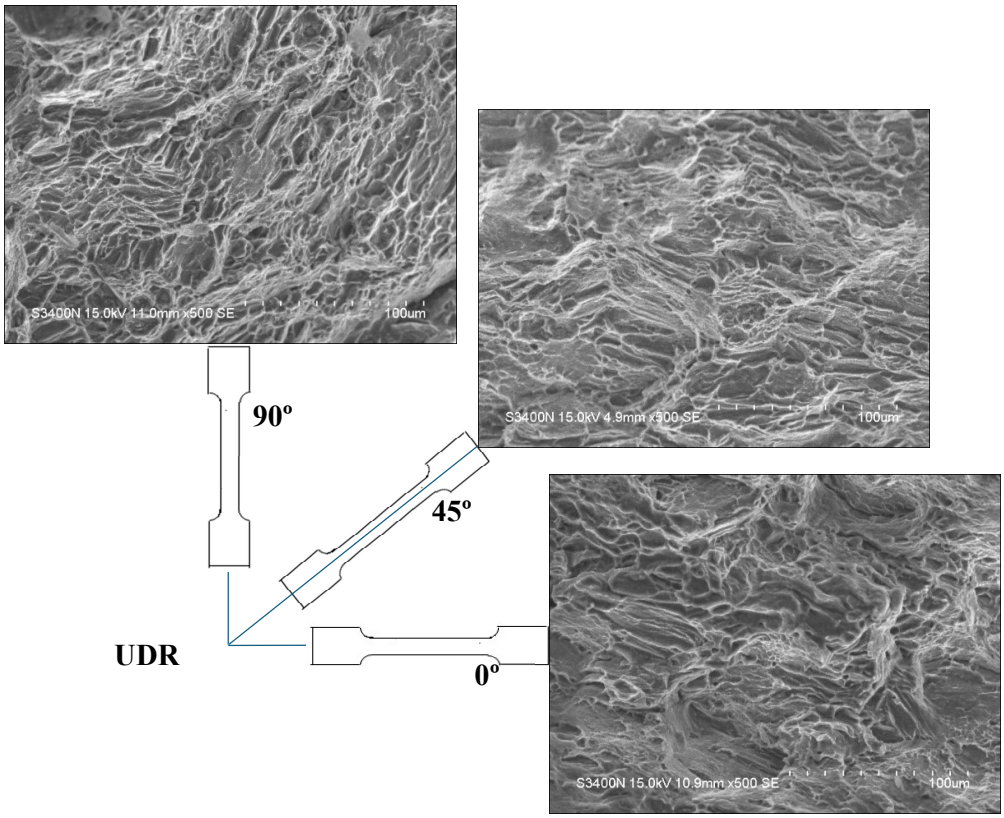

Fig. 4.33 Fractography of tensile tested UDR sheets cut along final RD at 0º, 45º, 90º.

The intra-granular fracture is observed in UDR samples as shown in Fig. 4.33. UDR 45º shows shallow dimples and cleavage planes are clearly visible as well as signs of void formation inside the grains which are signature of near brittle failure. However, fractured surfaces in UDR 0º and UDR 90º show deep dimples on the fractured surface can be distinguished by strong slip at boundary region.

During UDR, profuse twinning initiates shear bands which in-turn reorient the basal poles in shear direction. But the twinned region makes the reoriented basal poles

to splits and then introduces the non-basal planes along RD. This reorientation brings in softening of texture leading to dynamic recovery and consequently fracture under such conditions shows deeper dimples indicating ductile failure in UDR 0º and UDR 90º. However, if the reorientation of basal poles delay, then basal poles orient themselves toward shear direction with no chance for restoration leading to cleavage type fracture primarily because of shear band as depicted in UDR 45º.

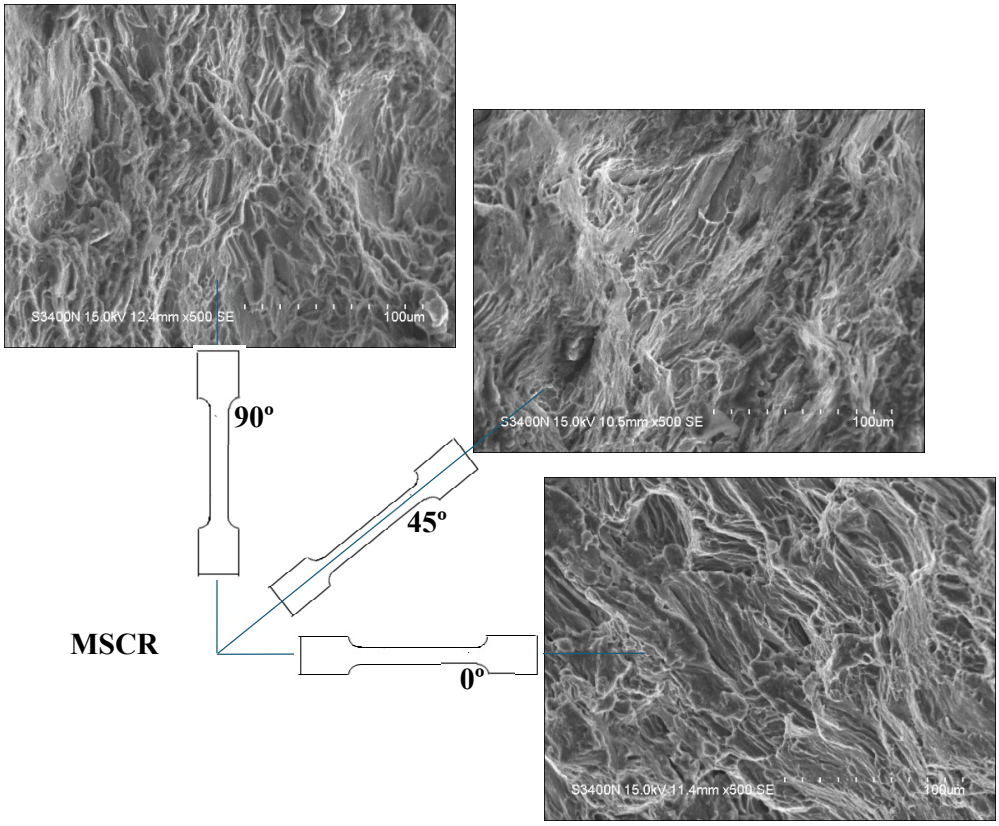

Fig. 4.34 Fractography of Tensile Tested MSCR sheets cut along final RD at 0º, 45º, 90º.

All the fractured samples of MSCR shown in Fig. 4.34 planar fracture features revealing twin boundaries successively to create planar fracture. During MSCR, continuous interchanging of rolling plane helps to compensate the strain concentration from tensile stress and compressive stress and simultaneously also introduces variety of twins. These twins consistently reorient the basal poles leading to localized softening of dynamic recovery type, cause all the MSCR specimens to fail in a planar fashion dedicated by twinned region.

4.3 Effect of Deformation Modes on Corrosion Behaviour of Mg-0.5wt%Ce alloy

The hot rolled sheets of UDR and MSCR obtained from the starting materials of Mg-0.5wt%Ce alloy (test materials) in the extruded rod form was subjected to hot rolling. These hot rolled sheets and as-extruded samples were subjected to the material testing and microstructural characterization as discussed in section 4.2. Now the basic corrosion response of these samples of UDR and MSCR sheets that were extruded and hot-rolled becomes imperative. As the extruded and the hot rolled samples are processed by three different routes such as extrusion, UDR and MSCR, so it becomes imperative to understand their basic corrosion behaviour. The basic corrosion response as a function of deformation mode can be identified by electrochemical test carried out polarization test and electrochemical impedance spectroscopy. Prior to these tests, surface roughness is also an important aspect to identify.

4.3.1. Surface Roughness Measurement before Corrosion Test

Surface roughness showed in Fig. 1 of extruded rods, UDR and MSCR sheets specimens of test materials. Evidently, the average surface roughness (R_a) lowered in relation to the increment in the stress in forming direction.

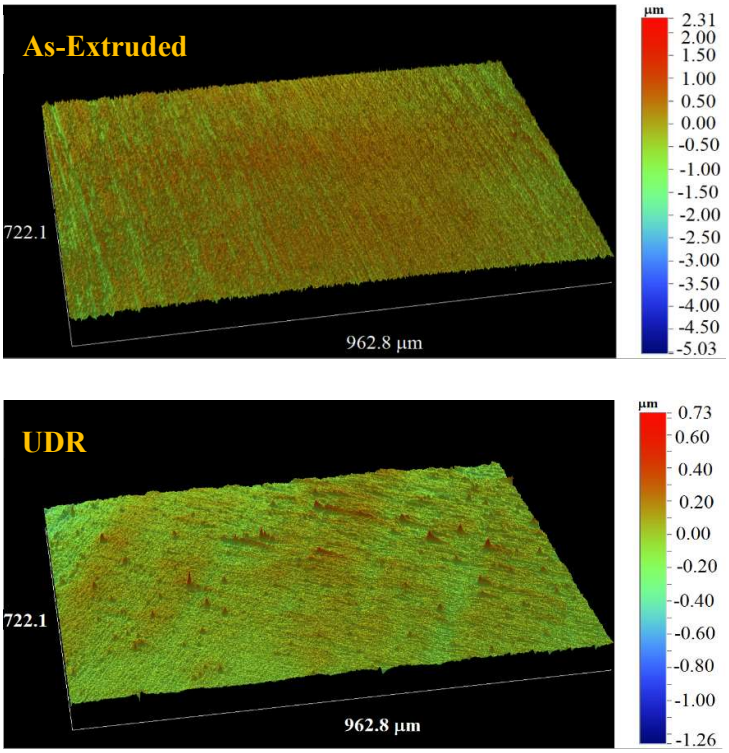

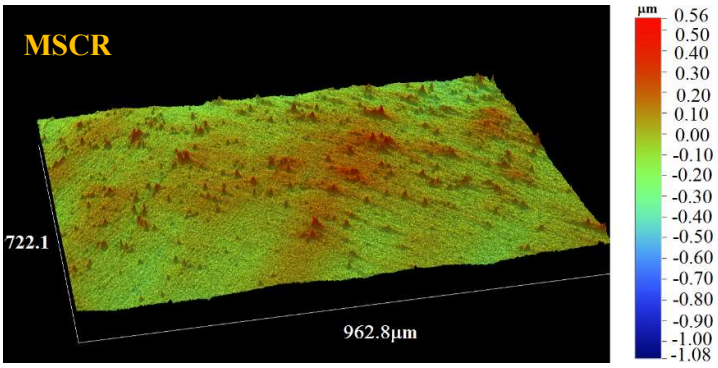

Fig. 4.35: Surface roughness images of extruded rod, UDR and MSCR sheet specimens

Table 4.4: Surface roughness data of extruded rod, UDR and MSCR sheet specimens

Condition	R_a, µm	R_p, µm	R_q, µm	R_t, µm	R_v, µm
Extruded	0.20467	5.03967	0.265	10.9167	-5.8777
UDR 0	0.06805	0.69833	0.0886	2.094	-1.3957
MSCR 0	0.05778	0.555	0.076	1.637	-1.082

Relative peak roughness (R_p – Peak to Peak variation from the surface), Root mean square roughness (R_q – Taking mean value of wavy surface), Transverse surface roughness (R_t – Roughness along transverse direction), and Normal surface roughness (R_y - Roughness along normal direction). The Surface roughness images of extruded rod, UDR and MSCR sheet specimens is shown in Fig. 4.35 and the corresponding values are tabulated in Table 4.4. The rolling technique smoothens the surface of the test materials sheets. The passivation tendency is impacted by an increase in surface roughness and subsequently increased the possibility of localize corrosion. [236]. Most of the metallic system shows development of a continuous corrosion product film forms more easily on a smooth surface than a rough one. All specimens were wet polished by 3000 grit size SiC polishing paper to remove the effects of surface roughness on corrosion dynamics before conducting the corrosion tests.

4.3.2 Corrosion/Electrochemical Testing

Potentiodynamic polarization test and Electrochemical Impedance measurements is conducted using Potentiostat - Galvanostat equipment of AUTOLAB

302N model. Software used for the Electrochemical Impedance measurement is GPES (General Purpose Electrochemical System) Manager.

4.3.2.1 Potentiodynamic Polarization (PDP) Measurements

Potentiodynamic polarization (PDP) curve of test materials samples in extruded rods, UDR and MSCR sheets were measured in a unstirred test solution made with 3.5wt.% NaCl (Standard Electrolyte) and saturated with $Mg(OH)_2$ in distilled water at 25±1°C are shown in Fig. 2. Electrochemical data observed during PDP test is displayed in the table 2 indicates that the polarization occurs at same open circuit potential (OCP) for extruded rods, UDR and MSCR sheets specimens with marginal variation in Ecorr, Icorr and corrosion rates.

First, the choice of test solution 3.5wt.% NaCl solution saturated with Mg $(OH)_2$) (Test Electrolyte) (becomes very crucial in the electrochemical study of the system. 3.5wt.% NaCl (Standard Electrolyte) in aqueous solution (distilled or deionized water) corresponds to the concentration similar as that in seawater. According to ASTM G44 [237], the threshold of the aggressiveness of Cl^- in seawater is observed in standard electrolyte. Standard electrolyte in aqueous solution has a pH ranging from 6.8 to 7.8 that is used to simulate the corrosion rate because of presence of Cl^- ions in aggressive environment, more abundant as corrosive reagent, dissociation of Cl^- ions from Na+ ions is easy through the electron emission, salinity is high and easy formation of corrosion product.

When magnesium or its alloy is immersed in standard electrolyte solution, then there is a tendency for it to spontaneously transform into its oxidized states (MgO or Mg $(OH)_2$), in presence of oxygen or water content. As a result, this solution containing NaCl with Mg $(OH)_2$ increases the pH from 6.8 - 7.8 to approximately 10.5 which does not remain stable in the electrode surface causing unstability in the corrosion conditions. [238] [239][240]. But when standard electrolyte contains saturated Mg $(OH)_2$, then the pH value increases to about 11 which is equal to the pH of Mg $(OH)_2$ formation that indicates the formation of Mg $(OH)_2$ film on electrode surface. [241]

Whereas, MgO develops incomplete surface oxide film or porous film because the Pilling-Bedworth value of MgO is less than 1 [242]. On other hand, Cl^- ions in 3.5 wt.% NaCl solution are sufficient to break Mg $(OH)_2$ layer developed on the surface of Mg alloy and hence, unable to establish even OCP. But with saturated Mg $(OH)_2$ in standard electrolyte solution, the dissolved Mg $(OH)_2$ forms a robust film on the

specimen surface such that a barrier develops toward the action of Cl^- ions to break the film. Since the definite proportion (1M or 3M or 5M solution) of Mg $(OH)_2$ required to carry out this exercise remains unknown, hence saturated Mg $(OH)_2$ in NaCl works for this task. As dissolved Mg $(OH)_2$ depletes from the solution, then saturated particles of Mg $(OH)_2$ goes into solution and in turn avoids the breakage of film by Cl^- ions [240]. Meanwhile, oxidation reaction occurs by giving Mg^{2+} ions to the electrolyte which reacts with $2(OH)^-$ ions to form Mg $(OH)_2$. As a result, an OCP gets stabilized and electrochemical cells will become stable to show response as cathodic and anodic reactions occurring in the system.

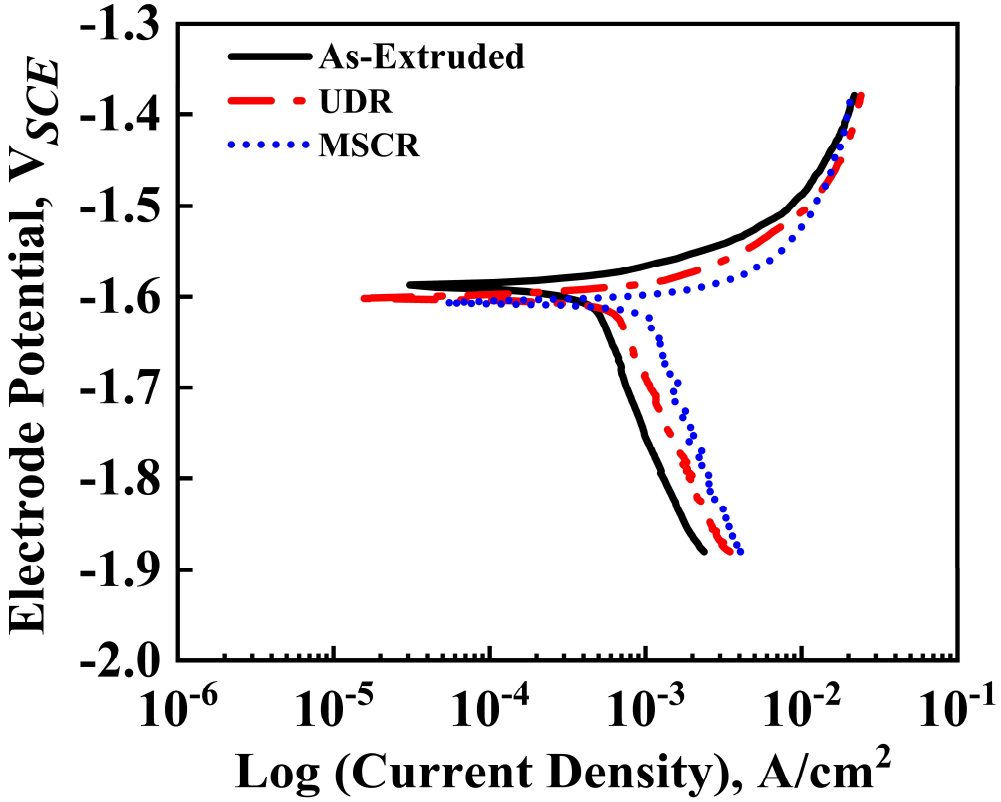

Fig. 4.36 PDP curves of extruded, UDR and MSCR specimens after 1½ h immersed in a Test Electrolyte.

Table 4.5: Electrochemical data observed during Polarization test.

Parameters	Mode of Deformation		
	Extruded	UDR	MSCR
Open Circuit Potential, (OCP), V	-1.63	-1.63	-1.63
Corrosion Potential, (Ecorr), V	-1.587	-1.609	-1.607
Corrosion Current, (Icorr), A/cm^{-2}	4.187 x 10^{-4}	5.963 x 10^{-4}	9.633 x 10^{-4}
Corrosion Rates, mpy	0.00209	0.00296	0.00480

Corrosion rate in mil per year, $$r = C\frac{M}{n\rho}i_{corr} \quad (1)$$

where

Conversion factor, C = 1.29

Atomic wt.(g/mol), M = 24.305 for Mg and 140.115 for Ce

Valency e^- , n =2 for Mg and 3 for Ce

Density (g/cc), ρ = 1.738 for Mg and 6.78 for Ce

Based on these attributes, 3.5 wt.% NaCl solution saturated with $Mg(OH)_2$ was chosen as test electrolyte. $Mg(OH)_2$ film is developed on the surface of magnesium alloy [243]. The PDP curve as shown in Fig. 4.36 is obtained after 15 min to stabilize the open-circuit potential (OCP) at -1.63 V in the same solution at 25 ± 1° C.

The PDP test parameters obtained are tabulated in Table 4.5. The corrosion rates were determined for small deviation from *Icorr* according to Eq.1. The obtained *Icorr* values are 4.187 x 10^{-4} A/cm^2, 5.963 x 10^{-4} A/cm^2, 9.633 x 10^{-4} A/cm^2 for extruded, UDR, and MSCR respectively, but high purity Mg has 3.04 x 10^{-5} A/cm^2 at lowest immersion time of 3 h. The corrosion rate values are 0.00209 mpy, 0.00296 mpy, and 0.00480 mpy for extruded, UDR, and MSCR respectively, but high purity Mg has ~0.3 to 0.5 mmpy [244] and 0.38 mmpy [245].

Table 4.6 consolidates the electrochemical data of PDP test after Tafel fitting of polarization curve. Fig. 4.37 (a) represents the corrosion rates in mil per year (mpy) deduced from Eq. (1) and *Icorr* from Table 4.5 and Table 4.6. The corrosion rates of UDR sample exhibits intermediate value between highest of MSCR and lowest of extruded. On a relative basis, UDR sample shows slight increment in corrosion rates

than that observed in extruded sample. Higher rates of corrosion are seen in MSCR sample in comparsion with extruded verified by the higher slope for the MSCR curve and low for UDR.

In the PDP curve, the anodic curve for MSCR becomes steeper than the curves of UDR and Extruded samples. This fact indicates that corrosion rates are on rise at greater rates. At the same time, anodic curve of Extruded, UDR and MSCR also gets parallel to electrode potential indicating some sort of passivation behaviour without decreasing the current density deviating from ideal behaviour of passivation. Such kind of 'breakdown' event being displayed at potentials above -1.4 V_{SCE} causes the anodic current to escape leading to spontaneous passivity attributable to the behaviour of intermetallic compound $Mg_{12}Ce$ [38].

Table 4.6: Electrochemical data of Polarization test after Tafel Fitting

Parameters	**Deformation Modes**		
	Extruded	**UDR**	**MSCR**
I_{corr}, **Acm^{-2}**	4.55 x 10^{-4}	6.28 x 10^{-4}	9.48 x 10^{-4}
E_{corr}, **V**	-1.588	-1.601	-1.605
β**c, V decade^{-1}**	0.073	0.067	0.452
β**a, V decade^{-1}**	0.445	0.429	0.053
Rp (Tafel fitting)	31.1	19.8	10.9
B=(βa.βc)/(2.3(βa+βc)) V	0.0272662	0.02519548	0.020625054
***Rp=B / Icorr*, Ω (Calc)**	59.952158	40.0946481	21.76327299
I_c, **Acm^{-2}**	0.0017111	0.0017027	0.00107644
I_a, **Acm^{-2}**	0.0003659	0.0005378	0.00031981
η_c, **V**	-0.042008	-0.029005	-0.0250045
η_a, **V**	-0.042008	-0.029005	-0.0250045
Corrosion Rates, mpy	0.00226	0.00313	0.00472

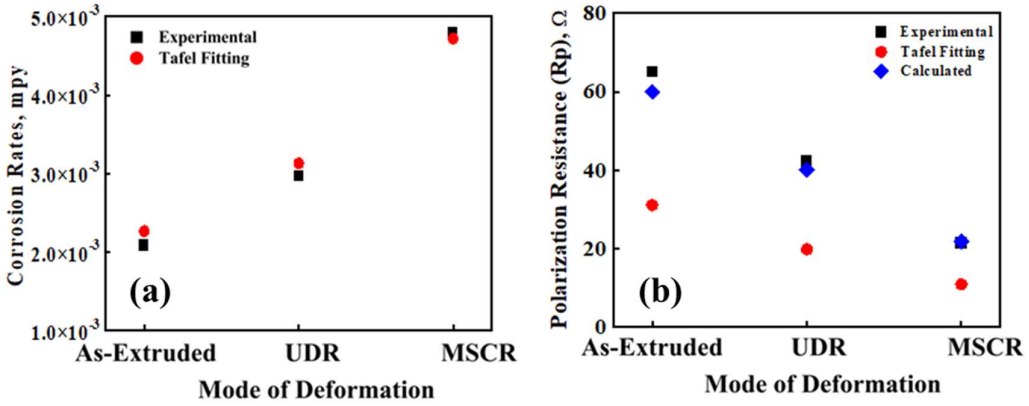

Fig. 4.37 (a) Corrosion rates and (b) Polarization resistance (Rp) of extruded, UDR and MSCR specimens after 1½ h immersion in the test electrolyte during Potentiodynamic Polarization test.

Corrosion rates of extruded, UDR and MSCR samples as illustrated in Fig. 4.37 (a) indicate the experimental plots exhibit a two-stage linear agreement with Tafel fitting plots. Extruded and UDR samples shows minor difference in their corrosion rates values but for MSCR corrosion rates accelerates.

Polarization resistance (*Rp*) measurements are used to determine the ability to form protective layer on the specimen to avoid the oxidation when potential is applied externally. Polarization resistance (*Rp*) of extruded, UDR and MSCR samples as depicted in Fig. 4.37 (b) indicate the experimental plot are in linearly co-related with slight agreement for Tafel fitting plot. The Polarization Resistance (Rp) is the slope of the potential-current density plot near Ecorr,

$$R_p = \frac{\Delta E}{\Delta I}, \qquad \text{where } \Delta E ==> 0$$

Reaction under activation, $R_p = \frac{B}{-I_{corr}}$

Stern-Geary equation, $B = \frac{(\beta_a \beta_c)}{2.3(\beta_a + \beta_c)}$

where, β_a, β_c Tafel constants for calculated values from the anodic and cathodic segments of the Tafel plots. Polarization Resistance (*Rp*) derived from experimental data deviates slightly with the calculated value of *Rp*, whereas a large gap is seen with Tafel (conventional) fitting. The higher the polarization resistance (*Rp*) corresponds to lower corrosion current, *Icorr* and vice-versa as seen in Table 4.6. MSCR shows the lowest value of polarization resistance corresponds to highest anodic current, while extruded sample has completed reverse order.

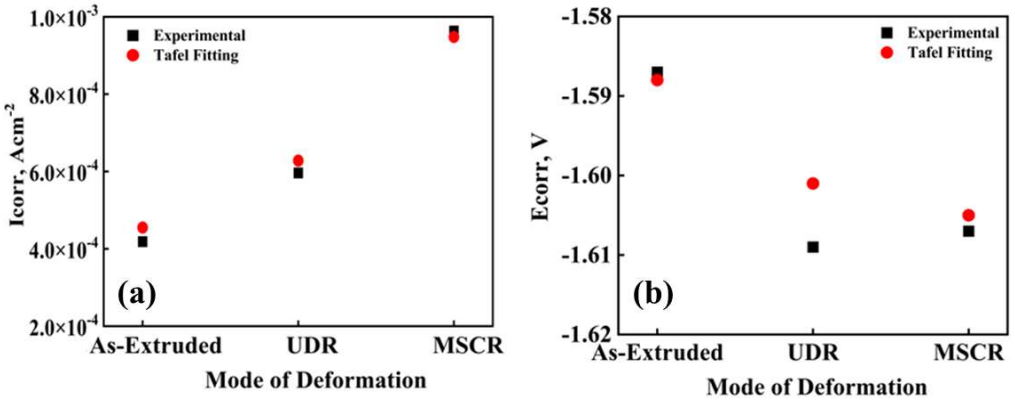

Fig. 4.38 (a) Corrosion current and (b) Corrosion potential of As-Extruded, UDR and MSCR specimens after 1½ h submersion in the test electrolyte during Potentiodynamic Polarization (PDP) test.

Current density (*Icorr*) as demonstrated in Fig. 4.38 (a) during the occurrence of corrosion is low in extruded, but rather varies with different modes of rolling. MSCR samples has comparatively more current density than UDR, thereby imply its vulnerability towards corrosive environment.

Corrosion potential (*Ecorr*) displayed in Fig. 4.38 (b) for extruded is slightly less negative than rolled sheet samples of UDR and MSCR. *Ecorr* values for UDR and MSCR vary marginally, indicating higher susceptibility for corrosion.

The corrosion current density and corrosion potential both significantly rely on the parameters of deformations (stress and temperature). Extruded material processed from hot extrusion, by applying stress under controlled condition on hot cast ingot. Hot-rolled UDR sheets were produced without changing RD, TD, and ND at each pass, whereas hot-rolled MSCR sheets were processed by maintaining ND is constant while RD and TD interchanging at each pass on the hot extruded starting material samples.

In extruded material low corrosion rate is attributed to the more uniform stress distribution and well-annealed sizes of the grains (25-50 μm) in the microstructure is the primary requirement even though in non-basal orientation. The precipitates ($Mg_{12}Ce$) appeared within the grains and grain boundaries are ranging in different sizes from 4 μm to 9 μm with a volume percentage of 1.5% for as-extruded sample. Smaller grain size and wide range of precipitate sizes decreases the anodic reaction resulting in low corrosion rates.

The hot rolled UDR also shows low corrosion rates because the microstructure contains strong basal orientation (higher atomic density plane) delays anodic reaction and has marginally coarser grain sizes (35-55 μm) than that of extruded but consist of same area fraction of 26%. The precipitates ($Mg_{12}Ce$) in UDR sample have narrow size range of 4.5 μm to 5.6 μm with a volume percentage of 1.6% indicating their fragmentation during 20 passes of hot rolling with a total true strain of 2.0. The finer size and slight increase in the volume percentage of precipitates ($Mg_{12}Ce$) and in UDR compared to extruded sample resulted in marginal increase in corrosion rates because the matrix undergo anodic dissolution preferentially beneath the precipitates.

The hot rolled MSCR microstructure consists of weak basal orientation with substantially coarser grain sizes (40-90 μm) with a larger area fraction 36%. The precipitate ($Mg_{12}Ce$) particles sizes range from 3.4 μm to 8 μm with a volume percentage of 0.9% for MSCR sample. These particles get entrapped in the shear bands formed in weaker basal planes (highest atomic density) orientation during hot rolling which are not visible to be counted. The smaller content of precipitates in the matrix and weaker basal orientation causes more corrosion rates in MSCR.

The corrosion rates of MSCR are higher than UDR and extruded samples because anodic dissolution kinetics is faster where its coarser grains weakly oriented toward basal planes in more quantity. The corrosion parameters evaluate the electrochemical response to mechanical behaviour, indicating an increase in anodic current densities and a decrease in potential values due to deformation. [239].

4.3.2.2 Electrochemical Impedance Spectroscopy (EIS) Measurements:

Electrochemical Impedance Spectroscopy (EIS) is an effective method to characterize metal corrosion behaviour [215]. A simple electrochemical system involves double layer capacitance (C_{dl}), a solution resistance (R_s), capacitance (C_{dl}), and a charge transfer resistance (R_{ct}) (understood with Polarization resistance (R_P). Electrochemical Impedance Spectroscopy (EIS) is an AC signal-based test gives more data than that of a DC polarization. Later impedance values are given from the variation of potential with current when sinusoidal potential is applied to potentiostatic circuit. The EIS measurement of the Mg-0.5wt.% Ce alloy samples obtained from different modes of deformation extruded, UDR and MSCR in 3.5 wt.% NaCl solution saturated with Mg $(OH)_2$ (test electrolyte) in distilled water at 25±1°C showed more or less identical behaviour as indicated in Fig. 4.39.

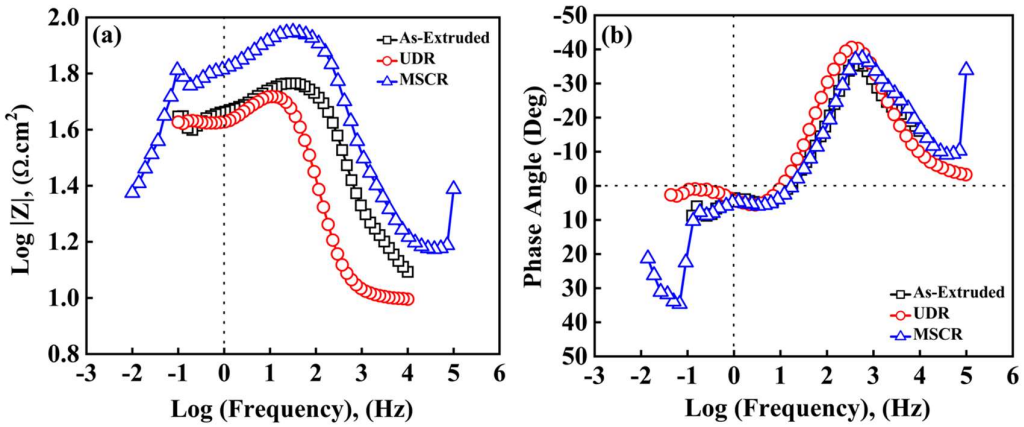

Fig. 4.39 Bode Plot - Variation of Frequency with Impedance (a) and Phase Angle (b) from Electrochemical Impedance Spectroscopy Test of As-Extruded, UDR and MSCR specimens after 1½ h immersion in the test electrolyte.

The Bode plot in Fig. 4.39 displays the variation of the frequency with the impedance (a) and with the phase angle (b) after exposure to the open-circuit potential at E_{corr} in the test electrolyte. The increment levels of impedance signify the variation in the corrosion resistance. These outcomes confirms that the generation of a passive film on the specimens was possible irrespective of deformation modes i.e., samples of extruded and hot-rolled sheets of UDR and MSCR. In the 1½ hour test period, the impedance at low frequencies increased by a very tiny order of magnitude, showing an increase in the corrosion resistance offered by the protective film. The magnitude of impedance spectra and its spread on the frequency range for MSCR is much higher than that of extruded and UDR.

When the test samples of extruded and hot-rolled sheets of UDR and MSCR are immersed in test electrolyte, then three time-constant observed in Bode plot. The corrosion potential (*Ecorr*) consisted of one capacitive loop in the high-frequency (*HF*), another capacitive loop in the medium-frequency (*MF*) and one inductive loop in the low-frequency (*LF*). The *HF* spectra lines corresponds to the corrosion process carried by double layer capacitance and a charge transfer resistance which recognizes the localized surface defects. The *MF* spectra lines corresponds to induced film effect that recognizes the incomplete layer of the corrosion products over the entire specimen surface influenced by the successive developments by mass transport inside the film based on the values of capacitance and resistance obtained. The *LF* impedance spectra lines increased by very small range of magnitude identifies the sequence of progression

(such as reduction of species absorbed) at the metal-film interface depending on the metastable Mg+ concentration identifies by inductive loop [208][244][246] [250] [247]

A wide frequency range of capacitive response can be seen especially in MSCR covering *HF*, *MF*, and *LF*. The two capacitive arcs at *HF* and *MF* reveals that their diameters depend on the modes of processing and in-turn subsequent microstructure of these alloys. The diameter of capacitive arc for *MF* is linked to the charge transfer resistance which signifies the resistance related to the addition or removal of electron. The *MF* capacitive response was followed by a *LF* resistive behaviour. The *HF* spectra lines in UDR and extruded are reasonably smaller than MSCR and display considerable spread, whereas extruded shows minimal spread.

The phase angle represents the phase difference between the voltage and current in a circuit. The variation of frequency with the phase angle illustrates that increase in frequency decreases the phase angle, because the response of the circuit component is more evident than their resistance. The impedance spectra display a capacitive response with a range of phase angle between -40° and -30°, which is consistent with the presence of passive film Chen, Wang [5], The maximum phase angle of high-frequency capacitive arc goes beyond -30° in Bode plots, where UDR shows maximum phase angle of -40°. The capacitive response of extruded and MSCR angular phase is similar throughout the frequency range except at the extremities.

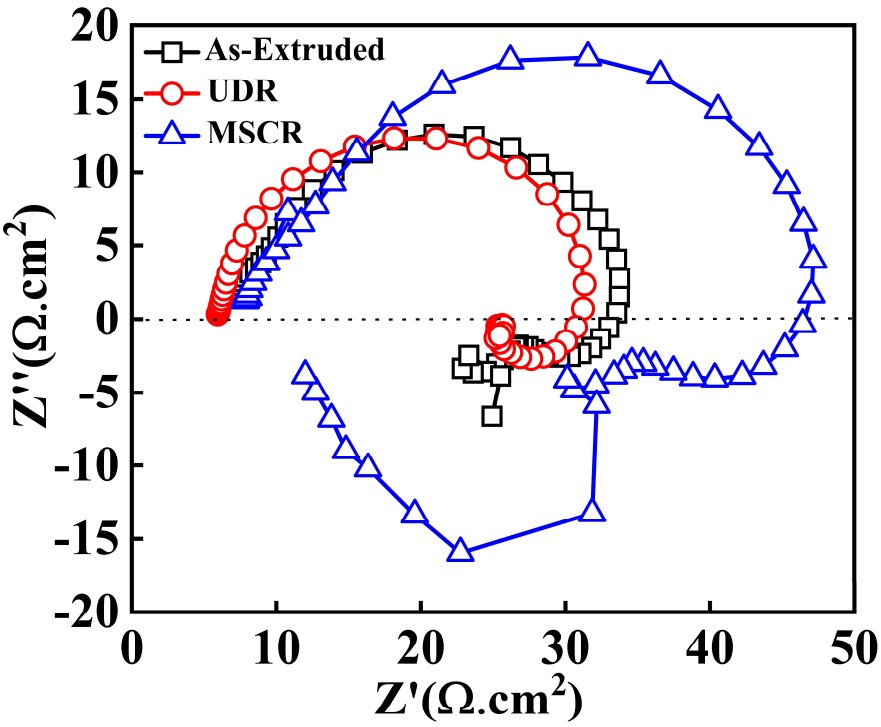

Fig. 4.40 Nyquist Plot – Variation between Real and Imaginary parts of Impedance from Electrochemical Impedance Spectroscopy Test of As-Extruded, UDR and MSCR specimens after 1½ h immersion in the test electrolyte.

The typical Nyquist plots displayed in Fig. 4.40 drawn in a complex plane shows variation in the real value and imaginary value of the impedance data measured from Electrochemical Impedance Spectroscopy Test of extruded, UDR and MSCR samples of Mg-0.5 wt.% Ce alloy. All the samples shows the existence of depressed semi-circles with presence of capacitive loop. The area enclosed by Nyquist plots corresponds to the resistance against corrosion rates in the present electrochemical system. The wider the area enclosed by Nyquist plot, higher will be the resistance toward corrosion attack.

The radius of semi-circle increases in MSCR, while extruded shows marginally more than UDR. The Nyquist plots exhibits MSCR capacitive loop extends to larger frequency range about ~ 45 Ωcm^2 of real impedance magnitude. The depressed semi-circle (deviating from Cole-Cole Diagram) of MSCR approaches 15 Ωcm^2 of positive imaginary impedance making a shape of near parabolic curve. UDR and extruded samples exhibit smaller semi-circle just exceeding 30 Ωcm^2 of real impedance magnitude. The depressed semi-circle of UDR and extruded samples exceeds 10 Ωcm^2 of positive imaginary impedance magnitude, while MSCR loop approaches 30 Ωcm^2. Larger impedance in MSCR corresponds to proportionate resistance to the anodic dissolution is attributed to shear band network dispersed homogeneously along rolling direction in weakly oriented basal plane and few fragmented $Mg_{12}Ce$ precipitate particles during hot rolling get distributed within planes of shear band.

The EIS spectra exhibit one capacitive loop followed by the sharp ending with arc in negative range of imaginary impedance. Such values of imaginary branch proceed below zero representing the inductive behaviour of the circuit represented by negative slope in the real part of the plot corresponding to inductor (a circuit element) which stores energy. The inductor initiates a change in phase angle between the voltage and current which results in negative impedance value of real part in the Nyquist plot. [215][216]

UDR and extruded exhibit their capacitive loop ends below -5 Ωcm^2, whereas MSCR loop exceeds -15 Ωcm^2 values of negative imaginary impedance. These values suggest that MSCR continues to have more inductive behaviour than UDR and extruded samples. In such cases, an inductor might be used in combination with other circuit elements such as capacitor, and switches to control the flow of electrical energy, control

voltage, and regulate current within the system. At low frequencies (LF), an arc or tail in the Nyquist plots indicates an inductive behaviour for all systems, with this arc occasionally being less noticeable [215]. The outcome of Nyquist plot from Electrochemical Impedance Spectroscopy test results is displayed in Table 4.7.

Table 4.7. Electrochemical Impedance Spectroscopy Test results

S. No.	OCP	|Z| (minimum)	|Z| (maximum)
Extruded	-1.62	1.09×10^{0}	1.77×10^{0}
UDR	-1.62	9.96×10^{-1}	1.72×10^{0}
MSCR	-1.63	1.17×10^{0}	1.95×10^{0}

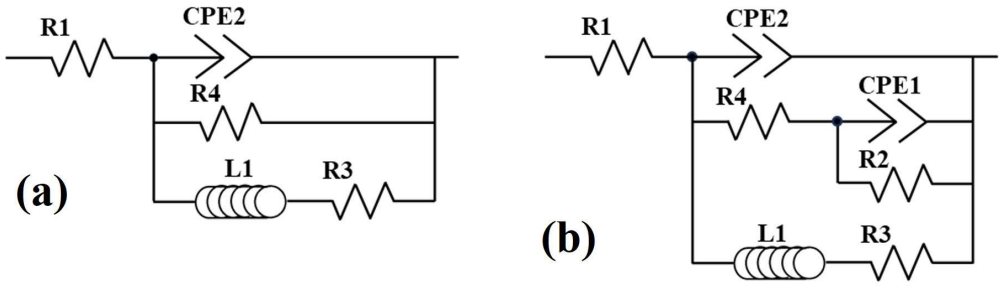

Fig. 4.41 Equivalent Circuit Model for fitting Electrochemical Impedance Spectroscopy Test data of (a) UDR, (b) Extruded, and MSCR specimens after 1½ h immersion in the test electrolyte.

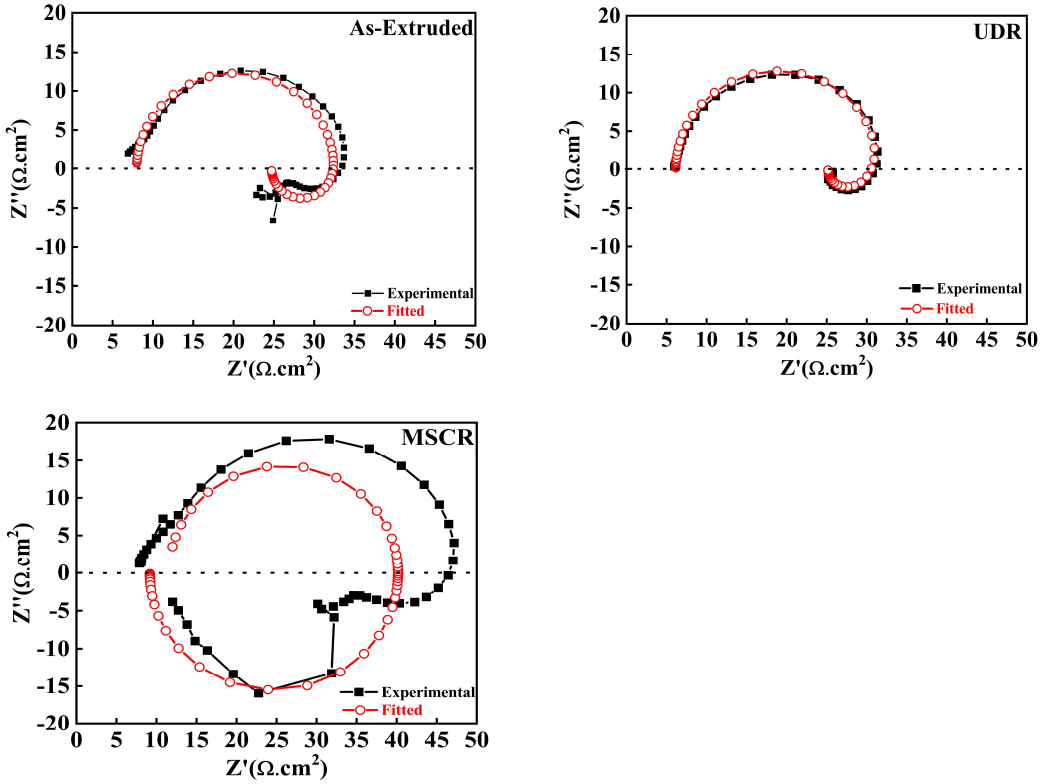

Fig. 4.42 Equivalent Circuit Model values fitted with Electrochemical Impedance Spectroscopy Test data of (a) UDR, (b) Extruded, and MSCR specimens after 1½ h immersion in the test electrolyte.

EIS data were obtained from 0.1 kHz to 10 Hz and an AC amplitude of ±10 mV. EIS scans were examined and fitted to an equivalent circuit utilizing the software program ZView Version 2.9C observed in Fig. 4.41 and were fitted to low frequency limit of 0.09 Hz for extruded, 0.523 Hz for UDR and 0.109 for MSCR. The depressed semi-circle experimental data from the Electrochemical Impedance Spectroscopy test was compared with the fitted values of equivalent circuit model as depicted in Fig. 4.42. The fitted values are in complete agreement with the experimental data for UDR sample whereas in extruded sample minor deviation is observed. The depressed semi-circle in MSCR sample is deviated from the fitted values of equivalent circuit model attributed to shear bands formation in which intermetallic ($Mg_{12}Ce$) precipitates get entrapped, shows scattered response toward electrochemical system created in EIS test. Consequently, the approximate fitting of experimental data of MSCR with equivalent circuit model is difficult to identify. The equivalent circuit parameter values of fitted Nyquist Plots is displayed in Table 4.8.

Table 4.8: Equivalent Circuit Parameter values of Fitted Nyquist Plots

Parameter	Modes of Deformation		
	As Extruded	**UDR**	**MSCR**
R1	$5.807x10^{-5}$	10.07	14.84
CPE2	$7.7882x10^{-7}$	$9.6027x10^{-5}$	$1.6901x10^{-6}$
R4	17.32	45.35	19.48
L	12.84	5.124	140.4
R3	176.3	109	8.591
R2	39.83	**----**	42.54
CPE1	$1.7694x10^{-5}$	**----**	$3.7328x10^{-6}$

The equivalent circuit contains of series and parallel sets of resistor, capacitor and inductor organized in *R1*/*CPE2*//*R4*//*CPE1*//*R2*//*L*/*R3* where "/" and "//" symbolizes series and parallel circuits respectively. *R1* is the resistance due to electrolytic solution between the reference electrode and the working electrode. *R2* refer to the resistance of the pores and other defects in the entire film, and *R4* specify to the charge transfer resistance which emerges due to oxides and hydroxides along with anodic and cathodic reactions with exchange of electrons on the Mg surface or oxide/film interface influenced by the local environment [248][249]. The corrosion resistance reduces with time as the charge transfer resistance value falls.

R3 refers to the charge transfer resistance in series with *L* specify the inductor implies initiation of localized corrosion due to metastable Mg^{+} ions. *L* symbolizes the inductor of a reaction rate that varies with the reaction [248] varying for different processing route as shown in Table 4.8.

CPE1, and *CPE2* are constant phase elements represents the total capacitance of the film, and interfacial capacitance two layers electric at electrolyte and Mg substrate. *CPE1* constant phase element capacitance associated with the oxide/hydroxide layers. *CPE2*, constant phase element capacitance due to formation of double layer occurs with growth of corrosion layer. [248]. The average value of corrosion current density is derived from polarization test, whereas EIS measurements give the instantaneous value. Increasing the immersion time of samples in test electrolyte, increase the H^{+} ion consumption, thereby increase in local pH value, suggesting OH^{-} ions resulted on the alloy surface, leading to passivation of anodic

event. Corrosion resistance improves because of the defensive film formed on the metallic surface, thereby inhibiting extended corrosion. The attack of Cl^- deteriorates the alloy surface during the corrosion process but subsides simultaneously by the formation of defensive corrosion product film at the same alloy.

4.3.2.3 Corrosion product film

The corroded surface of Mg-0.5 wt. % Ce alloy of extruded rod, UDR and MSCR sheets specimens after PDP test are seen in Fig. 4.43. The appearance of corrosion product film in extruded, UDR and MSCR samples are distinctly similar.

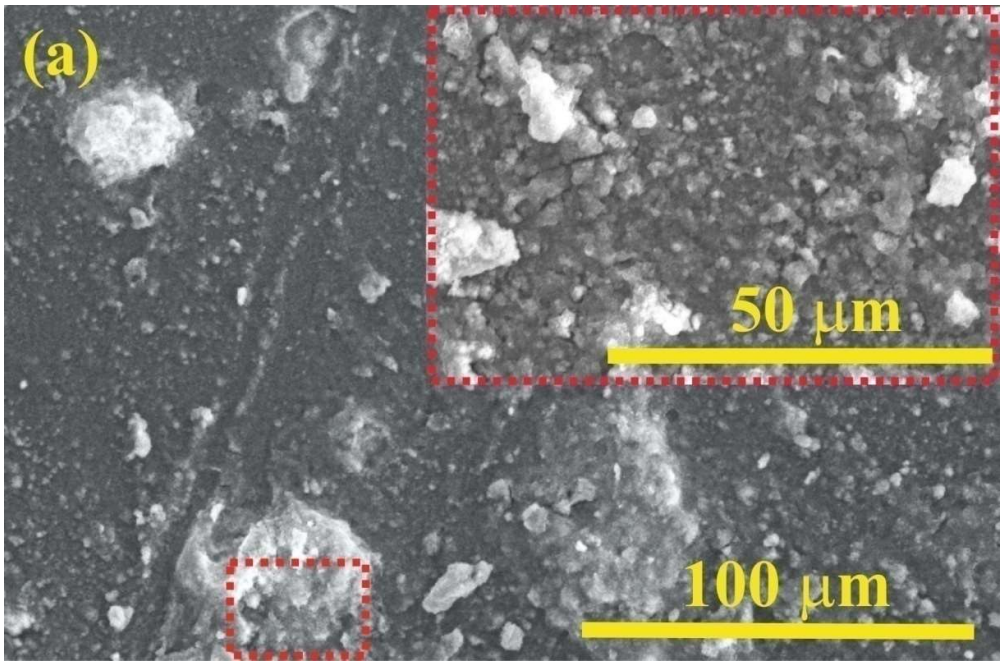

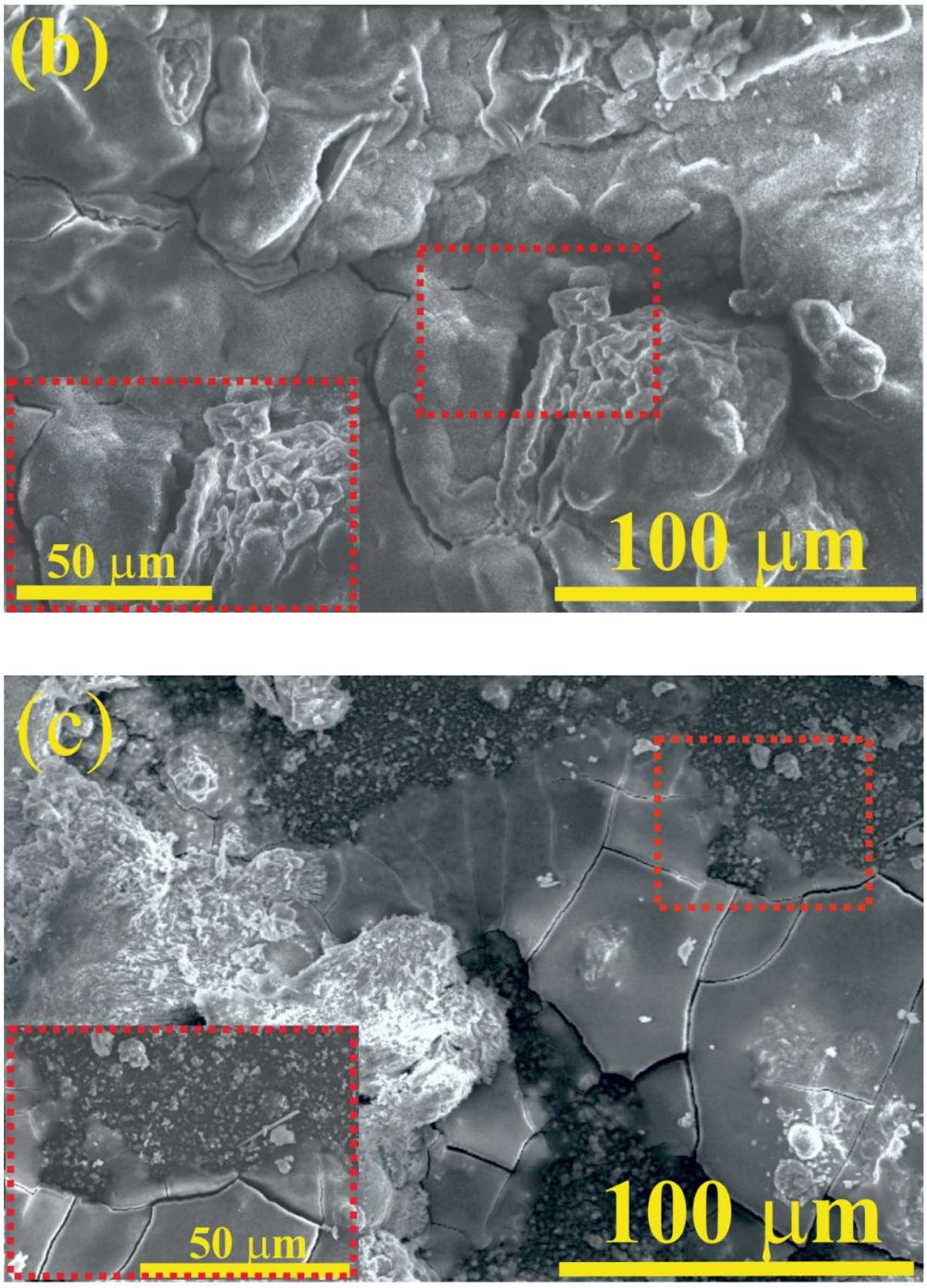

Fig. 4.43 SEM microstructure at 500X and 1000X of (a) extruded rod, (b) UDR and (c) MSCR sheets specimens after 1½ h immersion in the test electrolyte.

The intermetallic compounds ($Mg_{12}Ce$) in extruded sample appear to be larger in size than that in MSCR, whilst covered mostly with the film in UDR. This corresponds to crystal formation of corrosion products on the grain boundaries. After 1½ h immersion, an apparent formation of defensive film seen on a matrix, and later

covers the intermetallic compound phase indicating ennoblement than matrix. Birbilis et. al. [38] identified the Ecorr value of intermetallic compounds ($Mg_{12}Ce$) is -1.5 V_{SCE}, representing it to be substantially stable than Mg bearing -1.63 V_{SCE} Ecorr value. Hence, the intermetallic compounds ($Mg_{12}Ce$) are inert and act as reduction sites, initiating the oxidation activity of Mg matrix. In the extruded sample, corrosion occurs more preferentially due to presence of non-closely packed pyramidal plane as depicted in its XRD pattern. In UDR sample, corrosion product film completely covers avoiding further corrosion shows comparatively strong intensity of closely packed basal plane peak in its XRD pattern. In MSCR sample, breakdown potential reached quickly to rupture the passive film, leading to corrosion attack because of weak intensity of closely packed basal plane in its XRD pattern during its mode of deformation. A minor addition of Ce improves the features of the thin and compact passive film of corrosion product, delaying the corrosion.

4.3.2.4 Corrosion Morphology

The corrosion morphology of extruded, UDR and MSCR samples are markedly different. Extruded samples show compact corrosion product with superficial cracks, whilst in UDR denser feature of corroded surface appears relative no sign of cracks. In MSCR, cracks and dissolution of corrosion product film is well evident. Cracks and pores accelerate the corrosion rate by passage for Cl^- into Mg matrix. Corroded surface as seen in Fig. 4.43 of Mg-0.5wt.%Ce alloy exhibits localized form of corrosion on some selected portion with porous characteristic, whereas other portion inhibits. A brighter acicular phase appeared in the corroded surface depicts rich content of Ce (intermetallic compounds ($Mg_{12}Ce$), improves the corrosion resistance. In these electrochemical tests, corrosion attacks more on the Mg matrix, while intermetallic compounds ($Mg_{12}Ce$) remain visually unaffected. Consequently, the matrix corrosion is more pronounced with intermetallic compounds ($Mg_{12}Ce$) left intact. [38]. Overall, minor content of Ce has significant effect on corrosion morphology of Mg-0.5wt% Ce alloy, irrespective of processing routes because Ce ennobles the Ecorr value, being thermodynamically stable than the Mg.

The hot rolled product conventional UDR and modified MSCR processed for this work was essentially to decrease the plastic anisotropy and inhomogeneity in the cast extruded starting material of Mg-0.5wt.% Ce alloy. Even though plastic anisotropy decreased to maximum level in MSCR, the corrosion anisotropy appears to be higher.

Hence, proportionate balance between improved mechanical properties and corrosion resistance is required for rational design and development of such Mg alloy considering its corrosion properties clearly.

CONCLUSIONS:

The following are the conclusions made on the study presented in this thesis.

1. Hot-compression test of Mg-0.5wt%Ce alloy the true stress-strain curves highlight steady state owing to dynamic softening i.e., DRV. As the strain rate increases, then flow stress grows but decreases with rise in the deformation temperature.
2. Hot deformation behaviour of Mg-0.5wt% Ce alloy used to establish CE. The cross-slip and dislocation climb controls the deformation mechanism. The Q for the experimental alloy is very high to that of Mg because of diffusion and dissolution of Ce atoms in the matrix initiating enhanced obstacles to dislocation motion.
3. The peak value of AARE is 15.16% at 723K/1s^{-1} obtained for 0.4 strain . The cumulative AARE is implying that the Constitutive Equations is fairly fitted to experimental values. The coefficient (R) showing linear correlation involving the values of experimental and predicted flow stress.
4. The stability regimes in processing maps occurs mostly in the low strain rate zone where the higher efficiency of power dissipation, η which exists at 673–723K/10^{-3} to 1s^{-1} region. In this region, steady state flow stress curve occurs owing to the softening mechanism of DRV.
5. Instability domain occurs at 523–623K/10^{-3} to 1s^{-1} because the power dissipation is mostly utilized for plastic deformation rather than required microstructure development and hence, softening mechanism of DRV during deformation is insufficient. Shear bands are formed at the boundary of fine and coarse grains, results into flow instability.
6. Instability domain also occurs at 623–723 K/1 to 10 s^{-1} because of high deformation temperature suitable for DRV, while high strain rate will restrict growth of grains. The concurrence of original coarse grain and very fine grains will trigger instability such that crack nucleates.
7. The microstructure from EBSD-IPF maps of MSCR 15 appears very close to the As-extruded sample which shows well defined recrystallized grains in order of 25-50 μm with no sign of coarsening. UDR sample has $Mg_{12}Ce$ precipitates

sizes in narrow range of 4.48 μm to 5.57 μm with a volume fraction of 0.01638 and more homogeneous distributions of 35-55 μm grains. MSCR has coarsest grain size 40-90 μm, while $Mg_{12}Ce$ precipitates are 3.39 μm to 8.19 μm in size with a volume fraction of 0.0087.

8. MSCR 20 has largest proportions of LAGBs due to large amount of strain compensation of tensile and compressive stresses during change in strain path, whereas UDR 15, UDR 20 and MSCR 15 all of them shows equal amount of LAGBs.
9. The basal and prismatic poles of starting material (extruded sample) are oriented towards the extrusion direction, thereby large numbers of grains in a more suitable orientation for hot working. In UDR and MSCR, basal plane (0001), shows splitting of poles along RD towards TD, while prismatic plane $(10\bar{1}0)$ and pyramidal plane $(2\bar{1}\bar{1}0)$ pole figures show alignment of poles along RD.
10. Anisotropy in ductility and fracture strain is lower for UDR compared to MSCR, whereas anisotropy in strength (YS and UTS) is lower for MSCR compared to UDR.
11. Vickers Hardness values lie in the range between 37 to 47 HV for different mode of deformation As-Extruded, UDR and MSCR hot rolled sheets at regular interval of rolling i.e., after 10^{th} pass,15^{th} pass and 20^{th} pass,
12. Fractography images of MSCR shows Planar facets reflecting twin boundary failure whereas in UDR fractured surface shows deep dimples at 0^0 and 90^0 due to large number of deformation twins and cleavage at 45^0 because of shear bands do not under required amount softening and thus shows considerable anisotropy.
13. Lankford parameter, R-value in MSCR is decreasing gradually from 0º (RD) to 90º (TD). The R-value of UDR samples at 0º (RD) and 90º (TD) are nearly same but the relative plastic strain experienced by the tensile specimen is 50% at 0º (RD) compared to 90º (TD). the R value is ranging from 0.1802 (MSCR) to 0.2222 (UDR) depicts that anisotropy is more in UDR than in MSCR with marginal widening of the sheets.
14. In both the cases of UDR and MSCR hot rolled sheets, as the Normal anisotropy, $\bar{R}$ value range between 0 to 1 indicating of restricted formability. Planar anisotropy ΔR, value in UDR is -0.019598159 and in MSCR is -0.007267731. As $\Delta R<0$, then probability of formation ears will occur at 45º because of shear

texture created by dense network of shear bands where localized softening in the form of dynamic recovery is insufficient than compared to 0º (RD) to 90º (TD).

15. The anodic current density ascertained by potentiodynamic polarization curves for extruded, UDR and MSCR samples varies as a function of degree of plastic deformation. Variation in potentials (E) makes the similar agreement for all the samples.
16. Microstructural changes during stages of deformation at various processing routes set up a correlation with mechano-chemical phenomena.
17. MSCR samples had a higher corrosion rate than UDR. Extruded samples showed lower rates of corrosion with UDR and even MSCR. Thus, the anodic current of MSCR is more active than UDR and extruded.
18. Polarization resistance (Rp) from potentiodynamic polarization test and the electric double layer capacitance (CPE_{dl}) measured from EIS plots increases with variation in stress from extruded, UDR and MSCR. Henceforth, EIS measurements disclose the crucial behaviour of processed Mg-0.5wt.%Ce alloy with different routes in service application environment.
19. The cathodic reaction causes the formation of protective film made of corrosion product appears to be compact with superficial cracks in extruded sample, while completely covers with no cracks in UDR. In MSCR, breakdown potential reaches to rupturing the protective corrosion film.

SCOPE OF FUTURE WORK:

- Bulk texture analysis of hot compression tested samples.
- Bulk texture analysis of hot rolled sheets of UDR and MSCR.
- Effect of Deformation behaviour in Simulated Body Fluid and Hank solution using Scanning Electrochemical Microscopy.
- Weight Loss Corrosion Test of hot rolled sheets of UDR and MSCR.

REFERENCES

[1] R.W.G. Wyckoff, Crystal Structures, II ed., Interscience Publishers1963.

[2] A. Powell, A Magnesium Clean Energy Ecosystem Vision, Magnesium Technology 2022, Springer2022, pp. 121-126.

[3] M.M. Avedesian, H. Baker, ASM specialty handbook: magnesium and magnesium alloys, ASM international1999.

[4] M. Yeganeh, N. Mohammadi, Superhydrophobic surface of Mg alloys: A review, Journal of magnesium and alloys 6(1) (2018) 59-70.

[5] C. Romanowski, Magnesium alloy sheet for transportation applications, Magnesium Technology 2019 (2019) 3-12.

[6] K. Matucha, Structure and properties of nonferrous alloys, R.W. Cahn, P. Haasen, E.J. Kramer ed., VCH Verlagsgesellschaft GmbH, P. O. Box 10 11 61, Weinheim, D-69451, Germany, Germany, 1996.

[7] H.E. Friedrich, B.L. Mordike, Magnesium technology, Springer2006.

[8] J. Bohlen, D. Letzig, K.U. Kainer, New perspectives for wrought magnesium alloys, Materials Science Forum, Trans Tech Publ, 2007, pp. 1-10.

[9] T. Mukai, Ductility enhancement in AZ31 magnesium alloy by controlling its grain structure, Scripta Materialia 45(1) (2001) 6.

[10] M.F. Ashby, Materials selection in mechanical design, 1992.

[11] D. Klaumünzer, J.V. Hernandez, S. Yi, D. Letzig, S.-h. Kim, J.J. Kim, M.H. Seo, K. Ahn, Magnesium process and alloy development for applications in the automotive industry, Magnesium Technology 2019, Springer, 2019, pp. 15-20.

[12] S. Wang, C. Chou, Effect of adding Sc and Zr on grain refinement and ductility of AZ31 magnesium alloy, Journal of Materials Processing Technology 197(1-3) (2008) 116-121.

[13] D. Eliezer, E. Aghion, F. Froes, Magnesium science, technology and applications, Advanced Performance Materials 5 (1998) 201-212.

[14] R.V. Mises, Mechanics of plastic deformation of crystals, Journal of Applied Mathematics and Mechanics 8(3) (1928) 161-185.

[15] M. Yoo, Slip, twinning, and fracture in hexagonal close-packed metals, Metallurgical and Materials Transactions A 12A (1981) 161-185.

[16] J. Bohlen, S. Yi, D. Letzig, K.U. Kainer, Effect of rare earth elements on the microstructure and texture development in magnesium–manganese alloys during extrusion, Materials Science and Engineering: A 527(26) (2010) 7092-7098

[17] J. Bohlen, Nürnberg, MR; Senn, JW; Letzig, D; Agnew, SR, The texture and anisotropy of magnesium–zinc–rare earth alloy sheets, Acta Materialia 55(6) (2007) 2101-2112.

[18] T. Al-Samman, Sheet texture modification in magnesium-based alloys by selective rare earth alloying, Materials Science and Engineering A 528(10-11) (2011) 14.

[19] Y. Chino, Kado, M; Mabuchi, M, Compressive deformation behavior at room temperature – 773 K in Mg–0.2 mass% (0.035at.%)Ce alloy, Acta Materialia 56(3) (2008) 387-394.

[20] I. Basu, T. Al-Samman, G. Gottstein, Shear band-related recrystallization and grain growth in two rolled magnesium-rare earth alloys, Materials Science and Engineering: A 579 (2013) 50-56.

[21] A. Imandoust, C. Barrett, T. Al-Samman, K. Inal, H. El Kadiri, A review on the effect of rare-earth elements on texture evolution during processing of magnesium alloys, Journal of materials science 52 (2017) 1-29.

[22] A.K.G. Raja K. Mishra, P. Rama Rao, Anil K. Sachdev,, A.M.K.a.A.A. Luo, Influence of cerium on the texture and ductility of magnesium extrusions, Scripta Materialia 59 (2008) 562-565.

[23] R. Sabat, Mishra, RK, Sachdev, AK, Suwas, Satyam, The deciding role of texture on ductility in a Ce containing Mg alloy, Materials Letters 153 (2015) 158-161.

[24] A.B. Raja K. Mishra, Rama Krushna Sabat, Li Jin, Kaan Inal, Twinning and Texture Randomization in Mg and Mg-Ce alloys, J of Plasticity 117 (2019) 157-162.

[25] R. Sabat, A. Brahme, R. Mishra, K. Inal, S. Suwas, Ductility enhancement in Mg-0.2% Ce alloys, Acta Materialia 161 (2018) 246-257.

[26] J.S.D. F.A. Slooff, J. Zhou, J. Duszczyk, L. Katgerman, Hot workability analysis of extruded AZ magnesium alloys with processing maps, Materials Science and Engineering A 527 (2010) 735–744.

[27] Y. Prasad, K. Rao, S. Sasidhar, Hot working guide: a compendium of processing maps, ASM international2015.

[28] C. Roucoules, P. Hodgson, S. Yue, J. Jonas, Softening and microstructural change following the dynamic recrystallization of austenite, Metallurgical and Materials transactions A 25 (1994) 389-400.

[29] H. Zhang, G. Huang, D. Kong, G. Sang, B. Song, Influence of initial texture on formability of AZ31B magnesium alloy sheets at different temperatures, Journal of Materials Processing Technology 211(10) (2011) 1575-1580.

[30] S. Yi, J. Bohlen, F. Heinemann, D. Letzig, Mechanical anisotropy and deep drawing behaviour of AZ31 and ZE10 magnesium alloy sheets, Acta Materialia 58(2) (2010) 592-605.

[31] J. Robson, A. Twier, G. Lorimer, P. Rogers, Effect of extrusion conditions on microstructure, texture, and yield asymmetry in Mg–6Y–7Gd–0.5 wt% Zr alloy, Materials Science and Engineering: A 528(24) (2011) 7247-7256-N.

[32] J. Szpunar, Icotom-12: Proceedings of the Twelfth International Conference on Textures of Materials, McGill University, Montreal, Canada August 9 - 13, 1999, NRC Research Press1999.

[33] A. Böcker, H. Klein, H. Bunge, Development of cross-rolling textures in AlMn1, Textures and Microstructures 12 (1990)-N.P. Gurao, S. Suwas, Study of texture evolution in metastable β-Ti alloy as a function of strain path and its effect on α transformation texture, Materials Science and Engineering: A 504(1-2) (2009) 24-35.

[34] T. Al-Samman, Gottstein, G, Influence of strain path change on the rolling behavior of twin roll cast magnesium alloy, Scripta Materialia 59(7) (2008) 760-763.

[35] X. Gu, Zheng, Yufeng, Cheng, Yan, Zhong, Shengping, Xi, Tingfei, In vitro corrosion and biocompatibility of binary magnesium alloys, Biomaterials 30(4) (2009) 484-498.

[36] H. Wang, Estrin, Yuri, Fu, Huameng, Song, Guangling, Zúberová, Zuzana, The effect of pre-processing and grain structure on the bio-corrosion and fatigue resistance of magnesium alloy AZ31, Advanced Engineering Materials 9(11) (2007) 967-972.

[37] N.N. Aung, Zhou, Wei, Effect of grain size and twins on corrosion behaviour of AZ31B magnesium alloy, Corrosion Science 52(2) (2010) 589-594.

[38] N. Birbilis, Easton, Mark A, Sudholz, AD, Zhu, Su-Ming, Gibson, MA, On the corrosion of binary magnesium-rare earth alloys, Corrosion Science 51(3) (2009) 683-689.

[39] P. Partridge, The crystallography and deformation modes of hexagonal close-packed metals International Metallurgical Reviews 12 (1967) 26.

[40] B. Cullity, Elements of X-Ray Diffraction', , Addison-Wesley Publishing Company Inc1956.

[41] G. Gottstein, Physical Foundation of Materials Science Springer-Verlag Berlin Heidelberg GmbH2004.

[42] R. von Mises, Mechanics of plastic deformation of crystals. , Journal of Applied Mathematics and Mechanics (1928) 24.

[43] B Beausir, Tóth, László S.; Qods, Fathallah; Neale, Kenneth W, Texture and Mechanical Behavior of Magnesium During Free-End Torsion. , Journal of Engineering Materials and Technology 131 (2009) 15.

[44] S. Graff, Yielding of magnesium: From single crystal to polycrystalline aggregates, International Journal of Plasticity 23(12) (2007) 1957-1978.

[45] D. Hull, Introduction to Dislocations, Butterworth Heinmann (1965) 268.

[46] B. Wonsiewicz, Plasticity of magnesium crystal, , Transaction of the Metallurgical Society (1967).

[47] A. Akhtar, Teghtsoonian, E, Solid solution strengthening of magnesium single crystals—I alloying behaviour in basal slip. , 17(11), 1339–1349, Acta materialia 17(11) (1969) 1339–1349.

[48] M.F. Stefanie Sandlöbes, Jörg Neugebauer, Dierk Raabe, Basal and non-basal dislocation slip in Mg–Y, Materials Science & Engineering A 576 (2013) 8.

[49] H. Conrad, Effect of temperature on the flow stress and strain-hardening coefficient of magnesium single crystals. , Journal of Metals 9(4) (1957) 10.

[50] R. Reed-Hill, Deformation of Magnesium Single Crystals By Nonbasal Slip, Journal of Metals (1957) 7.

[51] W. Hutchinson, Effective values of critical resolved shear stress for slip in polycrystalline magnesium and other hcp metals, Scripta Materialia 63 (2010) 4.

[52] T. Obara, {11-22}<-1-123SLIP SYSTEM IN MAGNESIUM, Acta materialia 21 (1973) 9.

[53] J. Stohr, Electron Microscope Study of Pyramidal Slip {11-22} 〈11-23〉 in Magnesium, philosophical Magazine 25(6) (1972) 18.

[54] S. Agnew, Duygulu, O, Plastic anisotropy and the role of non-basal slip in magnesium alloy AZ31B, International Journal of Plasticity 21(6) (2005) 33.

[55] J. Koike, The activity of non-basal slip systems and dynamic recovery at room temperature in fine-grained AZ31B magnesium alloys, Acta Materialia 51(7) (2003) 2055-2065.

[56] H. Wang, Evaluation of self-consistent polycrystal plasticity models for magnesium alloy AZ31B sheet, International Journal of Solids and Structures 47(21) (2010) 2905-2917.

[57] G. Martin, Microscale plastic strain heterogeneity in slip dominated deformation of magnesium alloy containing rare earth, Materials Science and Engineering: A 603 (2014) 37-51.

[58] F. Xu, Modeling lattice strain evolution during uniaxial deformation of textured Zircaloy-2, Acta Materialia 56(14) (2008) 3672-3687.

[59] B. Hutchinson, A minimum parameter approach to crystal plasticity modelling, Acta Materialia 60(15) (2012) 8.

[60] A. Akhtar, Substitutional solution hardening of magnesium single crystals, Philosophical Magazine 25(4) (1972) 897-916.

[61] A. Chapuis, Temperature dependency of slip and twinning in plane strain compressed magnesium single crystals, Acta materialia 59(5) (2011) 9.

[62] W. Puschl, Models for dislocation cross-slip in close-packed crystal structures: a critical review, Progress in Materials Science 47 (2002) 47.

[63] A. Couret, An in-situ study of prismatic glide in magnesium—I. The rate controlling mechanism. , , Acta materialia 33(8) (1985) 7.

[64] A. Couret, Prismatic glide in divalent h.c.p. metals, Philosophical Magazine A 63(5) (1991) 1045-1057.

[65] J. Friedel, Dislocations: international series of monographs on solid state physics, Elsevier2013-B. Escaig, Thermal activation of low-stress deviations in h.c. and c.c. structures Para. , physica status solidi 28(2) (1968).

[66] Y. Tang, Formation and slip of pyramidal dislocations in hexagonal close-packed magnesium single crystals, Acta materialia 71 (2014) 14.

[67] M. Yoo, Nonbasal deformation modes of HCP metals and alloys Role of dislocation source and mobility, Metallurgical and Materials Transactions A 33(3) (2002) 10.

[68] M. Yoo, Non-basal slip systems in HCP metals and alloys source mechanisms, Materials Science and Engineering A 319-321 (2001) 6.

[69] Y. Minonishi, The core structure of 1/3⟨1123⟩ {1122} edge dislocations in h.c.p. metals, Philosophical Magazine A 43(4) (1981) 1017-1026.

[70] H. Numakura, 1123 1011 slip in titanium polycrystals at room temperature, Scripta Materialia 20(11) (1986) 6.

[71] C. Greeff, Ab initioi thermoelasticity of magnesium, Physical Review B 59(5) (1999) 7.

[72] D. Bacon, Computer simulation of dislocation cores in h.c.p. metals I. Interatomic potentials and stacking-fault stability, Philosophical Magazine A 53(2) (1986) 163-179.

[73] C. Pascal, Paleostress Inversion Techniques: Methods and Applications for Tectonics, Elsevier2021.

[74] J. Christian, Encyclopedia of Materials: Science and Technology, Elsevier2001.

[75] B. Li, Atomic shuffling dominated mechanism for deformation twinning in magnesium, Phys Rev Lett 103(3) (2009) 035503.

[76] Hertzberg, Deformation and fracture mechanics in engineering materials, John Wiley and Son Inc. Singapore1996.

[77] M. Nave, Microstructures and textures of pure magnesium deformed in plane-strain compression, Scripta Materialia 51(9) (2004) 881-885.

[78] M. Arul Kumar, Deformation twinning and grain partitioning in a hexagonal close-packed magnesium alloy nature communications 9 (2018) 8.

[79] M.R. Barnett, Twinning and the ductility of magnesium alloys-Part II. “Contraction” twins, Materials Science and Engineering: A 464(1-2) (2007) 8-16.

[80] L. Jiang, Twinning and texture development in two Mg alloys subjected to loading along three different strain paths, Acta Materialia 55(11) (2007) 3899-3910.

[81] N. Thompson, Twin formation in cadmium, Philosophical Magazine 43(339) (1952) 18.

[82] E.K. Orowan, JS; Cohen, M; Seitz, F; Read, WT; Shockley, W, Dislocations in metals, 1954.

[83] R. Bell, The Dynamics of Twinning and the Interrelation of Slip and Twinning in Zinc Crystals, Proc. R. Soc. Lond. A 239 (1957) 43.

[84] P.B. Price, Pyramidal glide and the formation and climb of dislocation loops in nearly perfect zinc crystals, Philosophical Magazine 5(57) (1960) 873-886.

[85] S. Mendelson, Dislocation Dissociations in hcp Metals, Journal of Applied Physics 41(5) (1970) 1893-1910.

[86] M. Yoo, Deformation twinning in h.c.p. metals and alloys, philosophical Magazine 63(5) (1991) 15.

[87] A. Jain, Modeling the temperature dependent effect of twinning on the behavior of magnesium alloy AZ31B sheet, Materials Science and Engineering: A 462(1-2) (2007) 29-36.

[88] S. Agnew, Application of texture simulation to understanding mechanical behaviour of Mg and solid solution alloys containing Li or Y, Acta materialia 49(20) (2001) 13.

[89] C. Tome, A model for texture development dominated by deformation twinning: Application to zirconium alloys, Acta materialia 39(11) (1991) 14.

[90] M. Barnett, Non-Schmid behaviour during secondary twinning in a polycrystalline magnesium alloy, Acta materialia 56 (2008) 11.

[91] J. Jonas, The role of strain accommodation during the variant selection of primary twins in magnesium, Acta Materialia 59(5) (2011) 2046-2056.

[92] M. Barnett, Microstructural features of rolled Mg-3Al-1Zn, Metallurgical and Materials Transactions A 36(7) (2005) 8.

[93] D. Sarker, Detwinning and strain hardening of an extruded magnesium alloy during compression, Scripta Materialia 67(2) (2012) 165-168.

[94] D. Brown, Twinning and detwinning during cyclic deformation of Mg alloy AZ31B.f>, Materials Science Forum 539-543 (2007) 7.

[95] M.R. Barnett, Twinning and the ductility of magnesium alloys-Part I: “Tension” twins, Materials Science and Engineering: A 464(1-2) (2007) 1-7-J. Scott, Room Temperature Shear Band Development in Highly Twinned Wrought Magnesium AZ31B Sheet, Metallurgical and Materials Transactions A 44(1) (2013) 5.

[96] S. Sandlobes, Zaefferer, S; Schestakow, I; Yi, S; Gonzalez-Martinez, R, On the role of non-basal deformation mechanisms for the ductility of Mg and Mg–Y alloys, Acta materialia 59(2) (2011) 11.

[97] J.P. Hadorn, K. Hantzsche, S. Yi, J. Bohlen, D. Letzig, J.A. Wollmershauser, S.R. Agnew, Role of Solute in the Texture Modification During Hot Deformation of Mg-Rare Earth Alloys, Metallurgical and Materials Transactions A 43(4) (2011) 1347-1362.

[98] N. Stanford, Barnett MR The origin of "rare earth" texture development in extruded Mg-based alloys and its effect on tensile ductility, Materials Science and Engineering: A 496(1-2) (2008) 399-408.

[99] X. Li, Orientational analysis of static recrystallization at compression twins in a magnesium alloy AZ31, materials Science & Engineering A 517(1-2) (2009) 10.

[100] M.R. Barnett, Influence of microstructure on strain distribution in Mg–3Al–1Zn, Scripta Materialia 57(12) (2007) 1125-1128.

[101] S. Harren, Shear band formation in plane strain compression, Acta materialia 36(9) (1988) 46.

[102] S. Ion, Dynamic recrystallisation and the development of microstructure during the high temperature deformation of magnesium, Acta materialia 30(10) (1982) 11.

[103] S. Couling, Unique deformation and aging characteristics of certain magnesium-base alloys, Transactions of the ASM 51 (1959) 14.

[104] M. Barnett, Deformation microstructures and textures of some cold rolled Mg alloys, Materials Science & Engineering A 386(1-2) (2004) 7.

[105] A. Yamashita, Improving the mechanical properties of magnesium and a magnesium alloy through severe plastic deformation. , Materials Science and Engineering A 300(1-2) (2001) 6.

[106] W. Kim, Texture development and its effect on mechanical properties of an AZ61 Mg alloy fabricated by equal channel angular pressing, Acta materialia 51(11) (2003) 15.

[107] J.A. del Valle, Carreño, F; Ruano, O. A., Influence of texture and grain size on work hardening and ductility in magnesium-based alloys processed by ECAP and rolling, Acta Materialia 54(16) (2006) 4247-4259.

[108] H. Riedel, Fracture at High Temperatures, 1987.

[109] M.R. Barnett, Influence of grain size on the compressive deformation of wrought Mg–3Al–1Zn, Acta Materialia 52(17) (2004) 5093-5103.

[110] F. Hauser, Fracture of magnesium alloys at low temperature, JOM 8(5) (1956) 589-592.

[111] J. Koike, Grain-Boundary Sliding in AZ31 Magnesium Alloys at Room Temperature to 523 K. , MATERIALS TRANSACTIONS 44(4) (2003) 7.

[112] S. Agnew, Study of slip mechanisms in a magnesium alloy by neutron diffraction and modeling, Scripta Materialia 48(8) (2003) 6.

[113] S. Agnew, A Mechanistic Understanding of the Formability of Magnesium: Examining the Role of Temperature on the Deformation Mechanisms, Materials Science Forum 419-422 (2003) 13.

[114] R. Lebensohn, A self-consistent anisotropic approach for the simulation of plastic deformation and texture development of polycrystals Application to zirconium alloys, Acta materialia 41(9) (1993) 14.

[115] S. Ando, Non-Basal Slip in Magnesium-Lithium Alloy Single Crystals. , Materials Transactions 41(9) (2000).

[116] M. Pérez-Prado, Microstructural evolution during large strain hot rolling of an AM60 Mg alloy, Scripta Materialia 50(5) (2004) 661-665.

[117] G. Taylor, Plastic Strain in Metals, Transaction of the Metallurgical Society (62) (1938) 14.

[118] A. Styczynski, Hartig, Ch; Bohlen, J; Letzig, D, Cold rolling textures in AZ31 wrought magnesium alloy, Scripta Materialia 50(7) (2004) 943-947.

[119] F.H. Humphreys, M, Recrystallization and Related Annealing Phenomena II Ed, , Elsevier2004.

[120] D. Sastry, On the stacking fault energies of some close-packed hexagonal metals, Scripta Materialia 3(12) (1969) 3.

[121] H. Somekawa, Dislocation creep behavior in Mg–Al–Zn alloys, Materials Science and Engineering: A 407(1-2) (2005) 53-61.

[122] G. Gottstein, Dynamic recrystallization and dynamic recovery in 111 single crystals of nickel and copper, Acta materialia 31(1) (1983) 14.

[123] A. Galiyev, Correlation of plastic deformation and dynamic recrystallization in magnesium alloy ZK60., Acta materialia 49(7) (2001) 8.

[124] Y. He, Microstructure and mechanical properties of ZK60 alloy processed by two-step equal channel angular pressing, Journal of alloys and compound 492(1-2) (2010) 10

[125] M. Tan, Dynamic continuous recrystallization characteristics in two stage deformation of Mg–3Al–1Zn alloy sheet, Materials Science and Engineering A 339 (2003) 9.

[126] D.J. Mote JD, Deformation and Fracture of Magnesium Bicrystals, Transaction of Metallurgical Society AIME 218(3) (1960) 491-497.

[127] R. Doherty, Current issues in recrystallization a review, Materials Science and Engineering A 238 (1997) 56.

[128] T. Al-Samman, Dynamic recrystallization during high temperature deformation of magnesium, Materials Science & Engineering A 490(1-2) (2008) 10.

[129] V. Nesterenko, Shear localization and recrystallization in high-strain, high-strain-rate deformation of tantalum, Materials Science and Engineering A 229(1-2) (1997) 19.

[130] K. Zhu, A study of recovery and primary recrystallization mechanisms in a Zr–2Hf alloy, Acta Materialia 53(19) (2005) 5131-5140.

[131] T. Al-Samman, Softening and dynamic recrystallization in magnesium single crystals during c-axis compression, Acta materialia 60(2) (2012).

[132] H. Yan, Twins, shear bands and recrystallization of a Mg–2.0%Zn–0.8%Gd alloy during rolling, Scripta Materialia 64(2) (2011) 141-144.

[133] H. Paul, Shear banding and recrystallization nucleation in a Cu–2%Al alloy single crystal, Acta materialia 50(4) (2002) 16.

[134] L. Mackenzie, The recrystallization and texture of magnesium–zinc–cerium alloys, Scripta Materialia 59(6) (2008) 665-668.

[135] É. Martin, Effect of twinning on recrystallisation textures in deformed magnesium alloy AZ31, Philosophical Magazine 91(27) (2011) 3613-3626.

[136] A. Jäger, Influence of annealing on the microstructure of commercial Mg alloy AZ31 after mechanical forming, Materials Science and Engineering: A 432(1-2) (2006) 20-25.

[137] T. Al-Samman, Modification of texture and microstructure of magnesium alloy extrusions by particle-stimulated recrystallization, Materials Science and Engineering A 560 (2013) 6.

[138] J. Robson, Particle effects on recrystallization in magnesium–manganese alloys: Particle-stimulated nucleation, Acta Materialia 57(9) (2009) 2739-2747.

[139] E.A. Ball, Prangnell, P.B, Tensile-compressive yield asymmetries in high strength wrought magnesium alloys. , Scripta Metallurgica 31(2) (1994) 111-116.

[140] J. Robson, Particle effects on recrystallization in magnesium–manganese alloys: Particle-stimulated nucleation, Acta materialia 57(9) (2009) 6.

[141] M. Barnett, Quenched and Annealed Microstructures of Hot Worked Magnesium AZ31. , MATERIALS TRANSACTIONS 44(4) (2003) 7.

[142] R. Cottam, Dynamic recrystallization of Mg and Mg–Y alloys: Crystallographic texture development, Materials Science and Engineering: A 485(1-2) (2008) 375-382.

[143] G. Gottstein, Texture Development in Pure Mg and Mg Alloy AZ31, Materials Science Forum 495-497 (2005) 623-632.

[144] K. Lucke, Orientation relationships in the recrystallization of polycrystalline, hexagonal metals, Metallurgical Transactions 1 (1970) 8.

[145] K.D. Molodov, Mechanisms of exceptional ductility of magnesium single crystal during deformation at room temperature: Multiple twinning and dynamic recrystallization, Acta Materialia 76 (2014) 314-330.

[146] B. Liebmann, Investigations on the orientation dependence of the growth rate during the primary recrystallization of aluminum single crystals, International Journal of Materials Research 47(2) (1956) 7.

[147] D. Juul Jensen, Growth rates and misorientation relationships between growing nucleigrains and the surrounding deformed matrix during recrystallization. , , Acta materialia 43(11) (1995) 13.

[148] R. Doherty, Nucleation of recrystallization in cold and hot deformed polycrystals, (1995).

[149] O. Engler, On the origin of theRorientation in the recrystallization textures of aluminum alloys, Metallurgical and Materials Transactions A 30(6) (1999) 11

[150] G.S. Gottstein, I; Nadella, R K, Static recrystallisation and textural changes in warm rolled pure magnesium, in: D.K. Kainer (Ed.) Magnesium: Proceedings of the 6th International Conference Magnesium Alloys and Their Applications, Wiley Online Library, 2003, pp. 1052-1057.

[151] S. Suwas, Evolution of hot rolling textures in a two-phase (α2+β) Ti3Al base alloy, Acta materialia 47(18) (1999) 14.

[152] F. Wagner, Evolution of recrystallisation texture and microstructure in low alloyed titanium sheets, Acta materialia 50(5) (2002) 15.

[153] S. Biswas, Grain Growth in ECAE Processed Pure Magnesium, Proc Int conf. Microstructure and texture in steels and other materials,ISBN 978-1-848. (2009) 9.

[154] L.L. Rokhlin, Magnesium Alloys Containing Rare Earth Metals: Structure and Properties, CRC Press2003.

[155] I. Polmear, Magnesium alloys and applications, Materials Science and Technology1994.

[156] N. Stanford, Effect of microalloying with rare-earth elements on the texture of extruded magnesium-based alloys, Scripta Materialia 59(7) (2008) 772-775.

[157] A. Nayeb-Hashemi, Ce-Mg System, Bulletin of Alloys Phase Diagram 9(2) (1988) 10.

[158] A. Miller, The crystal structure of the intermetallic compound Mg12Ce. II. Reaction products of gamma-picoline and iodine, California Institute of Technology, 1957.

[159] J. Robson, Effect of extrusion conditions on microstructure, texture, and yield asymmetry in Mg–6Y–7Gd–0.5wt%Zr alloy, Materials Science and Engineering: A 528(24) (2011) 7247-7256.

[160] K. Hantzsche, Effect of rare earth additions on microstructure and texture development of magnesium alloy sheets, Scripta Materialia 63(7) (2010) 725-730.

[161] J. Hadorn, Role of Solute in the Texture Modification During Hot Deformation of Mg-Rare Earth Alloys, Metallurgical and Materials Transactions A 43A(4) (2011) 16.

[162] S. Farzadfar, On the deformation, recrystallization and texture of hot-rolled Mg–2.9Y and Mg–2.9Zn solid solution alloys—A comparative study, Materials Science & Engineering A 534 (2012) 11.

[163] N. Stanford, The effect of rare earth elements on the behaviour of magnesium-based alloys: Part 1—Hot deformation behaviour, materials Science & Engineering A 565 (2013) 9.

[164] P. Wellstead, Introduction to Physical System Modelling, Academic Press1979.

[165] Y. Prasad, Modelling of hot deformation for microstructural control. International Materials Reviews, , International Materials Reviews 43(6) (1998) 16.

[166] Y. Prasad, Processing maps: A status report, Journal of Materials Engg and Performance 12(6) (2003) 7.

[167] V. Gopala Krishna, Processing map for the hot working of near-α titanium alloy 685, J. Mater. Process. Technol 71(3) (1997) 6.

[168] H. Ziegler, Some Extremum Principles in Irreversible Thermodynamics, with Application to Continuum Mechanics, Swiss Federal Institute of Technology, Eidgenössische Technische Hochschule, 1962.

[169] Y. Prasad, Recent advances in the science of mechanical processing, Indian Journal of Technology 28(6-8) (1990) 435-451.

[170] Y. Prasad, K. Rao, S. Sasidhar, Hot working guide: a compendium of processing maps, ASM international2015.

[171] O. Sivakesavam, Characteristics of superplasticity domain in the processing map for hot working of as-cast Mg–11.5Li–1.5Al alloy. , 323(1-2), 270–277. , Materials Science and Engineering A 232 (2002) 270-277.

[172] O. Sivakesavam, Processing Map for Hot Working of Hot Rolled Mg-11.5Li-1.5Al Alloy, International Journal of Materials Research 93(2) (2002) 5.

[173] N. Srinivasan, Hot deformation behaviour of Mg–3Al alloy — A study using processing map, materials Science & Engineering A 476 (2008) 11.

[174] B. Deogade, N and Kalsar, R and Acharyya, SG and Suresh, KS, Constitutive Modelling of Hot Deformation Behaviour of Mg-0.5wt% Ce Alloy, Transactions of the Indian Institute of Metals 76(11) (2023) 2953–2962.

[175] S.B. Davenport, Development of constitutive equations for modelling of hot rolling, Materials Science and Technology 16(5) (2000) 8

[176] F. Zerilli, Dislocation-mechanics-based constitutive relations for material dynamics calculations, Journal of applied physics 61(5) (1987) 1816-1825.

[177] U. Kocks, Realistic constitutive relations for metal plasticity, Materials Science & Engineering A 317(1-2) (2001) 7.

[178] G. Johnson, A constitutive model and data for metals subjected to large strains, high strain rates and high temperatures, Proceedings of the 7th International Symposium on Ballistics. (1983) 7.

[179] C. Sellars, On the mechanism of hot deformation. , Acta materialia 14(9) (1966) 3.

[180] J. Gao, Microstructure and kinetics of hot deformation WE43 magnesium alloy, Rare Metals 27(4) (2008) 405-409.

[181] P. Changizian, The high temperature flow behavior modeling of AZ81 magnesium alloy considering strain effects, Materials & Design 39 (2012) 384-389.

[182] A. Hadadzadeh, Analysis of the hot deformation of ZK60 magnesium alloy, Journal of Magnesium and Alloys 5(4) (2017) 369-387.

[183] H. Mirzadeh, Developing constitutive equations of flow stress for hot deformation of AZ31 magnesium alloy under compression, torsion, and tension, International Journal of Material Forming 12(4) (2018) 643-648.

[184] Y. Lin, Constitutive modeling for elevated temperature flow behavior of 42CrMo Steel - 2008, Computational Materials Science 42 (2008) 470-477.

[185] A. Kumar, Gupta, A; Khatirkar, R K; Bibhanshu, N; Suwas, S, Strain Rate Sensitivity Behaviour of a Chrome-Nickel Austentic-Ferritic Stainless Steel and its Constitutive Modelling, ISIJ International 58(10) (2018) 1840-1849.

[186] E. Yukutake, J. Kaneko, M. Sugamata, Anisotropy and non-uniformity in plastic behavior of AZ31 magnesium alloy plates, Materials Transactions 44(4) (2003) 452-457.

[187] K. Matsubara, Y. Miyahara, Z. Horita, T. Langdon, Developing superplasticity in a magnesium alloy through a combination of extrusion and ECAP, Acta materialia 51(11) (2003) 3073-3084

[188] A. Davis, J. Robson, M. Turski, Reducing yield asymmetry and anisotropy in wrought magnesium alloys–A comparative study, Materials Science and Engineering: A 744 (2019) 525-537.

[189] B. Bay, N. Hansen, D. Kuhlmann-Wilsdorf, Deformation structures in lightly rolled pure aluminium, Materials Science and Engineering: A 113 (1989) 385-397

[190] R.S.C. H. Hu, On the mechanism of texture transition in face centered cubic metals,, Textures Microstructure 8 & 9 (1988) 191-206

[191] M. Huh, S. Cho, O. Engler, Randomization of the annealing texture in aluminum 5182 sheet by cross-rolling, Materials Science and Engineering: A 315(1-2) (2001) 35-46.

[192] J. Schmitt, J. Fernandes, J. Gracio, M. Vieira, Plastic behaviour of copper sheets during sequential tension tests, Materials Science and Engineering: A 147(2) (1991) 143-154.

[193] T. Öztürk, Deformation and recrystallization textures in cross-rolled sheets of copper and α-brass, (1988)

[194] B. Verlinden, J. Driver, I. Samajdar, R.D. Doherty, Thermo-mechanical processing of metallic materials, Elsevier2007.

[195] M. Rout, S.K. Pal, S.B. Singh, Cross rolling: a metal forming process, Modern manufacturing engineering (2015) 41-64.

[196] ASM, Corrosion, 9th ed., 13 (1987).

[197] L. Shreir, R. Jarman, G. Burstein, Corrosion, vol. 1, Butterworth-Heinemann, Oxford1994.

[198] D.A. Jones, Principles and Prevention of Corrosion, Prentice-Hall1996.

[199] R.W. Revie, Corrosion Handbook, John Wiley and Sons, New York, New York, 2011.

[200] M.G. Fontana, N.D. Greene, Corrosion engineering, McGraw-hill2018.

[201] G.S. S-Z Oo, F Carpignano, A Nouat, K Pechstedt, L Mateos, JA Grant Jacob, B Brocklesby, P Horak, M Charlton, St A Boden, T Melvin, Supplimentary Information - A nanoporous gold membrane for sensing applications, 3 (2016).

[202] M. Pourbaix, Atlas of Electrochemical Equilibria in Aqueous Solutions, NACE II ed (1974).

[203] A.-M. Lafront, W. Zhang, S. Jin, R. Tremblay, D. Dubé, E. Ghali, Pitting corrosion of AZ91D and AJ62x magnesium alloys in alkaline chloride medium using electrochemical techniques, Electrochimica Acta 51(3) (2005) 489-501.

[204] T. Zhang, Y. Shao, G. Meng, F. Wang, Electrochemical noise analysis of the corrosion of AZ91D magnesium alloy in alkaline chloride solution, Electrochimica Acta 53(2) (2007) 561-568.

[205] M. Santamaria, F. Di Quarto, S. Zanna, P. Marcus, Initial surface film on magnesium metal: A characterization by X-ray photoelectron spectroscopy (XPS) and photocurrent spectroscopy (PCS), Electrochimica Acta 53(3) (2007) 1314-1324.

[206] G. Song, A. Atrens, Understanding magnesium corrosion—a framework for improved alloy performance, Advanced engineering materials 5(12) (2003) 837-858.

[207] G. Baril, N. Pebere, The corrosion of pure magnesium in aerated and deaerated sodium sulphate solutions, Corrosion science 43(3) (2001) 471-484.

[208] S. Fajardo, F.R. García-Galvan, V. Barranco, J.C. Galvan, S.F. Batlle, A critical review of the application of electrochemical techniques for studying corrosion of mg and mg alloys: Opportunities and challenges, 2018.

[209] A. Pardo, M. Merino, A.E. Coy, R. Arrabal, F. Viejo, E. Matykina, Corrosion behaviour of magnesium/aluminium alloys in 3.5 wt.% NaCl, Corrosion Science 50(3) (2008) 823-834.

[210] K. Ralston, N. Birbilis, C. Davies, Revealing the relationship between grain size and corrosion rate of metals, Scripta Materialia 63(12) (2010) 1201-1204.

[211] B. Wang, D. Xu, Y. Xin, L. Sheng, E. Han, High corrosion resistance and weak corrosion anisotropy of an as-rolled Mg-3Al-1Zn (in wt.%) alloy with strong crystallographic texture, Scientific Reports 7(1) (2017) 16014.

[212] G.-L. Song, Z. Xu, The surface, microstructure and corrosion of magnesium alloy AZ31 sheet, Electrochimica acta 55(13) (2010) 4148-4161.

[213] P. Yu, S.A. Hayes, M. O'Keefe, J.O. Stoffer, T.J. O'Keefe, The phase stability of cerium species in aqueous systems: II. the Ce (III/IV)-H_2O-H_2O_2/O_2 systems. Equilibrium considerations and Pourbaix diagram calculations, (2006).

[214] J. Fernandes, Curso de Espectroscopia de Impedância Electroquímica, Instituto Superior Técnico, Lisboa, 2008.

[215] R. Cottis, S. Turgoose, N. International, Electrochemical Impedance and Noise, NACE International1999.

[216] J.R. Macdonald, Impedance Spectroscopy, Theory, Experiment, and Applications, Wiley-Interscience2005.

[217] K.S. Cole, Cole, R. H, Dispersion and Absorption in Dielectrics - I Alternating Current Characteristics, J. Chem. Phys 9 (1941) 341-352.

[218] M.G.S. Ferreira, Melendres, C. A. , Electrochemical and Optical Techniques for the Study and Monitoring of Metallic Corrosion, Kluwer Academic Publishers Group1991.

[219] I. Singh, P. Gupta, A. Maheshwari, N. Agrawal, Corrosion resistance of sol–gel alumina coated Mg metal in 3.5% NaCl solution, Journal of Sol-Gel Science and Technology 73 (2015) 127-132.

[220] I. Singh, M. Singh, S. Das, A comparative corrosion behavior of Mg, AZ31 and AZ91 alloys in 3.5% NaCl solution, Journal of Magnesium and Alloys 3(2) (2015) 142-148.

[221] Y. Leng, Materials characterization: introduction to microscopic and spectroscopic methods, John Wiley & Sons2013.

[222] R. Leach, L. Brown, X. Jiang, R.T. Blunt, M. Conroy, D.T. Mauger, Guide to the measurement of smooth surface topography using coherence scanning interferometry, 2008.

[223] O. Sivakesavam, Processing map for hot working of as cast magnesium, Materials science and technology 9(9) (1993) 805-810.

[224] X.Z. Ding, F.; Shuang, Y.; Ma, L.; Chu, Z.; Zhao, Characterization of hot deformation behavior of as-extruded AZ31 alloy through kinetic analysis and processing maps. Journal of Materials Processing Technology,, Journal of materials processing technology 276 (2020).

[225] W.F. Jingfeng, Xie; Shijie, Liu; Song, Huang; Fusheng, Pan Hot Deformation Behavior and Processing Maps of As-Homogenized Mg-Gd-Y-Zn-Mn Alloy, Rare Metal Materials and Engineering 47(6) (2018) 1700–1707.

[226] O.K. Sitdikov, Rustam (2001). Dynamic Recrystallization in Pure Magnesium, MATERIALS TRANSACTIONS, 42(9) (2001) 1928-1937.

[227] J. Koike, Enhanced deformation mechanisms by anisotropic plasticity in polycrystalline Mg alloys at room temperature, J. Metall Mater Trans A 36(7) (2005) 1689-1696.

[228] S.R. Spigarelli, O.A.; El Mehtedi, M.; del Valle, J.A. , High temperature deformation and microstructural instability in AZ31 magnesium alloy. , Materials Science and Engineering: A 570 (2013) 135-148.

[229] Q.X. Chen, Xiangsheng; Yuan, Baoguo; Shu, Dayu; Zhao, Zude; Han, Jiecai Hot workability behavior of as-cast Mg–Zn–Y–Zr alloy, Materials Science and Engineering: A 593 (2014) 38–47.

[230] Z.L. Ge G, Xin J, Lin J, Mark Aindow and Zhang L, Constitutive modeling of high temperature flow behavior in a Ti-45Al-8Nb-2Cr-2Mn-0.2Y alloy, Scientific Reports 8(5453) (2018) 9.

[231] G.V. Raynor, The lattice spacings of the primary solid solutions of silver, cadmium and indium in magnesium, Proceedings of the Royal Society of

London. Series A. Mathematical and Physical Sciences 174(959) (1940) 457-471.

[232] X. Huang, K. Suzuki, N. Saito, Textures and stretch formability of Mg–6Al–1Zn magnesium alloy sheets rolled at high temperatures up to 793 K, Scripta materialia 60(8) (2009) 651-654.

[233] N. Gurao, S. Sethuraman, S. Suwas, Effect of strain path change on the evolution of texture and microstructure during rolling of copper and nickel, Materials Science and Engineering: A 528(25-26) (2011) 7739-7750.

[234] S. Biswas, D.-I. Kim, S. Suwas, Asymmetric and symmetric rolling of magnesium: Evolution of microstructure, texture and mechanical properties, Materials Science and Engineering: A 550 (2012) 19-30.

[235] J.P. Hadorn, R.P. Mulay, K. Hantzsche, S. Yi, J. Bohlen, D. Letzig, S.R. Agnew, Texture weakening effects in Ce-containing Mg alloys, Metallurgical and Materials Transactions A 44 (2013) 1566-1576.

[236] R. Walter, M.B. Kannan, Influence of surface roughness on the corrosion behaviour of magnesium alloy, Materials & Design 32(4) (2011) 2350-2354.

[237] A. International, Standard Practice for Exposure of Metals and Alloys by Alternate Immersion in Neutral 3.5 % Sodium Chloride Solution, in: A.C.G.-o.C.o. Metals (Ed.) Corrosion of Metals, ASTM, ASTM, 100 Barr Harbor Drive, West Conshohocken, PA 19428-2959, United States., 1999.

[238] M. Andrei, A. Eliezer, P. Bonora, E. Gutman, DC and AC polarisation study on magnesium alloys Influence of the mechanical deformation, Materials and Corrosion 53(7) (2002) 455-461.

[239] P. Bonora, M. Andrei, A. Eliezer, E. Gutman, Corrosion behaviour of stressed magnesium alloys, Corrosion Science 44(4) (2002) 729-749.

[240] F. Cao, Z. Shi, G.-L. Song, M. Liu, M.S. Dargusch, A. Atrens, Stress corrosion cracking of several hot-rolled binary Mg–X alloys, Corrosion Science 98 (2015) 6-19.

[241] J. Chen, J. Wang, E. Han, J. Dong, W. Ke, AC impedance spectroscopy study of the corrosion behavior of an AZ91 magnesium alloy in 0.1 M sodium sulfate solution, Electrochimica Acta 52(9) (2007) 3299-3309.

[242] F. Cao, G.-L. Song, A. Atrens, Corrosion and passivation of magnesium alloys, Corrosion Science 111 (2016) 835-845.

[243] G.-l. Song, A. Atrens, Corrosion mechanisms of magnesium alloys, Advanced Engineering Materials 1 (1999) 11-33

[244] F. Cao, Z. Shi, J. Hofstetter, P.J. Uggowitzer, G. Song, M. Liu, A. Atrens, Corrosion of ultra-high-purity Mg in 3.5% NaCl solution saturated with Mg (OH) 2, Corrosion Science 75 (2013) 78-99.

[245] Z. Shi, A. Atrens, An innovative specimen configuration for the study of Mg corrosion, Corrosion Science 53(1) (2011) 226-246.

[246] K.S. Shin, M.Z. Bian, N.D. Nam, Effects of crystallographic orientation on corrosion behavior of magnesium single crystals, Jom 64(6) (2012) 664-670.

[247] F. Zucchi, Grassi, V, Frignani, A, Monticelli, C, Trabanelli, G, Electrochemical behaviour of a magnesium alloy containing rare earth elements, Journal of Applied Electrochemistry 36 (2006) 195-204.

[248] X. Zhang, G. Wu, X. Peng, L. Li, H. Feng, B. Gao, K. Huo, P.K. Chu, Mitigation of corrosion on magnesium alloy by predesigned surface corrosion, Scientific Reports 5(1) (2015) 17399.

[249] L.G. Bland, K. Gusieva, J. Scully, Effect of crystallographic orientation on the corrosion of magnesium: comparison of film forming and bare crystal facets using electrochemical impedance and Raman spectroscopy, Electrochimica Acta 227 (2017) 136-151.

Draft for Checking

by Bhomik k Deogade

Submission date: 14-Dec-2023 05:08PM (UTC+0530)
Submission ID: 2258820121
File name: Thesis_Section_2_Intro_to_Future_Scope_-_Final-II.pdf (28.23M)
Word count: 41932
Character count: 230270

Draft for Checking

ORIGINALITY REPORT

10%	6%	6%	1%
SIMILARITY INDEX	INTERNET SOURCES	PUBLICATIONS	STUDENT PAPERS

PRIMARY SOURCES

1	fenix.tecnico.ulisboa.pt Internet Source	2%
2	www.tandfonline.com Internet Source	<1%
3	"Magnesium Technology 2017", Springer Science and Business Media LLC, 2017 Publication	<1%
4	worldwidescience.org Internet Source	<1%
5	"Magnesium Technology 2011", Wiley, 2011 Publication	<1%
6	Y.V.R.K. Prasad. "Processing Maps: A Status Report", Journal of Materials Engineering and Performance, 12/01/2003 Publication	<1%
7	"Essential Readings in Magnesium Technology", Wiley, 2014 Publication	<1%
8	R.K. Sabat, P.K. Samal, Muzzamil Ahamed S. "Effect of strain path on the evolution of	<1%

microstructure, texture and tensile properties of WE43 alloy", Materials Science and Engineering: A, 2018
Publication

9	Sivakesavam, O.. "Hot deformation behaviour of as-cast Mg-2Zn-1Mn alloy in compression: a study with processing map", Materials Science & Engineering A, 20031205 Publication	<1 %
10	Jianlei Yang, Guofeng Wang, Xueyan Jiao, You Li, Qing Liu. "High-temperature deformation behavior of the extruded Ti-22Al-25Nb alloy fabricated by powder metallurgy", Materials Characterization, 2018 Publication	<1 %
11	www.mdpi.com Internet Source	<1 %
12	Mandal, S.. "Constitutive equations to predict high temperature flow stress in a Ti-modified austenitic stainless steel", Materials Science & Engineering A, 20090125 Publication	<1 %
13	link.springer.com Internet Source	<1 %
14	Leslie G. Bland, K. Gusieva, J.R. Scully. "Effect of Crystallographic Orientation on the Corrosion of Magnesium: Comparison of Film	<1 %

	Forming and Bare Crystal Facets using Electrochemical Impedance and Raman Spectroscopy", Electrochimica Acta, 2017 Publication	
15	ebin.pub Internet Source	<1 %
16	eprints.iisc.ac.in Internet Source	<1 %
17	Submitted to Indian Institute of Science, Bangalore Student Paper	<1 %
18	Submitted to Indian Institute of Technology, Madras Student Paper	<1 %
19	espace.library.uq.edu.au Internet Source	<1 %
20	www.researchgate.net Internet Source	<1 %
21	Figueiredo, R.B.. "Evolution of texture in a magnesium alloy processed by ECAP through dies with different angles", Materials Science & Engineering A, 20100325 Publication	<1 %
22	vdoc.pub Internet Source	<1 %
23	Submitted to Sheffield Hallam University	

	Student Paper	<1%
24	www.hindawi.com Internet Source	<1%
25	I. Basu, T. Al-Samman. "Triggering rare earth texture modification in magnesium alloys by addition of zinc and zirconium", Acta Materialia, 2014 Publication	<1%
26	O. Sivakesavam, Y.V.R.K. Prasad. "Hot deformation behaviour of as-cast Mg–2Zn–1Mn alloy in compression: a study with processing map", Materials Science and Engineering: A, 2003 Publication	<1%
27	University of Tennessee, Knoxville Publication	<1%
28	iopscience.iop.org Internet Source	<1%
29	K. Ishikawa. "High temperature compressive properties over a wide range of strain rates in an AZ31 magnesium alloy", Journal of Materials Science, 04/2005 Publication	<1%
30	ir.lib.uwo.ca Internet Source	<1%

31	J.A. del Valle, O.A. Ruano. "Effect of annealing treatments on the anisotropy of a magnesium alloy sheet processed by severe rolling", Materials Letters, 2009 Publication	<1 %
32	Yudai Miyake, Yukio Sato, Ryo Teranishi, Kenji Kaneko. "Effect of heat treatments on the microstructure and formability of Al–Mg–Mn–Sc–Zr alloy", Micron, 2017 Publication	<1 %
33	Zehua Yan, Jingkai Zhou, Wei Zhang. "Microstructural evolution and dynamic recrystallization model of extruded homogenized AZ31 magnesium alloy during hot deformation", International Journal of Materials Research, 2023 Publication	<1 %
34	archive.org Internet Source	<1 %
35	coek.info Internet Source	<1 %
36	Yellapregada Venkata Rama Krishna Prasad. "Hot Workability, Microstructural Control and Rate-Controlling Mechanisms in Cast-Homogenized AZ31 Magnesium Alloy", Advanced Engineering Materials, 03/2009 Publication	<1 %

37	Yuan Zhang, Jianxing Li, Jingyuan Li. "Effects of microstructure transformation on mechanical properties, corrosion behaviors of Mg-Zn-Mn-Ca alloys in simulated body fluid", Journal of the Mechanical Behavior of Biomedical Materials, 2018 Publication	<1 %
38	Siying Deng, Hongwu Song, Huan Liu, Shi-Hong Zhang. "Effect of uniaxial loading direction on mechanical responses and texture evolution in cold pilgered Zircaloy-4 tube: Experiments and modeling", International Journal of Solids and Structures, 2021 Publication	<1 %
39	mdpi-res.com Internet Source	<1 %
40	Beausir, B.. "Analysis of microstructure and texture evolution in pure magnesium during symmetric and asymmetric rolling", Acta Materialia, 200910 Publication	<1 %
41	Dejin Wei, Ruirui Liu, Chengkun Zuo, Haitao Zhou. "High Temperature Plastic Deformation Constitutive Equation of a New Alloy for Piston Ring", Metals and Materials International, 2019 Publication	<1 %

42	Submitted to Middle East Technical University Student Paper	<1 %
43	d-nb.info Internet Source	<1 %
44	www.hereon.de Internet Source	<1 %
45	core.ac.uk Internet Source	<1 %
46	hrcak.srce.hr Internet Source	<1 %
47	Submitted to Coventry University Student Paper	<1 %
48	Qiang Wang, Xiyu He, Yunlai Deng, Jiuhui Zhao, Xiaobin Guo. "Experimental study of grain structures evolution and constitutive model of isothermal deformed 2A14 aluminum alloy", Journal of Materials Research and Technology, 2021 Publication	<1 %
49	Wen, W, M Borodachenkova, A Pereira, F Barlat, and J Gracio. "Hardening behavior and texture evolution of TWIP steel during strain path change", IOP Conference Series Materials Science and Engineering, 2015. Publication	<1 %

50	Zheng, Yufeng. "Biodegradation Mechanism and Influencing Factors of Mg and Its Alloys", Magnesium Alloys as Degradable Biomaterials, 2015. Publication	<1 %
51	ir.imr.ac.cn Internet Source	<1 %
52	A. Pardo, M.C. Merino, A.E. Coy, F. Viejo, R. Arrabal, S. Feliú. "Influence of microstructure and composition on the corrosion behaviour of Mg/Al alloys in chloride media", Electrochimica Acta, 2008 Publication	<1 %
53	M. Rajamuthamilselvan, S. Ramanathan. "Development of Processing Map for 7075 Al/20% SiCp Composite", Journal of Materials Engineering and Performance, 2011 Publication	<1 %
54	Rasool Ahmad, Binglun Yin, Zhaoxuan Wu, W.A. Curtin. "Designing high ductility in magnesium alloys", Acta Materialia, 2019 Publication	<1 %
55	S. W. Allison, G. T. Gillies. "Dual-doped thermographic phosphor particles as surrogates for green fluorescent protein-labeled cells in tests of cytometric	<1 %

neurocatheters", Journal of Applied Physics, 2010
Publication

56	S.L. Semiatin. "Plastic Flow and Microstructure Evolution during Low-Temperature Superplasticity of Ultrafine Ti-6Al-4V Sheet Material", Metallurgical and Materials Transactions A, 12/16/2009 Publication	<1 %
57	Watanabe, H.. "Effect of texture on high temperature deformation behavior at high strain rates in a Mg-3Al-1Zn alloy", Materials Science & Engineering A, 20091015 Publication	<1 %
58	Xiaoxue Chen, Guoqun Zhao, Xingting Zhao, Yongxiao Wang, Xiao Xu, Cunsheng Zhang. "Constitutive modeling and microstructure characterization of 2196 Al-Li alloy in various hot deformation conditions", Journal of Manufacturing Processes, 2020 Publication	<1 %
59	dr.ntu.edu.sg Internet Source	<1 %
60	www.ippt.pan.pl Internet Source	<1 %
61	C. Deslouis, D. Festy, O. Gil, V. Maillot, S. Touzain, B. Tribollet. "Characterization of	<1 %

calcareous deposits in artificial sea water by impedances techniques: 2-deposit of Mg(OH)2 without CaCO3", Electrochimica Acta, 2000
Publication

---

62 H. Wang, D.T. Zhang, C. Qiu, W.W. Zhang, D.L. Chen. "Achieving superior strength-ductility synergy in a heterostructured magnesium alloy via low-temperature extrusion and low-temperature annealing", Journal of Materials Science & Technology, 2023 <1%
Publication

---

63 Markandeya, R.. "Effect of prior cold work on age hardening of Cu-3Ti-1Cr alloy", Materials Characterization, 200612 <1%
Publication

---

64 Qin Qin, Mingliang Tian, Jinmiao Pu, Jianlin Huang. "Constitutive investigation based on the time-hardening model for AH36 material in continuous casting process", Advances in Mechanical Engineering, 2018 <1%
Publication

---

65 R. Vinjamuri, P. K. Dwivedi, R. K. Sabat, K. Dutta, M. Kumar, S. K. Sahoo. "Role of crystallographic orientation on the deformation behaviour of Ti-6Al-4V alloy during low cycle fatigue", Philosophical Magazine, 2023 <1%
Publication

66	Samantaray, D.. "A thermo-viscoplastic constitutive model to predict elevated-temperature flow behaviour in a titanium-modified austenitic stainless steel", Materials Science & Engineering A, 20091125 Publication	<1 %
67	V.V. Balasubrahmanyam. "Hot Deformation Mechanisms in Ti-5.5Al-1Fe Alloy", Journal of Materials Engineering and Performance, 12/01/2001 Publication	<1 %
68	Xiaoqiang Li, Qichi Le, Chenglu Hu, Tong Wang, Wenxin Hu, Lei Bao, Ping Wang, Dandan Li, Xiong Zhou. "Hot tensile deformation behaviour and microstructure evolution of Al3La phase reinforced Mg-5Li-3Al-2Zn alloy formed in-situ by La2O3 particle", Materials Characterization, 2022 Publication	<1 %
69	"Proceedings of the 6th International Conference on Recrystallization and Grain Growth (ReX&GG 2016)", Springer Science and Business Media LLC, 2016 Publication	<1 %
70	C. Dharmendra, K.P. Rao, M.K. Jain, Y.V.R.K. Prasad. "Role of loading direction on compressive deformation behavior of extruded ZK60 alloy plate in a wide range of	<1 %

temperature", Journal of Alloys and Compounds, 2018
Publication

71	hdl.handle.net Internet Source	<1 %
72	usermanual.wiki Internet Source	<1 %
73	www2.mdpi.com Internet Source	<1 %
74	Alvi, M.H.. "Cube texture in hot-rolled aluminum alloy 1050 (AA1050)-nucleation and growth behavior", Acta Materialia, 200808 Publication	<1 %
75	Qing Xiang, Bin Jiang, Yuxin Zhang, Xiaobo Chen, Jiangfeng Song, Junyao Xu, Liang Fang, Fusheng Pan. "Effect of rolling-induced microstructure on corrosion behaviour of an as-extruded Mg-5Li-1Al alloy sheet", Corrosion Science, 2017 Publication	<1 %
76	Rong Shi, Jiang Zheng, Tianjiao Li, Haoge Shou, Dongdi Yin, Jinsong Rao. "Quantitative analysis of the deformation modes and cracking modes during low-cycle fatigue of a rolled AZ31B magnesium alloy: The influence of texture", Materials Science and Engineering: A, 2022 Publication	<1 %

77	Yueming Du, Penghao Pei, Tao Suo, Guozhong Gao. "Large deformation mechanical behavior and constitutive modeling of oriented PMMA", International Journal of Mechanical Sciences, 2023 Publication	<1 %
78	www.jmaterenvironsci.com Internet Source	<1 %
79	A. Araghi, M. H. Paydar. " Wear and corrosion characteristics of electroless Ni–W–P–B C and Ni–P–B C coatings ", Tribology - Materials, Surfaces & Interfaces, 2014 Publication	<1 %
80	Sánchez-Martín, R., M.T. Pérez-Prado, J. Segurado, and J.M. Molina-Aldareguia. "Effect of indentation size on the nucleation and propagation of tensile twinning in pure magnesium", Acta Materialia, 2015. Publication	<1 %
81	Yeqing Cai, Song Xiang, Yuanbiao Tan. "Insight into the Dynamic Recrystallization Behavior and Microstructure Evolution of MP159 Superalloy During Hot Deformation", Metals and Materials International, 2022 Publication	<1 %
82	Madan Patnamsetty, Ari Saastamoinen, Mahesh C. Somani, Pasi Peura. "Constitutive	<1 %

modelling of hot deformation behaviour of a CoCrFeMnNi high-entropy alloy", Science and Technology of Advanced Materials, 2020
Publication

---

83 Matruprasad Rout, Surjya Kanta Pal, Shiv Brat Singh. "Finite Element Analysis of Cross Rolling on AISI 304 Stainless Steel: Prediction of Stress and Strain Fields", Journal of The Institution of Engineers (India): Series C, 2016 <1%
Publication

---

84 Submitted to Universidade Estadual de Campinas <1%
Student Paper

---

85 Submitted to University of Oklahoma <1%
Student Paper

---

86 Jiang, L.. "Effect of dynamic strain aging on the appearance of the rare earth texture component in magnesium alloys", Materials Science & Engineering A, 20110815 <1%
Publication

---

87 LÜ, Wen-quan, Guo-zheng QUAN, Chun-tang YU, Lei ZHAO, and Jie ZHOU. "Effect of strain, strain rate and temperature on workability of AZ80 wrought magnesium alloy", Transactions of Nonferrous Metals Society of China, 2012. <1%
Publication

88	M. C. Mataya. "Flow localization and shear band formation in a precipitation strengthened austenitic stainless steel", Metallurgical Transactions A, 07/1982 Publication	<1 %
89	Qidong Nie, Xiang Wang, Xinlin Li, Xudong Liu, Tingliang Yan, Jie Li. "Study on dynamic recrystallization behavior of 1MnCrMoNi steel during hot compression deformation", Materials Research Express, 2019 Publication	<1 %
90	Submitted to The University of Manchester Student Paper	<1 %
91	Wanru Tang, Zheng Liu, Shimeng Liu, Feng Zhang, Pingli Mao, Zhi Wang. "Deformation behaviour of ultrafine grained Mg–7Gd–5Y–1.2Nd–0.5Zr alloy under high strain rates", Materials Science and Technology, 2019 Publication	<1 %
92	dalspace.library.dal.ca Internet Source	<1 %
93	electrochemsci.org Internet Source	<1 %
94	Julien Couturier, Pierre Tamba Oularé, Blanche Collin, Claire Lallemand et al. "Yttrium speciation variability in bauxite residues of	<1 %

various origins, ages and storage conditions", Journal of Hazardous Materials, 2023
Publication

95	Uzumaki, E.T.. "Evaluation of diamond-like carbon coatings produced by plasma immersion for orthopaedic applications", Diamond & Related Materials, 200604/08 Publication	<1 %
96	Xiang, Song, and Guo Quan Liu. "Characterization of Hot Deformation of Nb-V-Ti Microalloyed Steel Using Processing Map", Advanced Materials Research, 2009. Publication	<1 %
97	jcsp.org.pk Internet Source	<1 %
98	Chaoyue Zhao, Xianhua Chen, Jingfeng Wang, Teng Tu, Yan Dai, Kwang Seon Shin, Fusheng Pan. "Strain Hardening Behavior in Mg–Al Alloys at Room Temperature", Advanced Engineering Materials, 2018 Publication	<1 %
99	Khaled, K.F.. "Studies of iron corrosion inhibition using chemical, electrochemical and computer simulation techniques", Electrochimica Acta, 20100901 Publication	<1 %

100	N. Srinivasan, Y.V.R.K. Prasad. "Hot-working characteristics of nichrome and the development of a processing map", Journal of Materials Processing Technology, 1994 Publication	<1 %
101	S. Jin. "Electrochemical Impedance Spectroscopy Evaluation of the Corrosion Behavior of Die Cast and Thixocast AXJ530 Magnesium Alloy in Chloride Solution", Advanced Engineering Materials, 02/2007 Publication	<1 %
102	Zhibin Yin, Zhouyi Xu, Rong Liu, Wei Hang, Benli Huang. "Microtrace Analysis of Rare Earth Element Residues in Femtogram Quantities by Laser Desorption and Laser Postionization Mass Spectrometry", Analytical Chemistry, 2017 Publication	<1 %
103	e-archivo.uc3m.es Internet Source	<1 %
104	repository.ubn.ru.nl Internet Source	<1 %
105	tsukuba.repo.nii.ac.jp Internet Source	<1 %
106	www.science.gov Internet Source	<1 %

107	C.Y. Wang, X.J. Wang, H. Chang, K. Wu, M.Y. Zheng. "Processing maps for hot working of ZK60 magnesium alloy", Materials Science and Engineering: A, 2007 Publication	<1 %
108	Lee, J.H.. "Effect of Al additions in WC-(Cr"1"-"xAl"x)N coatings on the corrosion resistance of coated AISI D2 steel in a deaerated 3.5 wt.% NaCl solution", Surface & Coatings Technology, 20050121 Publication	<1 %
109	Li Lu, Huihu Lu, Qingwei Kong, Kun Wang, You Li, Wei Liang, Huihui Nie. "Twinning and recrystallization behavior of AZ31 Mg-rolled sheets during the corrugated wide limit alignment process", Materials Science and Engineering: A, 2021 Publication	<1 %
110	Li, M.. "High temperature deformation behavior of near alpha Ti-5.6Al-4.8Sn-2.0Zr alloy", Journal of Materials Processing Tech., 20070305 Publication	<1 %
111	M. Suresh, R. Kalsar, A.M. More, A. Bisht, N. Nayan, S. Suwas. "Evolution of microstructure and texture in the third generation Al–Li alloy AA2195 during warm hybrid processing", Journal of Alloys and Compounds, 2020	<1 %

Publication

112	Manuel E. Palomar. "Imidazolium, Pyridinium and Dimethyl-Ethylbenzyl Ammonium Derived Compounds as Mixed Corrosion Inhibitors in Acidic Medium", Journal of Surfactants and Detergents, 10/28/2010 Publication	<1 %
113	Mingjia Wang, Wenrui Wang, Zhongli Liu, Chaoyang Sun, Lingyun Qian. "Hot workability integrating processing and activation energy maps of Inconel 740 superalloy", Materials Today Communications, 2018 Publication	<1 %
114	Mondal, D.P.. "Effect of SiC concentration and strain rate on the compressive deformation behaviour of 2014Al-SiCp composite", Materials Science & Engineering A, 20061015 Publication	<1 %
115	Nuno M. Pereira, Oana Brincoveanu, Aida Ghiulnare Pantazi, Carlos M. Pereira et al. "Electrodeposition of Co and Co composites with carbon nanotubes using choline chloride-based ionic liquids", Surface and Coatings Technology, 2017 Publication	<1 %
116	Reshma Sonkusare, N.P. Gurao, Krishanu Biswas, Joysurya Basu et al. "Micro-mechanisms of deformation and	<1 %

strengthening during high pressure torsion of CoCuFeMnNi high entropy alloy", Materialia, 2023
Publication

117	Rolando Guidelli. "4 Electrochemistry of Biomimetic Membranes", Modern Aspects of Electrochemistry, 2012 Publication	<1 %
118	X. Zhang, D. Kevorkov, M.O. Pekguleryuz. "Study on the binary intermetallic compounds in the Mg–Ce system", Intermetallics, 2009 Publication	<1 %
119	Zidoune, M.. "Comparative study on the corrosion behavior of milled and unmilled magnesium by electrochemical impedance spectroscopy", Corrosion Science, 200412 Publication	<1 %
120	c.coek.info Internet Source	<1 %
121	etheses.bham.ac.uk Internet Source	<1 %
122	repository.sustech.edu Internet Source	<1 %
123	ro.uow.edu.au Internet Source	<1 %
124	www.lle.rochester.edu Internet Source	<1 %

125	Aliakbar Emdadi, Heiner Michels, Michael Tovar. "Hot Workability Investigation of an Fe-Al-Ta Alloy Using Deformation Processing Maps", Metals, 2023 Publication	<1 %
126	Ardelean, H., A. Seyeux, S. Zanna, F. Prima, I. Frateur, and P. Marcus. "Corrosion processes of Mg–Y–Nd–Zr alloys in Na2SO4 electrolyte", Corrosion Science, 2013. Publication	<1 %
127	B. D. Chen, F. Guo, J. Wen. "Constitutive modeling for the hot deformation behavior of Mg-3.06Zn-0.58Zr-1.07Y alloy", Materialwissenschaft und Werkstofftechnik, 2015 Publication	<1 %
128	B. H. Rao, A. M. Bhat, D. N. Singh. "Application of impedance spectroscopy for modeling flow of AC in soils", Geomechanics and Geoengineering, 2007 Publication	<1 %
129	Biswas, S.. "Room-temperature equal channel angular extrusion of pure magnesium", Acta Materialia, 201005 Publication	<1 %
130	Cong Li, Can Huang, Zhili Ding, Xing Zhou. "Research on High-Temperature Compressive	<1 %

Properties of Ti–10V–1Fe–3Al Alloy", Metals, 2022
Publication

131 D SPARKS. "Redox Chemistry of Soils", Environmental Soil Chemistry, 2003 <1 %
Publication

132 D. H. Jang, W. J. Kim. "Warm Temperature Deformation Behavior and Processing Maps of 5182 and 7075 Aluminum Alloy Sheets with Fine Grains", Metals and Materials International, 2018 <1 %
Publication

133 Easton, M.A., M.A. Gibson, D. Qiu, S.M. Zhu, J. GrÃ¶bner, R. Schmid-Fetzer, J.F. Nie, and M.-X. Zhang. "The role of crystallography and thermodynamics on phase selection in binary magnesiumâ€“rare earth (Ce or Nd) alloys", Acta Materialia, 2012. <1 %
Publication

134 Jason P. Hadorn, Kerstin Hantzsche, Sangbong Yi, Jan Bohlen, Dietmar Letzig, Sean R. Agnew. "Effects of Solute and Second-Phase Particles on the Texture of Nd-Containing Mg Alloys", Metallurgical and Materials Transactions A, 2012 <1 %
Publication

135 Jin, Xue, Yang, Zhang, Zhang, Wang, Luo. "Constitutive Equation of GH4169 Superalloy <1 %

and Microstructure Evolution Simulation of Double-Open Multidirectional Forging", Metals, 2019
Publication

---

136 Liu, Q, G Wu, B Duan, and H Zhang. "Prediction of hot deformation behavior of biomedical materials TiNiNb SMA", Frontiers of Energy and Environmental Engineering, 2012.
Publication

<1 %

---

137 M. M. Hutchison, F. P. Bullen. "Solute-dislocation interaction in copper-antimony solid solutions", Philosophical Magazine, 1962
Publication

<1 %

---

138 N. Srinivasa, Y.V.R.K. Prasad. "Hot working characteristics of nimonic 75, 80A and 90 superalloys: a comparison using processing maps", Journal of Materials Processing Technology, 1995
Publication

<1 %

---

139 N. Srinivasan, Y. V. R. K. Prasad. "Characterisation of dynamic recrystallisation in nickel using processing map for hot deformation", Materials Science and Technology, 2013
Publication

<1 %

---

140 Nilesh Gurao. "Study of Texture Evolution at High Strain Rates in FCC Materials",

<1 %

Applications of Texture Analysis, 10/17/2008
Publication

141	S. Venugopal, S.L. Mannan, Y.V.R.K. Prasad. "Optimization of cold and warm workability in stainless steel type AISI 316L using instability maps", Journal of Nuclear Materials, 1995 Publication	<1 %
142	Sheed, Digvijay J., Bhagawati P. Kashyap, and Rajkumar P. Singh. "Grain Refinement in Ti-6Al-4V Alloy during Thermo-Mechanical Processing and Investigation of Flow Properties", TMS 2014 Supplemental Proceedings, 2014. Publication	<1 %
143	Shibo Zhou, Aitao Tang, Tingting Liu, Yuanding Huang et al. "Development of High Strength-ductility Mg-Er Extruded Alloys by Micro-alloying With Mn", Journal of Alloys and Compounds, 2023 Publication	<1 %
144	Songmin Lee, Chang Eun Song, Du Hyeon Ryu, Jungyoon Kim, Joonghan Kim, In-Nam Kang. "Single and Double Alkoxybenzothiadiazole–Dithienosilole-Based Nonfused Ring Electron Acceptors for Organic Solar Cells", ACS Applied Energy Materials, 2023 Publication	<1 %

145	Sumantra Mandal, P. V. Sivaprasad, V. Subramanya Sarma. "Dynamic Recrystallization in a Ti Modified Austenitic Stainless Steel During High Strain Rate Deformation", Materials and Manufacturing Processes, 2010 Publication	<1 %
146	Xia, Xiangsheng, Qiang Chen, Shuhai Huang, Jun Lin, Chuankai Hu, and Zude Zhao. "Hot deformation behavior of extruded Mg–Zn–Y–Zr alloy", Journal of Alloys and Compounds, 2015. Publication	<1 %
147	Xu, S.W.. "Recrystallization mechanism of as-cast AZ91 magnesium alloy during hot compressive deformation", Materials Science & Engineering A, 20091215 Publication	<1 %
148	Yongquan Ning, Zekun Yao, Yingyi Lei, Hongzhen Guo, M.W. Fu. "Hot deformation behavior of the post-cogging FGH4096 superalloy with fine equiaxed microstructure", Materials Characterization, 2011 Publication	<1 %
149	ZhangSheng Liu, BianTao Wu, MingYuan Gu. "Effect of AlN particles on the corrosion behavior of Al/AlNP composites", Journal of Materials Science, 2007	<1 %

	Publication	
150	library.immaculata.edu Internet Source	<1 %
151	oaktrust.library.tamu.edu Internet Source	<1 %
152	perpustakaan.poltekkes-malang.ac.id Internet Source	<1 %
153	tigerprints.clemson.edu Internet Source	<1 %
154	trepo.tuni.fi Internet Source	<1 %
155	Łukaszek-Sołek, Aneta, and Janusz Krawczyk. "The analysis of the hot deformation behaviour of the Ti–3Al–8V–6Cr–4Zr–4Mo alloy, using processing maps, a map of microstructure and of hardness", Materials & Design, 2015. Publication	<1 %
156	Congzhong Wen, Hui Pan, Jinghu Li. "Flow characterization and microstructure evolution of high-temperature steel F92 during hot deformation", Applied Physics A, 2022 Publication	<1 %
157	Materials Forming Machining and Tribology, 2015. Publication	<1 %

158 S. Suwas, N.P. Gurao. "Development of Microstructures and Textures by Cross Rolling", Elsevier BV, 2014 <1%
Publication

159 Xiangsheng Xia, Qiang Chen, Kui Zhang, Zude Zhao, Minglong Ma, Xinggang Li, Yongjun Li. "Hot deformation behavior and processing map of coarse-grained Mg–Gd–Y–Nd–Zr alloy", Materials Science and Engineering: A, 2013 <1%
Publication

160 B.D. Bishoyi, R.K. Sabat, S.K. Sahoo. "Effect of temperature on microstructure and texture evolutions during uniaxial compression of commercially pure titanium", Materials Science and Engineering: A, 2018 <1%
Publication

161 Gurao, N.P.. "Study of texture evolution in metastable @b-Ti alloy as a function of strain path and its effect on @a transformation texture", Materials Science & Engineering A, 20090325 <1%
Publication

162 Jue Lu, Yanli Song, Lin Hua, Kailun Zheng, Dingguo Dai. "Thermal deformation behavior and processing maps of 7075 aluminum alloy sheet based on isothermal uniaxial tensile tests", Journal of Alloys and Compounds, 2018 <1%

Publication

163	Martien Duvall Deffo Ayagou, Thi Tuyet Mai Tran, Bernard Tribollet, Jean Kittel et al. "Electrochemical impedance spectroscopy of iron corrosion in H 2 S solutions", Electrochimica Acta, 2018 Publication	<1 %
164	Pardo, A.. "Corrosion behaviour of magnesium/aluminium alloys in 3.5wt.% NaCl", Corrosion Science, 200803 Publication	<1 %
165	S.V.S. Narayana Murty. "Hot working characteristics of powder metallurgy Nimonic AP-1 superalloy", Powder Metallurgy, 03/01/2001 Publication	<1 %
166	Tan, Qiyang, Andrej Atrens, Ning Mo, and Ming-Xing Zhang. "Oxidation of magnesium alloys at elevated temperatures in air: A review", Corrosion Science, 2016. Publication	<1 %
167	Zhanshou Yang, Yaping Dong, Wu Li, Xin Liu, Haitao Feng. "Effect of Sr on hot deformation behavior and microstructure of Al-4.6Mg alloy", Journal of Alloys and Compounds, 2023 Publication	<1 %
168	S Narayana Murty. "On the hot working characteristics of 6061Al–SiC and 6061–Al2O3	<1 %

particulate reinforced metal matrix composites", Composites Science and Technology, 2003

Publication

Exclude quotes	On	Exclude matches	Off
Exclude bibliography	On		